DISSERTATION

HYBRID FRAMEWORK FOR ANALYZING REINFORCED CONCRETE SKEWED AND CURVED BRIDGES WITH STOCHASTIC TRAFFIC LOADS

Submitted by

Luke Chen

Department of Civil and Environmental Engineering

In partial fulfillment of the requirements

For the Degree of Doctor of Philosophy

Colorado State University

Fort Collins, Colorado

Summer 2025

Doctoral Committee:

Advisor: Yanlin Guo

Hussam Mahmoud
Suren Chen
Rebecca Atadero
Alexander Brandl

ABSTRACT

HYBRID FRAMEWORK FOR ANALYZING REINFORCED CONCRETE SKEWED AND CURVED BRIDGES WITH STOCHASTIC TRAFFIC LOADS

Reinforced concrete (RC) bridge with skewness or curvature geometry is a common alternative design to overcome terrain obstacle or facilitate highway alignments. Irregular bridge geometric configuration results in completely different performances under earthquakes, traffic loading or long-term distress (e.g., corrosion, fatigue) compared to straight bridges. A better understanding of performances of irregular bridges is crucial for their design and maintenance. In current practice, there is lack of systematic understanding of influence of bridge skew angle and curvature on the structural performance. Also, the existing analysis methods adopt oversimplified structural modeling techniques that prevent proper consideration of traffic loads distribution on irregular bridges. In light of these limitations in the existing studies, the objective of this dissertation is to advance the performance analysis methods of RC skewed and curved bridges under more realistic loading conditions. This dissertation proposes a hybrid framework that integrates detailed finite element (FE) modeling with stochastic traffic simulations to realistically assess the performance of RC skewed and curved bridges. The framework begins with seismic fragility analyses of bridge models under varied geometric configurations, identifying how skewness and curvature amplify

vulnerability. A parametric study is conducted to investigate how different earthquake and traffic conditions affect the seismic performance of skewed and curved bridges. Then stochastic traffic loads are incorporated to study vehicle-bridge interactions under seismic events. Structural responses derived from these simulations are further utilized to conduct fatigue life assessments, accounting for both traffic-induced stresses and long-term deterioration like rebar corrosion. The proposed approach provides deeper insights into the combined effects of traffic, seismic loading, and fatigue on skewed and curved RC bridges, offering a more reliable basis for design, maintenance and retrofitting for these bridges.

ACKNOWLEDGEMENTS

I would like to express my deep appreciation to my committee member and former advisor Dr. Suren Chen for his great guidance and encouragement over the majority of my time at CSU. I am grateful to the opportunity he provided me for most of the research topics. His knowledge and patience have enabled me to overcome challenges of both academic and self-health issues. Without his patience, the completion of my dissertation would not have been possible. I would like to thank my current advisor, Dr. Yanlin Guo for her supervise and persistence for my last two years of research works and dissertation. I would also like to thank my committee members, Dr. Hussam Mahmoud, Dr. Rebecca Atadero, and Dr. Alexander Brandl for their invaluable suggestions and comments to this dissertation. Last but not least, I would like to thank my parents and my brother for their support and understanding throughout my research journey.

DEDICATION

To my parents

TABLE OF CONTENTS

LIST OF TABLES

LIST OF FIGURES

CHAPTER 1 INTRODUCTION

1.1 Background

Bridges are critical nodes of the modern highway network. Due to the limitations of budgets, spatial constraints, field construction environment, etc., 45% of bridges in the U.S. have lengths less than 60ft and are defined as “short-span bridges” (Azizinamini, 2009). Due to the need to overcome natural barriers and facilitate highway alignments, many short-span bridges are skewed and/or curved. Designs of skewed and/or curved bridges have steadily increased in the U.S. for the past decades. The development of the techniques to precast reinforced concrete girders with prestressed rebars has made the construction of skewed and curved bridges easier, which has boosted the design of more skewed or curved short- or medium-span concrete bridges. The trend of increasing skewed or curved concrete bridges is expected to continue in the future (Barnoff et al., 1984.; Sun et al., 2007). Nearly 33.5% of highway bridges in the U.S are skewed bridges (Chun, 2010). According to a well-cited report conducted by the Structural Stability Research Council (SSRC Task Group 14, 1991), 20% to 25% of newly built bridges in the U.S. were curved bridges by the time the report was published. Based on a count on the recently updated National Bridge Inventory (NBI) database in 2023, about 9,500 bridges in the U.S. contain skewness or curvature in their design.

In the U.S., after several devastating earthquake events, such as the 1971 San Fernando and 1994 Northridge earthquakes, studies about the dynamic response of bridges subjected to seismic excitations have gained more attention (Protection, 1983; Werner et al., 1987). According to the statistical analyses of the damaged bridges following the 1994 Northridge earthquake, 200 out of 221 damaged highway bridges were concrete girder box bridges with short and medium spans (Basöz et al., 1999; Basöz & Kiremidjian, 1998). Among all the vulnerable bridges damaged by previous major earthquakes, such as the 1992 Cape Mendocino earthquake (Goel & Chopra, 1997), 1994 Northridge Earthquake(Meng et al., 2001) and 2010 Chile earthquake (Mitchell et al., 2013), studies have noticed that that skewed and curved concrete bridges have unique failure modes and/or behavior during seismic events (Ates & Constantinou, 2011), which has not been considered in the bridge design when building those bridges (Mander et al., 1996). According to the damage investigation of reinforced concrete bridges with large skew angles, unseating of bridge girders or large deck displacement has been reported, which is more significant damage than the damage typically observed in straight bridges (Aldea et al., 2021; Dimitrakopoulos, 2011; Y. Wang, 2020; S. Wu et al., 2019). Field seismic assessments indicated that earthquakes could induce severe damage to piers of horizontally curved bridges (Billah et al., 2013; . Wang, 2020; Zhi et al., 2019). Tondini and Stojadinovic (Tondini & Stojadinovic, 2012) found that the column ductility in the transverse direction is inversely proportional to the deck radius through a probabilistic model. Li et al. (2015) performed shake table tests on a 1/10-scale

curved bridge model to study the effect of multidimensional excitations. It was found that site condition and ground motion characteristics can significantly influence the seismic behavior of curved bridges.

Besides bridges with either skewness or curvature designs, bridges with both skewness and curvature have become more common for short- or medium-span bridges. However, studies of both skewed and curved bridges under seismic excitations are still scarce. Wilson et al. (2014) conducted a numerical study investigating the combined effects of curvature and skewness on the bridge's seismic performance. Despite the limited deformation due to the low seismic intensity site condition, their results show that the demand increases for diagonally opposite columns as the skew angle increases; meanwhile, the low radius of curvature induced a higher moment for the interior pier columns. It was also observed that the coupling effects of skewness and curvature can lead to more considerable demand on bridge structural members than the sum of the individual loading effects due to skewness or curvature. Seismic performance assessment of simple-made-continuous (SMC) skewed and curved bridges in low-to-moderate seismic regions was performed by Hou and Chen (2017). Their comparative study, which focuses on the bent connections at the pier, indicated that skewness and curvature of bridges could significantly affect the seismic behavior regardless of the type of connection. It also suggested conducting a detailed fragility assessment when determining the optimal bent connection. Serdar and Folić (2018) selected the column drift ratio as the baseline of seismic demand to generate probabilistic seismic demand models for a set of bridge configurations, including skewness and curvature. They found that the column drift induced by skewness

may be reduced by the deck's curvature under low seismic intensities (i.e., arching effect). However, the arching effect disappears with the further reduction of bearing capacity and pier stiffness, which can lead to increased seismic demand. Heidari and Gerami (2019) examined the damage mechanisms of the column and diaphragm abutment failures of skewed and curved bridges. They found that the ground motion direction and the bridge skew angle are key parameters affecting seismic demand. In summary, past field inspections and experiments have identified the unique failure modes for bridges with irregular geometric configurations, such as skewness and curvature.

Apart from seismic analysis, there is also dedicated research on traffic loading effects on bridges. In the early studies, vehicles were typically considered as moving forces (Weaver Jr et al., 1991) or moving masses (Blejwas et al., 1979), which have been incorporated in the bridge design guidelines such as Japan Road Association codes (2002) and AASHTO guide specifications for LRFD seismic bridge design (Transportation Officials. Subcommittee on Bridges, 2011). In many later studies, loads caused by moving vehicles were either modeled as a static load at specific locations or implicitly considered in the analytical response equations by introducing a load modification coefficient (Frýba & Yau, 2009; C. Lu et al., 2011; Zhu & Frangopol, 2013). Other studies focused on optimizing the live load distribution factors based on the simplified traffic loads, resulting in a significant variation of live loads on superstructures (Leahy et al., 2015; Song et al., 2003). Morales-Nápoles and Steenbergen (2015) have proposed a method of hybrid nonparametric Bayesian networks for modeling traffic loads. The traffic load model was found

trustworthy but required a large amount of weigh-in-motion data in the modeling process. Li, et al. (2018) found that vehicles often have eccentric loads applied on curved bridges, which could induce possible torsion and vibration on the bridge structure. Ashebo et al. (2007) conducted a full-scale field test about load distribution on a skewed bridge in normal traffic conditions. Their numerical model results show good agreement with the field test experiment under a single truck load with 27° degrees skew angle. Their parametric study shows that the influence of skewness on structural behavior becomes significant for the skew angle greater than 30°.

Beyond the pure seismic or traffic load analysis, researchers have also investigated the coupling effects of seismic ground motion and traffic load on bridges. There have been only a few studies on the bridge seismic analysis considering vehicle and bridge dynamic interactions, including numerical studies by Kameda (1992) and Kim et al. (2007) with simple vehicle and bridge models. Ghosh et al. (2014) proposed a framework of joint seismic and traffic load fragility assessment of bridges, where the traffic load is modeled using the assumed traffic flow with a constant speed for a representative truck. Kameshwarand Padgett (2018) studied the impacts of vehicles on the bridge's seismic response and fragility by assuming that the vehicles were not in motion. The study covered three types of stationary trucks and found that traffic load can significantly impact the bridge's seismic fragility. Borjigin et al. (2018) applied both a single cargo truck loading and a vertical ground motion to a simplified 3D pier-beam bridge model. They found that the vehicle loadings would likely change the bridge's seismic behavior. Another study by

Zhou and Chen (2018) revealed that the coupling effects between the bridge–traffic system and the earthquake excitations significantly influence the pseudo-static and dynamic response of the bridge girder in the vertical and torsional directions.

Studies on how the skewness/curvature of the superstructure affects traffic loads and how they may influence the bridge's seismic response are sparse. There is a lack of studies that consider both seismic and traffic loads simultaneously for skewed or curved bridges. Only a few researchers studied the coupling of traffic and seismic loads on curved bridges. Wibowo et al. (2012) conducted the large-scale shake table experiment with a single platoon of H-20 trucks as static live loads on the 2/5-scale three-span and horizontally curved bridge model. Benedettini et al. (2015) refined the modal dynamic analysis of curved bridges by involving the traffic load influence in the bridge's modes. It was found that the vehicular traffic load caused a substantial increase in the shearing stiffness of seismic isolator, which may reduce the bridge horizontal deformation due to lateral seismic load.

The deck slab is considered as one of the most vulnerable components of a concrete bridge to fatigue damage due to high cycle loads of moving vehicles. Oh (1986) proposed an experimental test to fit the Weibull probability distribution to predict the flexural fatigue strength of concrete. Tests in later studies focused on acquiring S-N curve-related parameters like strength envelopes, failure modes, and cyclic deformations to describe fatigue behavior (Ahmed et al., 1999a; Graf & Brenner, 1934; Yin & Hsu, 1995a). These experiments led to the establishment of standards/codes for concrete fatigue assessment based on

material strength, such as the EN 1992-1-1 (EN 1992-1-1: Eurocode 2: Design of Concrete Structures - Part 1-1: General Rules and Rules for Buildings, 2004). Further improvement in recent standards/codes includes changing the testing loads from static to dynamic loads or cyclic loads (FIB model code 2010., 2013; ACI PRC-215-21, 2021). Such concrete fatigue assessment specified in standards/code is limited to concrete specimens at the material level, which are tested in the laboratory. Next, the fatigue studies were extended to the structural level. Probability and reliability methods were introduced to determine the influence of numerous variables on fatigue, such as concrete compressive strength and impacts of vehicle mass and velocity (Basaga et al., 2012; Frangopol et al., 2008). Kwon and Frangopol (2010) collected field monitoring data from existing bridges to generate probability density functions (PDFs) of parameters for fatigue performance assessment. Wang et al. (2018) adopted one of the two main key parameters from the Kwon and Frangopo study, i.e., equivalent stress range, and performed the Monte Carlo simulation to calculate a fatigue reliability index. Bridge fatigue performance could also be affected by the occurrence and propagation of cracking. Schläfli and Brühwiler (1998) conducted experiments based on the ACI 318M-02 code and concluded that the code is only satisfactory when the bridge deck is in good condition. Firouzi and Rahai (2011) applied PDFs and homogenous Gaussian 2D random field to predict the spatial distribution of fatigue damage with Monte Carlo simulation. However, selecting variables for fatigue reliability assessment may not be straightforward for users and heavily based on the researchers' choice. For example, Kwon and Frangopol (2010) defined two variables, i.e., "equivalent stress range" and

"detailed coefficient". Zhang et al. (2024) use the following variables in their fatigue reliability analysis: critical fatigue damage, fatigue strength coefficient, equivalent stress range, cycle count, etc. Some variables in Zhang et al. (2024)'s study, such as fatigue strength coefficient, cycle count and stress ranges, are determined based on Euro3 and ACI-215 (PRC, 2021; British Standards, 1993). Soriano et al. (2017) investigated different representative variables, such as truck traffic intensity, duration of weight-in-motion data collection, etc., in their fatigue reliability analysis. Kim and Song (2021) studied the effects of reinforcement rebar corrosion on fatigue reliability, thus using variables related to both corrosion states and traffic loads.

Highway bridges are exposed to various aggressive environmental conditions throughout their service life. Most of the highway bridges in the U.S. were designed for approximately 50 years in service. However, 42% of bridges in the U.S. (259,175 bridges) are over 50 years old, according to the ASCE Infrastructure Report Card (ASCE Committee on America's Infrastructure, 2021). The report card also pointed out that the structurally deficient bridges are 69 years in service on average. These old bridges have been exposed to aggressive environmental conditions, such as moisture ingress, CO_2 penetration, and chloride ion attack for extended periods, which may increase their risk of steel bar corrosion and various concrete deteriorations, including spalling, patching, scaling, or cracking. Rebar corrosion is very common, especially for highway bridges in coastal areas where the air is full of chloride ions and in many northern states where deicing material is often applied during winter. Concrete deterioration can be classified as

surface or subsurface defects based on their visible or measurable signs (Bien et al., 2007; Maksymowicz et al., 2006; Yehia et al., 2007), and each type of defect may not be correlated to the other or belong to the same deteriorate mechanism. Based on past studies, it can be claimed that there is little or no relationship between crack width and corrosion (Gu et al., 2015; Jang et al., 2011; Matsumoto et al., 2008; Schießl & Martin, 1969; Tremper, 1947), but any visible surface cracks on the bridge deck will accelerate or immediately initiate rebar corrosion (Berrocal et al., 2015; Francois & Arliguie, 1999; W. Li et al., 2017; Misra & Uomoto, 1991), and eventually turn part of the rebar surface into rust mass (Jaffer & Hansson, 2008; Michel et al., 2016; Schießl & Raupach, 1997). Researchers have attempted to evaluate the rebar corrosion in concrete decks. For example, Konecny and Lehner (2017) utilized Monte Carlo simulation for probabilistic evaluation of bridge deck chloride corrosion initiation. The use of field inspection method and data processing method is also a major research direction for evaluating rebar corrosion in concrete decks (Abdelkader et al., 2023; Alsharqawi et al., 2022; Faris et al., 2024). For example, the ground-penetrating radar (GPR) measures the reflected electromagnetic waveforms to detect rebar corrosion (Eisenmann et al., 2013; H. Liu et al., 2022; Martino et al., 2016). The electrical resistivity (ER) method uses resistivity values to measure corrosion rate (Chalhoub et al., 2020; Morris et al., 2004). The galvanostatic pulse measurement (GPM) detects the corrosion from the electrochemical potential drop between low resistance anodic and cathodic sites, which can only occur to a corrosive rebar (Ahn & Reddy, 2001).

The reinforced concrete failure attributed to coupled fatigue and corrosion has been recorded in the analysis report conducted in the early 2000s(Wardhana et al., 2003). In the 2010s, most of the fatigue-corrosion studies have been focus on the concrete beam component. Yi and Tang (2010) conducted fatigue test on reinforced concrete beam specimens and verified that mass loss percentage of corroded rebar is one of the major factors which significantly reduce fatigue life. Zhang and Yuan (2014) developed nonlinear cumulative fatigue damage models considering dynamic vehicle loads and corrosion states. Although the model was developed for steel bridges, the study found that corrosion induced fatigue strength reduction have a large effect on fatigue life. The study of coupled rebar corrosion and concrete bridge deck fatigue is limited. Yang et al. (2017) proposed theoretical assessment of concrete bridge deck with two ultimate states of fracture-failure modes for the tensile rebars and compressive concrete. The study indicates that fatigue safety of concrete bridge deck subjected to coupled fatigue and corrosion is controlled by tensile steel fatigue.

1.2 Limitations of existing studies

Several research gaps can be summarized from the aforementioned studies of the effects of seismic loads, traffic loads, concrete bridge fatigue, and rebar corrosion on the performance of skewed and curved concrete bridges.

Firstly, the modeling of bridges with skewness and curvature in the literature is oversimplified. The existing literature has focused on achieving computing efficiency with simplified models. The most

common simplification is to model the bridge superstructure (including girders and deck) as spine elements, which is based on the LRFD seismic design manual (Marsh et al., 2014). This modeling method has been widely adopted by many state departments of transportation (Caltrans, 2022). In the spine models, the bridge substructure is typically modeled to stay ductile, and the superstructure behaves elastically during earthquakes. This type of simplified model has been widely adopted for bridges with skewness and/or curvature. The skewed bridge modeling generally uses less detailed elements along the spine, whereas curved bridge modeling requires more elements to represent the spine with curvature (Kataria and Jangid, 2016; Seo and Rogers, 2017; Tan et al., 2024). However, these simplified spine models do not allow the modeling of realistic traffic loads that exhibit temporal and spatial variations. The existing studies chose a stationary load at the critical location of the bridge model (W. S. Kim et al., 2007; Nettis et al., 2024; T. Wang et al., 2023). The oversimplified single stationary vehicle load may lead to the risk of ignoring other non-critical location traffic loads and underestimation of dynamic loading effects due to vehicle-bridge interaction. The combination of low-fidelity spine models for skewed and/or curved bridges and the simplified traffic load has led to potentially inaccurate numerical results.

Secondly, the existing studies on the effects of seismic and traffic loads on skewed and curved bridges are limited. The existing studies on seismic effects on skewed and curved bridges have not systematically analyzed structural performance under a wide spectrum of characteristics of earthquakes (Haseli et al., 2024; Jeon et al., 2016; Pantelides et al.,2016.). Furthermore, the research on the coupling effects of seismic and

traffic loads on skewed and/or curved bridges is lacking (Kesharee Patra et al., 2024; Nguyen et al., 2019; Wibowo et al., 2013).

Thirdly, the reliability-based fatigue analysis in the literature discussed in Section 1.1 has a large discrepancy in the selection of variables, which renders the selection of reliability analysis frameworks difficult for a user. In addition, the validation of these reliability-based fatigue analyses relied on the weight-in-motion data. The results could be affected by the number and location of sensors in weight-in-motion stations (Bayane et al., 2019).

Fourthly, while most of the studies on coupled corrosion and fatigue effects focus on beam elements (Verma and Mishra, 2019; Yi and Tang, 2010; Zhang et al., 2016), few studies have investigated the influence of rebar corrosion on concrete deck fatigue (Yang et al., 2017). In the limited studies on this topic, realistic traffic conditions have not been modeled. Also, the current corrosion evaluation method based on monitoring or inspection data can be limited by the cost or logistical challenges due to traffic control and for difficult to access bridges, as well as the large uncertainties of inspection methods (Faris et al., 2024; Lim et al., 2020; Samson et al., 2018).

1.3 Motivation

Due to the progressive advancement of construction methods, more bridges have adopted the skewness and curvature design. However, the performance of skewed and curved bridges under earthquakes, coupled earthquakes and traffic loads, as well as their deck fatigue performance have not been well-

understood. In this context, this study focuses on developing numerical analysis frameworks to comprehensively investigate the performance of concrete skewed and curved bridges due to earthquake loads, coupled earthquake and traffic loads and fatigue. In the proposed frameworks, detailed 3D finite element models will be developed to address the limitations of oversimplified modeling scheme in the existing literature. The proposed detailed 3D finite element models will allow for accurate consideration of realistic traffic loads on bridges with irregular geometry, overcoming the limitation of the simplified traffic load currently used in the literature. Furthermore, this study will enable the prediction of fatigue damage of skewed and curved bridge decks due to coupled traffic loads and rebar corrosion, providing an alternative analytical fatigue analysis methods that do not rely on intensive data collection. The proposed analysis framework will allow designers/bridge managers to evaluate the potential coupled seismic and traffic risk and better understand long-term bridge performance due to fatigue and rebar corrosion.

1.4 Objectives

This dissertation aims at advancing the analysis of the structural performance of skewed and curved bridges and improving the understanding of risks of skewed and curved bridges. The objectives of the study are summarized as follows.

(1) Develop a framework to comprehensively analyze the performance/risks of concrete skewed and curved bridges under various loading conditions (e.g., earthquake, traffic loads);

(2) Develop a framework of deck fatigue analysis for concrete skewed and curved bridges that allows the consideration of traffic loads and rebar corrosion.

1.5 Dissertation layout

The objectives mentioned above are achieved via five tasks, described in Chapters 2-6, respectively. Chapter 2 presents analytical fragility studies on four typical bridge designs with different geometric configurations (i.e. straight, curved, skewed, skewed and curved) in Colorado to enhance understanding of the seismic risks and the impact from the irregular geometric configurations. Chapter 3 proposes a hybrid simulation approach to study the coupling effects among the bridge, moving vehicles and earthquake at the same time for skewed and curved bridges. This nonlinear analysis framework of the bridge/traffic/earthquake system integrates the stochastic traffic flow simulation, the model-based fully-coupled simulation technique of the bridge-traffic system and the nonlinear seismic analysis platform developed based on OpenSees. Using the proposed analysis framework proposed in Chapter 3, Chapter 4 conducts a parametric study to investigate the different seismic characteristics such as primary input directions, vertical ground motions, near-fault and pulse-like ground motions and three different traffic conditions to provide more insights about the critical contributing factors on the performance of a skewed and curved bridge. Chapter 5 presents a comprehensive fatigue performance assessment of reinforced concrete bridge decks under dynamic traffic-bridge interaction for skewed and curved bridges. Chapter 6 proposes a comprehensive framework to evaluate the fatigue performance of reinforced concrete bridge

decks by incorporating the coupling effects of traffic loading and rebar corrosion. The study highlights the importance of coupled traffic-corrosion fatigue modeling for more accurate service life predictions and informs maintenance planning by identifying critical deck areas for repair or replacement. Chapter 7 concludes the dissertation by discussing the major contributions and future research directions.

CHAPTER 2 SEISMIC PERFORMANCE OF CURVED AND SKEWED HIGHWAY BRIDGES

2.1 Introduction

Bridges are key components of modern transportation systems, which are typically classified as critical infrastructure. Based on rational vulnerability assessments, post-seismic functionality and serviceability of bridges can be evaluated, which directly affect the resilience of this type of critical infrastructure to seismic hazard. Seismic fragility analysis is a type of important seismic vulnerability assessment approach that can convert sophisticated seismic vulnerability of structures into a relation between conditional damage probability and ground motion intensity (e.g. Xiao and Ma 1997, Kowalsky and Priestley 2000 and Ellingwood and Kinali 2009). Its concept is widely adopted not only in academic research fields, but also in engineering and risk management practices, such as HAZUS-MH by Federal Emergency Management Agency (FEMA) (Vickery et al. 2006). During the past twenty years, extensive work has been conducted on bridge fragility analyses, which were primarily focused on bridges with regular geometric configurations.

Horizontally curved and/or skewed bridges are often built to accommodate local terrain constraints such as in the mountain west region of the United States. Fragility analyses of those bridges with special geometric features, such as curved and/or skewed bridges, are very rare. Sullivan and Nielson (2010) conducted sensitivity study of bridges with a variety of skewed angles and compared component responses

in longitudinal and transverse directions. Zakeri et al. (2014) investigated the impacts of skew on the seismic performance of integral abutments and suggested that the component fragilities are independent of the geometric configuration if shear keys are added. It was found that bridges with skew and those with curvature share some common vulnerabilities, such as being susceptible to deck unseating, tangential joint damage, pounding effects as well as large in-plane deformation and rotations of the superstructure (Saiidi and Orie 1992; Maragakis, 1984; Mwafy and Elnashi, 2007). As compared to studies on bridges only with skew or with curvature, the seismic performance studies on bridges with combined curved and skewed geometric configurations are very rare. Wilson et al. (2014, 2015) studied the seismic dynamic performance of both skewed and curved bridges in the states of Colorado and Washington, respectively. The comparative results between the both curved and skewed bridges and their respective straight counterparts suggest that some unique trends deserve further studies in order to guide future designs of this type of irregular bridges against seismic.

Mountain west area in Colorado is a typical low-to-moderate seismic region. In the present study, fragility analysis is conducted on the representative bridges with both curved and skewed configurations selected from the mountain west region in Colorado. A suite of 3-D finite element models (FEM) for the bridge considering various uncertainties are built by modifying those originally developed by Wilson et al. (2014) with SAP2000. With both recorded and synthetic ground motions ranging from 0.1g to 1.0g Peak Ground Acceleration (PGA), nonlinear time history analyses of the bridge models are carried out

considering uncertainties associated with ground motions and structural properties. Based on the time history analysis results, the Probability Seismic Demand Model (PSDM) and then fragility curves are further developed. Through the comparative studies of bridge models with four typical geometric configurations (i.e. straight, curved-only, skewed-only and both curved and skewed), the impacts of skew and curvature on the bridge fragility performance are assessed.

2.2 Bridge finite element modeling

2.2.1 Prototype bridge and 3-D finite element models

A typical straight bridge on the interstate I-25 located in Colorado is selected as the prototype for 3-D finite element models (FEM) in Fig. 1(a), based on which several bridge models with various skew and curvatures are further built (Wilson et al., 2014)). Multiple models with different combinations of bridge skew and curvature are established using SAP2000 and the related limit states for bridge seismic analyses are determined through extensive literature review of related studies.

In order to study skewed and curved bridges based on realistic designs, some reasonable geometric variations from the straight prototype bridge were made (Wilson et al., 2014). For low-to-moderate seismic region, curved and/or skewed bridges often adopt the same design criteria as the straight counterparts when the curvature and/or skew are moderate. Therefore, the design details for these bridges with geometric variations are same as those for the prototype bridge. Such an arrangement has two advantages: (1) same design detail as the straight counterpart is pretty common for curved and skewed bridges in the region, yet

without comprehensive evaluation in terms of seismic performance and risk; (2) same designs of these bridge models allow for better investigations on the effects from geometric configurations by excluding other possible influences. As illustrated in Table 1, three representatives bridge models with different curved and skewed configurations (i.e. curved only, skewed only and both skewed and curved) are modified from the straight bridge model. The FEM analytical models of the straight prototype bridge and the curved and skewed bridge are shown in Fig. 1 (b)-(c) and Fig. 1(d)-(e), respectively. In the following sections, detailed fragility analyses are conducted for the four bridge models as listed in Table. 1.

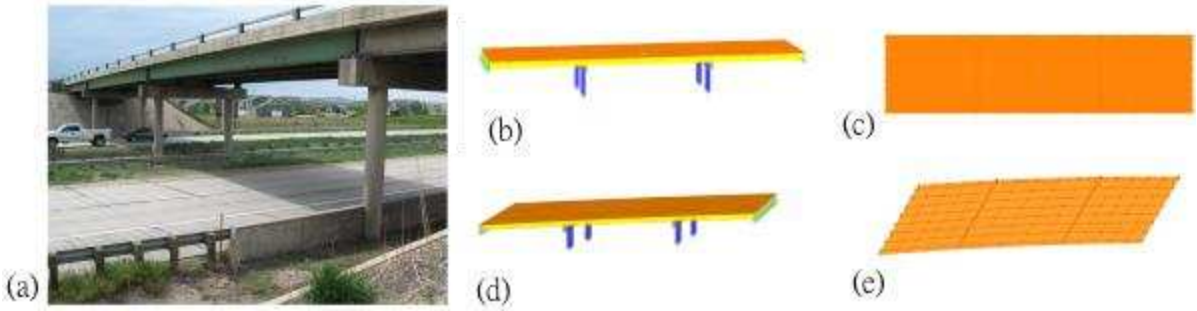

Fig. 1 Prototype 3D FEM bridge model and the variations (Wilson et al., 2014): (a) prototype bridge (Graphic by Google Map), (b) straight bridge side view, (c) straight bridge top view, (d) skewed and curved bridge side view, and (e) skewed and curved bridge top view

Table. 1 Geometric configurations of bridge model

Bridge type	Skew (degrees)	Curvature Radius (ft.)	Super Elevation (degrees)
Straight	0	0	0
Skewed only	30	0	0
Curved only	0	3000	6
Skewed and Curved	30	3000	6

3-D FEM numerical models are developed with SAP2000 (CSI 2011) for the four bridge models listed in Table. 1 (Wilson et al., 2014). Fig. 2 gives the modeling details of the bridge components including columns, integral abutments, bent caps and girders. The four semi-ellipse columns are labeled as column A-D, which are modeled as beam elements for both columns and pier caps with the bottom of the bridge pier fixed in the soil in all directions. In order to observe seismic inelastic response, plastic hinges are placed at both column ends with a relative distance suggested by the Washington State Department of Transportation Design Manual (WSDOT, 2002). Gaps between each span are simply supported by concrete bent cap rigidly connected with two RC columns on each side.

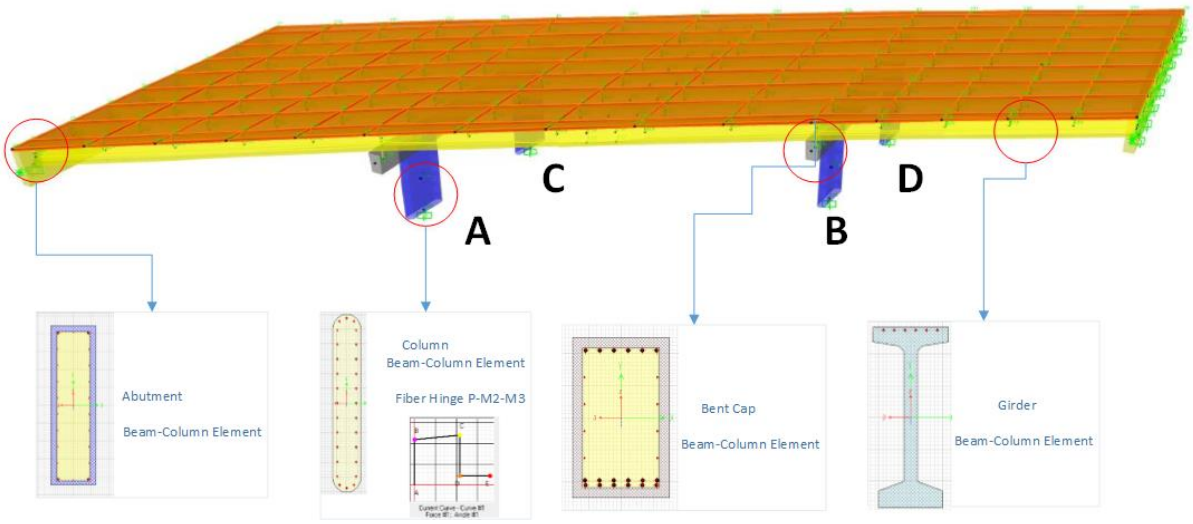

Fig. 2 Section modeling details

The integral abutments of the bridges are also modeled as beam elements with rigid connections to the end of the girders. Pile foundations of the abutments in all directions are fixed except for the longitudinal direction. Multi-linear compressive spring elements are applied in this direction based on the California Department of Transportation (Caltrans) design procedures for backing soil behind an integral abutment (Caltrans, 2006). Plastic hinges with a lumped plasticity model are implemented at the top and bottom of the pier-columns to account for the inelastic column behavior of the substructure. In most of the bridge fragility analyses, superstructures were modeled with simplified elements or lumped as concentrate mass attached to the substructure. However, in order to capture the horizontal curvature characteristics in a better way, bridge decks are modeled as thin shell elements with 4 by 4 meshing. The eight girders are modeled as frame elements, which are connected with the bridge deck by use of fully constrained rigid links.

2.2.2 Probability seismic demand model (PSDM)

The first step to generate fragility curves is to establish probability seismic demand model (PSDM). According to the study by Baker and Allin Cornell (2005), the median of structural demand S_d can be statistically described as an exponential distribution:

$$S_d = a * PGA^b \tag{2.1}$$

or

$$\ln(S_d) = \ln(a) + b * \ln(PGA) \tag{2.2}$$

where coefficients "*a*" and "*b*" can be determined by the regression analysis of the data points obtained from the time history analyses.

Based on Eq. (2.2), the cumulative conditional probability distribution of seismic demand exceeding a certain level of structural capacity C under the corresponding seismic intensity can be obtained once the standard deviation $\beta_{D|IM}$ is estimated:

$$P[D \geq C \mid IM] = 1 - \Phi\left(\frac{\ln(d) - \ln(aIM^b)}{\beta_{D|IM}}\right) \tag{2.3}$$

where $P[D \geq C|IM]$ is the conditional probability that the seismic demand of structure (D) is greater than structural capacity (C) under specific seismic intensity (IM). $\Phi(.)$ is the standard normal cumulative distribution function. S_d is the median value of seismic demand of the pre-defined limit state.

With the assumption that the structural capacity and its seismic demand both have lognormal distributions, the concept of demand/capacity ratio is incorporated into Eq. (2.4) (Nielson, 2005):

$$P[D \geq C \mid IM] = \Phi\left(\frac{\ln(S_d / S_c)}{\sqrt{\beta_{D|IM}^2 + \beta_c^2}}\right) \tag{2.4}$$

where S_c is the median of the estimated capacity of the pre-defined limit state; β_c is the standard deviation of the estimated capacity; $\beta_{D|IM}$is the seismic demand standard deviation under specific seismic intensity IM.

The key steps of developing the fragility curves are summarized as follows and also in the flowchart as shown in Fig. 3:

(1) Build 3-D FEM models for each bridge as listed in Table. 1, including the straight bridge and also the curved and skewed variations. Based on the sensitivity analysis, finalize uncertainties being considered in the study and apply those variables with uncertainties to the developed models.

(2) Select representative ground motions with intensities distributed from low to high based on the site characteristics. If the ground motion from the database record is lacking, synthetic ground motions are generated for appropriate intensity coverage.

(3) Perform nonlinear time-history analyses on the FEM bridge models with uncertainties being considered, subjected to the representative ground motions. Obtain component seismic demands and apply regression analysis to obtain the coefficients “a” and “b” in Eq. (2.1) and Eq. (2.2).

(4) Define appropriate structural limit states from literature, specifications and/or survey.

(5) Calculate analytical fragility curve following Eq. (2.4).

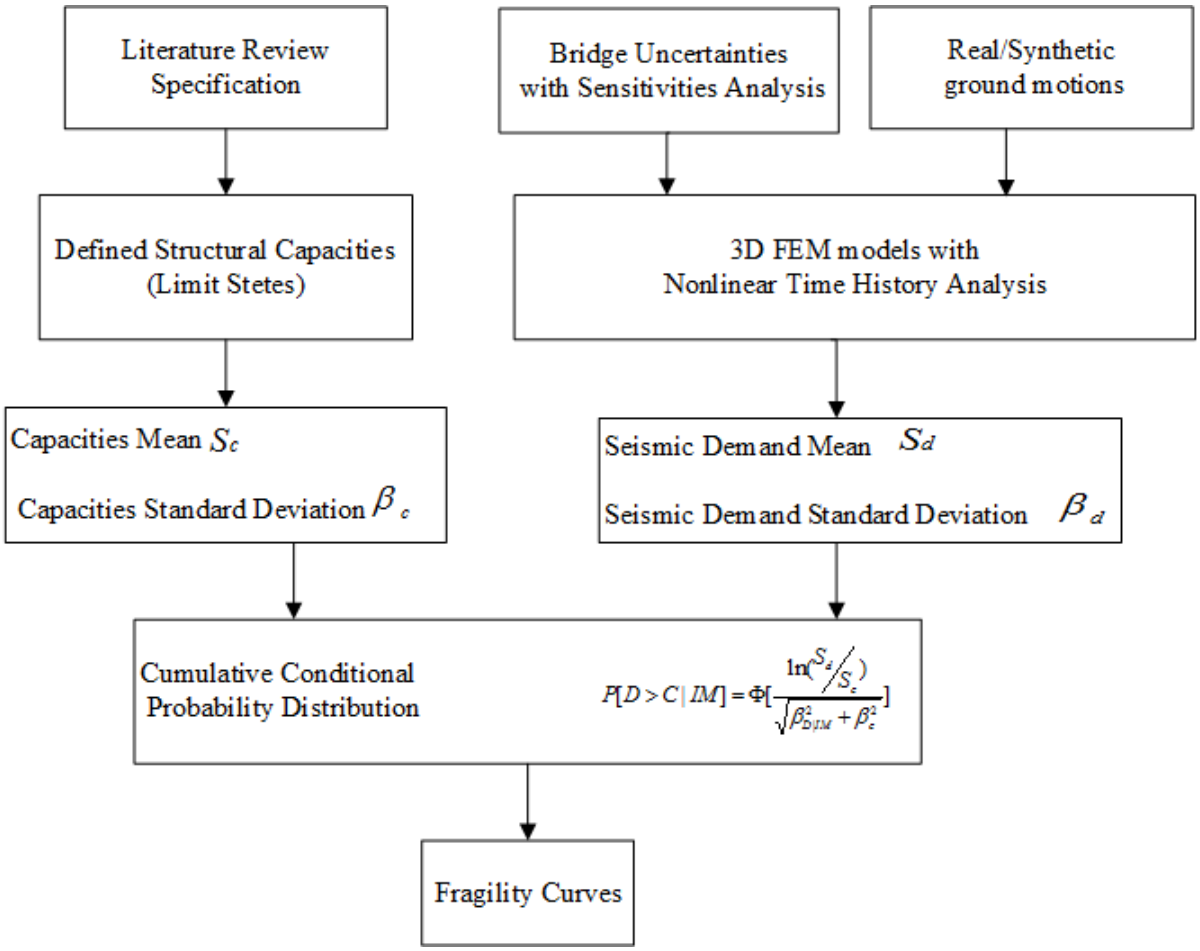

Fig. 3 Schematic diagram for component fragility curves construction

2.3 Uncertainties of bridge structures and sensitivity analysis

In order to conduct fragility analyses with limited samples, major uncertainties need to be appropriately considered. Most uncertainties associated with structures modeling can be classified into two categories: epistemic and aleatory uncertainties. The former one generally originates from model assumptions, simplified variables in formulas or lack of knowledge, which requires statistical uncertainties being

incorporated into the numerical model. The later one is attributed to the inherent randomness in the seismic demand and capacity models, which means that the aleatory uncertainties should be considered when input ground motions or structural capacity models are selected.

Before incorporating structural uncertainties into the FEM models, an extensive sensitivity analysis is conducted to evaluate which variables are more critical in terms of considering uncertainties during the fragility curve development process. The sensitivity analysis is conducted under the excitation of the Whittier Narrows-01 earthquake (PGA=0.2g). The results show that concrete strength, steel yield strength, damping ratio and superstructure weight affect the bridge seismic performance pretty significantly and should be included into the models with considerations of uncertainties (Fig. 4).

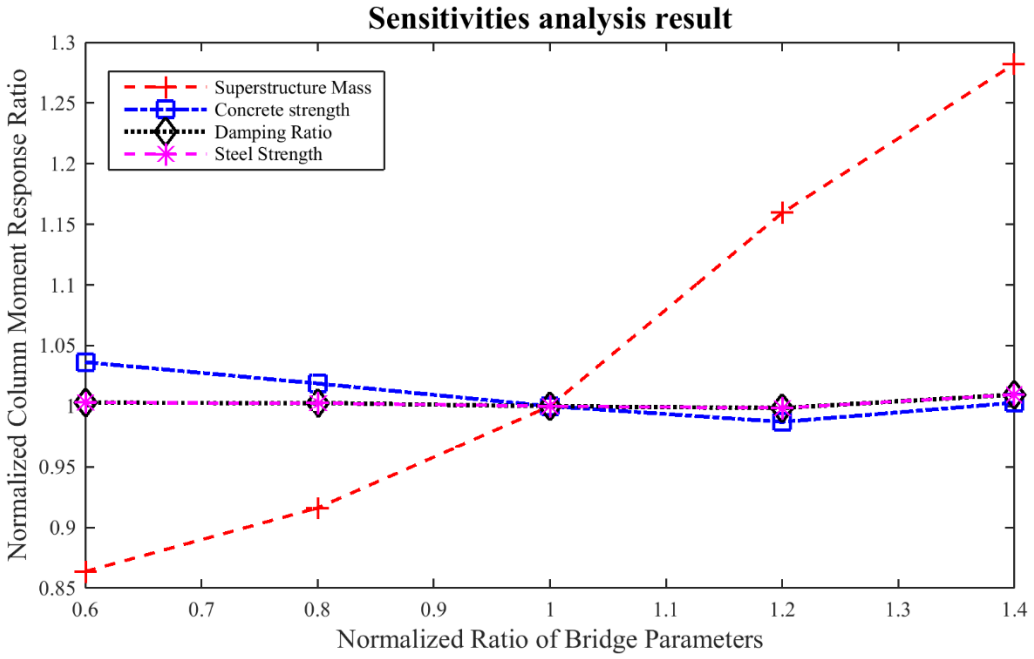

Fig. 4 Sensitivities analysis result

In the absence of site-specific data, the uncertainty distributions of the variables in this study are decided primarily based on a comprehensive literature review of similar variables in existing studies. Based on the site-specific conditions, several assumptions and modifications are made in order to accommodate the specific bridge conditions and the uncertainty results are summarized in Table. 2. The selected parameters based on the sensitivity analysis are then assigned to the models using Latin Hypercube Sampling (LHS) approach (Neves et al., 2006). The sampling method is used to ensure the variables allocated to model parameters based on particular probability distributions within a small number of samples, which will eventually lower the epistemic uncertainties. After applying the LHS, variables can be formed into a matrix, of which each row represents one FEM model with uncertainties (Table. 3). In this study, eight models are generated for different geometric configurations, each of which is paired with twelve ground motions, generating 96 data points in total.

Table. 2 Bridge uncertainties distribution

Bridge Parameter	Distribution Type	Mean	Deviation	Units	Reference
Compressive Concrete Strength	Normal	35.8	5.376	MPa	MacGregor et al. (1997)
Steel Yield Strength	Log-normal	463.3	37.07	MPa	Ellingwood & Hwang (1985)

Damping Ratio	normal	0.045	0.0125	Fang et al.(1999)
Superstructure Weight	Uniform	0.9–1.1	0	Nielson (2005)

Table. 3 Bridge uncertainties assignment based on LHS

	Density	**f'_c (kip)**	**F_y (kip)**	**Damping ratio**
1	0.151436	5.5166	66.3596	0.064486
2	0.14665	4.6244	68.0511	0.051163
3	0.16435	5.4006	72.1427	0.044602
4	0.139488	5.1094	59.4386	0.039779
5	0.145969	5.8012	75.9749	0.035814
6	0.161118	5.2671	64.6231	0.025715
7	0.136277	5.0403	62.5961	0.046521
8	0.156359	4.9216	69.8798	0.056484

Note: **f'_c** = Compressive Concrete Strength (Kip); **F_y** = Steel Yield Strength (Kip)

2.3.1 Compressive concrete strength

Generally, the compressive concrete strength of bridges follows normal distributions, but its mean value can vary considerably over different regions in the U.S. For example, eastern states such as New York State use 20.7 MPa in their standard design, which results in the mean value of 27.2 MPa and a standard

deviation of 4.24 MPa (Pan et al. 2007). However, in Central and Southeastern United States (CSUS), concrete strength typically has the mean value of 33.5 MPa and standard deviation of 4.3 MPa (Nielson 2005). In this study, by considering the site-specific conditions, the mean and standard deviation of the concrete strength are assumed to be similar to those obtained from the 5-ksi class experimental data (MacGregor et al. 1997), which are 35.8 MPa and 5.376 MPa, respectively.

2.3.2 Steel yield strength

For composite material like concrete, the specific failure mode (e.g. shear failure or flexure failure) for RC columns is usually dependent on individual components of the composite material. Thus, the uncertainty characteristics of reinforced steel and concrete are considered separately in this study. According to the findings in the statistical study by Ellingwood and Hwang (1985), the strength characteristics of the rebar are adopted to represent the steel strength uncertainty. The steel strength follows lognormal distribution, with mean and standard deviation for steel strength being 463.3Mpa and 37.07Mpa, respectively.

2.3.3 Damping ratio

The prototype bridge used in this study falls into the category of Multi-Span Continuous Concrete Girder (MSCCG) Bridges. In Nielson's study (Nielson, 2005), the damping ratio distribution for MSCCG was estimated based on the study results from tall building (Fang et al. 1999) and typical damping ratio for bridges (Bavirisetty et al., 2000). Without further site-specific data, the damping ratio in this study follows

the results by Nelson (2005) with a normal distribution and the mean and standard deviation values of 0.045 and 0.0125 respectively.

2.3.4 Superstructure weight

Although the bridge superstructure typically has less direct effect from seismic ground motions as compared to substructure and thus tends to remain elastic behavior, its weight could still have considerable effects on the seismic performance due to horizontal curvature and asymmetric layouts. Following the findings by Nielson (2005), the uncertainty of superstructure weight is attributable to the material density of the bridge deck, which is assumed to have a uniform distribution for a ratio between 0.9 and 1.1.

2.4 Ground motion simulation

Ground motions used in this study are a set of 96 earthquake records consisting of 48 real and 48 synthetic ground motions as described in the following sections. In order to study the impacts of skew and curvature on the bridge seismic performance, an input ground motion combination of 100% intensity in longitudinal direction and 40% in transverse direction was found to control the time history analysis (Wilson et al. 2014), which is also adopted in the following study.

2.4.1 Ground motion from database record

In order to properly reflect the seismic geographic features of Colorado, local seismic characteristics such as magnitude, Joyner-Boore distance and shear wave velocity have been considered during the selection of earthquake records from the Pacific Earthquake Engineering Research Center (PEER) ground motion database. Earthquake selection with a range from 4.5 to 8.5 Richter magnitude covers low-to-high seismic intensity. Ground motions with Joyner-Boore distance from 20 km to 100 km are selected according to the study of the fault lines distribution in Colorado by Matthews (2003). For the ground motion shear wave velocities (Vs30), their selection criteria are determined by site soil condition, which is the default D class soil with a range from 600 to 1200 ft./s according to the AASHTO LRFD specification (AASHTO 2013). Table. 4 shows a typical suit of ground motion records used in this study.

Table. 4 Ground motion records from PEER

Event	**Year**	**Station**	**Longitudinal PGA (g)**	**Transverse PGA(g)**
Morgan Hill	1984	SF Intern. Airport	0.04783	0.04781
Chalfant Valley-01	1986	Bishop - LADWP South St	0.12943	0.09441
Santa Barbara	1987	UCSB Goleta	0.34022	0.34022
Northridge	1994	5360 Saturn St., Los Angeles	0.42029	0.42029
Imperial Valley-06	1979	Delta	0.23776	0.35112
San Fernando	1971	LA – Hollywood Story FF	0.20988	0.17418

2.4.2 Synthetic ground motion

A reliable PSDM requires representative ground motion inputs for time-history analysis to reduce its aleatory uncertainties. In most of the interpolate regions such as California, ground motions can be selected from the database including PEER or U.S. Geological Survey (USGS) covering low to high seismic intensities. The mountain west region is lack of strong ground motion records and therefore synthetic ground motions are widely applied in fragility curve studies of the areas without sufficient seismic records (Choi 2002; Nielson and DesRoches 2007; Padgett and DesRoches 2007). Synthetic ground motions generated for this study follow Nielson's work (2005) with modification developed by Baker and Cornell (2005) in order to have a good coverage of different intensities. The generation procedure of synthetic ground motions is briefly introduced as follows: (1) Synthetic accelerograms are generated based on the determined parameters and corrected in frequency domain; (2) accelerograms are then adjusted to the site-specific target response spectrum according to the USGS map; and (3) every single synthetic ground motion is then used as a "seed" ground motion to generate orthogonal ground motions using correlation factors (Baker and Cornell 2005). Table. 5 shows the selected synthetic ground motions generated in this study.

Table. 5 Synthetic ground motions generated for this study

Magnitude	Rjb (km)	Longitudinal PGA (g)	Transverse PGA(g)
6.0	60	0.57925	0.42831
6.5	60	0.64219	0.47302
7.0	60	0.51839	0.36556
6.0	40	0.58859	0.44692
6.5	40	0.70115	0.46789
7.0	40	0.81668	0.6134

2.5 Limit states

Structural capacities discussed in the previous section are defined by limit states (or damage states), which determine the structural quantitative seismic demands causing damage to bridge components. In general, limit states can be determined through physics-based (e.g. experimental) approach, descriptive (e.g. expert survey) approach (Padgett and DesRoches, 2007) or Bayesian approach (Nielson, 2005). In this study, limit states are decided based on the literature review of the related studies and the selected ones are listed in Table. 6 with details illustrated in the following.

Table. 6 Limit States used in the study with mean values and correlation factors

	Slight		**"Moderate"**		**Extensive**		**Complete**	
Component	S_c	β_c	S_c	β_c	S_c	β_c	S_c	β_c
Col-Long	0.0025	0.59	0.0040	0.51	0.0067	0.64	0.0010	0.65
Col-Trans	0.00033	0.59	0.00055	0.51	0.00092	0.64	0.00140	0.65
Shr-Long (Kips)	N/A		N/A		N/A		731.59	N/A
Shr-Trans (Kips)	N/A		N/A		N/A		630.85	N/A
Abut-p (ft.)	0.12	0.25	0.24	0.25	0.85	0.46	2.43	0.46
Abut-a (ft.)	0.06	0.25	0.12	0.25	0.36	0.46	0.71	0.46
Wing (ft.)	0.12	0.25	0.24	0.25	0.85	0.46	2.43	0.46

Note: S_c = Median values of component limit states; β_c = dispersions of component limit states; Col-Long = column longitudinal curvature; Col-Trans = column transverse curvature; Shr-Long = Pier-Column Longitudinal shear strength; Shr-Trans = Pier-Column Transverse shear strength; Abut-a = abutment active deformation; Abut-p = abutment passive deformation; Wing = wing wall deformation

2.5.1 Column moment curvature

Bridge columns are one of the critical components to seismic response that can result in different failure modes. In most of the fragility curve studies, flexural damage to bridge column is generally quantified based on the drift ratio (Shinozuka et al. 2002; Mackie and Stojadinović 2007; Zhang and Huo 2009) or

ductility (Nielson and DesRoches 2007; Padgett and DesRoches 2008). For fragility analysis in this study, curvature ductility is determined as the limit state following the capacity estimation by Hwang's (2000) work and Federal Highway Administration's Seismic Retrofitting Manual for Highway Bridges (FHWA, 1995) equation. Hwang (2000) proposed limit states in terms of displacement ductility as 1.0, 1.2, 1.76 and 4.76 to respectively represent "light", "moderate", "extensive" and "complete" damage states in FEMA (2003). While the transformation equations for displacement ductility (μ_Δ) and curvature ductility (μ_ϕ) can be found in Ref (FHWA, 1995):

$$\mu_\phi = 1 + \frac{\mu_\Delta - 1}{3\frac{l_p}{l}\left(1 - 0.5\frac{l_p}{l}\right)} \tag{2.4a}$$

where l is the column length and l_p is the plastic hinge follow by Eq. (2.4a) which is based on the diameter of the longitudinal reinforcement d_b:

$$l_p = 0.08l + 9d_b \tag{2.4b}$$

The column ductility under "light", "moderate", "extensive" and "complete" damage states is defined with the mean values of 1.29, 2.1, 3.52 and 5.24, and with the corresponding parameter β_c of 0.59, 0.51, 0.64 and 0.65, respectively. The curvature ductility is later transfer into the curvature as shown in Table. 6.

2.5.2 Pier-column shear strength

Shear force on the bridge pier-column component is also one critical demand and could easily exceed its capacity during a seismic event. Because shear failure is a type of brittle failure and hard to be assessed

with different serviceability conditions, only the "complete" damage state for shear strength in both directions is considered based on its damage model. The shear damage model considers the column concrete shear strength V_c, steel shear strength V_s and axial shear strength V_p (Priestley et al., 1996).

$$V_{total} = V_c + V_s + V_p \tag{2.5a}$$

where

$$V_c = k\sqrt{f_c^{'}}A_e \cong 0.232\sqrt{f_c^{'}}A_g \tag{2.5b}$$

$$V_s = \frac{A_{sw}f_y D^{'}}{s}\cot\theta = \frac{A_{sw}f_y D^{'}}{s}\cot 30^o \tag{2.5c}$$

$$V_p = \tan\alpha = \frac{D-c}{L}P \tag{2.5d}$$

$f_c^{'}$ = concrete compressive strength; A_g =section gross area; s=rebar spacing; L=rebar spacing; f_y = steel yield strength; D= section diameter; P= axial force; c = compression zone depth; $D^{'}$ =rebar diameter.

2.5.3 Abutment and wing-wall deformation

Abutment is another critical component for bridge seismic design, which has been often investigated in fragility studies (e.g. Kwon and Elnashai 2007; Billah et al. 2012). Deformation due to seismic ground motions not only cause failure to the back wall, but also enhance particular behaviors such as pounding effect when skew is considered (Zakeri et al. 2014). According to the study by Choi (2002), passive deformation limit state of the integral abutment is defined as fraction of the maximum deformation capacity of the back fill soil ($y_{\max}$) such as 0.005 $y_{\max}$, 0.01 $y_{\max}$, 0.35 $y_{\max}$ and $y_{\max}$ for "light", "moderate",

"extensive" and "complete" damage, respectively. In this study, $y_{\max}$ is assumed to be 2.42 ft. following the study by Sucuoğlu and Erberik (2004).

2.5.4 Regression analysis to develop PSDM

The time-history seismic analysis results of the selected structural components are represented as data points in the response-seismic intensity plots for nonlinear univariable regression analysis. According to the observation in the previous studies, it was found that most of the bridge models experience stacking effect on different columns, causing different seismic behavior on the interior and exterior columns (Wilson et al. 2014). Thus, the regression analysis results for different columns are discussed individually.

With the assumption of lognormal distributions, the PSDM results of the longitudinal curvature for the skewed and curved bridge show considerable difference among different columns (Fig. 5). For comparison purposes, the longitudinal curvature PSDM results for the straight bridge are shown in Fig. 6. It is apparent that the PSDM results for the skewed and curved bridge are more scattered than those for the straight bridge. In the following fragility curve development, the differences among the regression lines of different columns will also be found to affect the results of probability distribution.

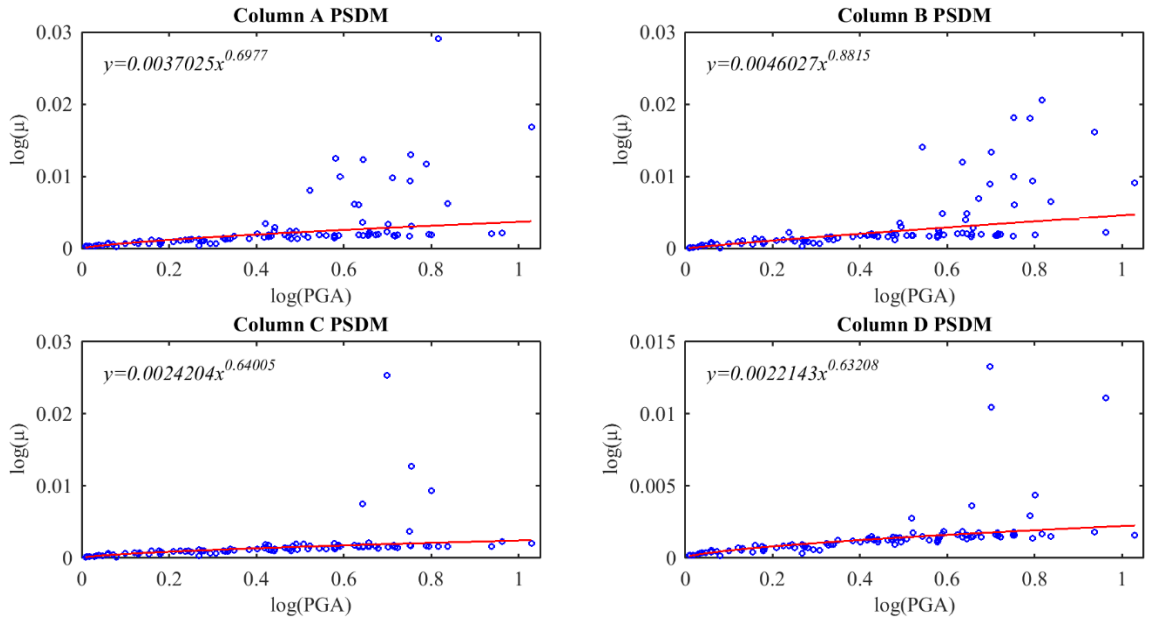

Fig. 5 Column longitudinal curvatures PSDM for the curved and skewed bridge

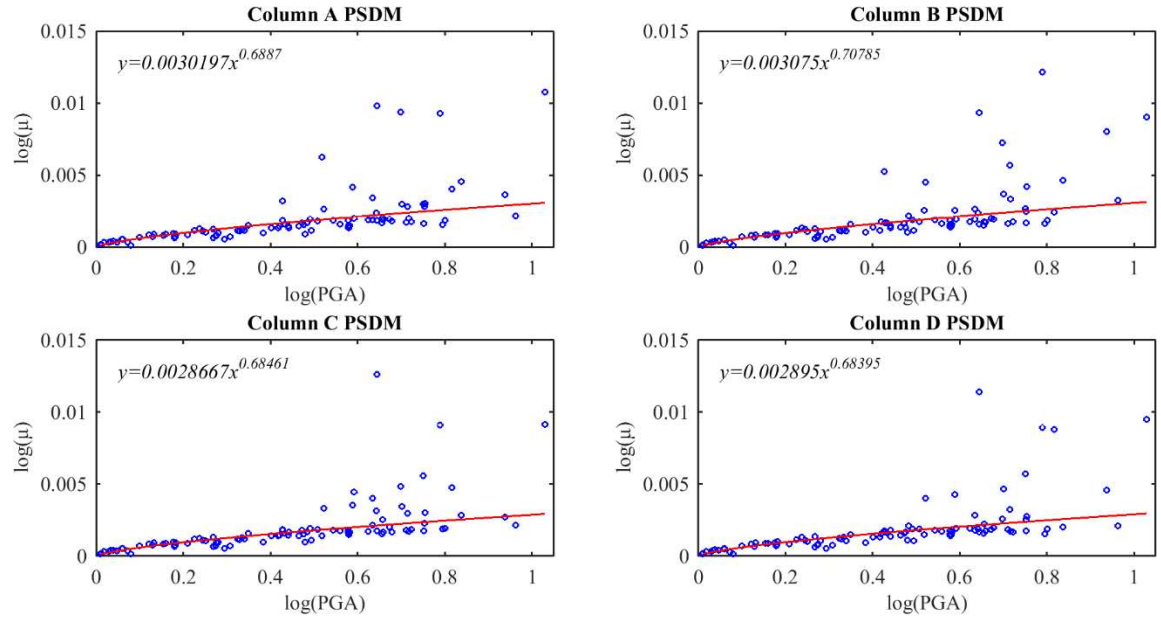

Fig. 6 Column longitudinal curvatures PSDM for the straight bridge

The PSDM results of the column-pier shear strength in the longitudinal and transverse directions for the skewed and curved bridge are shown in Fig. 7 and Fig. 8, respectively. The column shear PSDM results

for the skewed and curved bridge also vary among different columns (Fig. 7 and Fig. 8) and the largest one can reach almost twice as that for the straight counterpart (not listed for the sake of brevity).

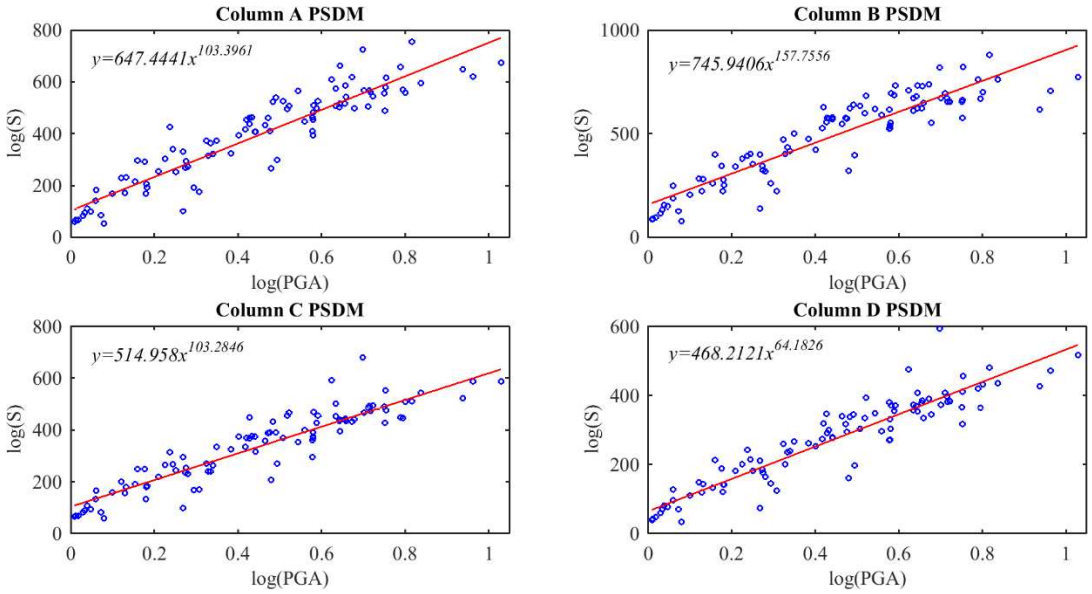

Fig. 7 PSDM of column longitudinal shear strength for the curved and skewed bridge

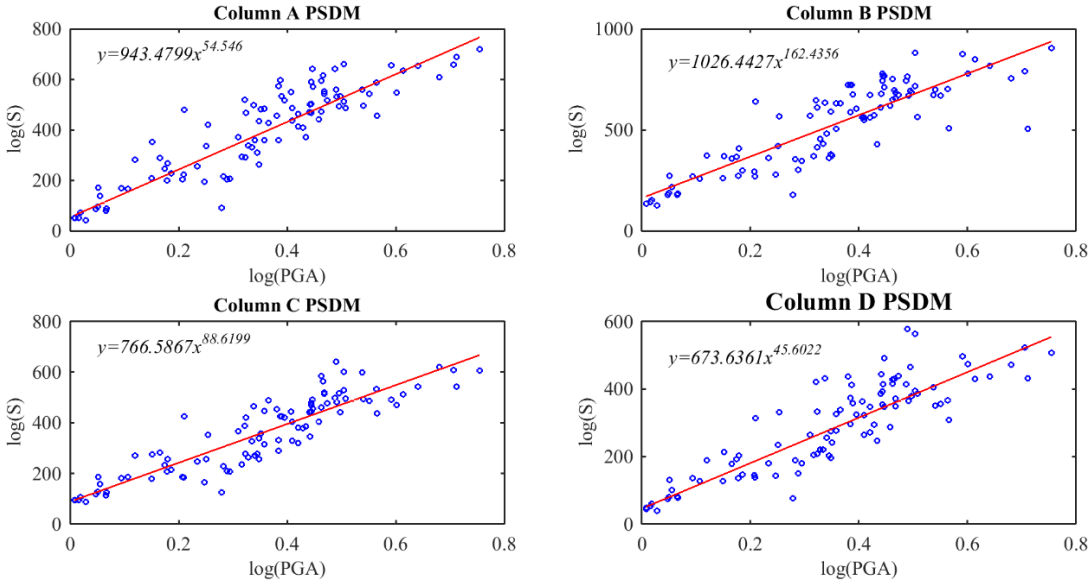

Fig. 8 PSDM of column transverse shear strength for the curved and skewed bridge

Fig. 9 shows the regression analysis results of the abutment deformation and wing wall response for the skewed and curved bridge. The passive and active longitudinal deformation only slightly vary from

each other for the skewed and curved bridge. Table. 7 summarizes the regression coefficients in Eq. (2.1) as well as their standard deviation "Beta" and coefficient of determination "R^2".

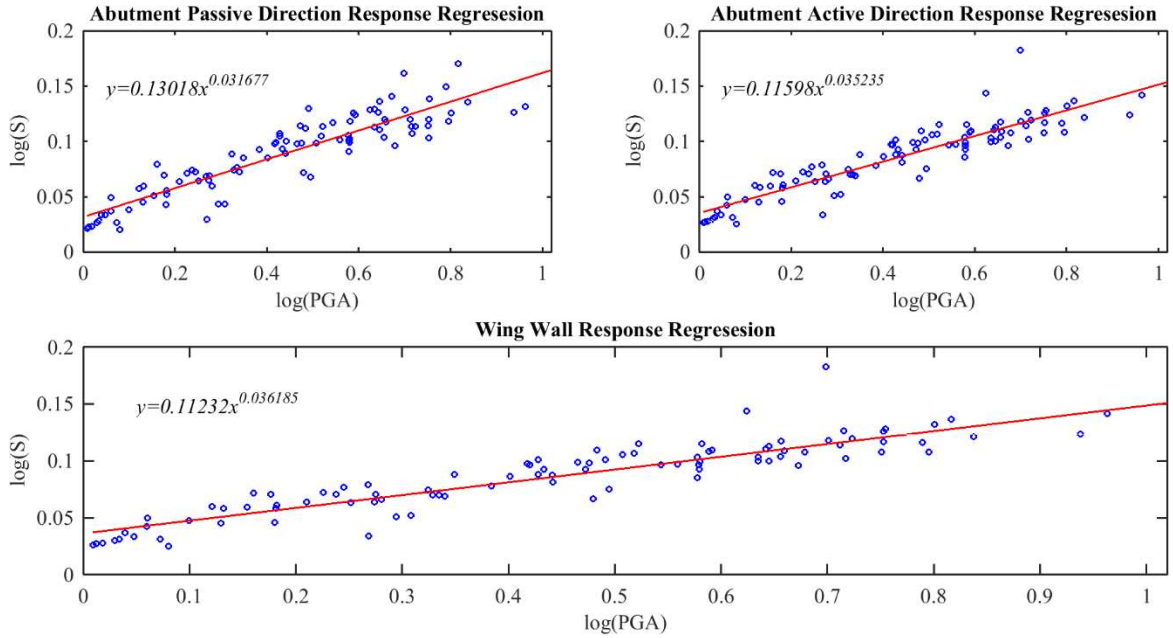

Fig. 9 PSDM of abutment deformation for the curved and skewed bridge

Table. 7 Probabilistic seismic demand parameter regression of straight bridge model

Demand Response	**a**	**b**	β_d	R^2
Col-Long (A)	0.0037	0.7011	0.928425	0.6977
Col-Long (B)	0.0045	0.882	1.081222	0.8815
Col-Long (C)	0.0024	0.6472	0.802926	0.642
Col-Long (D)	0.0022	0.6368	0.765687	0.6321
Col-Trans(A)	0.0009	0.8242	0.992762	0.7984

Col-Trans(B)	0.0018	0.972	1.239829	0.9671
Col-Trans(C)	0.0006	0.7088	0.883541	0.7028
Col-Trans(D)	0.0004	0.6132	0.73181	0.6249
Shr-Long (A)	658.16	0.5896	0.63103	0.5896
Shr-Long (B)	788.93	0.5475	0.586098	0.5475
Shr-Long (C)	533.3	0.5382	0.578591	0.5382
Shr-Long (D)	452.72	0.5913	0.631935	0.5913
Shr-Trans (A)	802.69	0.6645	0.67295	0.6645
Shr-Trans (B)	880.89	0.4825	0.506952	0.4825
Shr-Trans (C)	606.61	0.4897	0.516396	0.4897
Shr-Trans (D)	552.45	0.6126	0.629689	0.6126
Abut-p (ft.)	0.152	0.4892	0.513862	0.4747
Abut-a (ft.)	0.1263	0.4419	0.444565	0.4119
Wing (ft.)	0.1263	0.4419	0.444586	0.4119

Note: Col-Long = column longitudinal curvature; Col-Trans = column transverse curvature; Shr-Long = Pier-Column Longitudinal shear strength; Shr-Trans = Pier-Column Transverse shear strength; Abut-a = abutment active deformation; Abut-p = abutment passive deformation; Wing = wing wall deformation

2.5.5 Fragility curve

With the previously defined limit states, fragility curves can be developed following Eq. (2.4). Fig. 10(a-d) list the component fragility curves for the skewed and curved bridge model, including column flexural curvatures (column A), abutment passive deformation, abutment active deformation and wing wall deformation for different limit states. For the "complete" damage limit state, fragility curves of shear forces in the longitudinal and transverse directions (column A) are also displayed.

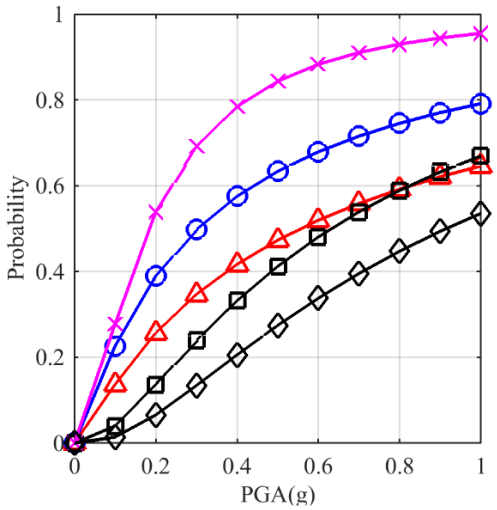

(a)

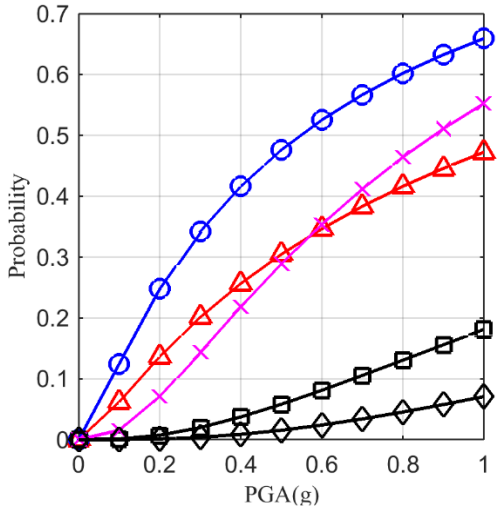

(b)

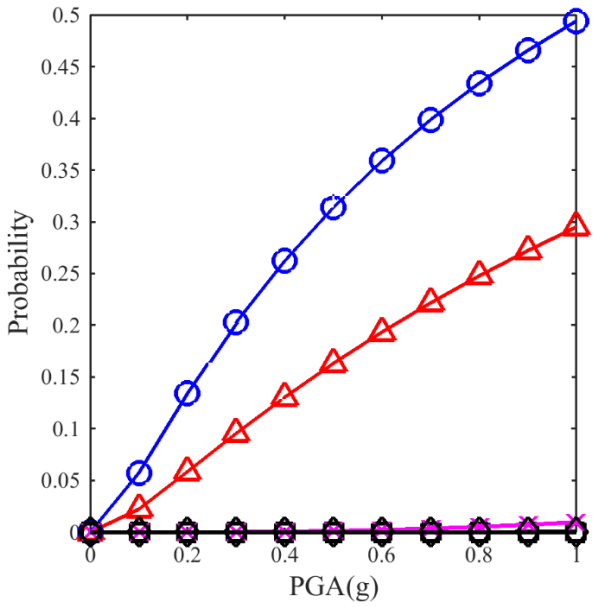

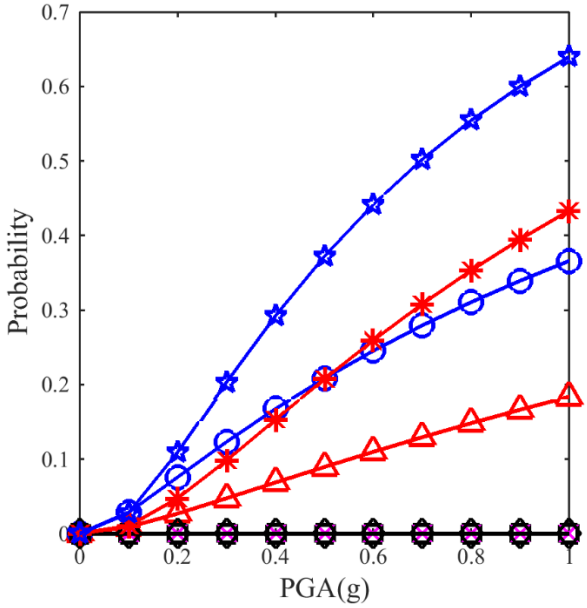

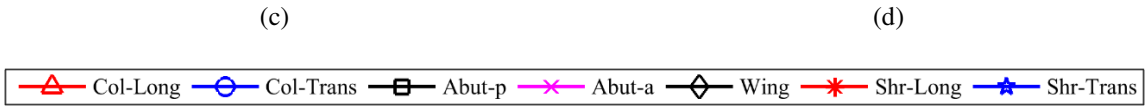

Fig. 10 Component fragility curves of the curved and skewed bridge: (a) “light” damage, (b) “moderate” damage, (c) "extensive” damage, and (d) “complete” damage

The results shown in Fig. 10 suggest that different bridge components may dominate the fragility performance in terms of exhibiting the highest fragility under different damage states. For instance, abutment active deformation (Abut-a in Fig. 10) tends to have the highest fragility among all limit states under the “light” damage state. For extensive or complete damage states, the abutment however has very small probability to experience excessive deformation. For moderate and “extensive” damage states, the column transverse moment curvature has the highest fragility. When “complete” damage is concerned, the structural damage is governed by the column transverse shear (Shr-Trans in Fig. 10). The results also show higher fragility associated with limit states related to transverse responses of the columns for almost all damage states, highlighting the importance of bridge transverse resistance to its fragility under seismic.

2.6 Comparative study of critical factors

With the previously defined limit states, fragility curves can be developed following Eq. (2.3). Fig. 11(a-d) list the component fragility curves for the skewed and curved bridge model, including column flexural curvatures (column A), abutment passive deformation, abutment active deformation and wing wall deformation for different limit states. For the “complete” damage limit state, fragility curves of shear forces in the longitudinal and transverse directions (column A) are also displayed.

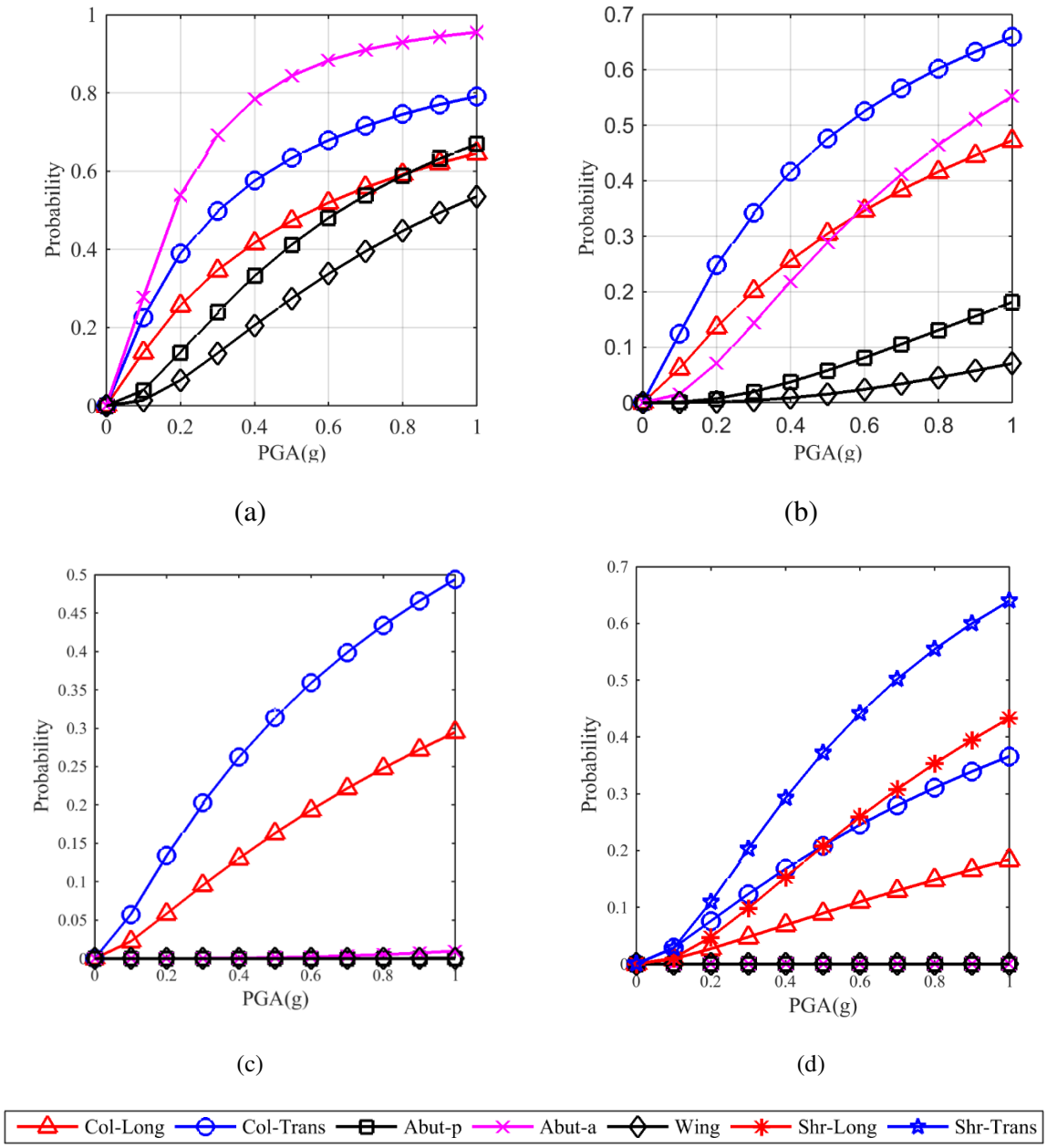

Fig. 11 Component fragility curves of the curved and skewed bridge: (a) “light” damage, (b) “moderate” damage, (c) “extensive” damage, and (d) “complete” damage

The results shown in Fig. 10 suggest that different bridge components may dominate the fragility performance in terms of exhibiting the highest fragility under different damage states. For instance, abutment active deformation (Abut-a in Fig. 10) tend to have the highest fragility among all limit states

under the “light” damage state. For “extensive” or “complete” damage states, the abutment however has very small probability to experience excessive deformation. For moderate and “extensive” damage states, the column transverse moment curvature has the highest fragility. When “complete” damage is concerned, the structural damage is governed by the column transverse shear (Shr-Trans in Fig. 10). The results also show higher fragility associated with limit states related to transverse responses of the columns for almost all damage states, highlighting the importance of bridge transverse resistance to its fragility under seismic.

2.7 Conclusions

This paper studies the seismic risk of a skewed and curved bridge in low-to-moderate seismic regions by developing analytical fragility curves. A typical 3-span concrete straight bridge located in Denver, CO was selected as the prototype bridge, from which three bridge models with complex geometric variations were modified. Based on the nonlinear FEM analysis results of these bridge models, fragility analyses were carried out considering the uncertainties of the bridge model and also ground motions. Comparative studies were also made to investigate the influences from the geometric configurations. Some main conclusions are summarized as following:

1. For the skewed and curved bridge model investigated in this study, it was found that different bridge components may dominate the fragility performance in terms of exhibiting the highest fragility under different damage states. Given the complex seismic risk performance associated

with curved and/or skewed configurations, a comprehensive risk assessment of bridges with complex geometric configurations is found important even in low-to-moderate seismic regions.

2. For the skewed and curved bridge, columns are found to have high fragility associated with transverse demands for almost all the limit states, highlighting the importance of the transverse seismic resistance to the serviceability and safety of skewed and curved bridges. Comparatively, the bridges with curvature have overall the highest fragility of the longitudinal moment curvature, while the skewed-only bridge has the highest fragility of the transverse moment curvature.

3. As compared to pretty consistent seismic performance among the columns of the straight bridge, skew and curvature nature was found to cause different fragilities on individual columns. Fragility curves for different columns of the skewed bridge are pretty similar and tend to only "scatter" in the high seismic intensity region. For the bridges with curvature, fragilities of the interior columns of two intermediate piers are similar, which are considerably higher than the fragility of two exterior columns. The skew nature will cause some difference on the fragilities between two interior columns and two exterior columns, respectively. Such fragility difference among columns suggests the need of picking the right column to control the design or conducting column-specific design for individual columns of bridges with curvature.

4. For "light" damage state, the limit state for "Abut-a" has overall much lower median PGA than other limit states for all bridge models. Bridges with curvature are found to have lower median

PGA than other bridges for column longitudinal moment curvature. Bridges with skew have lower median PGA for column transverse moment curvature. For “moderate” damage state, lowest median PGA is found for the limit state related to column transverse moment curvature.

CHAPTER 3 HYBRID NONLINEAR SEISMIC ANALYSIS OF BRIDGES WITH MOVING TRAFFIC

3.1 Introduction

As a result of the current limitations on seismic forecast, it is very likely that normal traffic remains on a bridge when an earthquake occurs. In traditional seismic analyses, traffic was typically ignored. Existing seismic performance predictions of short- and medium-span bridges without considering traffic impact often show that some bridge components either experience or are on the verge of severe damage from earthquakes. Therefore, as an important type of service loads, traffic impact on the bridge seismic performance should not be ignored. More realistic seismic performance of the bridge can be critical to future bridge seismic design, prevention and planning, especially for those with narrow safety margins.

The current AASHTO (American Association of State Highway and Transportation Officials) specification defines the extreme event limit state I by introducing a “project-specific” load combination factor to superpose the bridge response result under the design traffic load to that under seismic load (AASHTO 2012). The superposition method, despite its popularity, cannot capture the full coupling effects between seismic excitation, traffic loads and bridge. The lack of considering bridge/vehicle coupling effects (Deng and Cai 2010; Deng et al. 2014) is especially critical for short- and medium-span bridges when nonlinear structural behavior, local damages to some bridge components and even structural collapse have

been observed under earthquakes. In addition to structural integrity, ignoring the dynamic interactions between the bridge, vehicles and earthquake will also pose challenges in terms of assessing the serviceability such as driving safety and ride comfort of vehicles on the bridge. Therefore, there still exists a gap between the reality and the current state-of-the-art in terms of seismic analysis of short- and medium-span bridge and traffic system, which may jeopardize the rational risk assessment of serviceability, member damage and progressive failure of the bridge during earthquakes.

In early studies related to traffic load modeling, vehicles were considered as moving forces (Timoshenko et al. 1974) or moving masses (Blejwas et al. 1979), which have been incorporated in the bridge design guidelines such as Japan Road Association codes (2002) and AASHTO Load Resistance Factor Design (LRFD) (2012). There have been only a few studies on the bridge seismic analysis considering vehicle and bridge dynamic interactions, including numerical studies by Kameda (1992) and Kim et al. (2011) with simple vehicle and bridge models. Ghosh Jayadipta et al. (2014) proposed a framework of joint seismic and live-load fragility assessment of bridges, where its truck presence model assumed traffic flow in a constant speed for a representative truck. Recently, Kameshwar and Padgett (2018) studied the impacts of vehicles on the bridge seismic response and fragility by assuming that the vehicles were not in motion. The study covered three different types of stationary trucks and found that traffic can cause large impact on bridge seismic fragility. Wibowo et al. (2012) conducted the large-scale shake table experiment with a single platoon of H-20 trucks as static live loads on the 2/5-scale three-span and

horizontally curved bridge model. Most of the existing studies considered a single vehicle or a platoon of stationary vehicles, rather than moving vehicles as a part of realistic traffic flow.

As compared to short- and medium-span bridges, some promising progress has been made in terms of modeling moving vehicles on long-span bridges with or without seismic excitations (Chen and Wu 2010, 2011; Zhou and Chen, 2015). Zhou and Chen (2014) proposed a fully coupled long-span bridge and traffic simulation framework based on the mode-superposition concept with detailed dynamic modeling of each vehicle and the bridge. With known limitations on incorporating nonlinearities, a mode-based approach may be appropriate for global seismic response prediction of long-span bridges due to limited local damage and nonlinearity of major bridge components. It is, however, not appropriate for the seismic performance prediction of short- and medium-span bridges, which often undergo considerable nonlinear effects, local damages and even total collapse of the bridge under earthquakes, as discussed previously. Moreover, traditional nonlinear seismic analyses of short- and medium-span bridges have been successfully conducted using some commercial software, such as ANSYS, SAP2000 or open-source software like OpenSees. Although being very versatile on nonlinear seismic analyses, existing commercial or open-source software, however, cannot directly incorporate complex dynamic interactions between multiple moving vehicles and bridges. Therefore, there is no appropriate methodology reported in literatures so far that can be used for nonlinear seismic analyses of typical short- and medium-span bridges while rationally considering the coupling effects between the bridge, moving vehicles and earthquake at the same time.

In the following sections, a new hybrid simulation approach is proposed to conduct the nonlinear seismic analysis of the bridge/traffic/earthquake system by integrating the stochastic traffic flow simulation, the mode-based fully-coupled simulation technique of the bridge-traffic system and the nonlinear seismic analysis capabilities offered by the open system for earthquake engineering simulation (OpenSees) (Mazzoni et al. 2006). A prototype bridge is studied as a demonstration under several earthquake scenarios and the numerical analyses are conducted to provide some insights on the bridge seismic performance and impacts of traffic.

3.2 Mode-based bridge/traffic dynamic interaction analysis

3.2.1 Stochastic traffic flow simulation

The instantaneous temporal and spatial information of every single vehicle was obtained through the traffic flow simulation via the two-lane cellular automaton (CA) model (Chen and Wu, 2011). The variables for each cellular were updated based on the vehicle information in adjacent locations and the probabilistic traffic rules regulating the accelerating, decelerating, lane changing and braking, which can be referred to the study by Chen and Wu (2011). The cellular-automaton (CA)-based traffic flow simulation was performed on a roadway-bridge-roadway system to simulate the stochastic traffic flow through the bridge in a more realistic way. Periodic boundary conditions were adopted in the traffic flow model, in which the total number of each type of vehicles in the roadway-bridge-roadway system remained constant. The

vehicles in the stochastic traffic flow can be categorized into several representative types from a variety of vehicle configurations (Chen and Wu, 2011).

3.2.2 Fully-coupled bridge-traffic interaction model

The bridge and vehicles were modeled as two subsystems in the bridge-traffic dynamic interaction analysis system. The bridge subsystem was constructed based on the degrees of freedom (DOFs) in modal coordinates corresponding to the total number of the selected modes for the bridge. The vehicles were modeled as a combination of several rigid bodies, wheel axles, springs and dampers. The vehicle subsystem was established with all the DOFs in physical coordinates of the vehicle dynamic models. Detailed information of the vehicle dynamic model and the fully-coupled bridge-traffic interaction analysis can be found in the Ref. (Zhou and Chen 2014, 2015). It was assumed that the tires of each vehicle and road surface have point contact without separation. The surface roughness of the approaching road and the bridge deck was modeled as a stationary Gaussian random process with zero mean value. The motion equations in a matrix form of bridge/traffic system can be expressed as follows:

$$\begin{bmatrix} \Phi^T M_b \Phi & 0 & 0 & \cdots & 0 \\ 0 & M_{v_1} & 0 & \cdots & 0 \\ 0 & 0 & M_{v_2} & \cdots & 0 \\ \vdots & \vdots & \vdots & \ddots & \vdots \\ 0 & 0 & 0 & 0 & M_{v_n} \end{bmatrix} \begin{Bmatrix} \ddot{\xi} \\ \ddot{q}_1 \\ \ddot{q}_2 \\ \vdots \\ \ddot{q}_n \end{Bmatrix} + \begin{bmatrix} \Phi^T C_b \Phi + \Phi^T \sum_{i=1}^{n} C_{bci} \Phi & \Phi^T C_{b,v_1} & \Phi^T C_{b,v_2} & \cdots & \Phi^T C_{b,v_n} \\ C_{v_1,b} \Phi & C_{v_1} & 0 & \cdots & 0 \\ C_{v_2,b} \Phi & 0 & C_{v_2} & \cdots & 0 \\ \vdots & \vdots & \vdots & \ddots & \vdots \\ C_{v_n,b} \Phi & 0 & 0 & \cdots & C_{v_n} \end{bmatrix} \begin{Bmatrix} \dot{\xi} \\ \dot{q}_1 \\ \dot{q}_2 \\ \vdots \\ \dot{q}_n \end{Bmatrix}$$
$$+ \begin{bmatrix} \Phi^T K_b \Phi + \Phi^T \sum_{i=1}^{n} K_{bci} \Phi & \Phi^T K_{b,v_1} & \Phi^T K_{b,v_2} & \cdots & \Phi^T K_{b,v_n} \\ K_{v_1,b} \Phi & K_{v_1} & 0 & \cdots & 0 \\ K_{v_2,b} \Phi & 0 & K_{v_2} & \cdots & 0 \\ \vdots & \vdots & \vdots & \ddots & \vdots \\ K_{v_n,b} \Phi & 0 & 0 & \cdots & K_{v_n} \end{bmatrix} \begin{Bmatrix} \xi \\ q_1 \\ q_2 \\ \vdots \\ q_n \end{Bmatrix} = \begin{Bmatrix} \Phi^T \sum_{i=1}^{n} F_{v_i}{}^G + \Phi^T F_b^r \\ F_{v_1}{}^r \\ F_{v_2}{}^r \\ \vdots \\ F_{v_n}{}^r \end{Bmatrix}$$

(3.1)

in which, M_b, K_b and C_b are the generalized mass, stiffness and damping matrices for the bridge structure, respectively; n is the number of vehicles travelling on the roadway-bridge-roadway system in the traffic flow; M_{v_i}, K_{v_i} and C_{v_i} are the mass, stiffness and damping matrices of the i^{th} vehicle in the traffic flow, respectively; K_{bci} and C_{bci} refer to the stiffness and damping contributions to the bridge structure due to the coupling effects between the i^{th} vehicle in the traffic flow and the bridge system, respectively; K_{b,v_i} and C_{b,v_i} are the coupled stiffness and damping matrices for the bridge structure corresponding to the i^{th} vehicle in the traffic flow, respectively; $K_{v_i,b}$ and $C_{v_i,b}$ are the coupled stiffness and damping matrices for the i^{th} vehicle in the traffic flow corresponding to the bridge structure, which are equal to the transposed matrices of K_{b,v_i} and C_{b,v_i}, respectively; ξ is a vector of generalized coordinates of the bridge corresponding to each mode involved in the analysis; Φ is the mode shape matrix of the bridge; q_i is a vector of the physical responses corresponding to each degree of freedom of the i^{th} vehicle in the traffic flow; one-dot and two-dot superscripts of the displacement vector denote the velocity and

acceleration, respectively; F_b and F_{v_i} denote the external applied loads for the bridge in modal coordinates and the i^{th} vehicle in physical coordinates, respectively. The superscripts r and G denote the loads due to road roughness and self-weight, respectively.

The equations of motion were solved through the Newmark-Beta method in time domain and the responses of the vehicles and the responses of the bridge corresponding to the generalized coordinates were obtained. Through the mode superposition of all the involved modes, the global physical response at any location of the bridge can be obtained from the full-coupled bridge-traffic interaction analysis, as shown in Eq. (3.2).

$$U^d = \sum_{j=1}^{m} \phi_j \xi_j = [\phi_1 \phi_2 \ldots \phi_m]\{\xi_1 \xi_2 \ldots \xi_m\}^T = \Phi\{\xi^d\} \tag{3.2}$$

3.3 Hybrid nonlinear analysis framework considering traffic impact with Opensees

3.3.1 Equivalent moving traffic loads (EMTL)

Considering that the elasticity and energy dissipation of the tires were modeled as springs and dampers in the lower locations of a vehicle, the dynamic wheel loads acting on the bridge structure are equal to the dynamic forces of the lower springs and dampers at the contact points. The equivalent wheel loads were obtained directly for each vehicle in the stochastic traffic flow from the time-history simulation results of the fully-coupled bridge-traffic interaction system as introduced above. The vertical and longitudinal equivalent moving traffic loads (EMTL) for the bridge girder nodes were further accumulated by distributing the equivalent wheel loads (EWL) for each vehicle using linear interpolation to the bridge girder

nodes both longitudinally and transversely. The EMTL for each bridge girder nodes can be applied on the bridge structure in the finite element analysis model using OpenSees under multiple loading scenarios in which both the material and geometric nonlinearities can be considered at the same time.

The vertical equivalent wheel load (EWL) for the i^{th} vehicle was determined as the summation of the vertical equivalent dynamic wheel loads and the gravity load:

$$F_{ewl}^{iz}(t) = F_{edwl}^{iz}(t) + G^i \tag{3.3a}$$

in which, G^i is the gravity load of the i^{th} vehicle; $F_{edwl}^{iz}(t)$ is the vertical dynamic wheel load for the i^{th} vehicle in the traffic flow at time instant t, which is defined as (Chen and Cai 2007):

$$F_{edwl}^{iz}(t) = \sum_{j=1}^{na} (K_{lzL}^{j} \hat{Z}_{ajL}(t) + C_{lzL}^{j} \dot{\hat{Z}}_{ajL}(t) + K_{lzR}^{j} \hat{Z}_{ajR}(t) + C_{lzR}^{j} \dot{\hat{Z}}_{ajR}(t)) \tag{3.3b}$$

in which, $\hat{Z}_{ajL(R)}(t)$ and $\dot{\hat{Z}}_{ajL(R)}(t)$ are the relative vertical displacement and the corresponding first derivatives between the lower mass block on the vehicle at the left (right) side and the contacting point on the bridge, respectively; na is the total number of wheel axles for the i^{th} vehicle; K and C are the stiffness and damping coefficients of the springs and dampers in the vehicle model, respectively; the subscripts l, z, L(R) represent lower position, vertical (z) direction and left (right) side for the springs or dampers, respectively.

3.3.2 EMTL-FE hybrid strategy

Fig. 12 shows the flowchart of the proposed simulation strategy with three parts: (1) traffic loads, (2) Opensees Finite Element Method (FEM) model, and (3) scaled ground motions. For the traffic load part,

the boundary conditions and driver behavior model of the CA-based traffic flow simulation were defined for the stochastic traffic flow simulation for a specific bridge and traffic scenario. With the simulated traffic flow results, the fully-coupled bridge/traffic interaction analysis was conducted to provide the time histories of the vertical equivalent wheel loads (EWL) for each vehicle of the traffic flow acting on the bridge under seismic loads. The EWL of each vehicle was linearly distributed in both longitudinal and transverse directions to the adjacent nodes of the bridge deck in the bridge finite element model in order to generate the cumulative time-dependent traffic loads acting on each node of the bridge deck, referred to as equivalent moving traffic loads (EMTL). The time-history excitations in vertical and longitudinal directions for each bridge deck node of the bridge finite element (FE) model can therefore be defined from the equivalent moving traffic loads (EMTL). Extreme load excitations (e.g. seismic loads) can be applied to the bridge FE model (e.g. Opensees) as the time-history inputs and the time-history nonlinear dynamic analysis is then conducted. Such a strategy is thus called "EMTL-FE hybrid strategy" because it integrates the fully-coupled bridge-traffic dynamic analysis model through EMTL and the nonlinear finite element (FE) analysis with the nonlinear FE software.

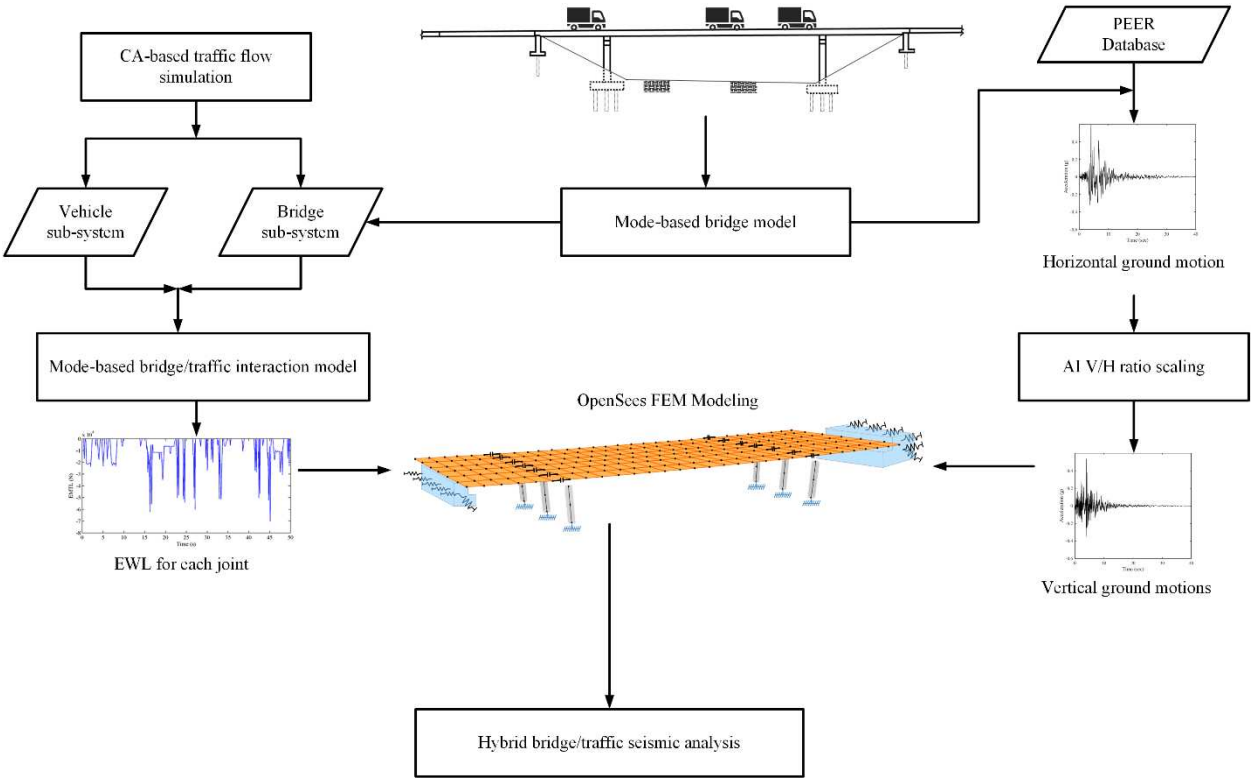

Fig. 12 Flowchart for EMTL-FE hybrid strategy

3.4 Numerical demonstration

3.4.1 Prototype bridge and scenario earthquake records

Although the proposed methodology is applicable to all short- and medium-span bridges, a 3-span skewed and curved bridge, located in Tacoma Washington, is selected in this study as the prototype bridge to give more insights on bridge seismic performance. The bridge location was considered as a moderate-to-high seismic region in the U.S. The six-lane freeway bridge has the radius of curvature of 436.1 m and the skew angles of 41.7 and 31.7 degrees at both ends. As shown in Fig. 13, the bridge deck is supported by concrete box girders over two sets of circular column bents, and connected with seat-type skewed abutments at both ends.

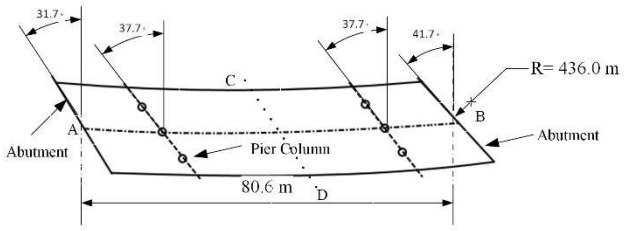

(a) Top view of girders

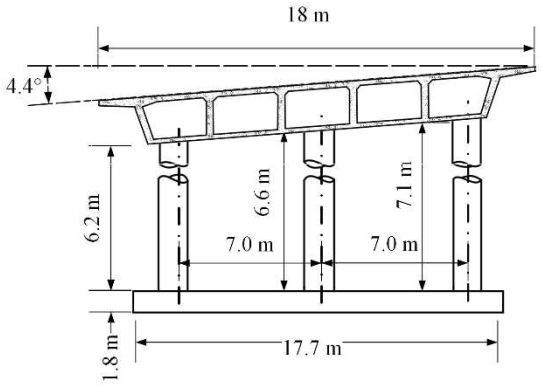

(b) Elevation view

Fig. 13 Geometries of prototype bridge: (a) top view of girders, and (b) elevation view

The numerical model for the prototype bridge was constructed using the 3D finite element software Opensees. The details of the 3-D OpenSees model for the prototype bridge including some key connections are shown in Fig. 14.

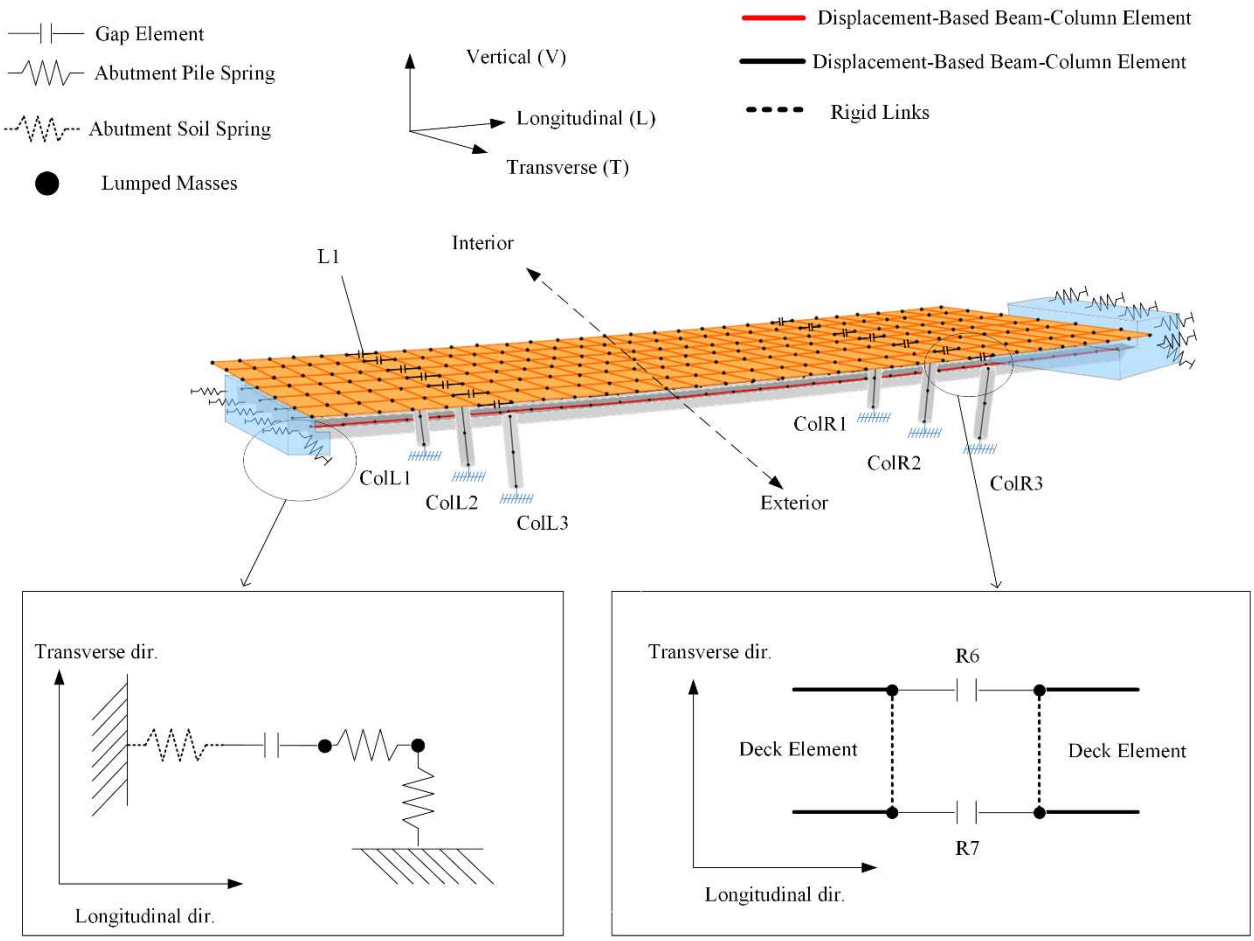

Fig. 14 3-D OpenSees model of the prototype bridge

The circular reinforced concrete columns were modeled using fiber elements with modified uniaxial Kent-Scott-Park concrete material, which accounts for plastic behaviors after cracks occur during an earthquake (Stanton and McNiven 1979). In order to simulate the bridge/traffic interactions with detailed time-history inputs in the 3-D domain, the bridge deck elements were modeled in refined details with shell elements and elastic membrane plate sections, supported by five segments of elastic frame elements for box

girders. Each segment has equivalent elastic properties of the prototype bridge girder since the bridge superstructure is usually deemed to remain elastic during seismic excitation. As shown in Fig. 14, for each girder element, rigid link elements were used to connect the bridge deck and the girder element to ensure they share the same degrees of freedom (DOF) on the interface. The 12.7 mm expansion joints were modeled with gap elements on the deck above the column bent. For the abutments, the stiffness contributed from the piles in the active direction was modeled with the abutment pile springs and the stiffness from the soil in the passive direction was modeled with additional soil springs connected to the pile springs, as shown in the bottom left of Fig. 14 (Nielson, 2005). Between the pile spring and soil spring, a 12.7 mm gap element was added to capture the available gap and for predicting the pounding forces between the girder-end and abutment. In the case study, the bridge model uses Rayleigh damping matrix to define structural damping. A typical damping ratio of 5% is selected and assigned to the first 2 modes for defining the corresponding mass and stiffness proportional damping coefficients. The mass proportional damping and stiffness proportional damping are assigned to equivalent lumped-mass nodes and abutment link elements.

In order to evaluate the impact of traffic loads to bridges, this study considered vertical vehicle loads along with horizontal-vertical direction ground motions. According to some existing studies on earthquake characteristics (Newmark et al. 1973; Kunnath et al. 2008), vertical ground motions were considered as those that come with lateral shear wave and their magnitudes were generally dependent on the horizontal component of a seismic component, either in longitudinal or transverse direction. To keep the numerical

demonstration within an appropriate scope, it was assumed that longitudinal ground motion was applied along with the vertical seismic component as the baseline case. A near-field record of the Northridge earthquake in 1994 was selected as the scenario earthquake excitation to justify the consideration of the vertical ground motion as the scenario excitation set. Ground motion used in this study was scaled following the method adopted by Wilson et. al. (2015) based on its peak ground acceleration (PGA), in which the longitudinal component was scaled to match the seismic design spectrum, while the vertical component was scaled accordingly by keeping the same Arias Intensity ratio (Table. 8). The scaled time histories of longitudinal and vertical seismic accelerations are shown in Fig. 15.

Table. 8 Scenario ground motion selection

Event	**Mw**	**Type**	**Station**	**R_{rup} (km)**	**L (sPGA[*2])**	**V (sPGA)**
Northridge	6.7	NF[*1]	Sylmar - Olive View Med FF	5.30	0.57	0.22

Note: *1: NF=Near-fault earthquakes; *2: sPGA=Scaled peak ground acceleration;

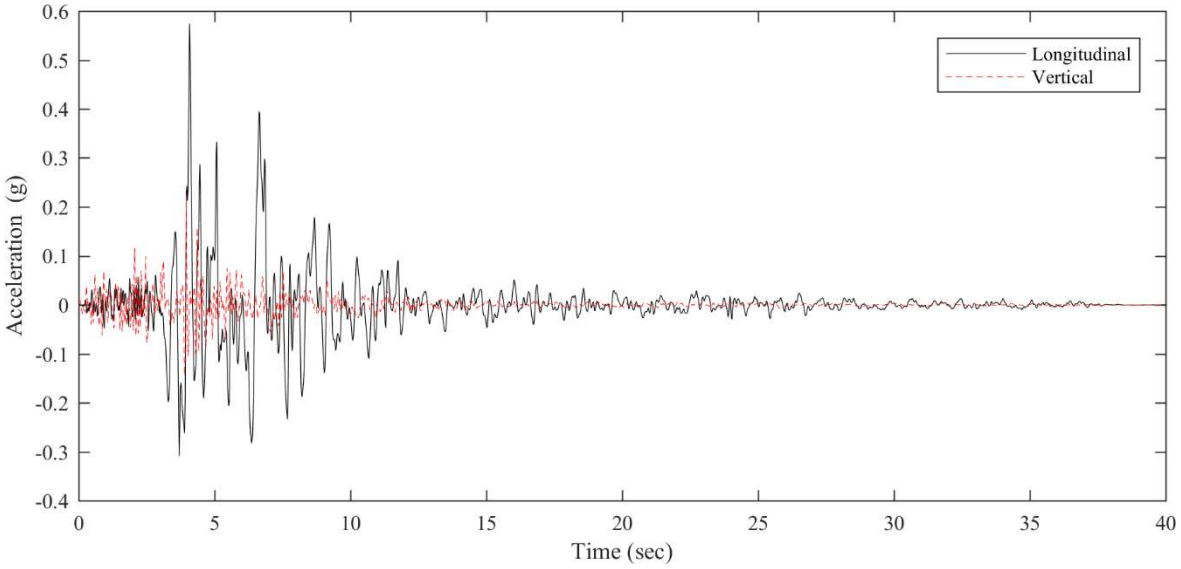

Fig. 15 Scenario seismic excitation

3.4.2 Traffic loads from bridge-traffic interaction effects

Traffic flow was assumed to be "busy traffic" with a density of 32 vehicles/km/lane for three lanes, which are the fast lane, middle lane and slow lane. The relative location between the traffic lanes and the girders is shown in Fig. 16.

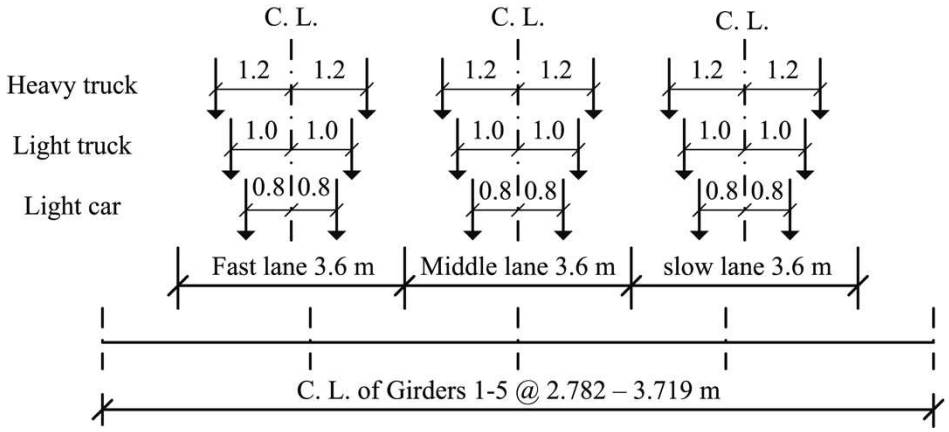

Fig. 16 Side view of the vehicle wheels on the traffic lanes for the prototype bridge

The percentages of the three types of vehicles in the traffic flow were assumed to be 25%, 25% and 50% for heavy trucks, light trucks and light cars, respectively, representing a typical vehicle composition in the traffic flow. The total length of the roadway-bridge-roadway path was 247.5 m, including two roadway segments in a length of 82.5 m each and the bridge in a length of 82.5 m. The simulated stochastic traffic flow at the busy traffic condition consisted of totally 24 vehicles in the roadway-bridge-roadway system, including 6 heavy trucks, 6 light trucks and 12 light cars. The total number of DOFs of the bridge-traffic system was 390, in which the first 60 DOFs were in the modal coordinates of the bridge corresponding to the first 60 modes and the later 330 DOFs were in the physical coordinates for all the vehicles. The busy traffic flow was simulated stochastically with a time duration of 40 seconds based on the spatial information of bridge deck and traffic flow density in Fig. 17. Fig. 17 shows the longitudinal locations of the vehicles with respect to time on the fast lane of the bridge in the traffic flow. Representative EMTLs at the center of the main span and west side span on the bridge deck are given in Fig. 18(a) and (b), respectively. The EMTL values varied significantly with respect to time due to the movement of vehicles in the traffic flow, and those values in the main span and side span were similar in terms of magnitude.

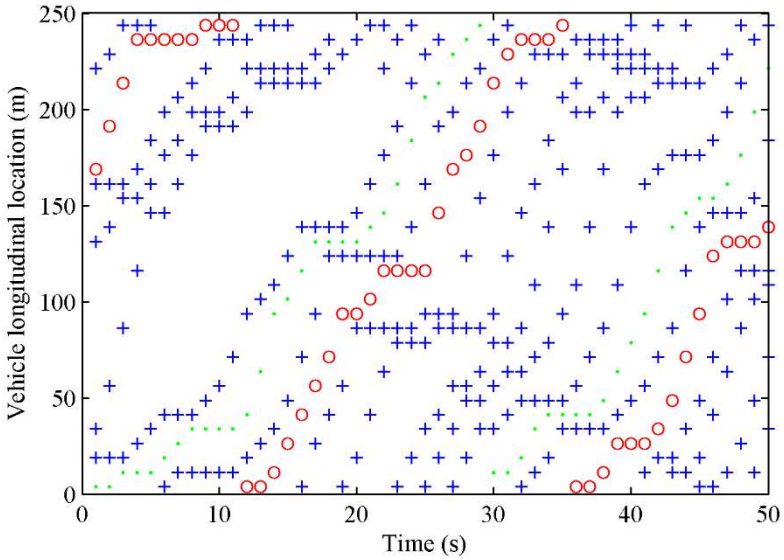

Fig. 17 Longitudinal locations of the vehicles on the fast lane in the busy traffic flow

(+ = light cars, O = light trucks, •=heavy trucks)

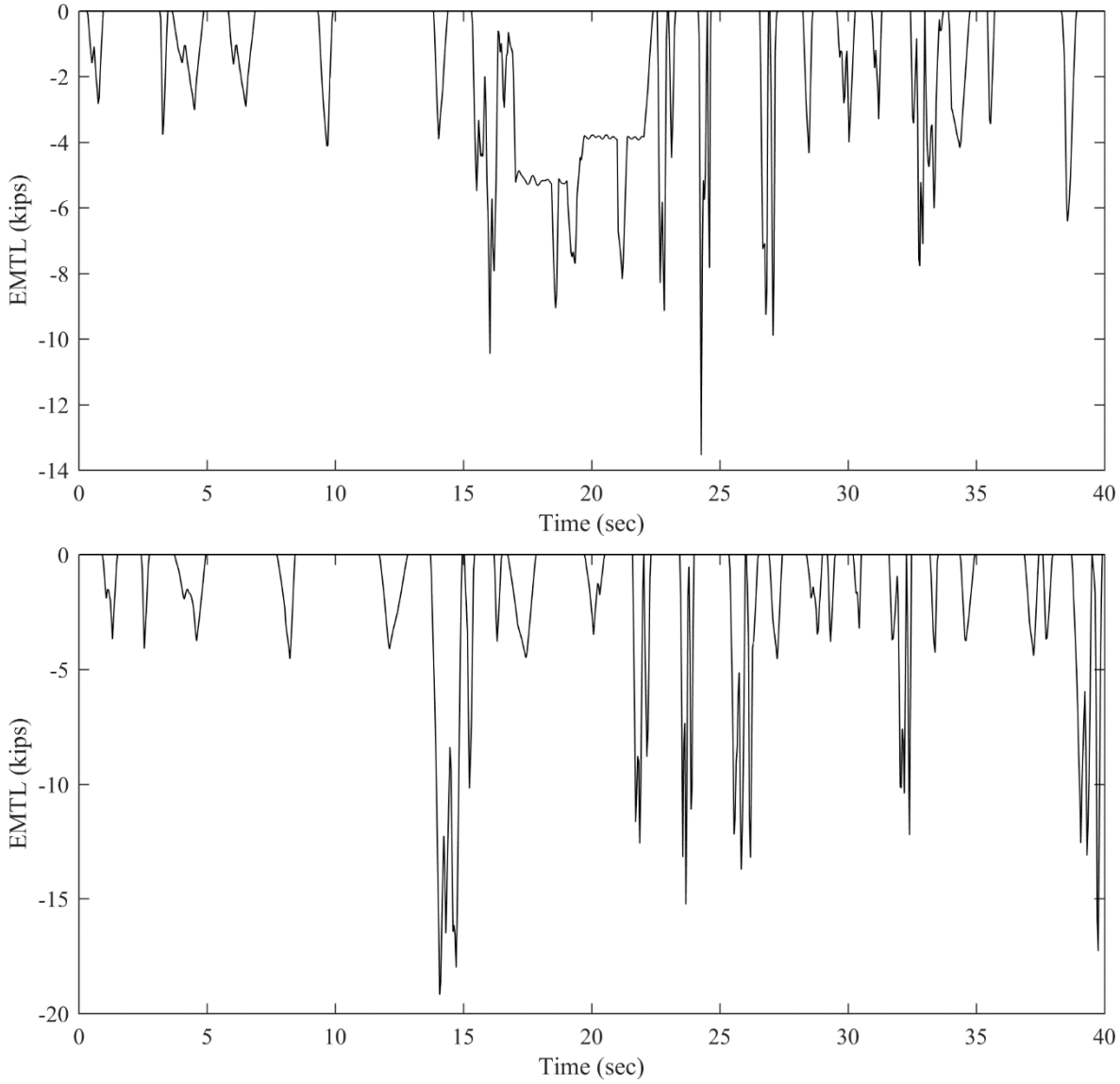

Fig. 18 EMTL at the center location: (a) main span, and (b) side span on the skewed bridge deck

3.4.3 Nonlinear seismic analysis results

The EMTL time histories obtained from the mode-based interaction analysis were applied to the corresponding bridge deck joints of the Opensees model as inputs (Fig. 14). For intermediate nodes of the bridge deck in both transverse and longitudinal directions, linear interpolation was applied to the EMTL to generate the time history inputs for adjacent nodes. It is noted that in this study EMTL derived based on

normal bridge-vehicle interaction was applied for the bridge nonlinear seismic analysis, with following two approximations:

(1) The EMTL on the bridge is obtained from bridge-traffic interaction analysis (Zhou and Chen, 2015), which assumes that the vehicle wheels have point contact with the bridge deck without separation. It is a necessary mathematical assumption in order to directly couple the bridge and each individual vehicle in the traffic flow. It is beyond the scope of the state-of-art research to realistically model the separation, reconnection and the coupling between the wheel and bridge deck in a single dynamic analysis due to the nature of dynamic equations.

(2) The driving behavior of the traffic flow when seismic event occurs was assumed to be same as normal condition. Based on several studies of driver behavior on bridges during several seismic events, it was reported that drivers usually realize the occurrence of seismic event and then apply braking only when the seismic intensity is very high (Maruyama and Yamazaki, 2006). For short- and medium-span bridges, the passing time of vehicles through the bridge is usually short, which may not allow the drivers to take action while they still remain on the bridge after the initial reaction time. Furthermore, there is lack of a general and well-accepted driving behavior model to characterize the driver response during earthquakes with different intensities. To propose a general approach for all seismic scenarios, the driving behavior change during the earthquake is ignored in this study.

Nonlinear time-history seismic analysis was then conducted on the OpenSees FEM model where the seismic inputs were applied at the base of the columns and the traffic inputs applied on the bridge deck. The nonlinear time-history analysis used direct integration of Hilber-Hughes-Taylor method with alpha, beta and gamma values of 0.0, 0.25, and 0.5, respectively. The analysis results of different bridge components are discussed in the following section.

In general, bridge columns are one of the critical components for bridge seismic analysis due to relatively higher vulnerability to damage than the superstructure. According to previous studies, the most common structural failure modes for columns can be categorized as displacement ductility (Sivaramakrishnan 2010; Nikoukalam and Sideris, 2016) and drift ratio (Fahmy et al. 2010; Ghobarah, 2001). Existing studies showed that different columns usually have different seismic performance for a skewed and curved bridge (Wilson et al,. 2015; Chen and Chen, 2016). The seismic response of all the columns is discussed in the following and the most critical column may be identified as a representative one for further discussions. Fig. 19 and Fig. 20 give the maximum longitudinal and transverse moments for six columns respectively, and the definitions of the column numbers can be found in Fig. 14. Longitudinal moments of the columns are pretty close among those three columns on the left side (L1-3) and also the three on the right side (R1-3), as shown in Fig. 19(a-b). The zoomed-out view of the moments in Fig. 19(b) shows slight difference for different columns on each side and column L1 (ColL1) is found to have the maximum longitudinal moment among all the columns and the moments for all the columns on the left.

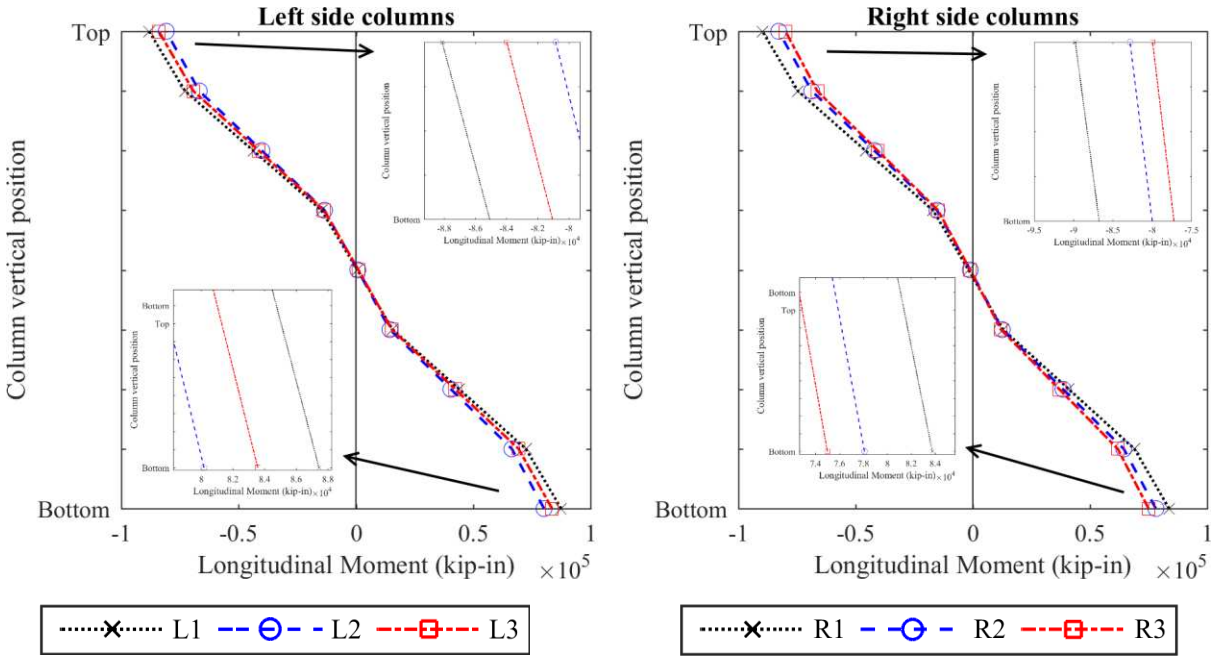

Fig. 19 Longitudinal moments of individual columns: (a) left side column L1, L2, L3, and (b) right side column R1, R2, R3

It is found in Fig. 20 that the left-side columns (L1-L3) have slightly higher transverse moments than those of the right-side columns (R1-R3). For the columns on the same side, it is obvious that the transverse moments of different columns vary considerably (Fig. 20). For example, for the left-side columns, column L1 can achieve over 4 times of the transverse moments at both ends than those of column L2. Similar trends can also be observed for the right-side columns (i.e. R1-R3). The transverse moments of columns vary considerably between the interior column (L3) and the exterior one (e.g. L1) on the same side. All the differences of the longitudinal and transverse moments on different columns are caused by the skew,

curvature and superelevation nature of the bridge, and the findings suggest that specific design of individual columns for skewed and curved bridges may be warranted to achieve both robust and economical designs.

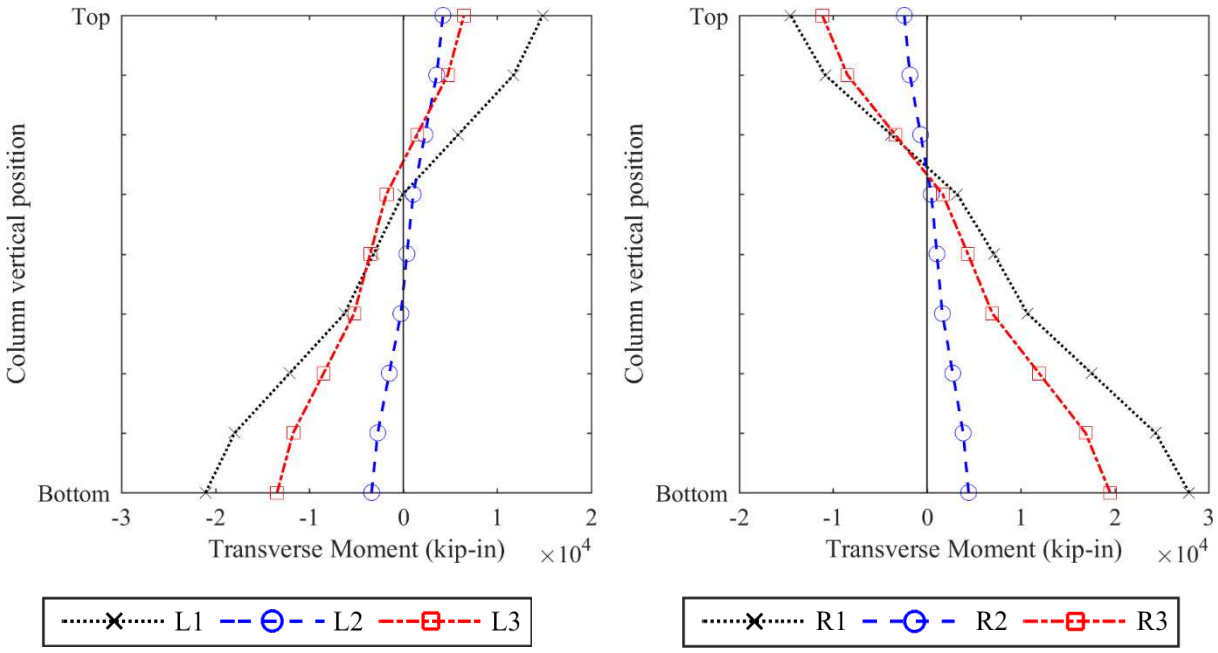

Fig. 20 Transverse moments of individual columns: (a) column L1, L2, L3, and (b) column R1, R2, R3

Fig. 21 summarizes the demand and capacity (D/C) ratio for shear, axial forces, transverse moments and longitudinal moments for all six columns. It is found the D/C ratios of both axial force and shear are very small for all the columns, showing very large safety margins. It is found that D/C ratio for the transverse moment is pretty small, i.e. around 0.2-0.3, which is understandable given the fact that the horizontal seismic excitation was only applied in the longitudinal direction. In contrast, the D/C ratios for

longitudinal moments of different columns are much higher (around 0.9). Among different columns, it is found that column L1 (Col L1) and column R1 (Col R1) have relatively larger transverse and longitudinal moments. By looking into the seismic response results of all the columns shown in Fig. 19 to Fig. 21, it is concluded that column L1 (ColL1) has the overall largest seismic response for most of the cases and is therefore selected as the representative column in the following discussion.

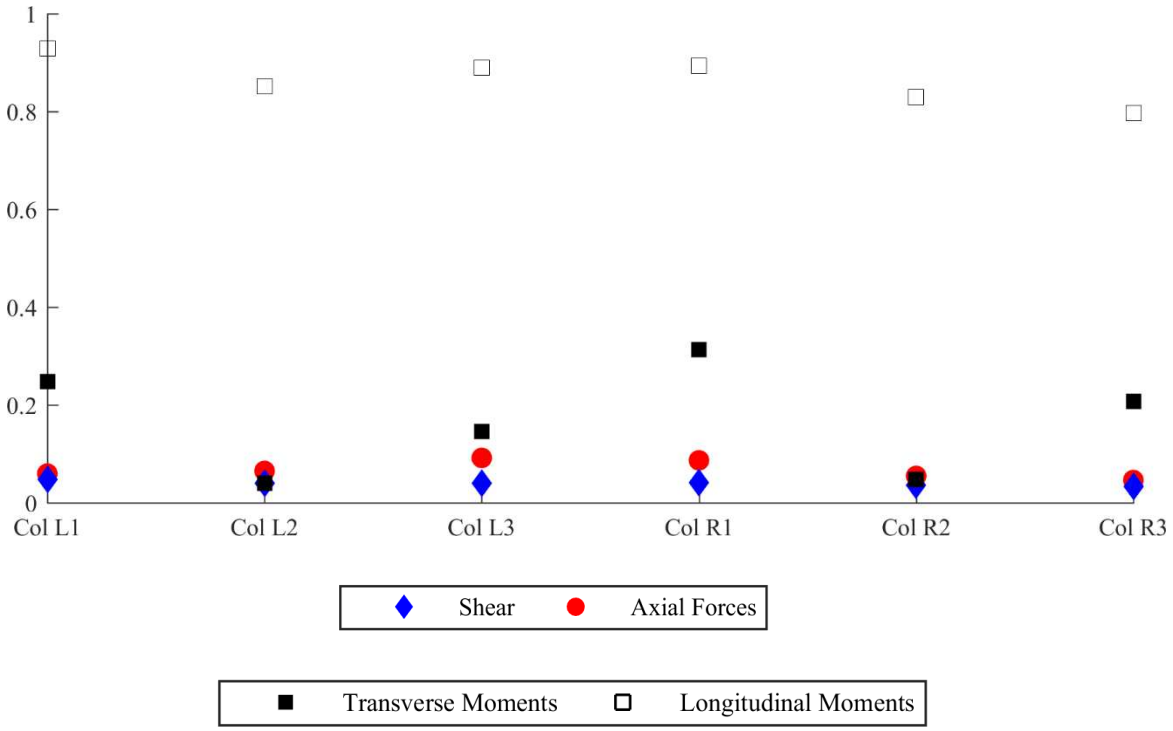

Fig. 21 Column demand / capacity ratio for individual column

The longitudinal pounding forces between the concrete components during seismic events, such as shear keys, girder ends and abutments, could induce spalling or crushing damage of concrete as well as damage to the expansion joints. Such an issue has been studied in several previous researches (DesRoches

and Muthukumar, 2002; Choi et al,. 2004; Chouw and Hao, 2008; Billah et al,. 2012) and is also investigated in the following. In Fig. 22, the variations of the gap width between the abutment and the girder on the right side over time are displayed with the gap width below 0 marked with red circles. As shown in Fig. 23, at the corresponding time instants with negative values of the gap width, large pounding forces over 4448.2216 kN (1000 kips) were observed. Without conducting detailed concrete damage assessment due to the scope limit, it is expected considerable damage to the expansion joints and concrete on the girders and abutment would occur under such large pounding forces.

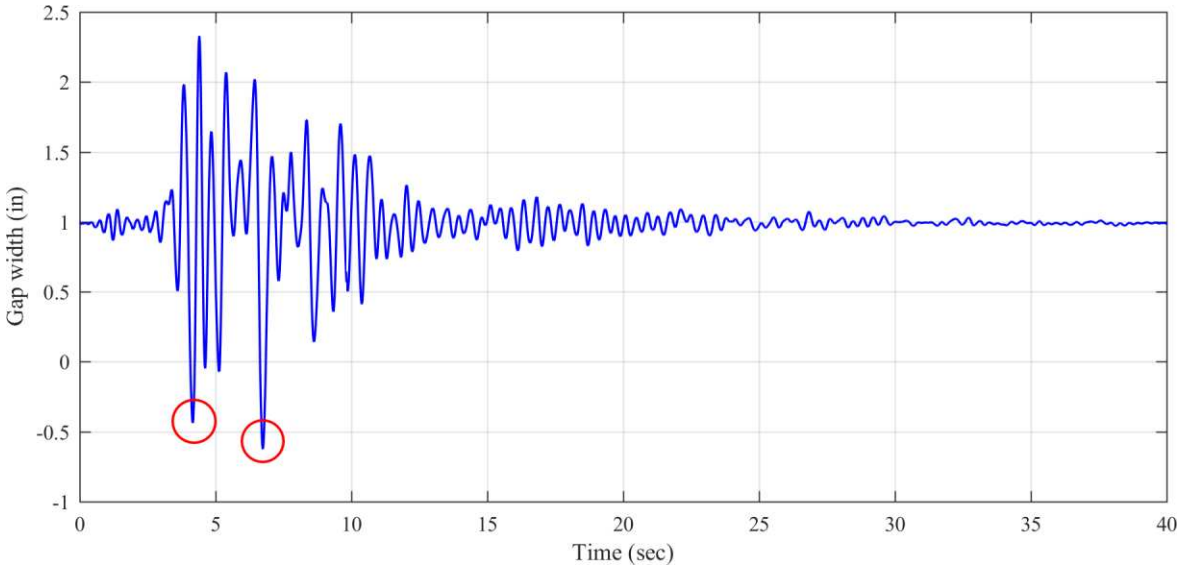

Fig. 22 Girder-abutment gap width between girder and abutment

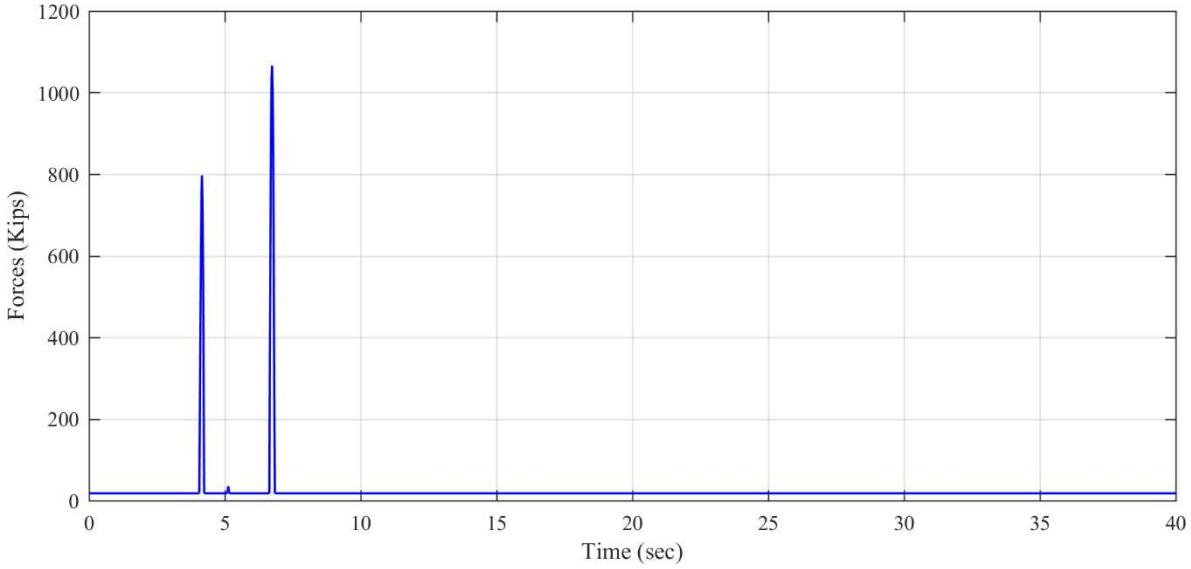

Fig. 23 Longitudinal pounding forces between girder and abutment

3.4.4 Impact of different excitation scenarios of ground motions

In general, ground motions are characterized and quantified in three primary directions, including vertical component and biaxial combination of two orthogonal horizontal components following the 30% rule (Rosenblueth and Contreras 1977), 40% rule (Newmark 1975) or CQC3 (Menun and Der Kiureghian 1998), which have been adopted in many seismic design codes (ICBO 1997 ; ASCE 2010).

In this study, the baseline scenario (baseline) includes 100% longitudinal component and 100% vertical component. To study the impact from transverse ground component, Scenario 1 is also studied by combining the longitudinal and transverse ground components following 40% rule, along with the vertical component. Details about the ground motion input directions (record file names SYL090 and SYL-UP from PEER strong ground motion database) for each directional combination are listed in Table. 9.

Table. 9 Input direction and intensities of different scenarios

Scenarios	Longitudinal	Transverse	Vertical
Baseline	100% SYL090	N/A	100% SYL-UP
Scenario 1	100% SYL090	40% SYL090	100% SYL-UP

Note: *1: Excitation in longitudinal direction *2: Excitation in vertical direction

Comparative results of both scenarios are shown in Fig. 24(a) and (b). Although the absolute difference between two case results seems small since the PGA of the transverse component of earthquake is 0.22g (40% of longitudinal earthquake), the deformation increment percentage can range from 8.82% (ColL1) to 81.75% (ColR2) at the diagonal locations being picked from Fig. 14. This shows a possibility that specific structural designs in the transverse direction, such as for wingwall or shear keys, may need to be considered specifically to avoid possible excessive deformation.

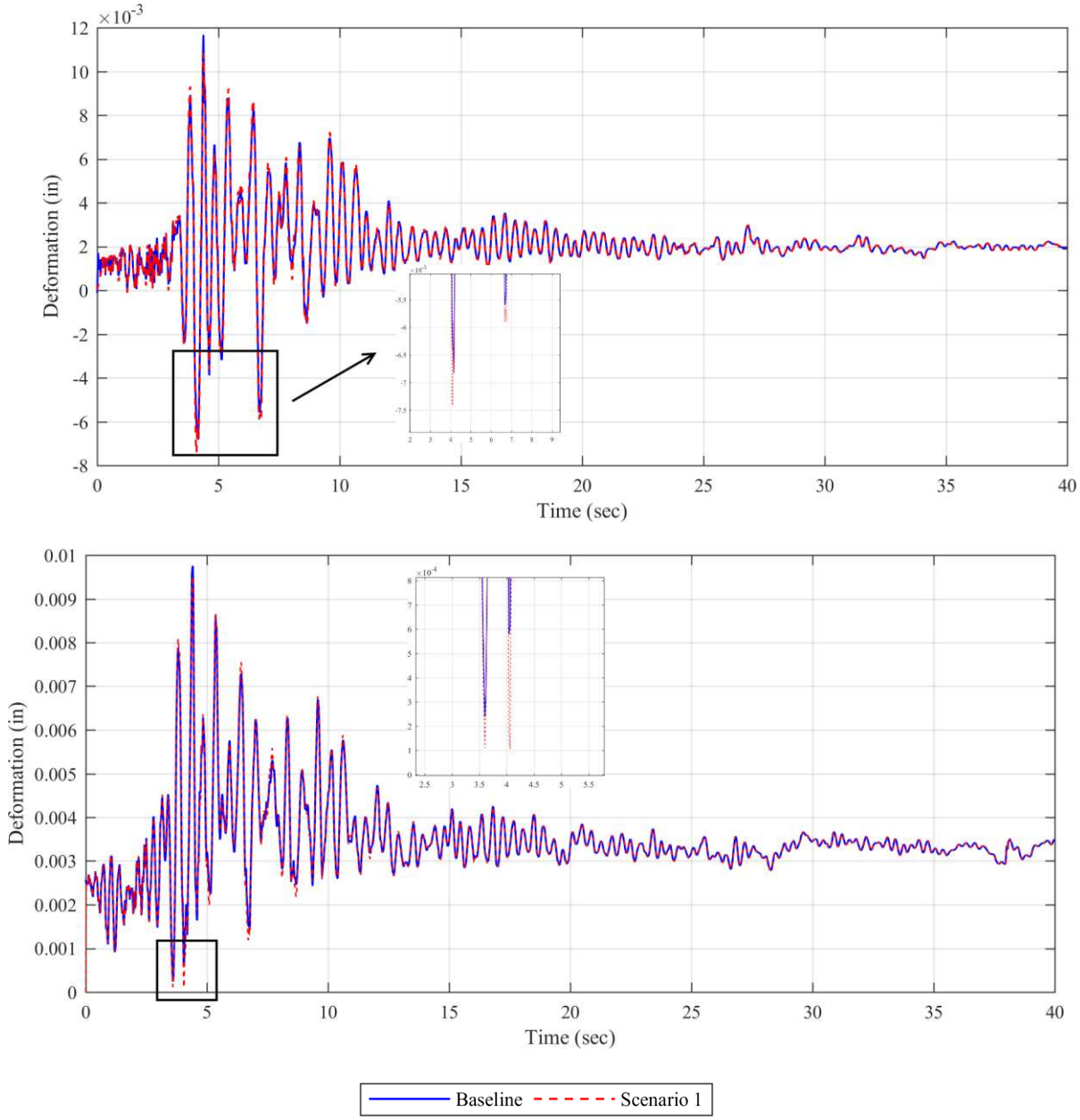

Fig. 24 Transverse deformations of columns: (a) ColR2, and (b) ColL1

Fig. 25 (a) shows the demand-capacity ratio of different columns under two scenarios and it is found that the addition of transverse earthquakes results in different levels of increase of transverse moments

among different columns and the largest increment of column transverse moment is about 18% increment on ColR1 (Fig. 25a)). The results suggest that even a small PGA of transverse earthquake (about 0.27g) can still make a considerable difference on the column moments. Fig. 25 (b) shows the time history of transverse moments of ColR1. Since the input ground motion characteristic is Near-fault pulse-like ground motion, one can see that most of the difference of the two scenarios has been observed during the first 15sec. Once the earthquake started to decapitate over time, the results of two scenarios become very similar.

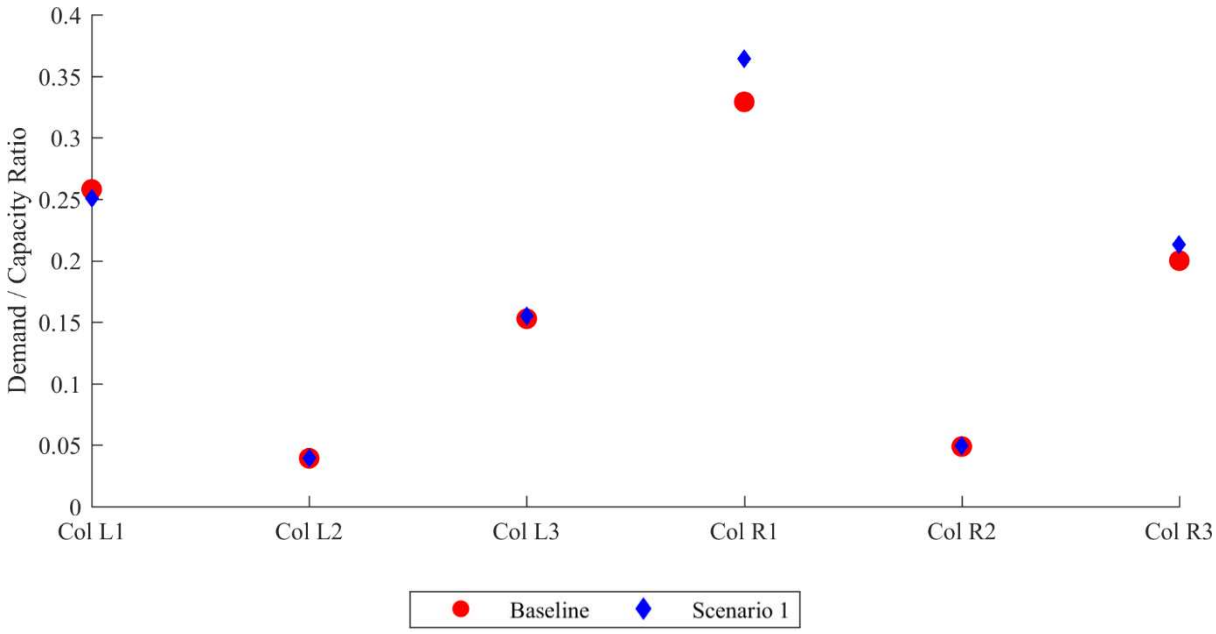

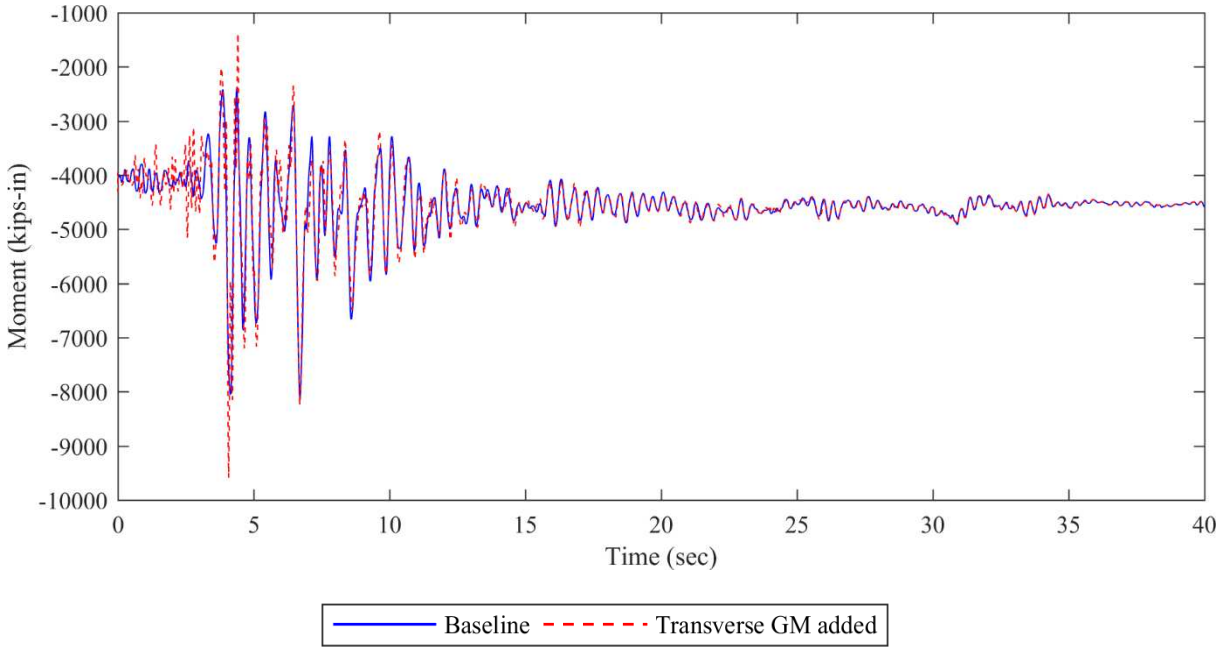

Fig. 25 Column transverse response comparison: (a) D/C ratio, and (b) time history of ColR1

For the vertical displacement distribution along line A-B on the bridge deck, it is found the addition of the transverse earthquake actually causes smaller vertical deck displacement and acceleration than the baseline case, as shown in Fig. 26 (a) and (b).

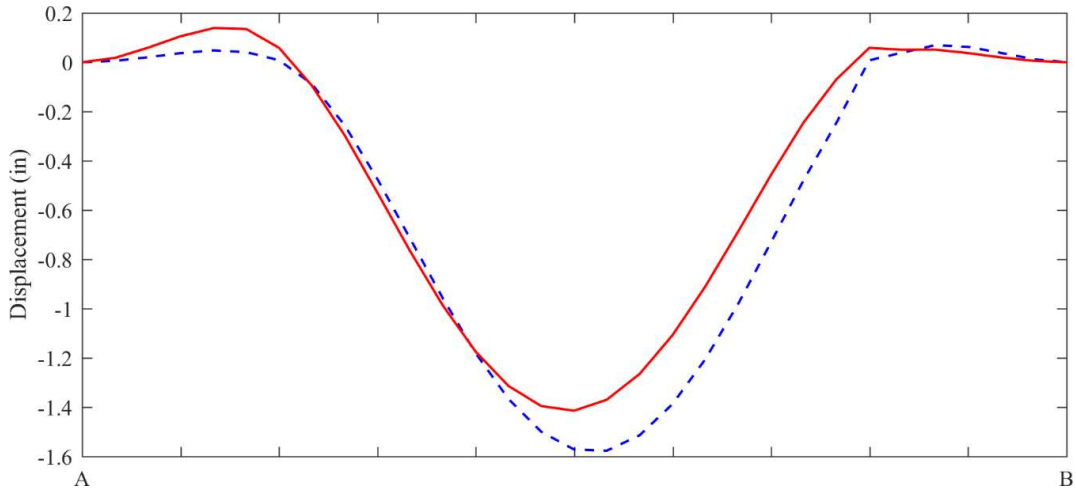

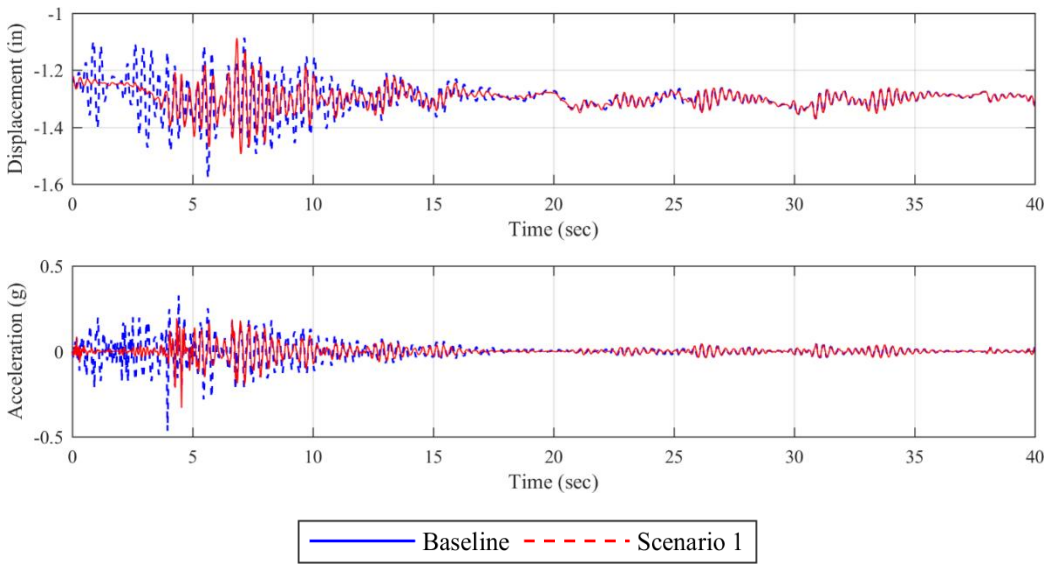

Fig. 26 Deck vertical response comparison: (a) displacements along line A-B, and (b) displacement and acceleration at midspan

3.5 Impact of traffic on seismic response

In normal conditions, traffic loads can cause considerable impacts on vertical displacements of the bridge deck and responses on bridge columns. As discussed earlier, the impact of realistic moving traffic on the bridge seismic response, however, was not clear. In this section, some comparative studies are conducted to look into such impacts. Since traffic loads as well as dynamic interactions primarily act in the vertical directions, the column response and vertical deck displacement response will be specifically studied in addition to other column responses.

3.5.1 Column response

As shown in Fig. 27(a) and Fig. 27(b), for the scenario earthquake with a high PGA, the traffic load only slightly affects the peak and residual column drift ratios, regardless of the possible longitudinal moment induced by superstructure curvature with vertical vehicle loadings. This is understandable since

the traffic dynamic interactions mainly occur in the vertical directions of the bridge. However, since the longitudinal moment and drift ratio are critical seismic response often with very narrow safety margin, any small increase of the seismic response by the inclusion of traffic load should not be overlooked.

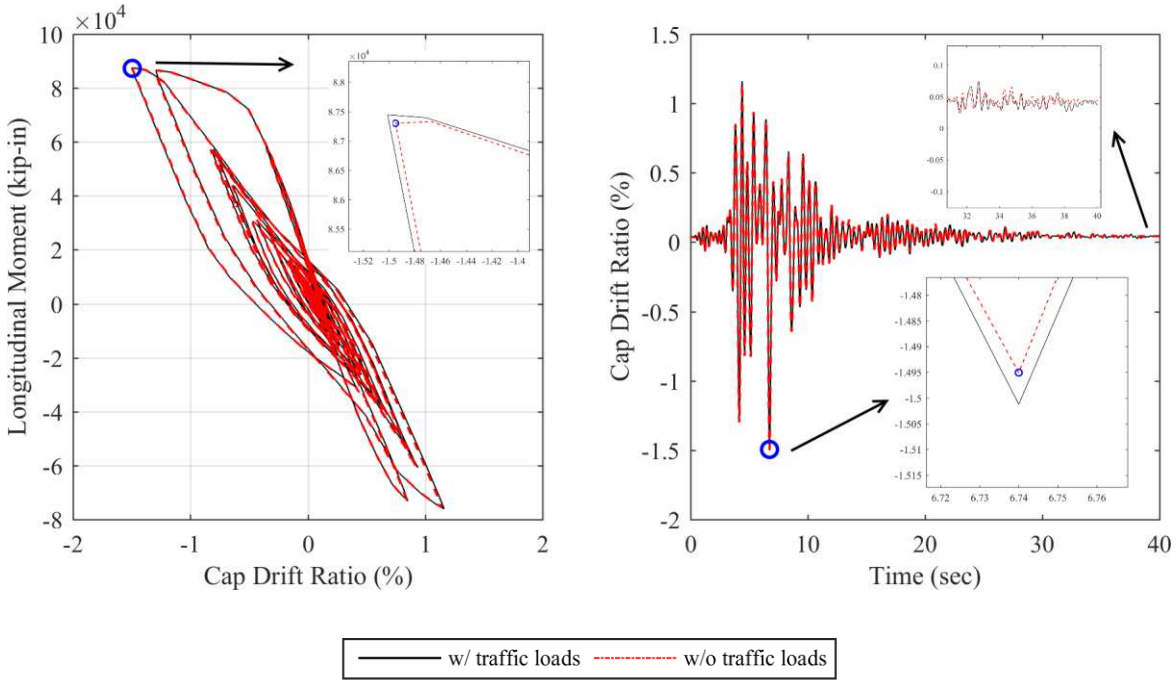

Fig. 27 Traffic effect to column ColL1: (a) hysteresis loop, and (b) drift ratio time history

The column axial forces of ColL1 were compared between those when the traffic load was considered or not. As shown in Fig. 28 (a), with the inclusion of the vertical traffic loading, column ColL1 has an increase of 3.48% on the peak axial force. It is also found that in addition to the seismic peak response the traffic loads can contribute considerably to the residue response and when the seismic load is gradually

dissipated (Fig. 28 (b)). For some bridges with limited safety margin and being vulnerable to progressive damage following initial local damage or during aftershocks, the traffic impact can become significant.

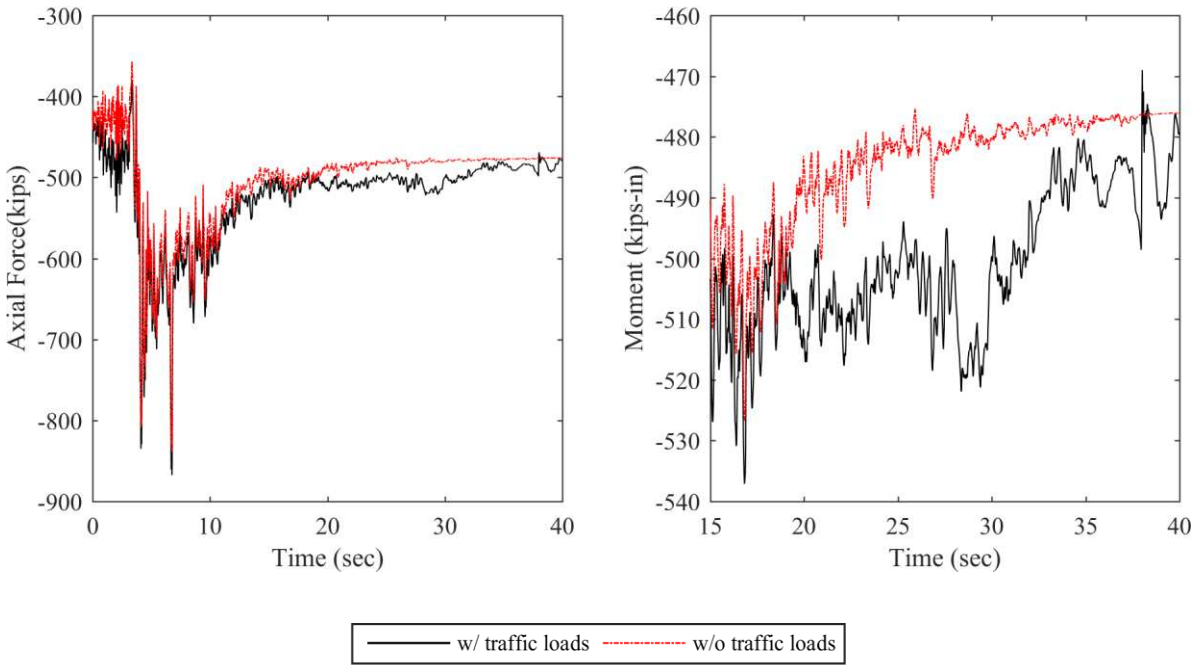

Fig. 28 Traffic effect to column ColL1: (a) axial forces, and (b) zoomed out view

3.5.2 Bridge deck response

As shown in Fig. 29(a), comparisons of the vertical peak displacements were made along the longitudinal and transverse lines A-B and C-D (marked on Fig. 13) respectively in the middle span of the bridge. The peak vertical displacement reaches 1.57 inch with the inclusion of traffic loads, which is 5.63% higher than the one when the traffic load is excluded. In terms of the mean displacement, the traffic load

causes increments of 5.69% and 5.30% along line A-B and line C-D respectively, due to the off-center deck curvature and expansion joints.

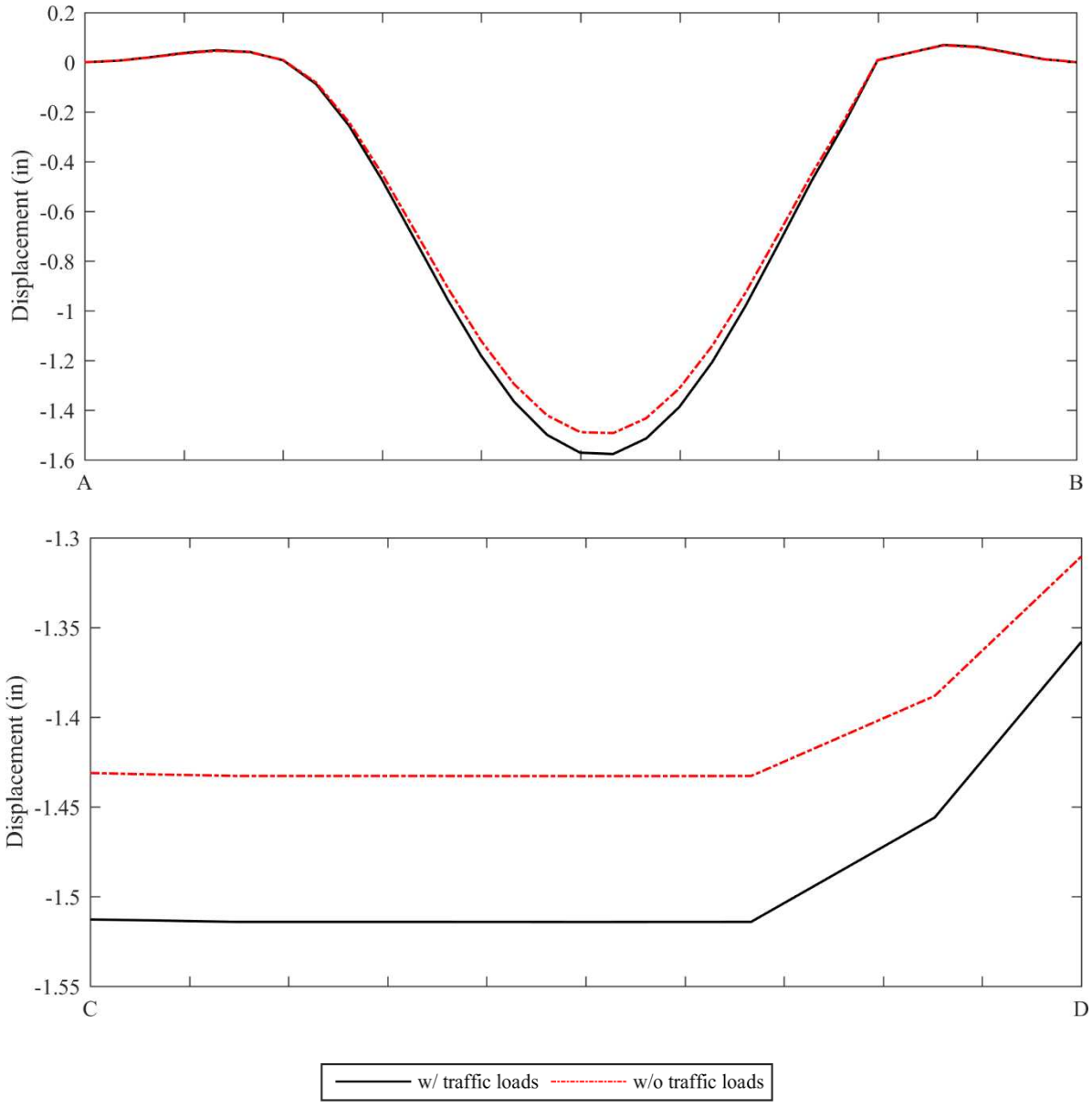

Fig. 29 Deck peak vertical displacements (a) along line A-B, and (b) along line C-D

Under the scenario seismic load, the impact of traffic loads on the bridge vertical displacement was further studied. Figs. 19 (a-b) show the time history results of the vertical displacement and the acceleration at the middle point of the bridge, respectively. On each subplot, the results with and without the inclusion of traffic loads were compared. It is found in Fig. 30 (a) that the inclusion of the traffic load in the seismic analysis of the prototype bridge can cause considerable increase of the vertical displacement from 38.35mm (1.51in) to 40.13 mm (1.58in, an increment of 5.63%) even during the time instants when the seismic-induced response reaches the maximum. As shown in Fig. 30(b), the bridge vertical acceleration responses exhibit different pattern from those of the displacement. The maximum vertical acceleration with traffic loads is about 3% less than that without traffic loads due to the dynamic coupling effects. Roughly after 15 seconds, the acceleration response caused by the earthquake becomes very mild and the contribution from the traffic excitations becomes dominant and exhibits small fluctuations on the time-history response. Comparatively, the existence of traffic loads can cause 11% larger bridge acceleration than that without traffic, which is mainly caused by the dynamic interactions between the bridge and moving vehicles.

The results suggest that the bridge seismic response considering the existence of traffic is more complex than simply superposing the responses of respective loads. The vertical displacement result is generally increased by the presence of the traffic almost all the time, while the acceleration result is only increased by the presence of the traffic when the seismic excitation becomes less significant. The pattern

of the bridge acceleration response may suggest that the impact of traffic during the later stage of the seismic excitation can be critical, especially when some local damages may have already occurred. Although the absolute percentage value of the increment is not large, it may cause pretty considerable difference in terms of the prediction accuracy of the potential damage on some bridge components when some members are already in the verge of damage or failure. For extreme loads induced by seismic excitation, such an increase can make a difference in terms of the seismic performance depending on the remaining safety margin for different bridge components under seismic events.

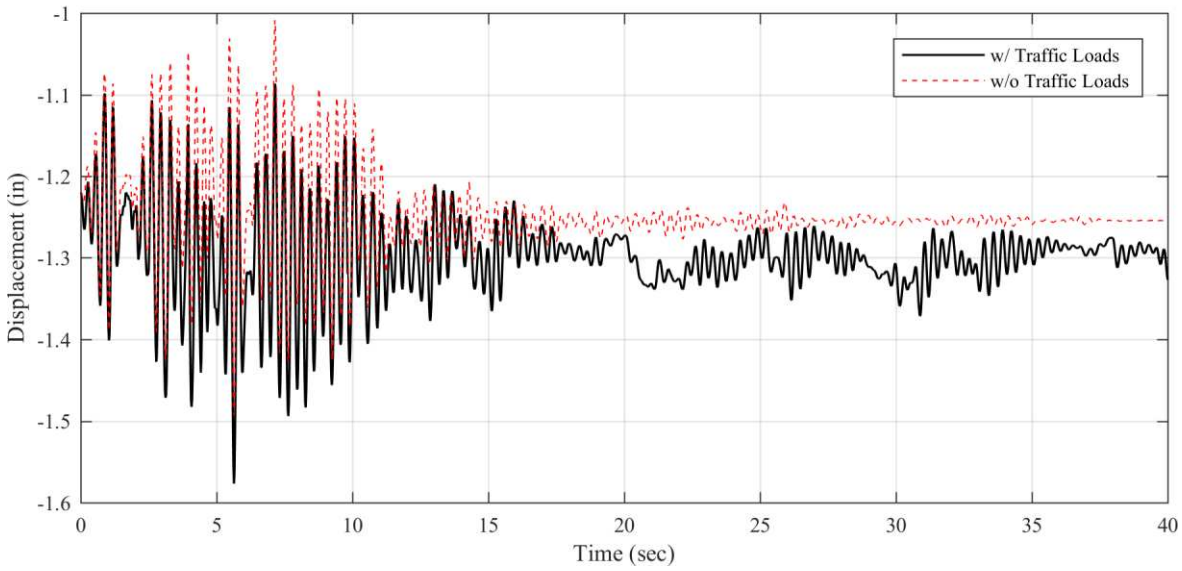

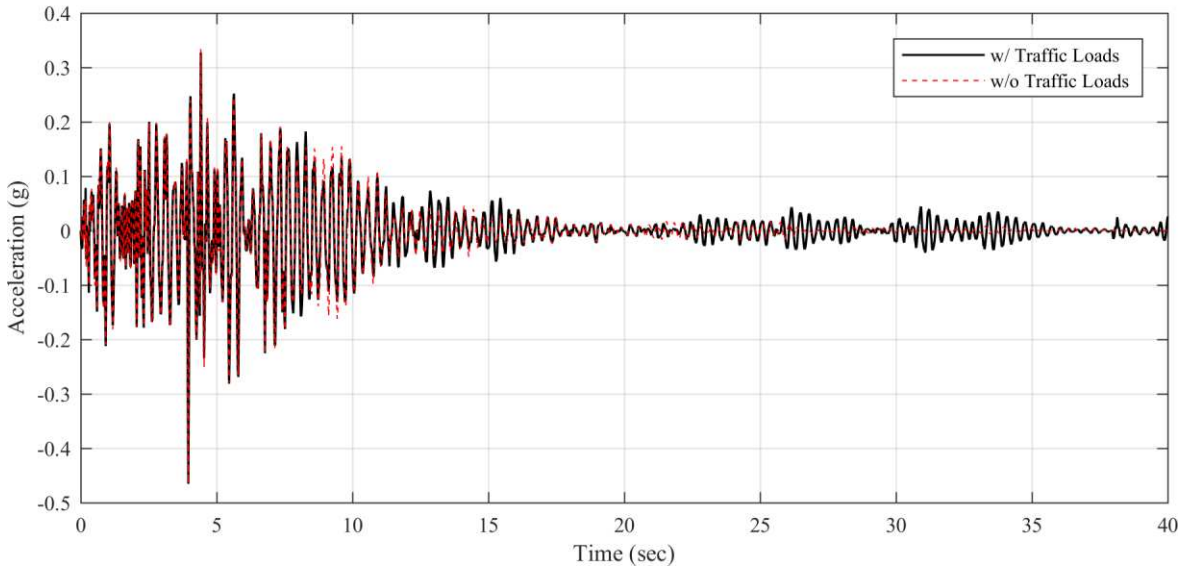

Fig. 30 Traffic load impact at midspan: (a) vertical displacement, and (b) vertical acceleration

3.6 Conclusion

A hybrid nonlinear seismic analysis approach was proposed for short- and medium-span bridges considering dynamic interactions with moving traffic by taking advantage of both mode-based bridge/traffic interaction analysis and nonlinear FEM seismic analysis with Opensees. A skewed and curved bridge under a scenario seismic input was studied for demonstration purposes. The baseline scenario including vertical and longitudinal seismic inputs were considered along with moving traffic in this study to demonstrate the proposed approach and provide some insights of the bridge seismic response. Due to the lack of the experimental data, a direct validation of the proposed approach is not yet possible.

For comparison purposes, the other scenario with the addition of transverse excitation was also studied. Numerical studies of the prototype bridge suggest that the proposed hybrid methodology can capture the complex dynamic interactions between the bridge and multiple vehicles as well as nonlinear bridge seismic

performance at the same time. Some observations from the numerical simulation results of the prototype skewed and curved bridge under the particular scenario earthquake are made as follows:

1. The skewed and curved bridge has very different seismic responses on different columns under both seismic and traffic loads, such as transverse moments due to the curved and skewed nature. The demand and capacity ratio of the longitudinal moments is much higher than other seismic response indicating limited safety reserve;
2. There exist large pounding forces between the girder and abutment, which may cause considerable damage to the concrete and expansion joints;
3. The comparison between the results of the prototype bridge substructures with and without considering traffic disclosed some interesting observations. The impact from traffic on bridge seismic response is more complex than simple superposition of the responses under individual loads. For this particular scenario earthquake excitation, the consideration of traffic causes little increase on the peak values of some seismic performance of the columns, such as end moments and drift ratios. The impacts on the axial forces of the columns become more significant on both extreme values and the residue response. These findings confirm that traffic impact mainly applies on the seismic response in vertical directions;
4. Compared to the impact on the seismic response of substructures, traffic impacts on the performance of superstructure, such as vertical displacement and acceleration are more significant.

Overall, traffic load has considerable impact on the overall seismic peak response even under the peak seismic response. It has pretty significant contribution to the residue response and also when the seismic load is gradually dissipated;

5. Traffic may cause pretty considerable difference in terms of the prediction accuracy of the potential damage on some bridge components when some members are already in the verge of damage or failure. The traffic impact can become critical for some bridges with limited safety margin and being vulnerable to progressive damage following initial local damage or during aftershocks.

The proposed methodology was demonstrated with only one scenario earthquake on a prototype bridge due to the scope limit. Therefore, some observations made above are only for this particular prototype bridge under the specific scenario seismic excitation, and more general conclusions can be made based on more systematic analyses of more bridges and seismic inputs.

CHAPTER 4 PARAMETRIC INVESTIGATION OF NONLINEAR SEISMIC PERFORMANCE OF CURVED AND SKEWED BRIDGES WITH MOVING TRAFFIC

4.1 Introduction

Bridges with unconventional geometric configurations such as skew and horizontal curvature are prevalent nowadays to accommodate complex terrain and achieve cost effectiveness for traffic access. Studies on the previous major earthquakes, such as the 1992 Cape Mendocino earthquake (Goel & Chopra, 1997), 1994 Northridge Earthquake (Meng et al., 2001) and 2010 Chile earthquake (Kawashima et al., 2011; Mitchell et al., 2012), have shown that geometric configurations of concrete bridges have different types of dominant failure modes during seismic events. For example, according to the damage investigation of reinforced concrete bridges with large skew angles, unseating of bridge girders or large deck displacement have been reported to be more prone to significant damage than other structural components (Deepu et al., 2014; Dimitrakopoulos, 2011; Mallick and Raychowdhury, 2015; Wu et al., 2019). Bridges with curved superstructures, on the other hand, have been observed to have unique seismic performance (Ates & Constantinou, 2011; N. Li et al., 2019; Monzon et al., 2016). Field seismic assessments indicated that earthquakes could induce serious damage to piers of horizontal curved bridges (Billah et al., 2013; Zhi et al., 2019). Tondini and Stojadinovic (2012) found that column ductility in the transverse direction is inversely proportional to deck radius through a probabilistic model. Li et al. (2015) performed shake table

tests on a 1/10-scale curved bridge model to study the effect of multidimensional excitations and found that site condition and ground motion characteristics have significant influence on the seismic behavior of curved bridges.

Although bridge superstructure designs which contain both skew and curvature have become more common for short- and medium-span overpass bridges, corresponding studies on seismic performance are still scarce as compared to those on bridges with only curvature or skew. Wilson et al (2014) carried out a numerical study to investigate the combined effects of both curvature and skew on seismic performance. Despite the limited deformation due to the low seismic region site condition, the results of the analyses showed coupled demand between diagonally opposite columns as skew angle increases, while low radius of curvature induced higher moment for the interior pier-columns. It was also observed that both skew and curvature exhibited stacking effects proportionally to each other. Seismic performance assessment of simple-made-continuous (SMC) curved and skewed bridges in low-to-moderate seismic regions was performed by Hou and Chen (2017). Their comparative study results indicated that unconventional geometric configurations of bridges can significantly affect the substructure seismic behavior and suggested detailed assessment is recommended when determining the optimal bent connection. Serdar and Folić (2018) developed detailed optimal probabilistic seismic demand models for seismic analysis. In a recent study, Heidari and Gerami (2019) examined the damage mechanisms of the column and diaphragm abutment

failures of skewed and curved bridges and found that the input ground motion direction and the bridge skew direction are the determining parameters for seismic performance.

The curvature and skew of superstructure also affect how traffic loads may influence the bridge seismic responses. For example, vehicles may act as eccentric loads on bridges with curvature and/or skew, which may introduce unsymmetric vertical loads and torsion on the bridge structure. In most existing seismic studies, traffic loads were usually simplified for specific scenarios or embedded into analytical response equations (Borjigin et al., 2018; Frýba & Yau, 2009; Ghosh et al., 2014; Liu et al., 2011; Zhu & Frangopol, 2013). Ashebo et al (2007) conducted a full-scale field test about load distributions on a skewed bridge in normal traffic conditions. The dynamic characteristics showed good agreement between the results from experimental studies and finite element models. Morales-Nápoles and Steenbergen (2015) proposed a method of hybrid non-parametric Bayesian networks for modeling vehicular weigh-in-motion systems. The traffic load model was found trustworthy but required a large amount of statistical buildup for the quantification process. In a study of vehicle-bridge interactive systems, Borjigin et al (2018) devised a single cargo truck sprung-mass model by applying the vertical ground motion to a simplified 3D pier-beam bridge model. Although the study focused on the transverse bridge response and corresponding Fourier spectra, it was found that vehicle loadings were likely to change bridge seismic behavior. Another study by Zhou and Chen (2018) revealed that the coupling effects between the long-span bridge-traffic system and

the earthquake excitations significantly influence the bridge component pseudo-static and dynamic responses in the vertical and torsional directions.

In a recent paper by the authors (Chen et al., 2020), a hybrid analysis framework of assessing seismic performance of the bridge and traffic system was developed by considering dynamic coupling effects between moving vehicles, bridges, and seismic excitations. The simulation results not only showed very different responses among individual columns and considerable pounding forces at the abutments, but also indicated that traffic load can affect the risk of potential damage on superstructures. In this study, a comprehensive parametric study based on the proposed new modeling techniques (Chen et al., 2020) is conducted to study the nonlinear seismic performance of a typical curved and skewed bridge with moving traffic. The study will investigate the impacts from different ground motion characteristics, traffic conditions, and superstructure geometry on the bridge seismic performance. Since earthquake-induced damages on bridges are heavily dependent on site-specific characteristics, this study will focus on component responses rather than failure mechanisms to provide more general insights.

4.2 Numerical analysis model

The analysis method adopted in this study is called the “Equivalent Moving Traffic Loads - Finite element (EMTL-FE)” hybrid strategy developed by the authors in a recent study (Chen et al., 2020). For completeness purposes, the analysis method is briefly introduced in the following with the flowchart shown

in Fig. 31. Firstly, the EMTL time histories for each vehicle are obtained from the traffic flow simulation via the two-lane cellular automaton (CA) model and the dynamic bridge-vehicle interaction analysis (Chen & Wu, 2011) in a format of time histories of nodal forces. The numerical finite element analytical models were constructed using the 3D finite element software "open system for earthquake engineering simulation (OpenSees)" (McKenna et al., 2010).

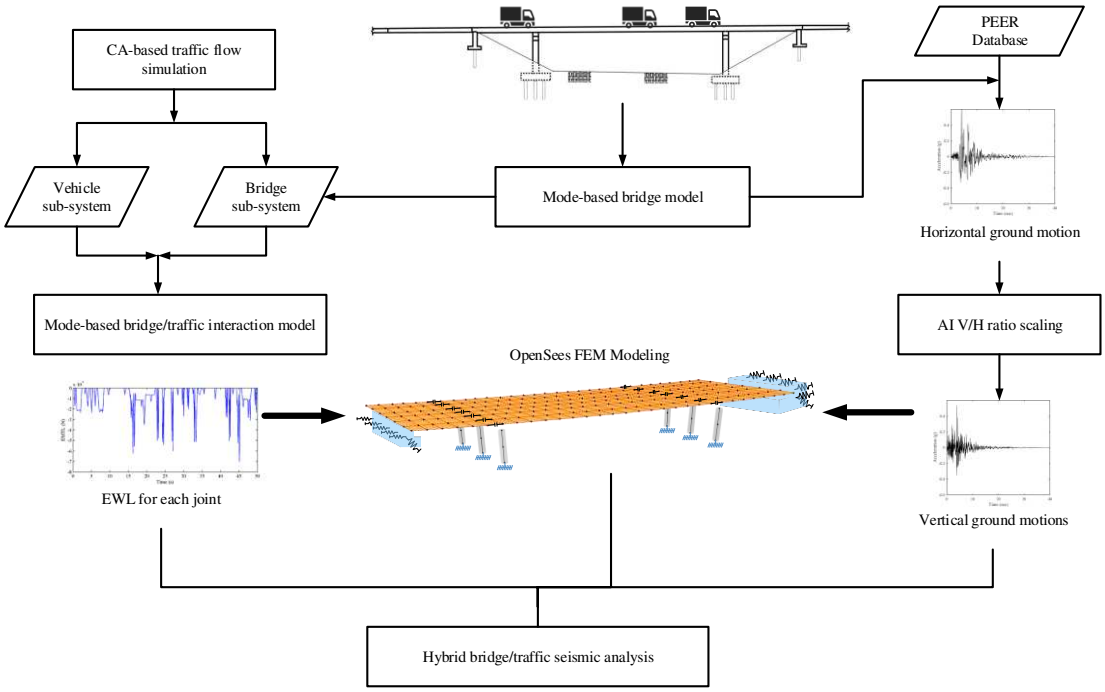

Fig. 31 Flowchart for EMTL-FE hybrid strategy (Chen et al., 2020)

The prototype skewed and curved bridge is a 3-span reinforced concrete bridge with six lanes and a radius of curvature of 436.1 m and skewness of 41.7 and 31.7 degree at both ends. The bridge deck is

supported by concrete box girders over two sets of circular column bents, and connected with seat-type skewed abutments at the ends, as shown in Fig. 32.

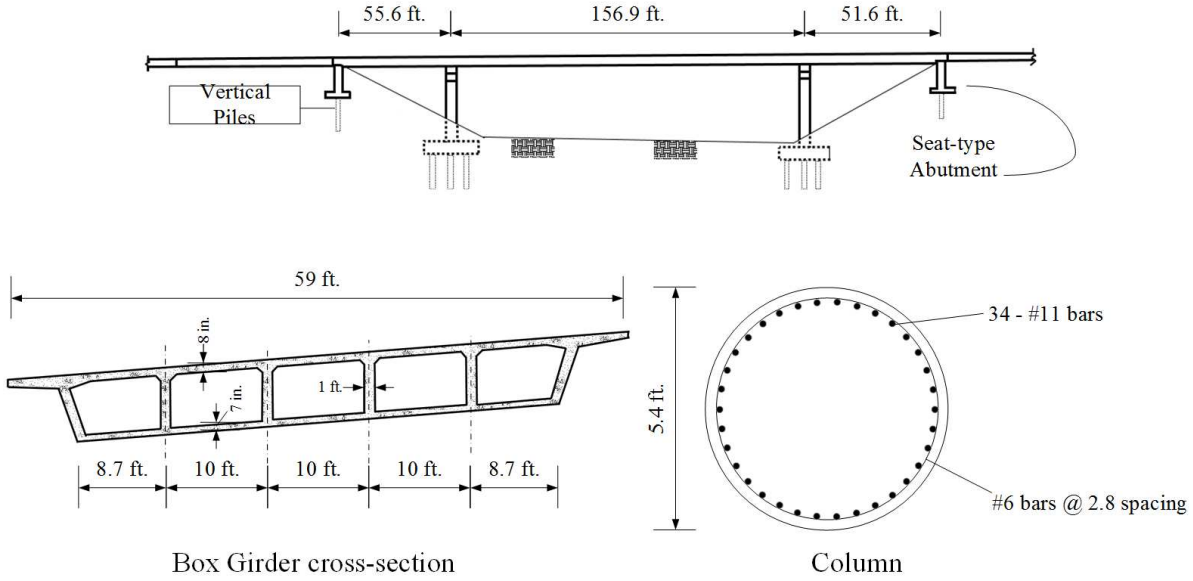

Fig. 32 Prototype bridge parameters

In addition to the prototype curved and skewed bridge serving as the baseline bridge, a counterpart straight bridge with similar geometries, parameters, and designs are modeled with Opensees for the following comparative analyses. The basic parameters and configurations of both the baseline bridge and the straight bridge are shown in Fig. 33.

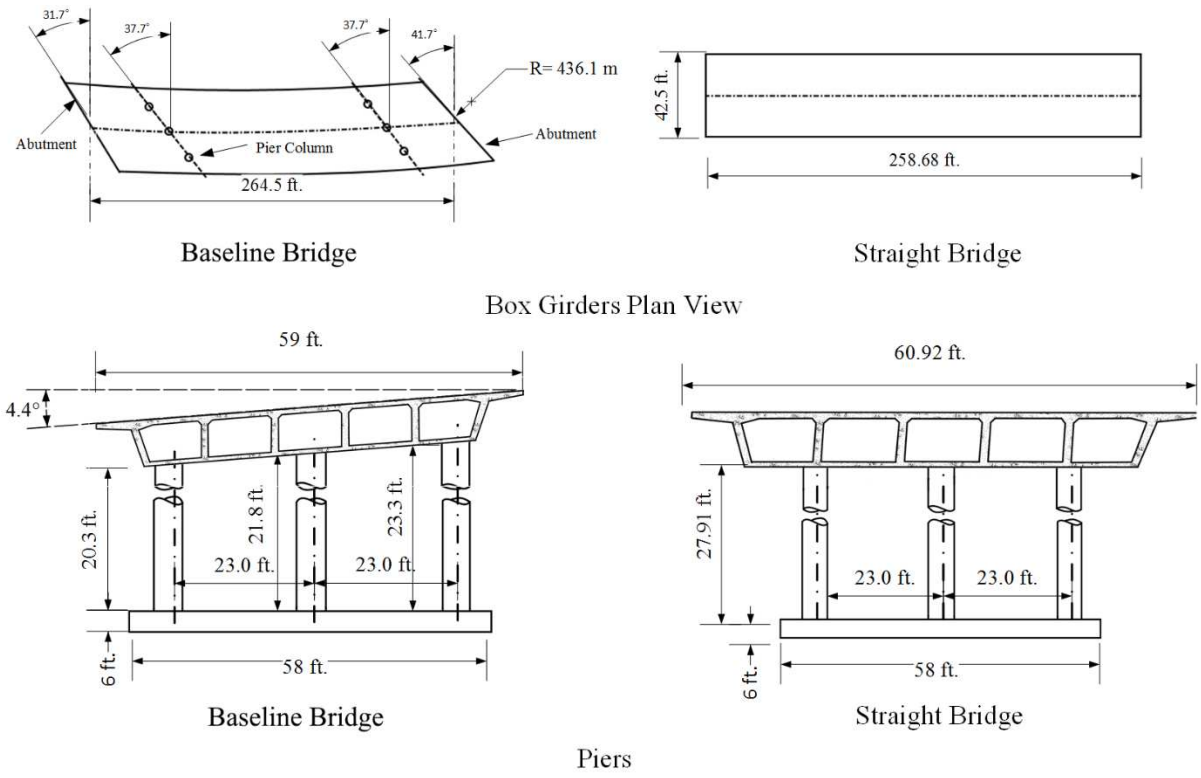

Fig. 33 Configurations of baseline bridge and straight counterpart bridges

The vehicle loads used in this study are modeled using the vertical equivalent wheel load (EWL) determined by the equivalent moving traffic loads (EMTL) (Zhou and Chen, 2015b & 2015a) and cellular automaton (CA) model (Chen and Wu, 2011). Fig. 34 shows the simulated EMTL time histories at the middle point of the middle span for the baseline bridge and straight bridge (traffic density = 32 vehicles/km/lane). Note that considering the traffic flow speed, each time history has a cycle of 50 sec and will repeat for longer input ground motions.

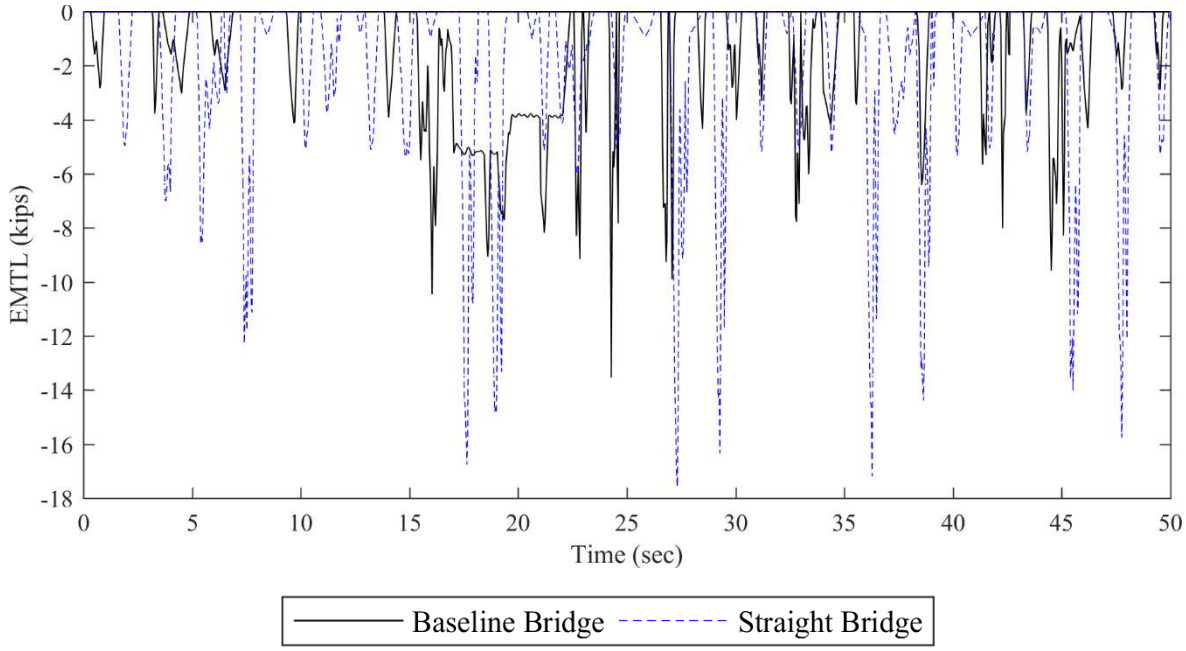

Fig. 34 Vertical traffic load time history at the middle point of the middle span

4.3 Parameters and case scenarios

This section describes parameters which will be considered to investigate the influence of the baseline bridge coupled with traffic loads in the next section. These parameters include different combinations of earthquake orthogonal directions and intensities, coupled traffic flow densities and earthquake occurrence moments, followed by comprehensive comparisons with the counterpart straight bridge model.

4.3.1 Ground motion multi-direction scenarios

In general, ground motions are characterized and quantified in three primary directions. Biaxial combinations of two orthogonal components, such as the 30% rule (Rosenblueth & Contreras, 1977), 40%

rule (Newmark et al., 1970), and CQC3 (Menun and Der Kiureghian, 1998), have become general considerations in several seismic design codes (Armstrong, 1997; Null, 2000).

In this study, the baseline combination (Dir 0) includes 100% longitudinal component and 100% vertical component scaled following the Vertical/Longitudinal Arial Intensity Ratio. For comparison purposes, two other combinations of excitations are also made: Dir 1 includes 100% transverse and 100% vertical components following the same scaling ratio as Dir 0; Dir 2 is to include 100% longitudinal, 100% vertical (same scaling ratio as Dir 0), and 40% transverse components. Details about the longitudinal ground motion (SYL090) and vertical ground motion (SYL-UP) used in this study are listed in Table. 10.

Table. 10 Input direction and intensities of each combination

Combination	Longitudinal	Transverse	Vertical
Dir 0	100% SYL090	N/A	100% SYL-UP
Dir 1	N/A	100% SYL090	100% SYL-UP
Dir 2	100% SYL090	40% SYL090	100% SYL-UP

4.3.2 Ground motion vertical/longitudinal arial intensity ratios

Field survey and simulations about bridges with curved superstructure have shown strong correlation between structural asymmetrical responses and vertical-horizontal ground motions (Han et al., 2009; Kataria and Jangid, 2016). Therefore, to study such characteristics, eight near-fault ground motion records

are selected from the Strong Motion Database (Haddadi et al., 2016.) and applied with a longitudinal and vertical directional combination (Dir 0) to the finite element model as shown in Table.11. The earthquakes components are selected from stations within 15 km of the fault rupture surface and cover a range of peak ground acceleration (PGA) and Vertical/Longitudinal Arial Intensity Ratio (V/L Ratio) from 0.1g to 0.9g and 0.33 to 0.98, respectively.

Table.11 Selected Ground motions for earthquake characteristic analysis

Case	**Station**	**R_{rup} (km)**	**L (sPGA*1)**	**V (sPGA)**	**V/L Ratio**
Baseline	Sylmar - Olive View Med FF	5.3	0.57	0.22	0.44
GM_1	Arleta - Nordhoff Ave Fire Station	8.66	0.44	0.96	1.37
GM_2	Saticoy St., Northridge	12.09	0.36	0.62	0.98
GM_3	Roscoe Blvd., Sun Valley	10.05	0.56	0.28	0.78
GM_4	Coldwater Cyn Av North Hollywood	13.91	0.45	0.35	0.75
GM_5	Mulholland Bavery hill	10.57	0.51	0.16	0.43
GM_6	Wonderlands Ave	15.11	0.47	0.10	0.37
GM_7	Van Nuys - 7 story Hotel	7	0.26	0.06	0.33

*1: sPGA=Scaled peak ground acceleration;

Fig. 35 (a) and (b) outline the 5%- damped acceleration response spectra of the selected ground motions in both longitudinal and vertical directions with periods between 0.02 sec and 4.00 sec. In this study, the longitudinal ground motions are scaled based on the design response spectrum (DRS) at the bridge fundamental periods of 0.30 sec and 0.26 sec for the baseline bridge and the straight bridge, respectively. The corresponding vertical components are then scaled accordingly while maintaining the same V/L Ratio.

The design spectrum is determined based on Class-D stiff soil as categorized for the prototype bridge in the region classified as moderate-to-high seismic level in the U.S.

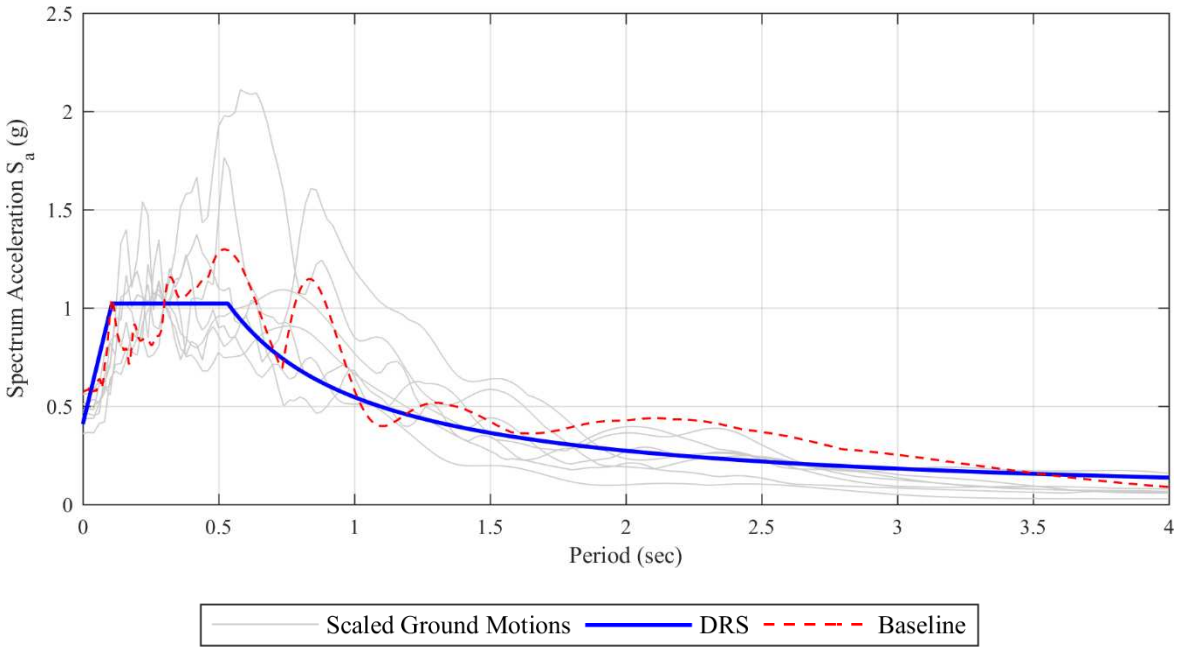

(a)

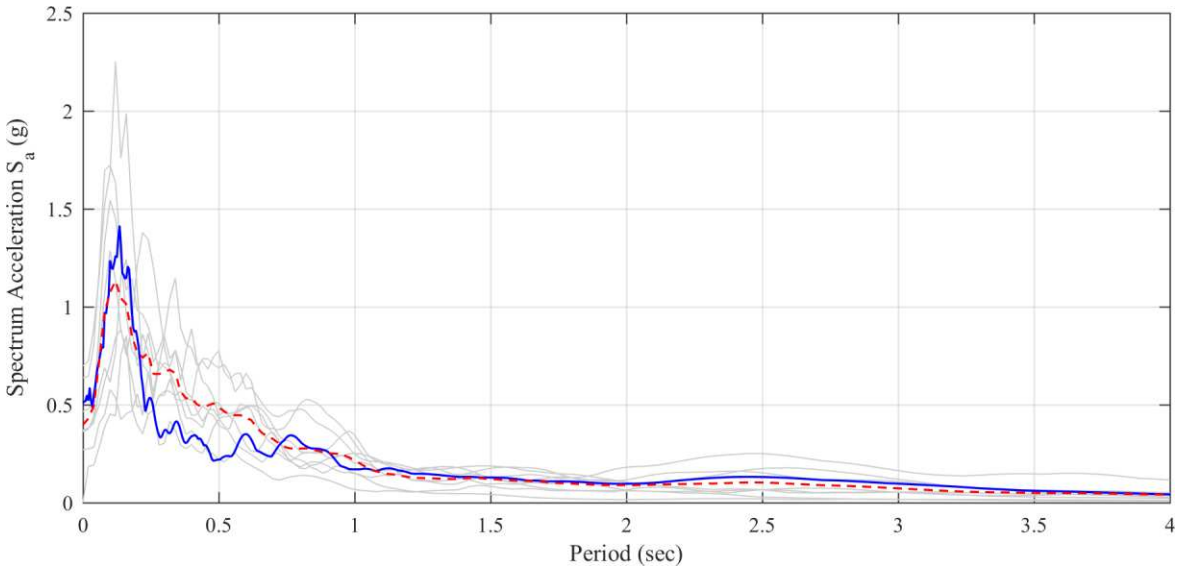

(b)

Fig. 35 Response spectra of selected acceleration spectra: (a) longitudinal direction, and (b) vertical direction

4.3.2 Geometric condition

To study the impact of bridge geometries, seismic performance of both the prototype bridge and the straight counterpart bridge as shown in Fig. 33 will be studied and compared in the following sections.

4.3.3 Traffic impact and earthquake occurrence moments

The previous study of EMTL-FE framework (Chen et al., 2020) has indicated that traffic loads could have significant contribution to the seismic performance of bridges. Therefore, the EMTL loads based on three traffic densities (free, moderate, and busy) and vehicle compositions, are simulated and applied to the bridge deck nodes for both analytical baseline model and straight counterpart bridge model, respectively.

Since earthquakes typically cannot be accurately forecasted, earthquakes may happen at any time when there are vehicles moving on the bridge. Realistic traffic flow on the bridge is stochastic in nature and it becomes important to study the time-dependent impact from the occurrence of earthquakes relative to the stochastic traffic flow. By applying the same simulated stochastic traffic flow, several earthquake occurrence moments (5 sec, 10 secs and 12 secs after the start of the EMTL load time histories) are selected to investigate the potential time-dependent influence.

4.4 Parametric analysis results

In the following, the longitudinal-vertical ground motion excitation (SYL090 and SYL-UP) coupled with traffic loads is set as the baseline ground motion excitation. Structural responses being studied in the following sections include column responses, abutment behaviors in both longitudinal and transverse directions, girder bending moments, and deck dynamic responses.

4.4.1 Seismic response of the baseline bridge

First, the seismic response of the baseline bridge is studied under the baseline load scenario. For the peak column seismic responses, the column on the inner side of the curve near the obtuse angle of the baseline bridge is identified to be the critical column according to the initial numerical assessment results. Under the baseline ground motion excitation coupled with traffic loads, the column axial force, longitudinal moment, and transverse moment are 1256.48 kips, 30983.80 kip-in, and 8131.13 kip-in, respectively (Fig. 36).

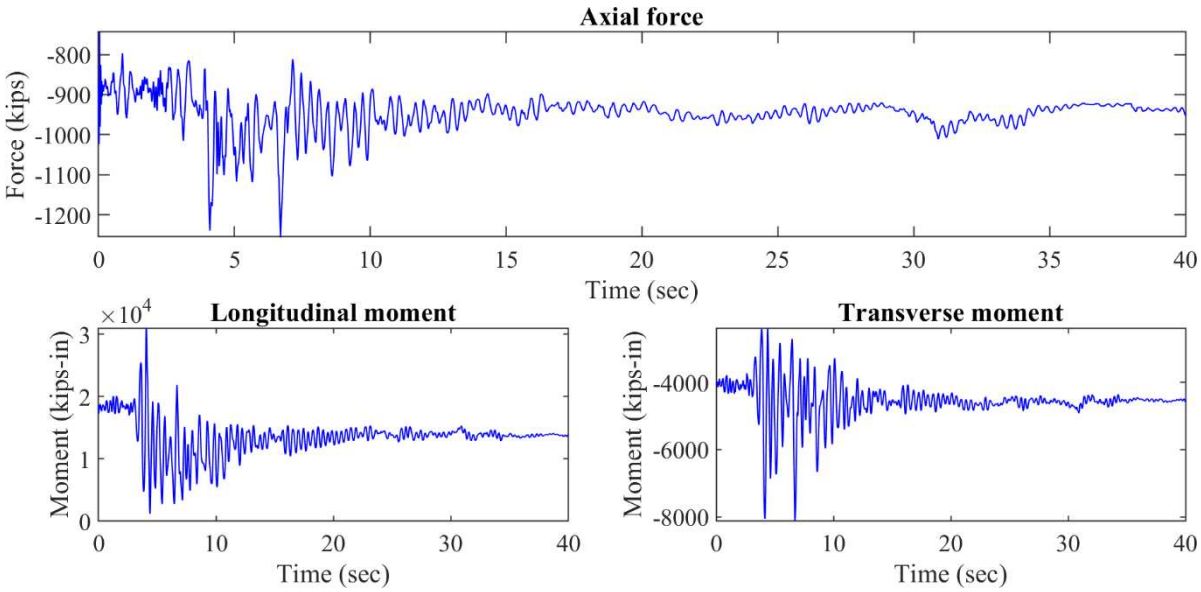

Fig. 36 Time histories of critical column

Fig. 37 shows the abutment-girder gap opening and pounding force in the longitudinal direction, as well as the deformation and reactions in the transverse direction, respectively. It should be noted that because the transverse reactions of the two abutments share similar characteristics in time histories but with different peak values, Fig. 37 only illustrates the transverse time history responses at one acute corner for the sake of brevity. Fig. 38 shows the maximum transverse reactions at the skewed abutment shear keys, where the reactions at the two acute corners are significantly higher than those at the obtuse corner.

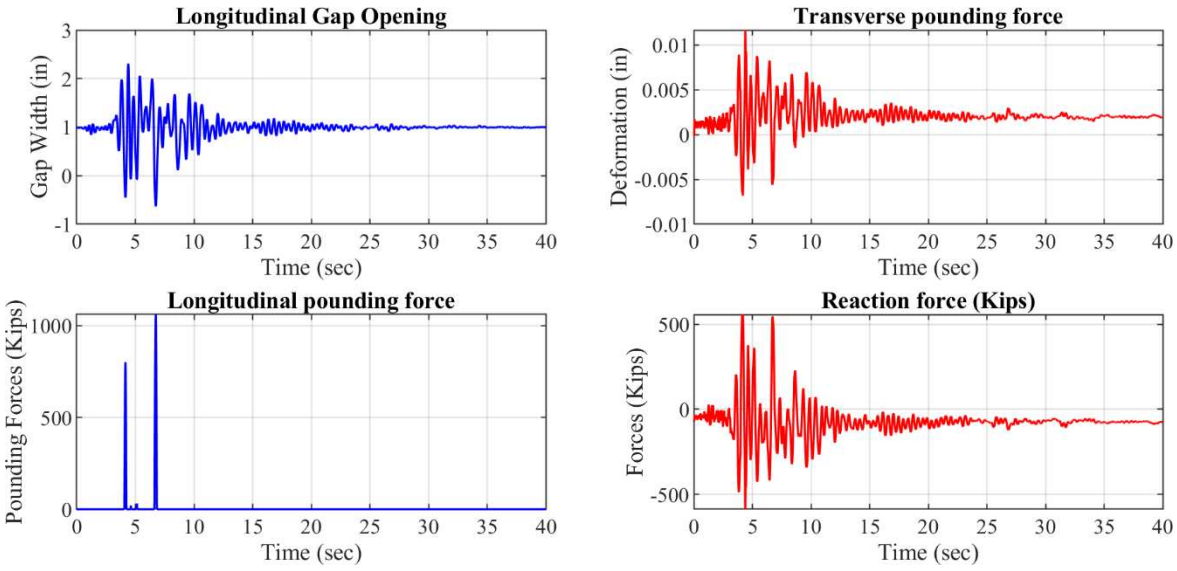

Fig. 37 Abutment responses for the baseline bridge

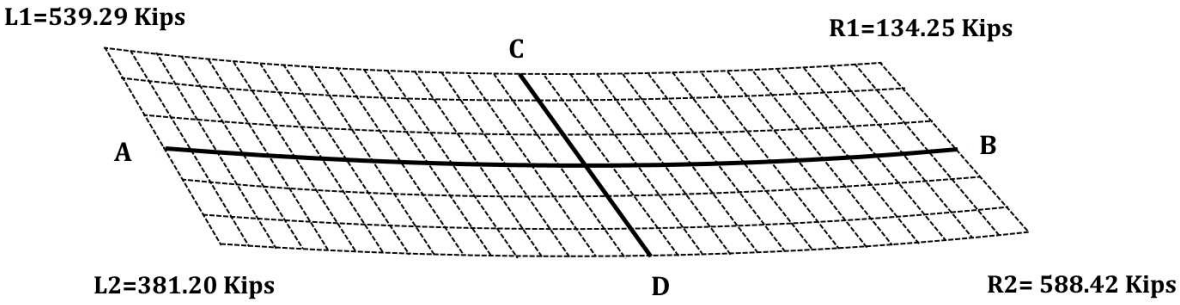

Fig. 38 Abutment transverse reactions at four corners

For the dynamic response of the superstructure, the longitudinal moments along the middle lines of the girder (i.e., A-B and C-D as marked in Fig. 38) are presented in Fig. 39. The results exhibit unsymmetric patterns in terms of where the maximum moments occur at the outer radius of the skewed and curved superstructure.

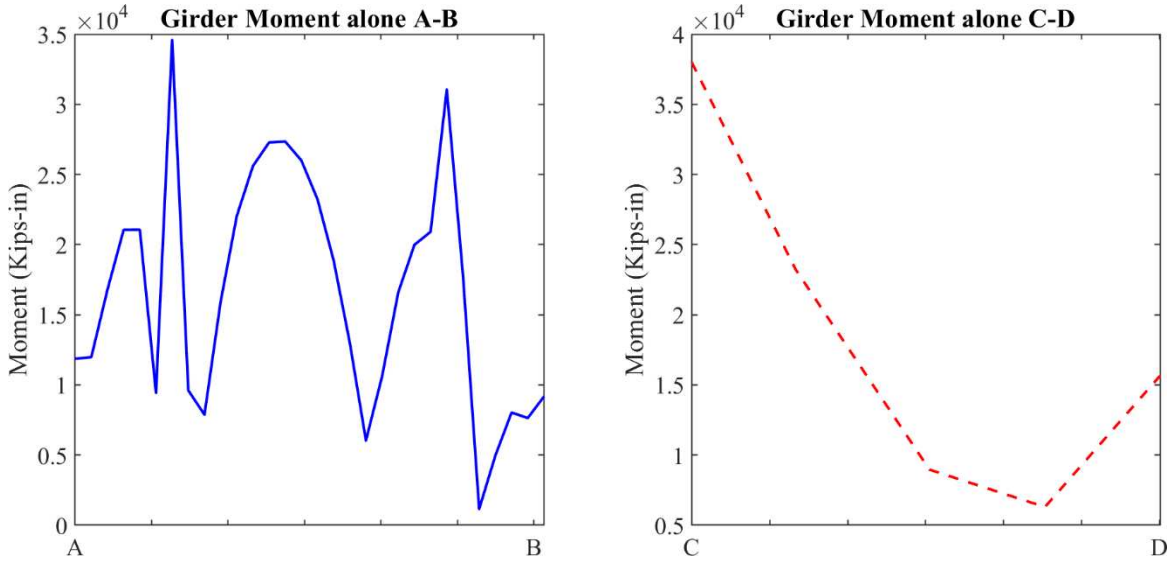

Fig. 39 Longitudinal girder moment along A-B and C-D

The mid-span displacement and acceleration of the bridge deck are presented in Fig. 40. The results show that the maximum mid-span vertical displacement and acceleration are 1.58 in and 0.46g, respectively.

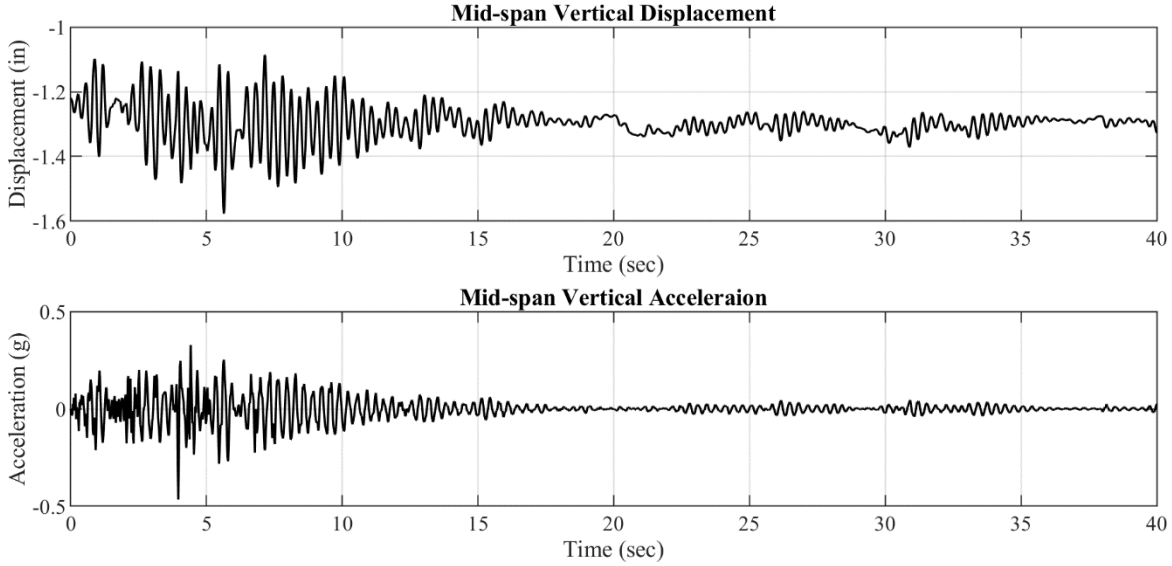

Fig. 40 Mid-span vertical displacement and acceleration time history

4.4.2 Impact of earthquake excitations

Girder moments and abutment responses are found to be most influenced by inclusion of transverse ground motion component. For example, as shown in Fig. 41, the longitudinal girder-abutment gap opening and pounding for the baseline case vary considerably over time during earthquakes and poundings occur two times with the pounding force magnitudes up to 1000 kips. By zooming into the short time period when poundings occur in Fig. 41, which are between 4.12sec to 4.20sec and 6.70sec to 6.78sec, respectively, the results as shown in Fig. 42 indicate that for abutment piles near the acute angle, the transverse-vertical ground motion case (Dir 1) has a slightly larger gap width and pounding force than the longitudinal-vertical ground motion case (Dir 0). In comparison with Dir 0 and 1, Dir 3 caused considerably larger gap width and pounding forces.

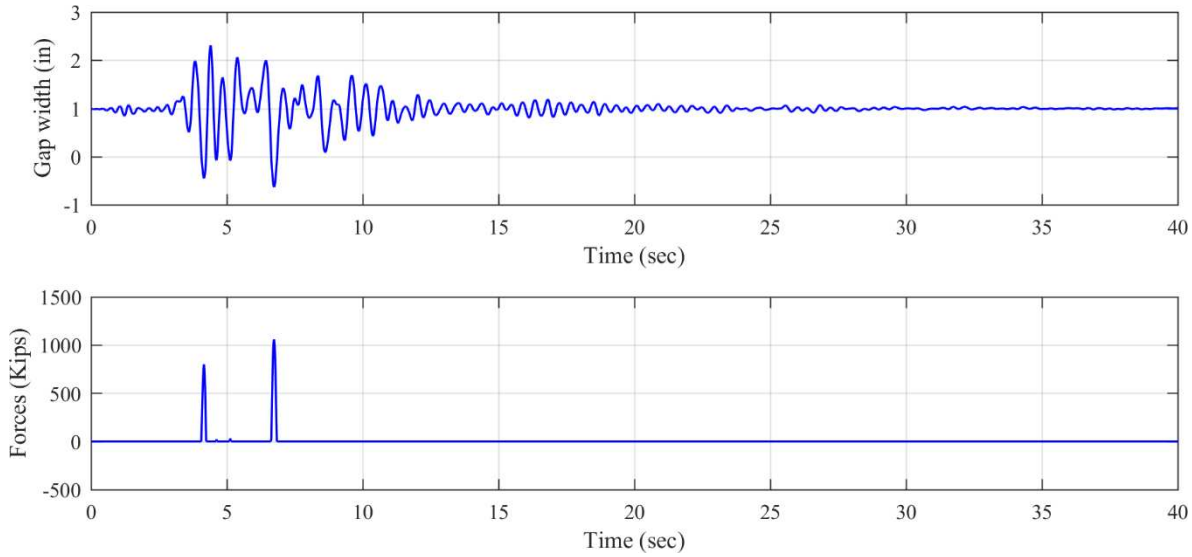

Fig. 41 Gap opening and pounding forces for baseline case (Dir. 0)

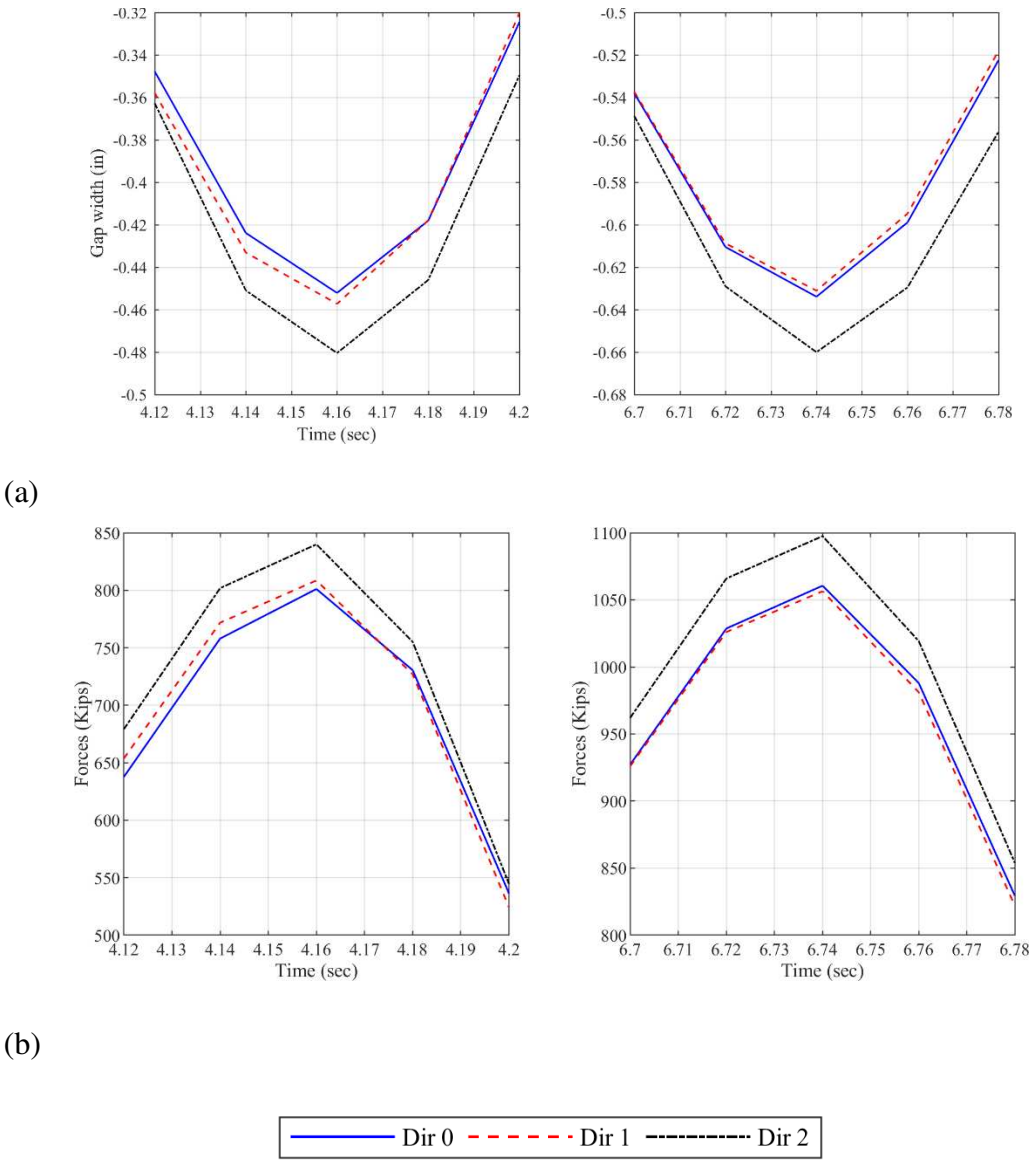

Fig. 42 Pounding effect at the two critical time-section: (a) gap opening between girder end abutment, and (b) pounding forces

In addition to the pounding effect, rotational overturn of the girder due to unbalanced moments may contribute to bridge unseating. In Fig. 43, the girder longitudinal moment is illustrated along line A-B, where the excitation directions Dir 0 to Dir 2 have been specified in Fig. 43. The results not only show an

unsymmetrical distribution of longitudinal moments for the baseline bridges, but also indicate the inclusion of transverse ground motion results in a considerable change of peak moment at the midspan as compared to the longitudinal ground motion case.

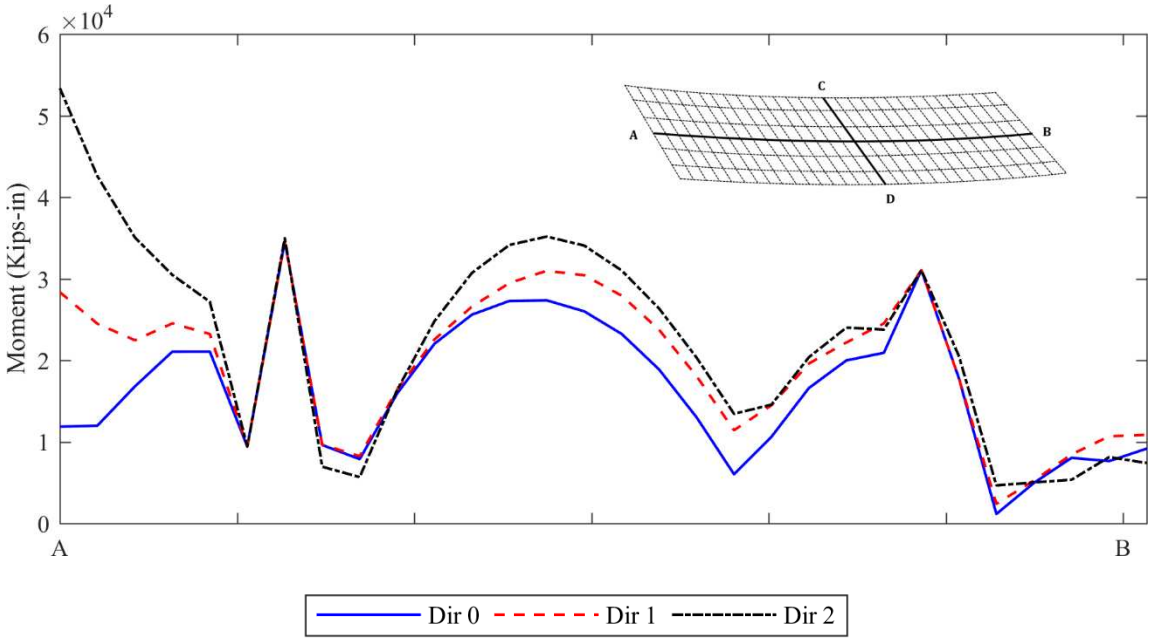

Fig. 43 Girder moment along direction A-B

V/L PGA ratio defines the ratio between vertical and longitudinal components of seismic excitations. Due to the unsymmetric nature of the baseline bridge, the seismic performance of individual columns may vary considerably. Fig. 44(a) and (b) show the demand/capacity (D/C) ratio moments and axial forces for each column of the baseline bridge under the selected ground motions as specified in Table.11. Based on the high D/C ratios in Fig. 44, column ColR1 is selected as the critical column for later comparative analysis.

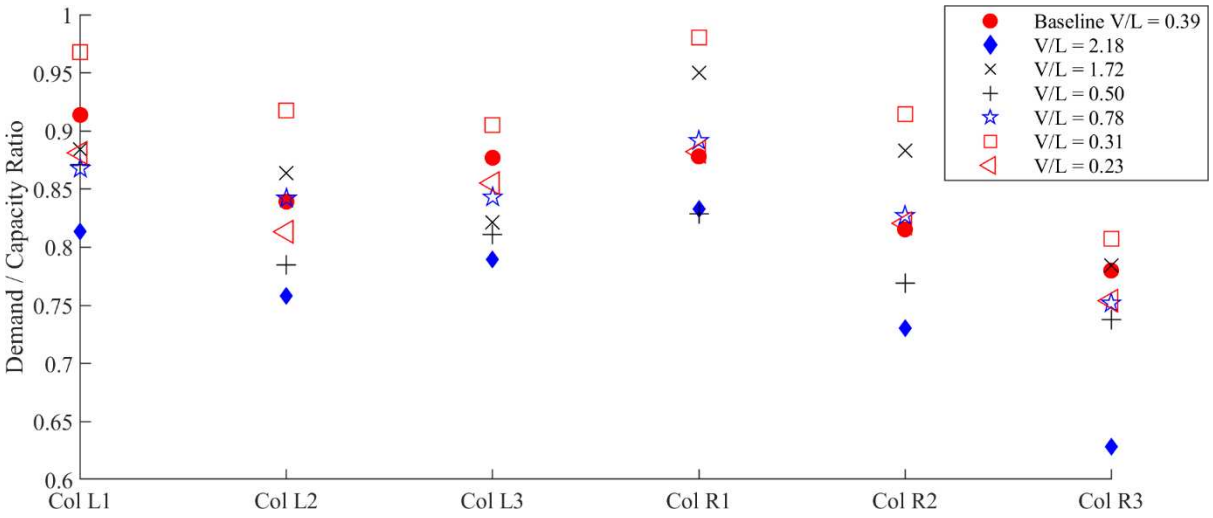

(a)

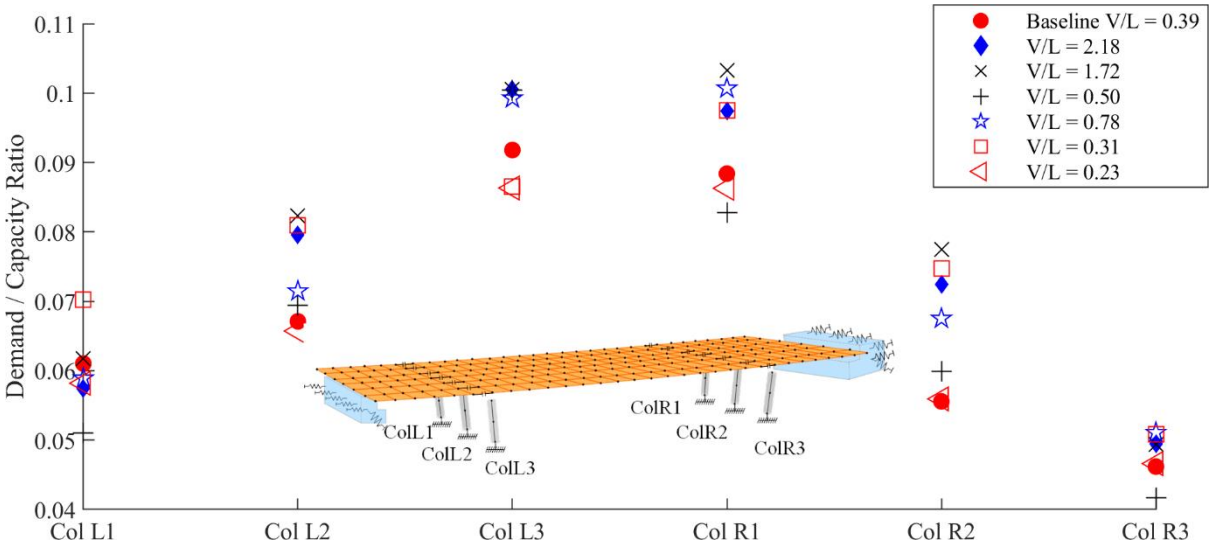

(b)

Fig. 44 D/C ratio comparison for individual column: (a) longitudinal moments, and (b) axial forces

The analysis results with different V/L PGA ratios for ColR1 are presented in Fig. 45 in terms of critical column axial forces, moments, and drift ratio as well as vertical displacement at the middle point of the middle span. Except for the results from Mulholland Bavery hill (GM_5 in Table.11) showing large column responses due to the response spectrum scaling, the vertical deck displacements are highly proportional to V/L PGA ratio: i.e., Ground motions with high V/L PGA ratios also lead to high column axial forces but their correlation is not as strong as deck responses. On the other hand, it seems that column bending moments and drift ratios are less influenced by the V/L PGA ratio than the vertical deck displacements with the percentage changes about 7% and 5%, respectively.

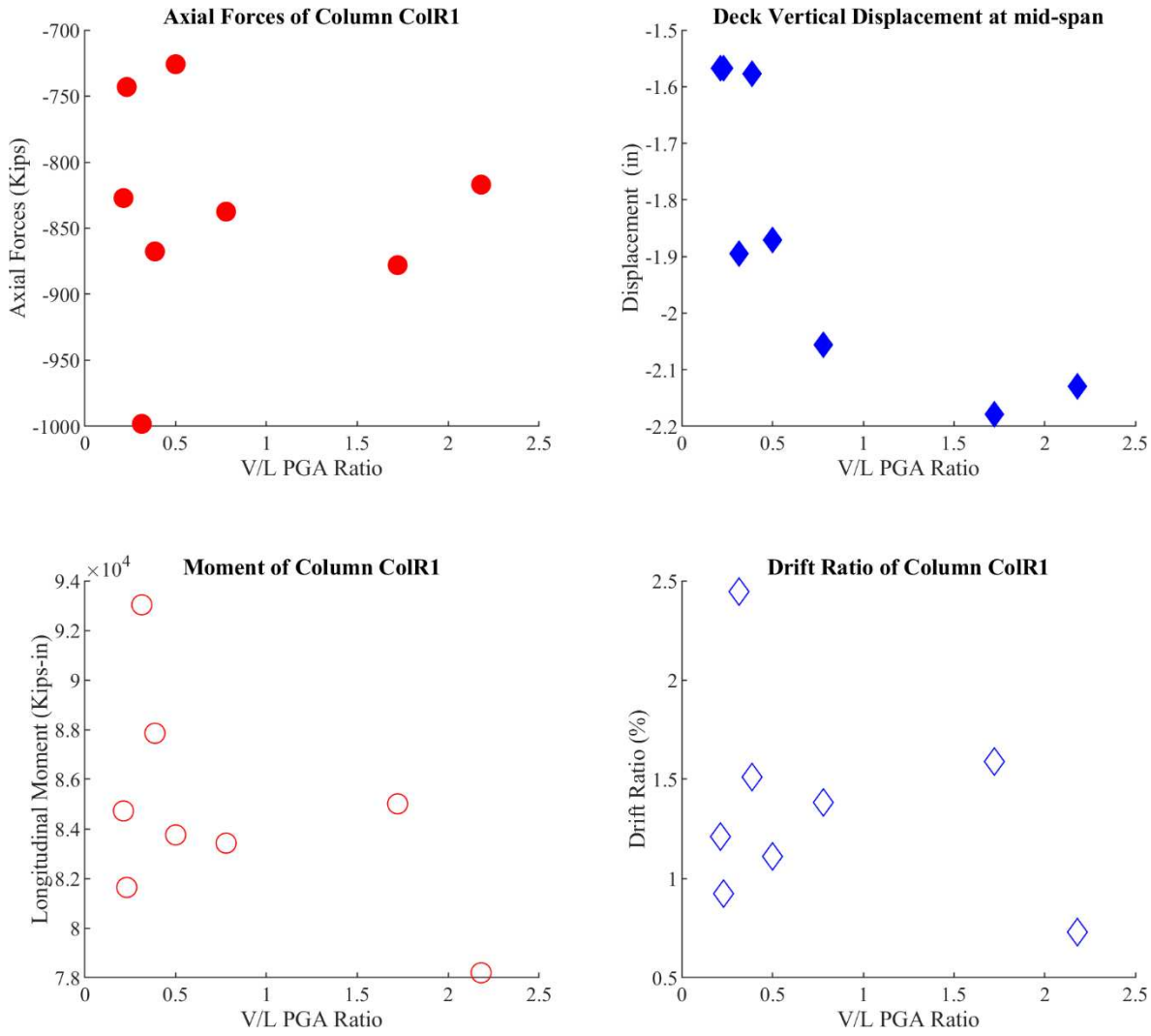

Fig. 45 V/L PGA ratio comparison of vertical and longitudinal structural response

To further investigate the column moments and drift ratio performance, the influence of the involvement of the vertical seismic excitation component is also studied and the results are presented in Fig. 46. It is observed that the vertical ground motion component has little effect on the column bending moments and negligible influence over the column-cap drift ratio. Fig. 47 shows two of the hysteresis loop

comparison between “longitudinal combined with vertical ground motions (Long.+Ver.)” and “longitudinal ground motion only (Long. only)” for case GM 1 and GM 7, respectively.

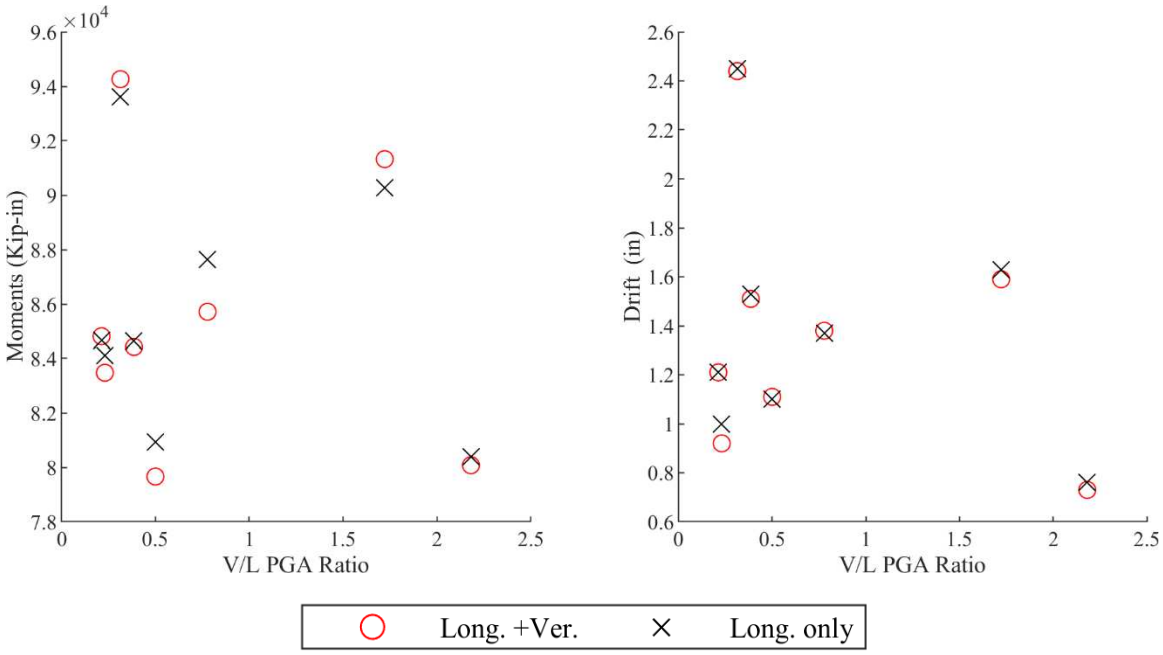

Fig. 46 Influence of vertical ground motion to column ColR1

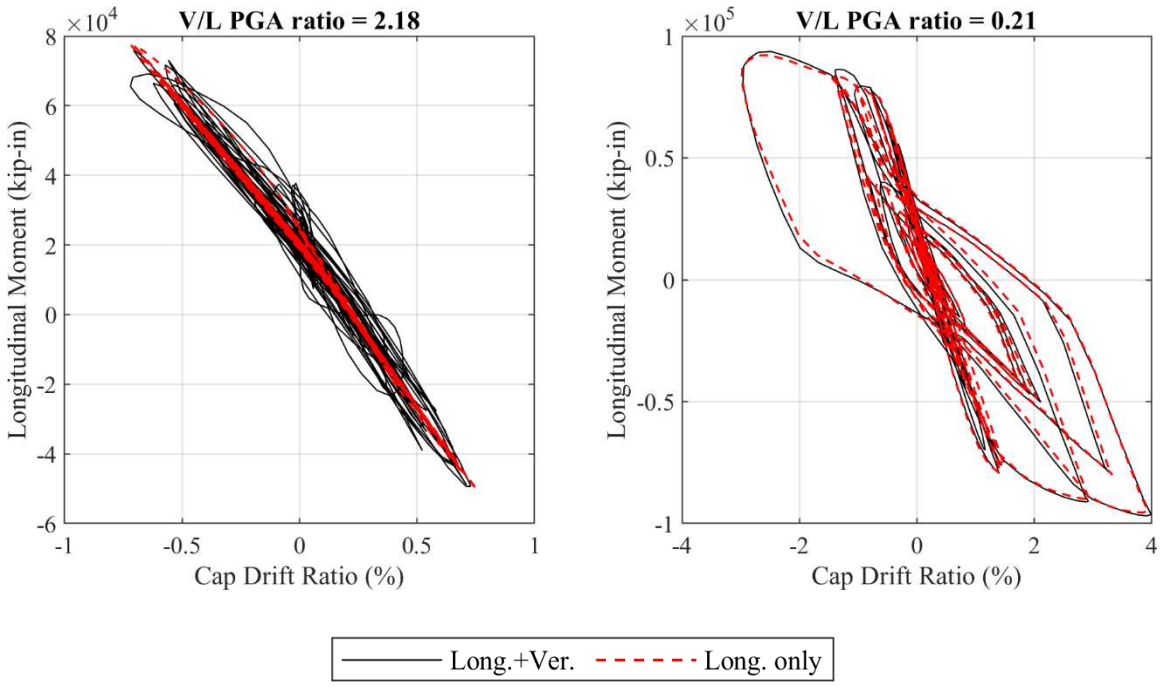

Fig. 47 Flexural hysteresis comparison

4.4.3 Impact of geometric configuration

The seismic performance is compared between the baseline bridge and the straight counterpart bridge to study the impact of bridge geometric configurations. Fig. 48 shows the peak values of axial force, longitudinal and transverse moments of ColR1. It is found that the seismic response is significantly larger for the baseline bridge than for the straight counterpart bridge. Fig. 49 shows the time history of the axial force and it also suggests that the axial force of the baseline bridge exhibits much larger fluctuations over the seismic excitation period than the straight bridge.

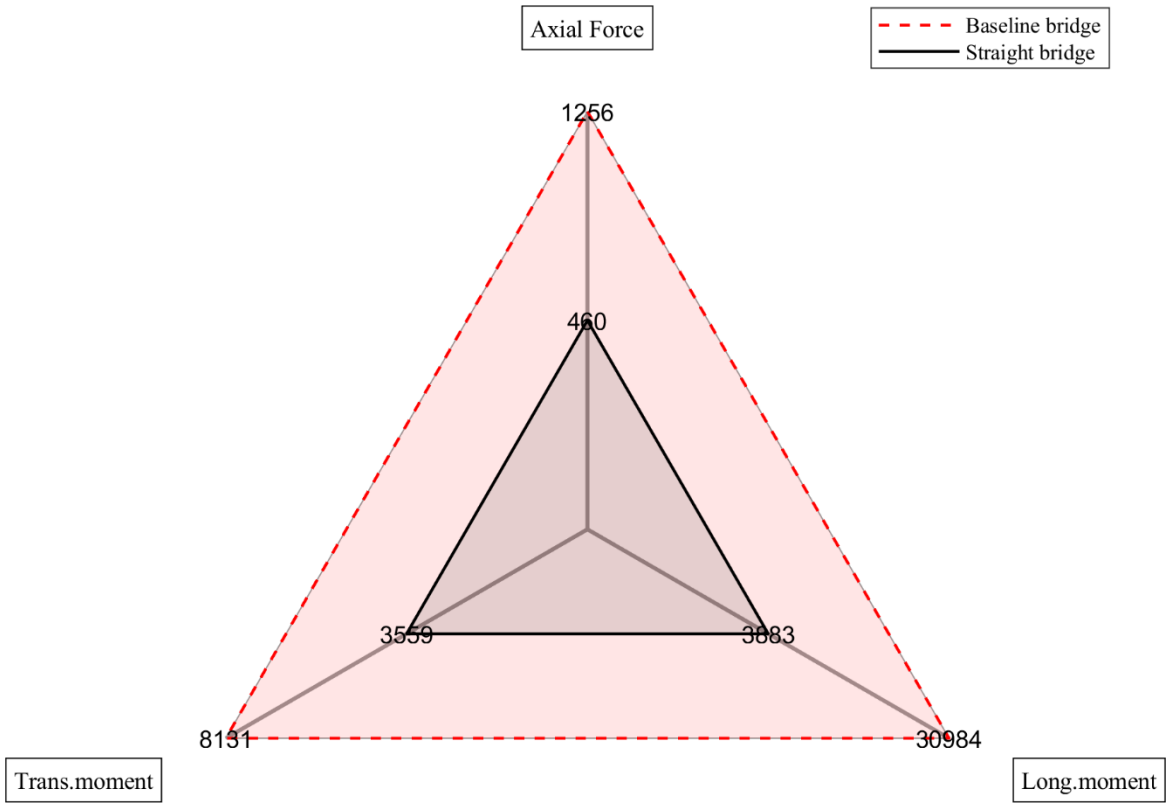

Fig. 48 Column response comparison for ColR1

For the longitudinal reaction of the abutments for the straight bridge, the time histories of the axial forces for ColR1 are shown in Fig. 49 and Fig. 50. The time histories of the deformation (gap width) and the longitudinal pounding forces between the girder end and the abutments in the longitudinal direction are displayed in Fig. 50 for both bridge models. It can be observed that the straight bridge doesn't seem to generate longitudinal pounding forces because the gap width doesn't reach 0 to induce pounding reactions. In other words, pounding effect has been mitigated by the 1-inch gap available between the abutment and girder end. It can also be found that the response of the baseline bridge is significantly larger than that of

the straight counterpart. Once the earthquakes started to attenuate after 15 seconds, the gap width of the straight bridge returned to its designed value relatively fast, while the opening of the baseline bridge maintained large variations for a longer period as shown in Fig. 50.

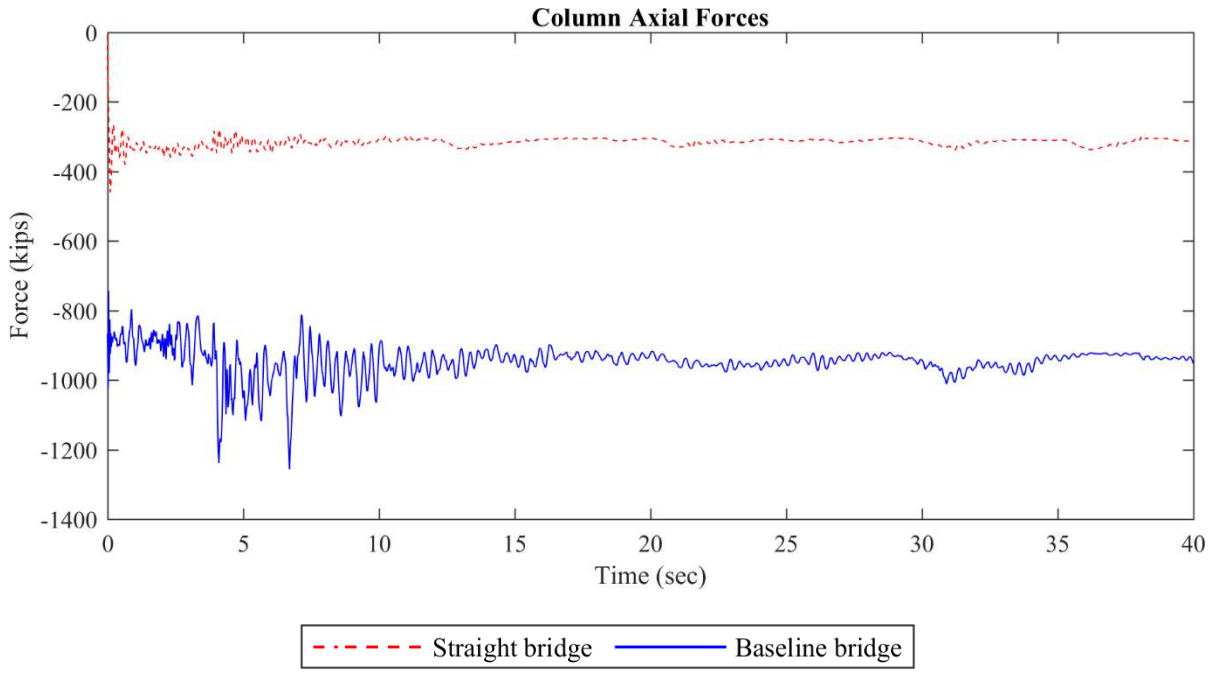

Fig. 49 Axial force comparison for column ColR1

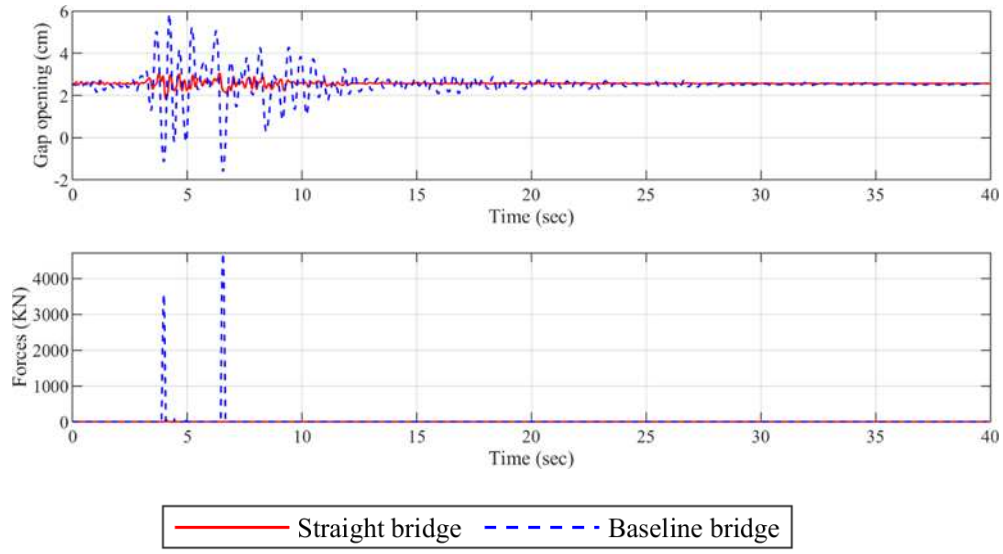

Fig. 50 Longitudinal pounding comparison: (a) gap opening between girder end and abutment, and (b) longitudinal pounding forces

A closer comparison of the transverse shear key reaction forces are shown in Fig. 51. The results indicate that the diagonal shear keys (L1 and R2 for baseline bridge) of the abutment have the most critical transverse forces for the baseline case due to abutment skew, whereas the other diagonal direction shear keys L2 and R1 do not show similar shear key forces, which is most likely due the horizontal curvature of the bridge deck. It is worth mentioning that the peak transverse responses occur at a different diagonal line from that of the columns with critical responses (ColL1 and ColR2).

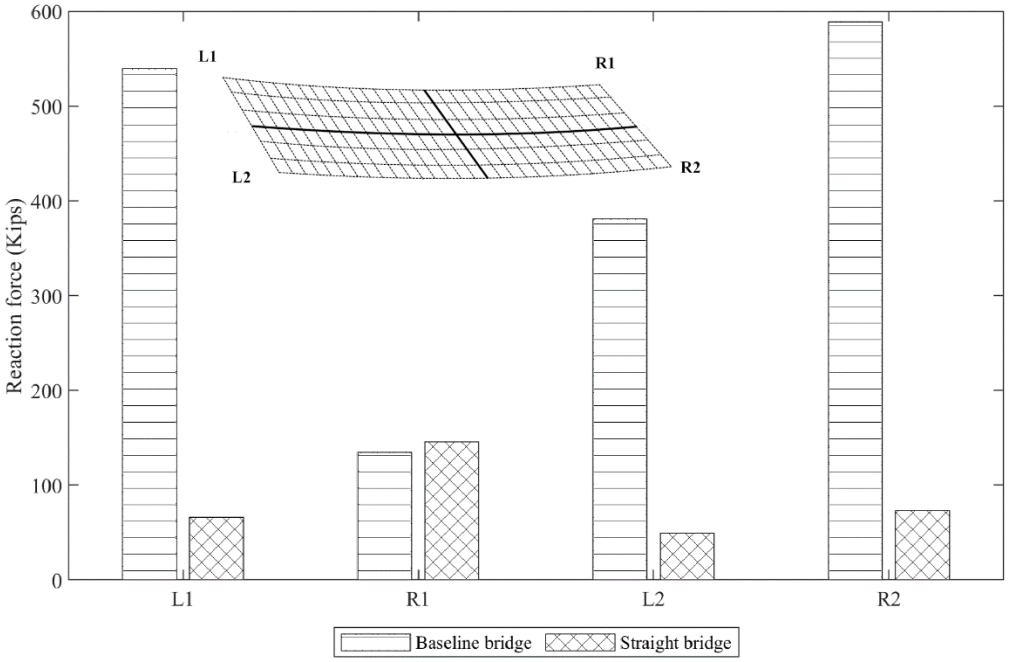

Fig. 51 Abutment transverse force comparison

4.4.4 Impact of traffic densities and earthquake occurrence moments

From prior studies, it is found that bridge deck to be the structural component most influenced by traffic density. Fig. 52(a) and (b) show the vertical displacements at deck midspan under different traffic densities for the baseline bridge and its corresponding straight counterpart. The results not only illustrated that moderate and busy traffic flows induce oblivious residual response after the ground motion mainshock dissipated (15 sec after excitation starts), but also indicate that deck skew and curvature can induce significant dynamic characteristic difference for traffic densities.

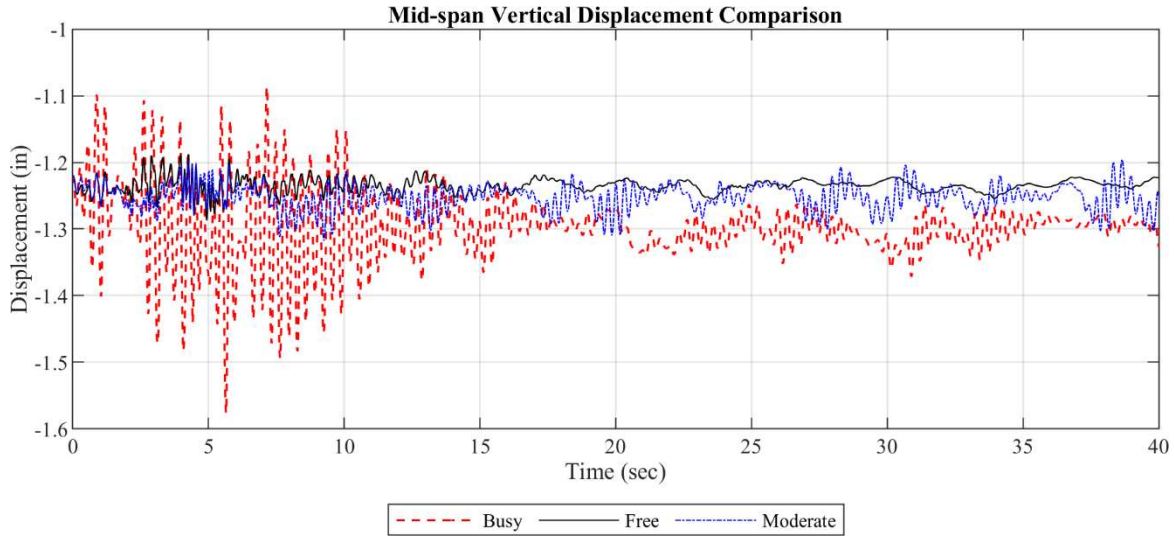

(a)

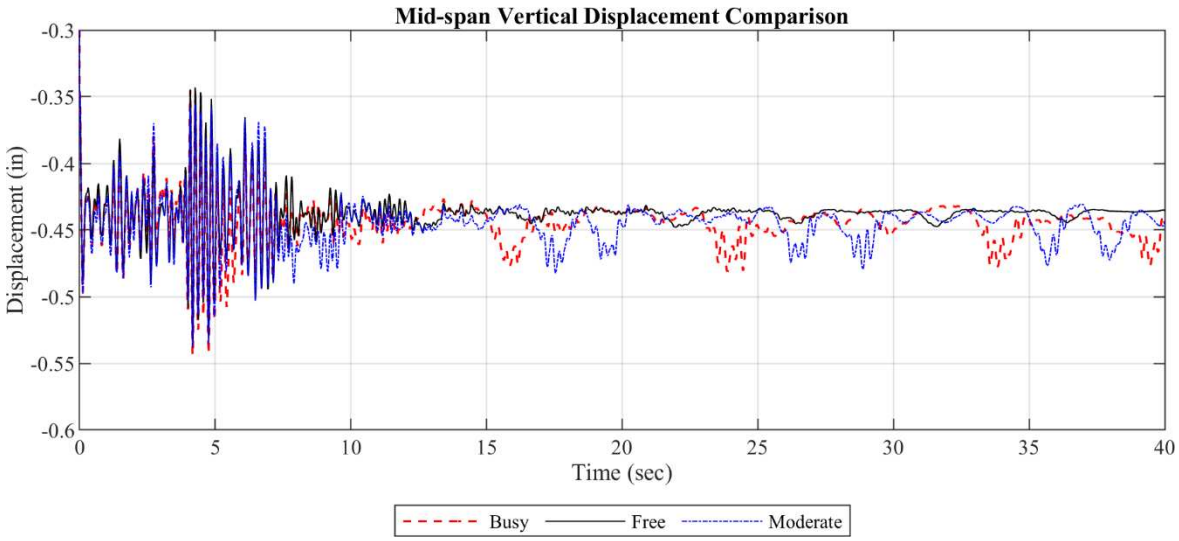

(b)

Fig. 52 Vertical displacement comparison at deck mid span:(a) baseline bridge, and (b) straight bridge

The comparison results of acceleration at the middle point of the bridge deck are presented in Fig. 53(a) and (b). It can be observed that for the baseline bridge, as the traffic density increases from ""Moderate"" to "Busy", the vertical acceleration at the midspan has been significantly amplified especially during the first 15 seconds of the ground motion. While in the case of straight bridge vertical deck acceleration, similar amplification due to traffic density increase has not been observed. Accordingly, traffic density could have a significant impact on the vertical superstructure responses for the baseline bridges once it reaches certain levels.

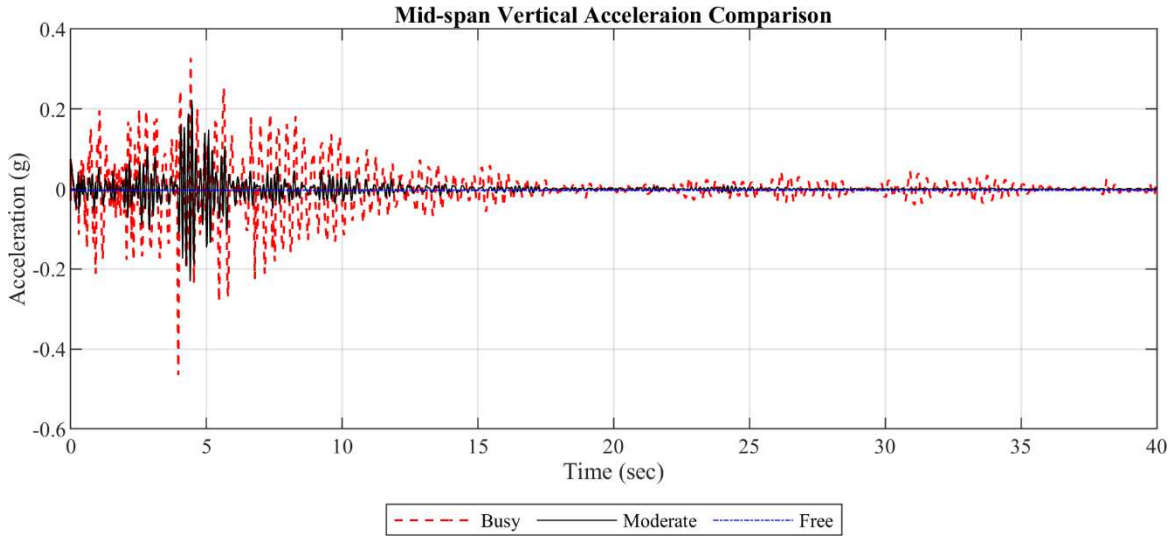

(a)

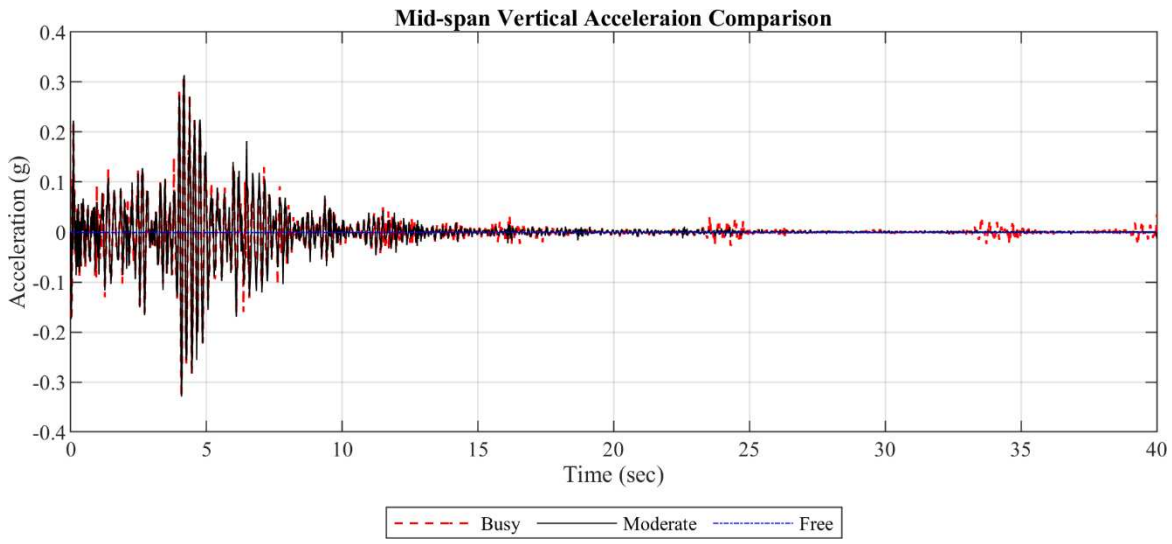

(b)

Fig. 53 Vertical acceleration comparison at deck mid span: (a) baseline bridge, and (b) straight bridge

Because traffic flow and earthquake loads coupling are stochastic, EMTL-FE analyses considering 3 additional earthquake occurrence moments as well as “no traffic condition”(ground motions only), are conducted. Fig. 54 shows the column axial forces and vertical maximum displacements at the mid-span deck for different earthquake occurrence moments, which are 5 sec, 10 secs and 12 secs following the start of the seismic simulation, respectively. Based on the comparison, it is found that even under the same seismic event, the occurrence moment of earthquake can affect the vertical seismic responses. The influence of earthquake occurrence moments may not be obvious for mid-span deck displacements due to the continuous deck nature of the prototype bridge. However, the column axial forces experience more significant variations under different occurrence moments of earthquakes. Such phenomenon suggests that

the stochastic traffic flow may have considerable effect on the bridge seismic response and comprehensive investigations are required to consider the stochastic nature of the traffic and associated various uncertainties.

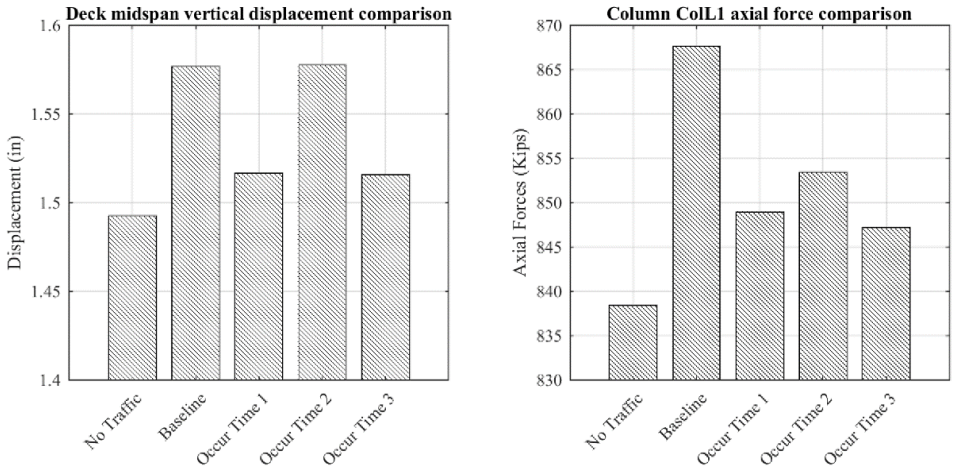

Fig. 54 Vertical response comparison for different earthquake occurrence moments

4.5 Conclusion

In this study, parametric comparative analysis is conducted to examine the applicability of the EMTL-FE strategy and more importantly provide more insights about the seismic performance of the baseline curved and skewed bridge. The parameters studied here are classified into three categories: geometric configurations, earthquake characteristics, and earthquake occurrence moments. Based on the analysis results, following conclusions are made:

1. It is found that girder moments and abutment pounding forces are most influenced by earthquake directional combined scenarios. While the structural behaviors remain similar patterns, the

involvement of the transverse earthquake component has amplified the moments and poundings more than those results with only vertical earthquake component being involved.

2. Seismic responses of the skewed and curved bridge are overall considerably higher than those of the counterpart straight bridge, especially for girder-abutment gap opening and some column internal forces. It is noteworthy that both the maximum magnitudes and variations of the gap openings for the baseline bridge can be significantly larger than those of the straight bridge, including instances of exceeding the design values. In other words, under the same loading condition, the straight bridge does not have any abutment-girder pounding in longitudinal direction and relatively identical transverse reactions at shear keys; while the baseline bridge not only have two longitudinal pounding instances, but also up to 6 times larger transverse reactions at particular acute corner than those for the straight bridge. The results suggest future needs to revisit the design guidelines and appropriately decide the girder gap design values for curved and skewed bridges to minimize possible girder pounding and unseating risks.

3. Same traffic loads but with different earthquake occurrence moments are found leading to different vertical response such as column axial forces and deck vertical displacements. Based on the results, it is suggested that the maximum nodal response alone may not be adequate to evaluate the influence of time-dependent stochastic traffic flow on bridge deck. More comprehensive investigations in terms of comprehensive design criteria for seismic designs of curved and skewed

bridges are deemed needed.

CHAPTER 5 BRIDGE DECK FATIGUE PERFORMANCE ASSESSMENT CONSIDERING DYNAMIC TRAFFIC INTERACTION

5.1 Introduction

Over the past several decades, reinforced concrete (RC) bridge decks have emerged as the predominant choice for short- to medium-span bridges globally. The dynamic interactions between moving vehicles and bridges have garnered significant research interest due to their profound impact on the bridge's dynamic performance since the 90s(Baumgartner, 1999; Fafard et al., 1997). At first, to account for traffic-bridge interaction (TBI), the Dynamic Amplification Factor (DAF) has been frequently employed in bridge service load design since the 1990s(AASHTO, 1989; Euro code, 2003; González & Znidaric, 2009; Puckett & Barker, 1997). Caprani (2013) conducted a comprehensive review of using DAF in designs for free-flowing traffic loads, taking into consideration various congested traffic flow conditions and bridge span lengths. The numerical study highlighted that even for shorter bridge spans, congested traffic conditions can influence traffic loads, necessitating the consideration of mixed traffic flow scenarios. The DAF based design later benefited from the advanced computation method for a more detailed finite element model. Xia et al. (2022) utilized simulated traffic flow based on the Cellular Automata (CA) method to evaluate the DAF method on multi-span simply supported bridges. Their findings revealed that dynamic displacements oscillate around static displacements, and the calculated DAF based on single-vehicle passage may be

underestimated. The study also suggested that DAFs across each span can vary significantly, with factors such as driver behaviors (e.g., acceleration and deceleration) influencing these values.

In recent years, TBI research has increasingly focused on simulated traffic based on weight-in-motion (WIM), monitoring data, and analytical models (González et al., 2012; Han et al., 2017; OBrien et al., 2013; H. Wu et al., 2023). To replicate the effects of actual traffic flow more accurately, studies of TBI have introduced random variables to the probabilistic distribution modeling within this field. Shao et al. (2022) integrated Monte Carlo-sampling-vehicle-gaps and hourly traffic flow monitoring data to simulate traffic flow on a long-span suspension bridge. Their analysis results indicated that in addition to the maximum displacements occurring at the deck midspan, other locations such as the 1/4 span are also sensitive to traffic-induced vibrations. In the research conducted by Zhang et al. (2018), an Ant Colony Optimization Back Propagation Neural Network was utilized to examine the Dynamic Responses of Traumatic Brain Injury in long-span bridges, with validation provided through experimental testing.

Traffic loads exert cyclic stresses on bridge decks through intricate dynamic interactions. Under the influence of cyclic flexural loading from moving traffic, the bridge deck emerges as a particularly susceptible component, potentially experiencing fatigue damage. Historically, assessments of concrete bridge fatigue safety have adhered to design codes such as ACI 318M-02, AASHTO, and Euro codes.(Subcommittee on Bridges, 2011; ACI Committee, 2005; EN 1992, 2004) The design limit states for these codes were predominantly derived from experimental data. These studies primarily aimed to gather

material parameters pertinent to S-N curves, including strength envelopes, failure modes, and cyclic deformations to elucidate fatigue behavior or to suggest fatigue strength for design (Ahmed et al., 1999b; Yin & Hsu, 1995b). As fatigue research broadened to encompass the structural level, methods for estimating fatigue in steel structures were also applied to RC components. Spathelf and Vogel (2018) undertook experimental investigations on RC slabs, concluding that the slab's residual fatigue life is more significantly influenced by sudden and disproportionately large deflection increases. Liu and Yang (2021) conducted both static and fatigue tests on steel-plate-concrete composite slabs, concluding that the amplitude of stresses primarily determines the slab's fatigue life.

Previous studies have verified that the fatigue performance could be simulated through finite element models(Chan et al., 2003; Charhi & Baba, 2023; T. Lu et al., 2025; M. Zhang et al., 2024b). Shao et al. (2022) utilized the Rain-flow counting method, Miner's rule, and statistical monitoring data from an existing suspension bridge that accommodates both highway and railway traffic for fatigue analysis. Their findings suggest that alterations in the stress spectrum significantly influence fatigue estimation, and the proposed methodology for calculating fatigue damage is deemed reasonable. Wysokowski (2020) investigated the impact of traffic flow randomness on steel girder bridges by introducing the probabilities of traffic loads applied to individual lanes. The results confirmed that factors such as the number of traffic lanes, traffic volume, and vehicle moving speeds can affect main girder fatigue performance. Furthermore, the study demonstrated that fatigue estimations for reduced traffic speeds could be up to 23% higher than those

calculated using PN-EN 1993-1-9. However, selecting appropriate fatigue variables can be challenging, and there are still gaps between traffic-bridge interaction analysis and fatigue analysis.

To date, these investigations have primarily concentrated on the influence of bridge properties such as the number of spans, the type of bridge, and road roughness on fatigue performance. However, the impact of the geometric configuration of the bridge deck, including factors like skewness and curvature, has rarely been investigated. It is well known that curved and skewed bridges exhibit unique dynamic characteristics under the excitation of moving traffic. Studying the bridge deck fatigue performance, including the impact of the skew and curved nature, is crucial to protecting these bridges from excessive fatigue damage on bridge decks. To bridge this research gap, this study proposes a bridge fatigue performance assessment framework based on the previously developed EMTL-traffic loads (Chen et al., 2020) from dynamic interaction analyses and a 3D Finite Element (FE) model of the entire bridge, including refined modeling of the bridge deck. Numerical comparative studies of the prototype bridge and its straight bridge counterpart are also conducted to provide further insights into traffic loads and potential fatigue damage risks for medium-short skewed and curved concrete bridges.

5.2 Methodology

5.2.1 Numerical model

The Finite Element Method (FEM) model used in this study is derived by adapting the existing model of a skewed and curved bridge located in Tacoma, Washington as the prototype with the software SAP2000,

which can be found in Chapter 3(Chen et al., 2020). To accurately represent the horizontal curvature of the bridge deck, a greater number of elements are allocated to the midspan section of the FEM model. Following the validation of modal analysis results, the entire bridge deck section of the skewed and curved bridge (Fig. 55(a) and (b)) is segmented into 6x30 area shell elements and meshed into 2x2 finite elements, as depicted in Fig. 55(c). Each element with a 2x2 mesh configuration will incorporate an additional five Gauss nodes for iteration, as illustrated in Fig. 55(d). The stress responses of the entire element are outputs across these nine nodes. A corresponding straight bridge counterpart model is also developed, following the same FE modeling scheme for comparative study purposes.

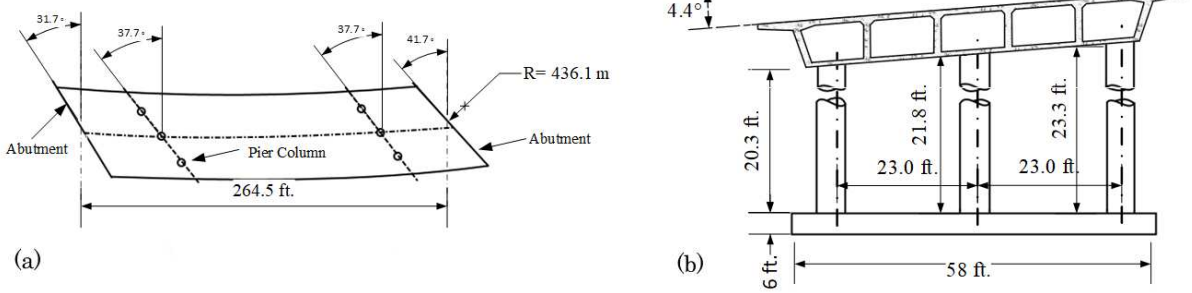

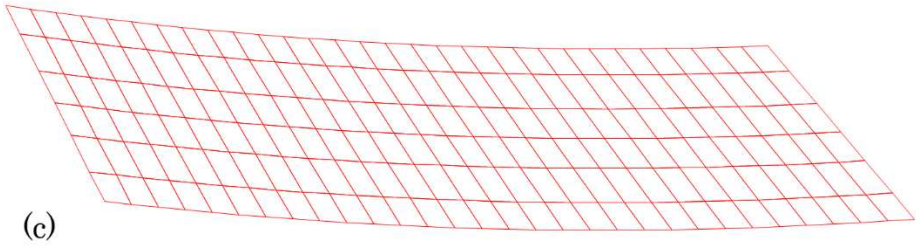

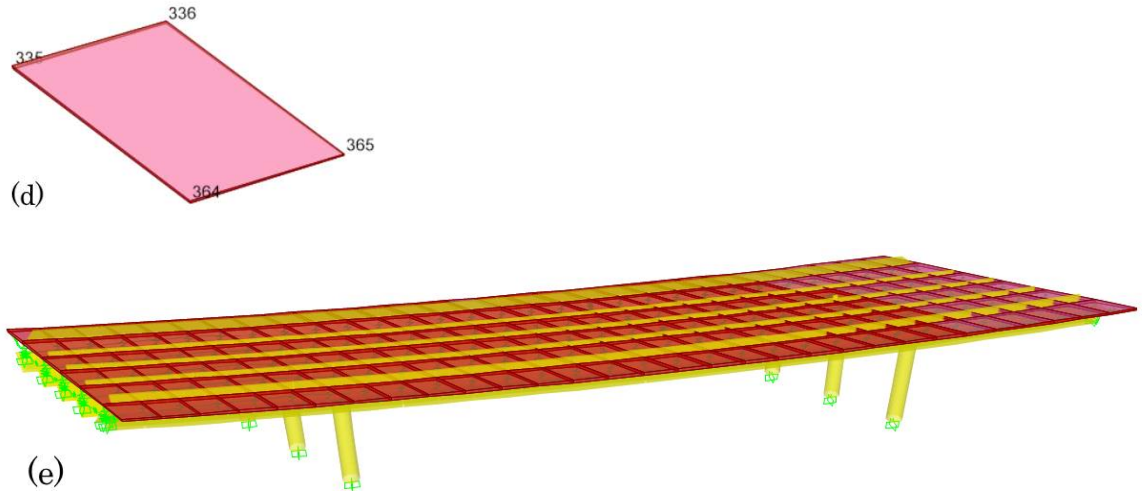

Fig. 55 Baseline skewed and curved bridge: (a) geometric configuration of bridge deck, (b) cross sectional view of bridge, (c) meshed area element for baseline skewed and curved bridge, (d) nodes of 2x2 meshing of area element, and (e) completed FE model in SAP2000

The vehicular live loads employed in this research are derived from the Equivalent Moving Traffic Loads (EMTL) as presented in a prior study by Chen et al. (2020). Three distinct EMTLs, corresponding to "Free", "Moderate", and “Busy” traffic scenarios, are generated for both the baseline (skewed and curved bridge) and its straight counterpart models. The characteristics of the traffic scenarios are based on stochastic traffic flow simulations detailed in the work of Chen and Wu (2011). The EMTLs for “Busy” traffic flow on the three-span bridge are modeled separately for the three segments of the bridge, i.e., two roadway segments and one bridge segment. The traffic density is set at 32 vehicles/km/lane, with the proportions of different vehicle types assumed to be 25%, 25%, and 50% for heavy trucks, light trucks, and light cars, respectively. Fig. 56 presents the EMTLs at the bridge midspan segment for various traffic scenarios. It is observed that the amplitude difference between “Free” traffic and “Moderate”/”Busy” traffic

conditions is more significant for the baseline skewed and curved bridge compared to that of the straight counterpart bridge. The EMTLs are then applied as nodal time-history loads on the FEM shell elements to compute the dynamic responses and stresses of the bridge deck.

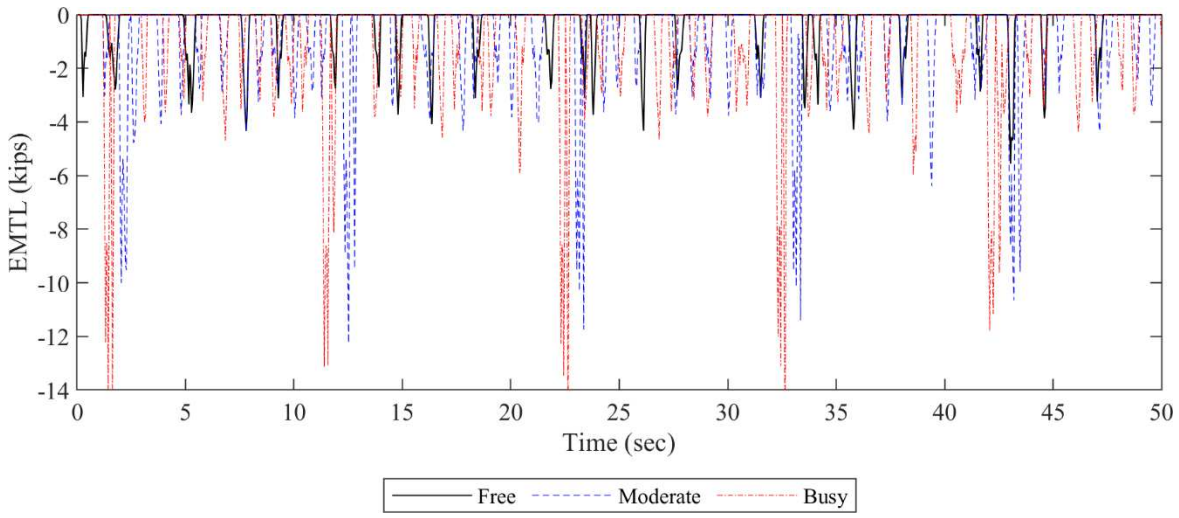

(a)

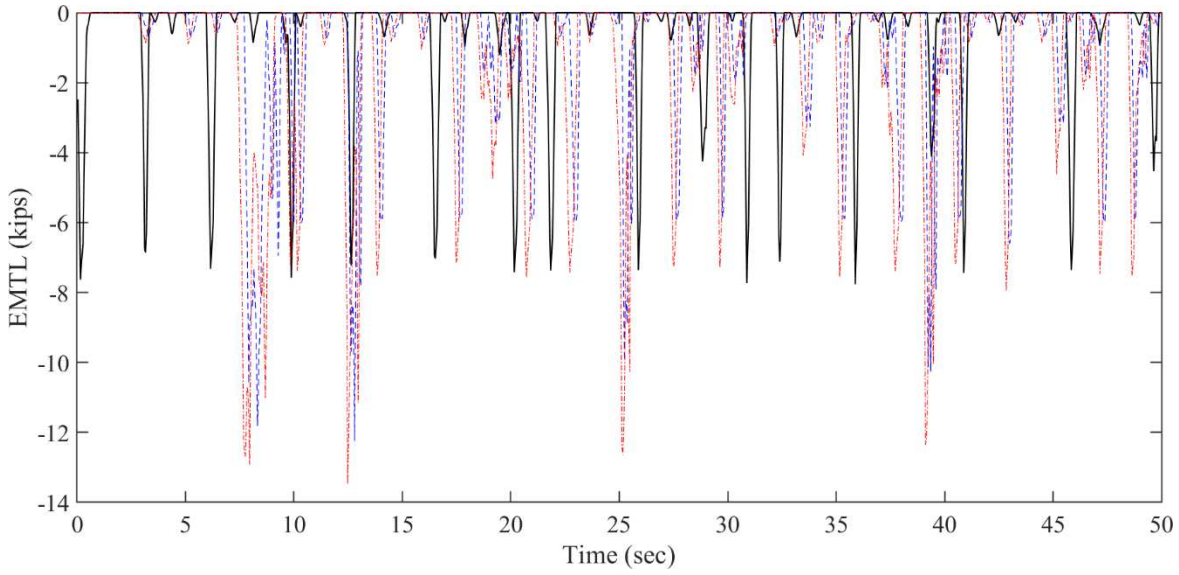

(b)

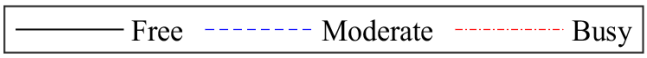

Fig. 56 Different traffic loads at midspan: (a) baseline bridge, and (b) counterpart straight bridge

5.2.2 S-N curves for reinforced concrete

In general, a bridge deck is designed to withstand its design traffic loads without permanent deformation. Consequently, this study applies the linear cumulative damage theory for fatigue assessment. The theory comprises two parts: stress-number of cycle curves and the Palmgren-Miner rule. The former is determined by material/component fatigue characteristics, while the latter governs the accumulation of fatigue damage caused by traffic loads. In the experimental fatigue tests on the reinforced concrete slab (Lei et al., 2021; Lindorf and Curbach, 2010; Miarka et al., 2022), data from the elastic region (from static strength to fatigue limit) are obtained. The analytical S-N curve can be fitted by Paris' curves and described as follows:

$$\sigma = AN^B \tag{5.1}$$

where σ is the stresses during load cycle; N is the number of cycles reaching fatigue failure; A and B are coefficients are determined from the fatigue test.

In this study, we employ the S-N curve for bridge deck fatigue analysis as presented by Miarka et al. (2022). The specific concrete used is C 50/60, as from the Eurocode 2(EN 1992, 2004). The material

exhibits a cylinder strength of 50 MPa, an elastic modulus of 37 GPa, and a tensile strength of 4.1 MPa. The coefficients for the S-N curve for the concrete are A=5.506 and B=-0.0301, respectively.

5.2.3 Fatigue accumulation

Since the bridge deck stress responses of the random traffic loads are different than those under cyclic loads of the fatigue test, this study employs the rain-flow counting method(Endo, 1974) to identify the stress cycles that contribute to the fatigue process. As an example, Fig. 57 illustrates the rain flow histogram of one out of four Gauss nodes in a single element, with its associated stresses contributing to fatigue.

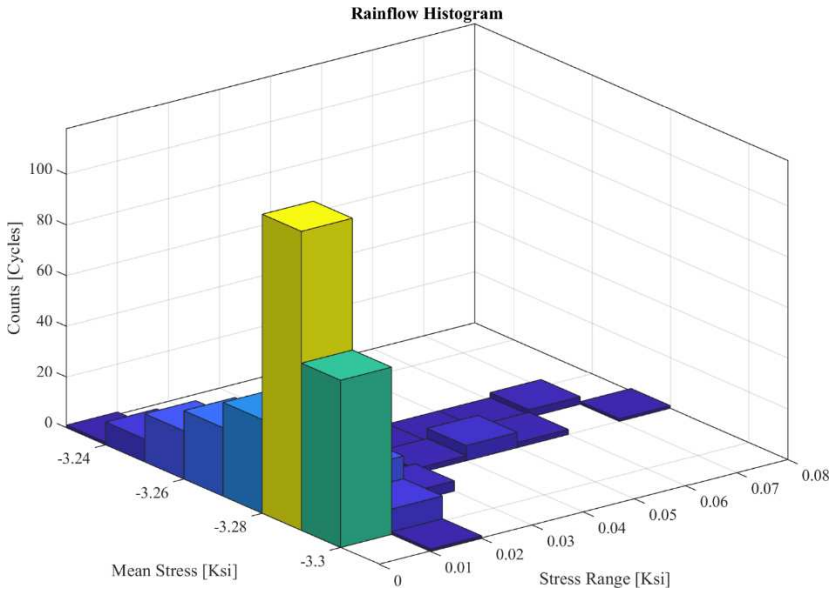

Fig. 57 Stress rain flow histogram at node 366 from upper left corner element

The counted stresses are then used to calculate the accumulated fatigue damage, following the empirical Palmgren-Miner damage rule (Manson and Halford, 1986) as:

$$d = \sum \frac{n_i}{N_i} \tag{5.2}$$

where n_i is the stress cycle count contributing to fatigue; N_i is the corresponding failure stresses, which are determined by S-N curves.

Fig. 58 presents the fatigue-contributing cycles of stresses depicted in Fig. 57, alongside the S-N curve for C50/60 concrete. The stresses resulting from traffic loads are significantly lower than the concrete's fatigue failure strength. Consequently, assuming an absence of crack propagation and bridge deck corrosion, it is reasonable to assume that fatigue damage can be superimposed linearly.

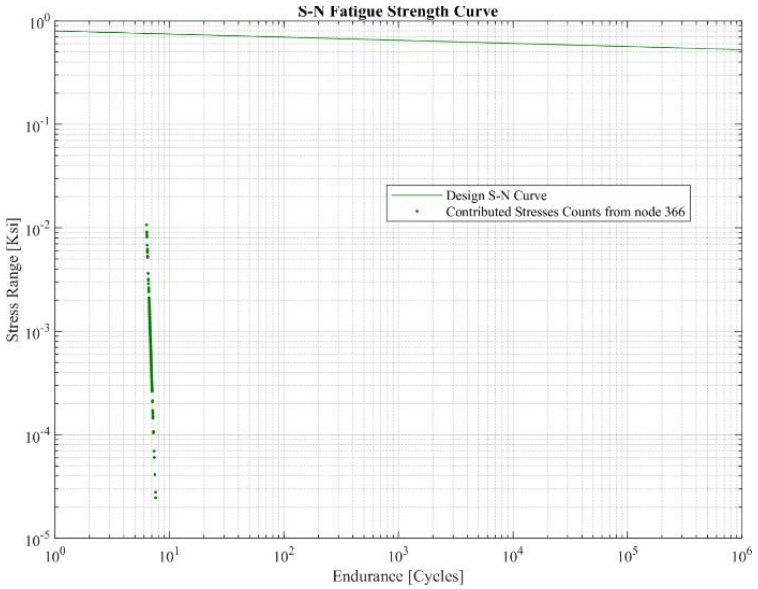

Fig. 58 Fatigue contributing stresses from Fig. 57 and the S-N curve adapted from Miarka et al. (2020)

5.3 Analysis of results

5.3.1 General dynamic responses

The vertical peak responses for the bridge deck, derived from time-history analysis, are depicted in a spatial plan view. Fig. 59 illustrates the comparison of vertical deck displacements under "Free" traffic loads. The maximum displacements at mid-span for the baseline bridge (baseline) and its straight counterpart exhibit significant differences: 0.3649 inches and 0.7556 inches, respectively. The spatial distributions of the vertical displacement for the prototype bridge range between 0.25 to 0.36 inches (Fig. 59(a)). For the straight bridge (Fig. 59(b)), the spatial distribution of the peak vertical displacement is slightly different from that of the baseline skewed and curved bridge, ranging between 0.2 inches and 0.76 inches. The displacement distribution in the baseline case not only exhibits asymmetry along the longitudinal direction but also highlights distinguished patterns between the two roadway-bridge segments and the bridge segment itself.

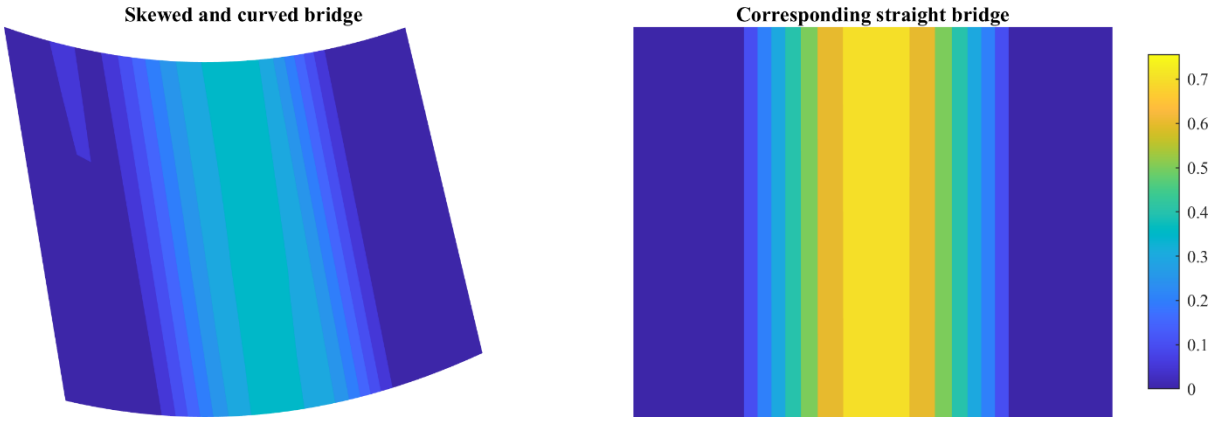

Fig. 59 Deck vertical peak displacement (unit: in) comparison under "Free" traffic condition: (a) skewed and curved bridge, and (b) counterpart straight bridge

5.3.2 Nodal dynamic response

Since the vertical displacements of the baseline bridge deck exhibit asymmetry due to its skewness and curvature (Fig. 59(a)), in addition to the nodal responses at midspan which generally examine during dynamic analysis, two additional groups of nodes at the roadway-bridge spans are selected in this study: nodes at mid-lane, exterior flange, and interior flange. Fig. 60 (a) to (c) present a comparison of stress time histories for skewed and curved bridges (baseline) subjected to identical "Free" traffic loads along the transverse direction. Upon analyzing the stress of the three locations, it becomes evident that the stress at the left span interior location is less than the stresses at both the mid-lane and exterior locations. On the other hand, the stress at the interior location is higher than those at the mid-lane and exterior locations for mid-span and right span. In other words, the relative stress levels at interior, mid-lane, and exterior of the bridge vary for the midspan, left span, and right span, showing asymmetric features. The results also reveal

that nodal stress ranges from 0.49ksi to 0.61ksi, 0.35ksi to 0.74ksi, and 0.4ksi to 0.51ksi for mid-lane, interior flange, and exterior flange, respectively.

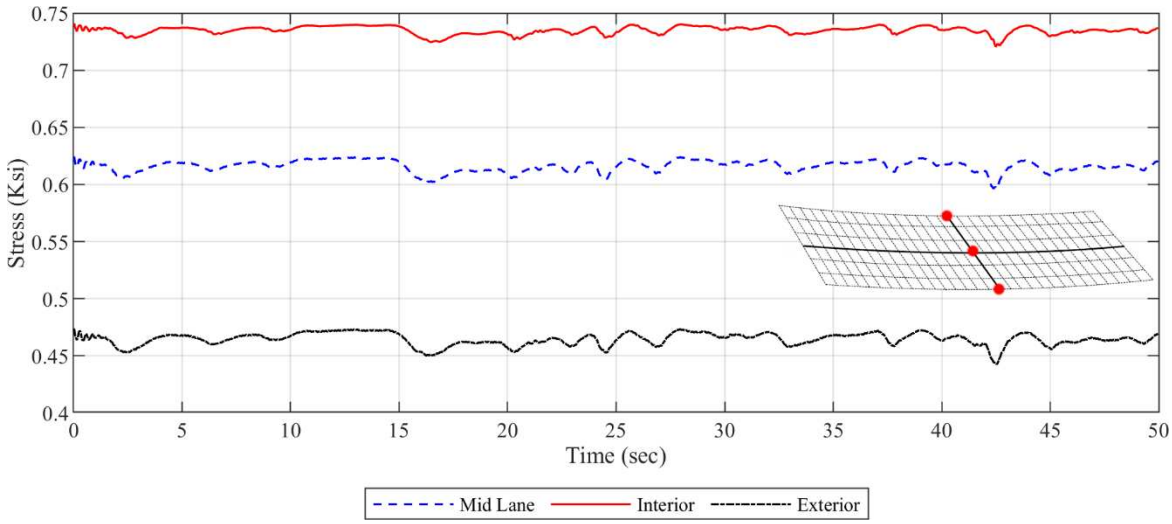

(a)

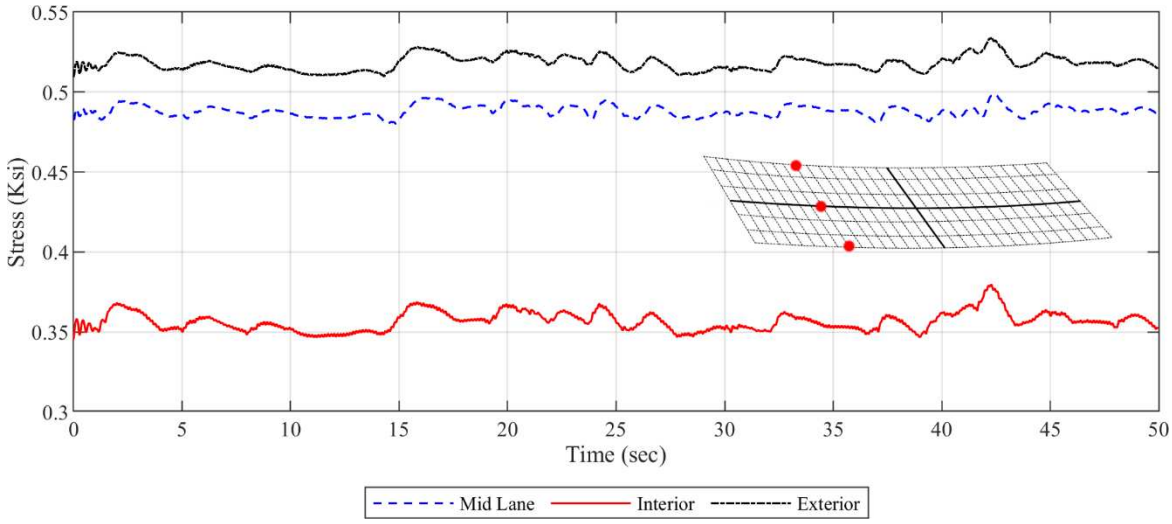

(b)

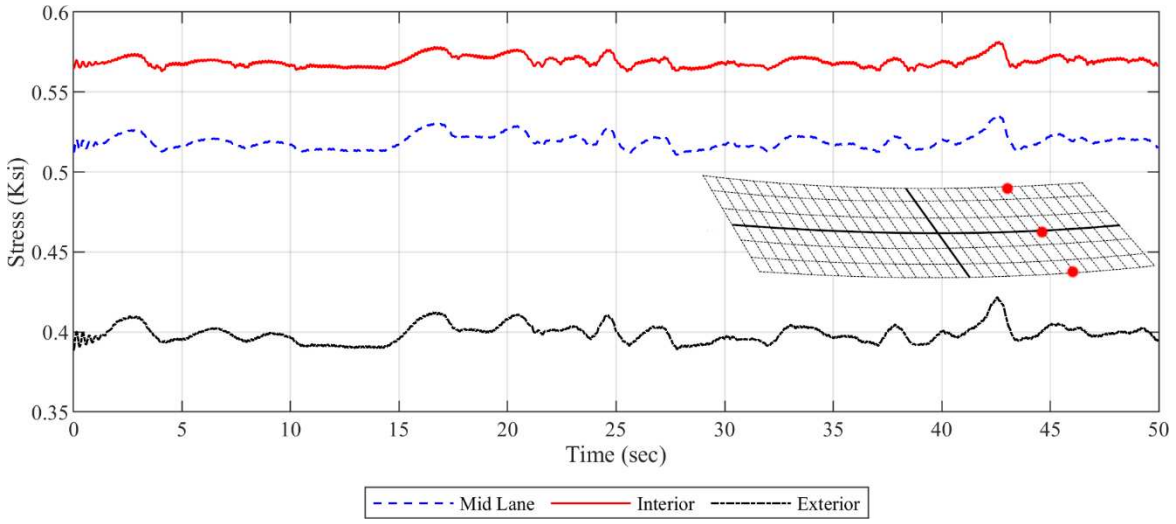

(c)

Fig. 60 Nodal stress comparison along a transverse direction: (a) mid-span, (b) left side span, and (c) right side span

As depicted in Fig. 60 (a) to (c), the nodal stresses at both the left and right roadway-bridge spans exhibit similar time history patterns to those at the midspan. Furthermore, elevated vertical stresses have been noted at nodes in the diagonal direction. Consequently, these two groups of nodal stresses are selected for a more detailed time history comparison across different traffic scenarios, as illustrated in Fig. 61 (a) and (b). The deck stresses induced by "Free" traffic appear to be significantly smaller and more stable than those caused by the other two scenarios. The stress results from "Moderate" traffic fluctuate more frequently than those induced by "Busy" traffic loads. However, the stresses under busy traffic loads display a dramatic shift between their peak and valley values.

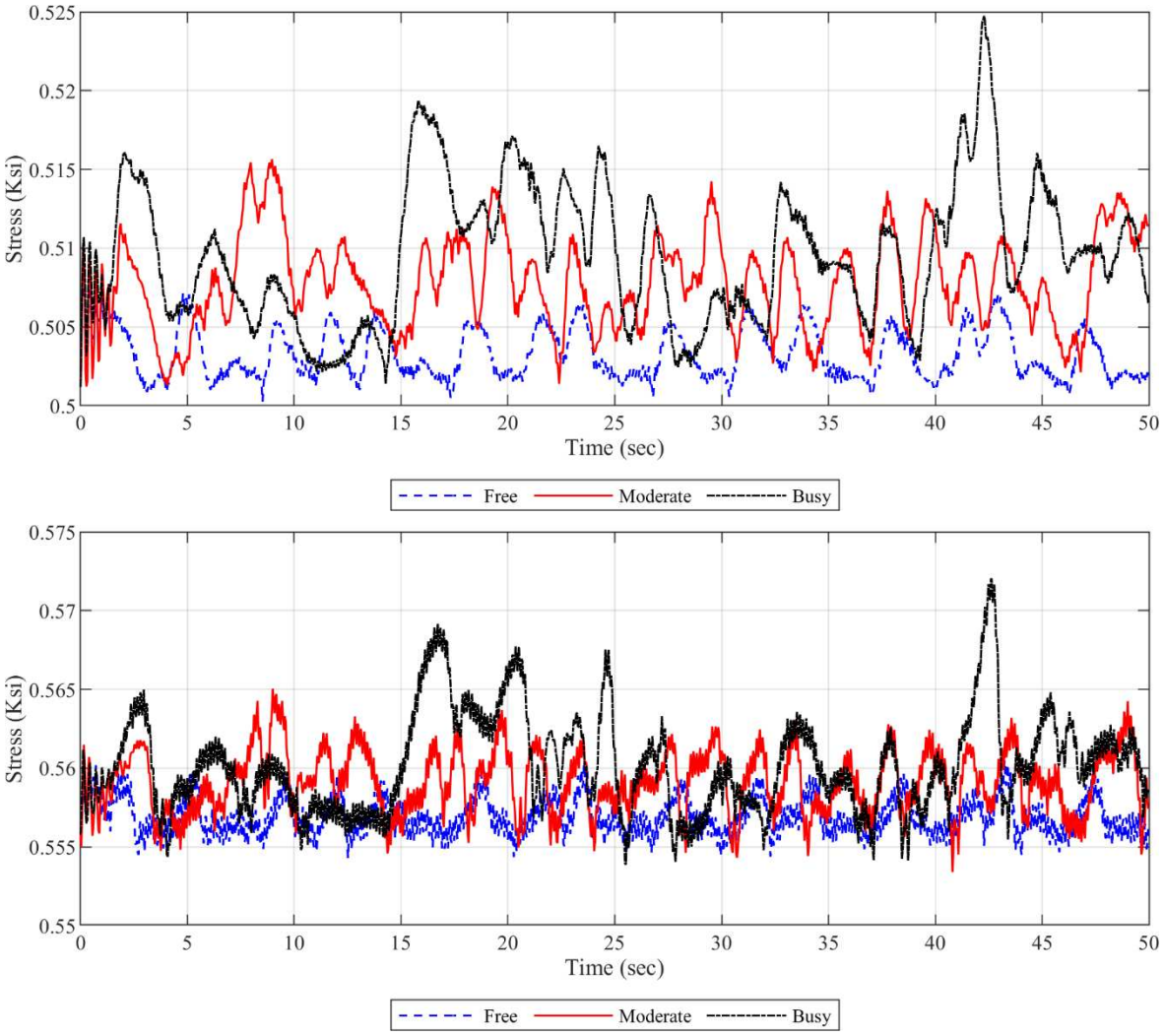

Fig. 61 Nodal stress histories for the skewed and curved bridge: (a) left span exterior flange, and (b) right span interior flange

Fig. 62 (a) to (c) depict the stress histogram derived from the stress histories presented in Fig. 60 The figures reveal a strong correlation between the distribution of the stress histogram and the longitudinal (paralleled to traffic lane direction) position on the bridge deck. Notably, the stress histograms at both the left span and right span mid-lane exhibit fewer cycle counts compared to other nodes. Furthermore, the data

indicates that stress levels at the left and right roadway-bridge segments are relatively lower, compared to the characteristic stresses observed at midspan.

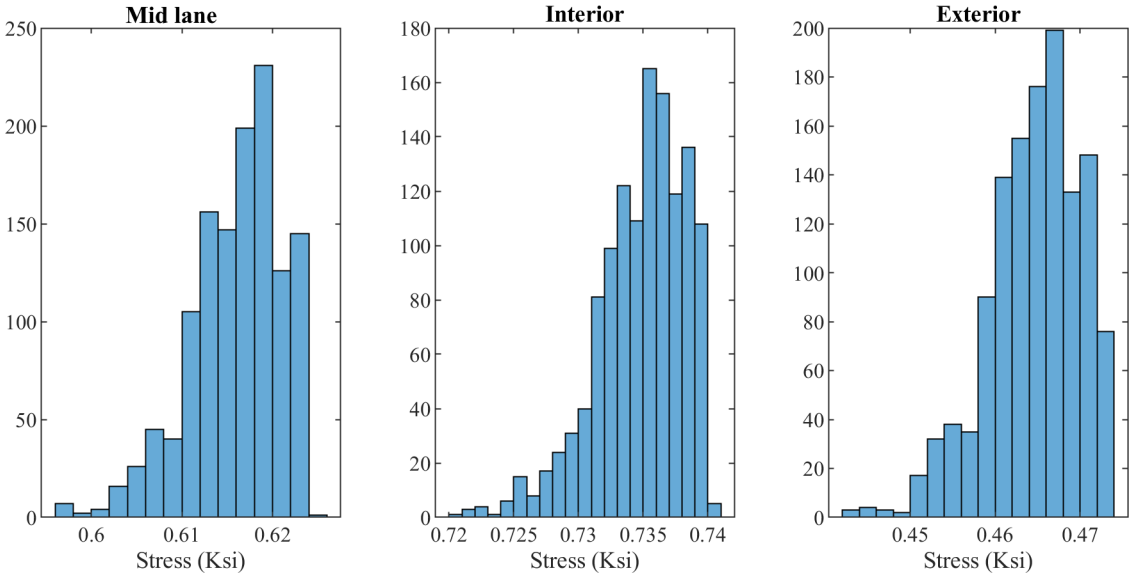

(a)

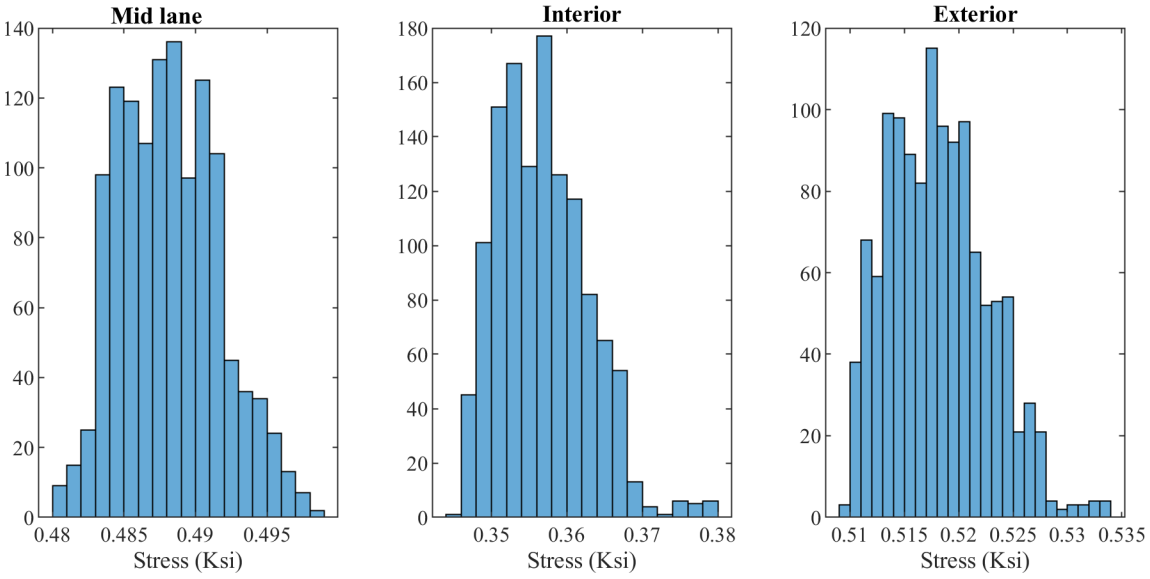

(b)

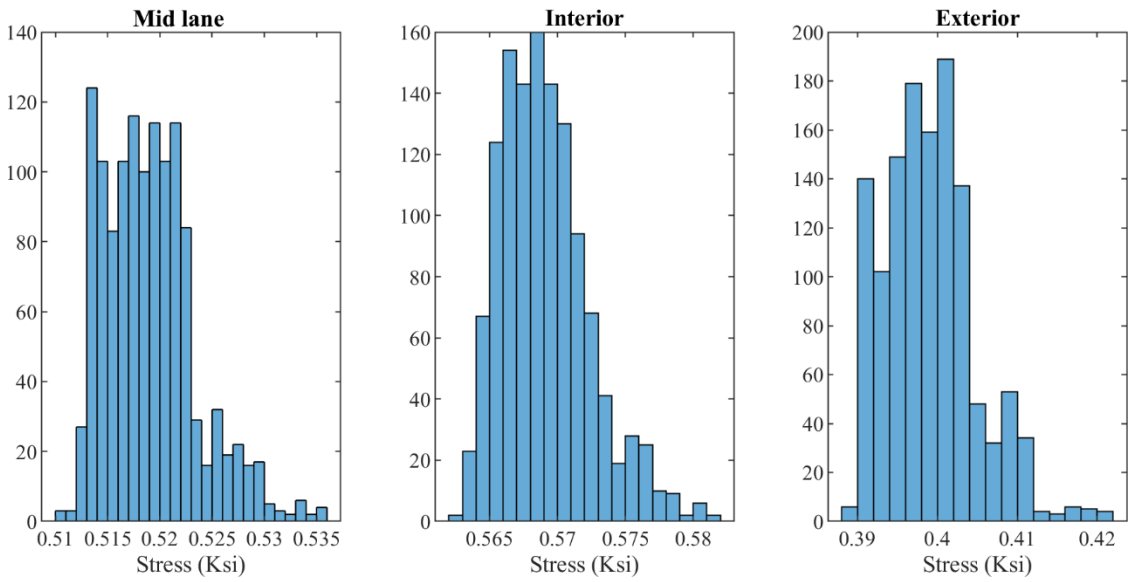

(c)

Fig. 62 Stresses histograms along the transverse direction: (a) mid-span, (b) left side span, and (c) right side span.

It is also noteworthy that under the "Busy" traffic scenario, the stress time history of the baseline exhibits significantly higher magnitudes compared to those of the corresponding straight bridge, as illustrated in Fig. 63. This phenomenon underscores the importance of conducting specific dynamic analysis and fatigue assessment on curved and skewed bridge under traffic loads.

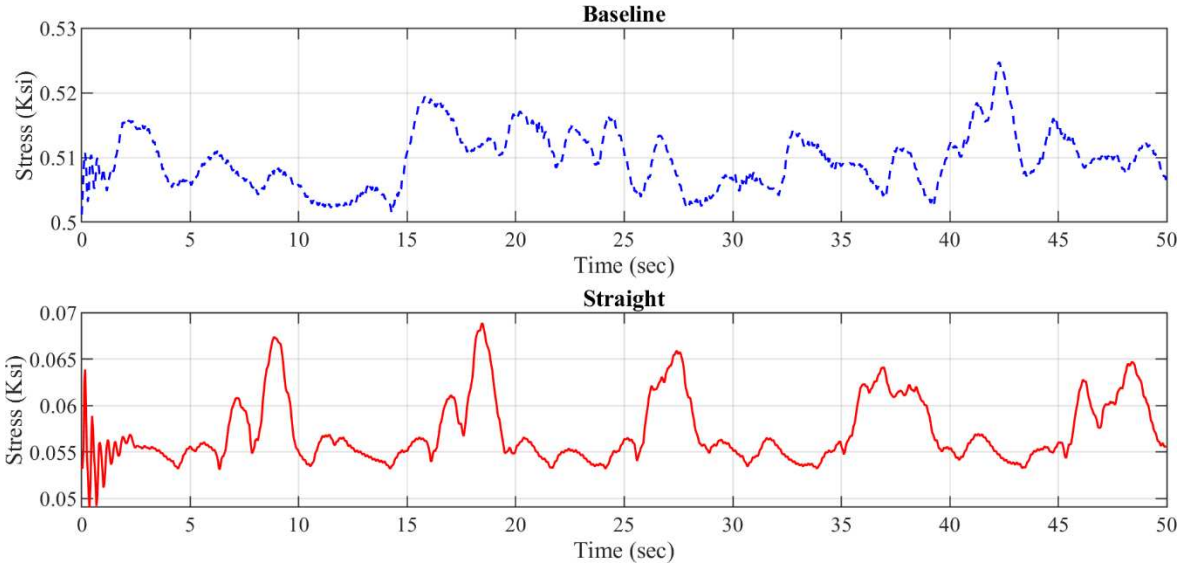

Fig. 63 Nodal stresses under "Busy" traffic loads at left span exterior flange

5.3.3 Statistical distribution of bridge decks

To further investigate the traffic impact under different scenarios, the standard deviation of stress responses at each node across the entire bridge deck is calculated. As depicted in Fig. 64, the standard deviation of the baseline bridge is presented from a top-down view under three distinct traffic conditions: "Free" traffic, "Moderate" traffic, and "Busy" traffic. While the spatial distributions of standard deviation of stress follow a similar pattern, the magnitude of standard deviation of stresses under "Moderate" traffic is nearly twice that under "Free" traffic. Nonetheless, similar attributes of the induced stresses are discernible between the "Moderate" traffic and "Busy" traffic conditions.

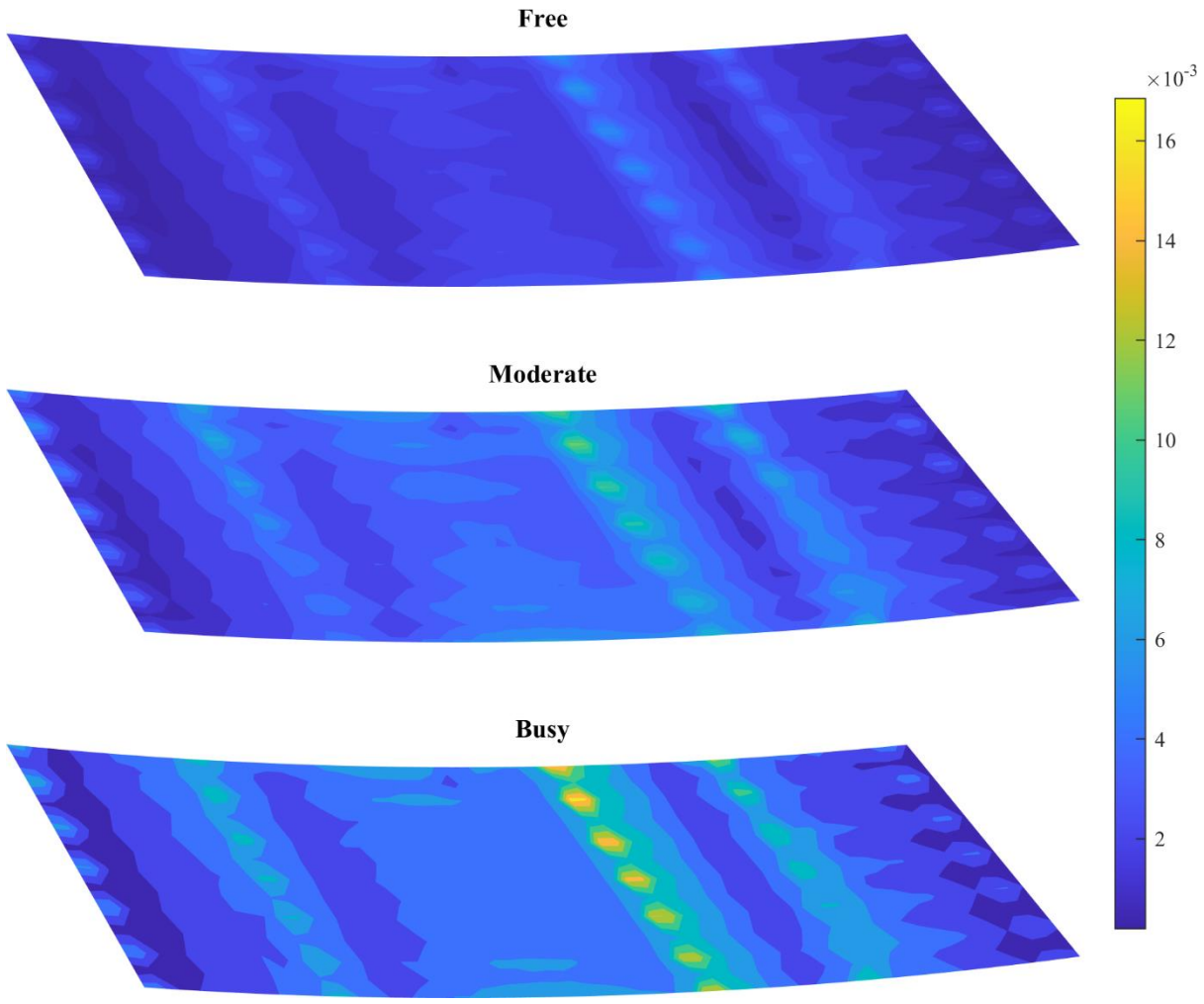

Fig. 64 Standard deviation of stress under different traffic conditions

5.3.4 Accumulated fatigue distribution of bridge decks

In this section, the bridge deck fatigue performance under stochastic traffic loads is assessed for both the baseline and its corresponding straight counterpart bridge. The cumulative bridge deck fatigue under "Free" traffic condition is illustrated in Fig. 65 (a) and (b), with pre-defined sections to indicate different bridge segments and traffic lanes for later analysis. Our findings reveal that the accumulation of bridge deck fatigue for the curved and skewed bridge (Fig. 65(a)) is markedly higher than that of its straight counterpart (Fig. 65(b)).

Moreover, for the straight bridge, fatigue distributions across various roadway-bridge segments and within individual bridge segments exhibit a high degree of symmetry along the bridge's centerline (Fig. 65(b)). Conversely, for both skewed and curved bridges, the results indicate not only asymmetrical fatigue distribution in all directions but also that high-fatigue areas in the baseline bridge are concentrated at the deck corners (Fig. 65(a), Sections A, B, C, and D). The high fatigue areas for the baseline bridge differ significantly from those of the counterpart straight bridge (Fig. 65(b), Sections E and F).

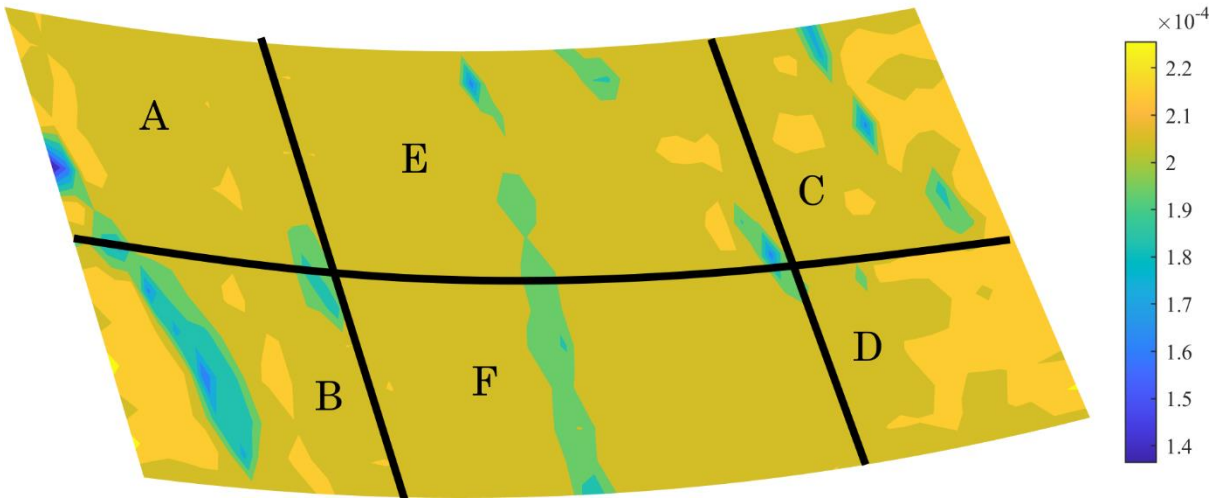

(a)

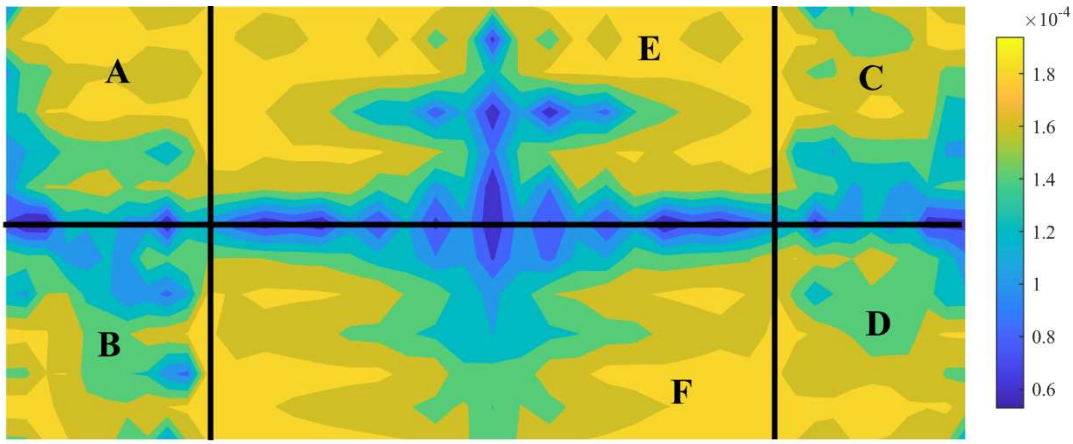

(b)

Fig. 65 Fatigue distribution under "Free" traffic loads: (a) baseline bridge, and (b) counterpart straight bridge

Based on the bridge's traffic design, the mid-lane along the longitudinal direction is designated as a traffic island where minimal traffic load is applied. Consequently, this lane exhibits the least fatigue accumulation compared to other regions (Fig. 65(b)). Fig. 65(b) also reveals a symmetrical characteristic due to the traffic design for both longitudinal directions for the straight bridge, with the fatigue damage distributed in directions parallel to the traffic flow. Conversely, the fatigue damage of baseline skewed and curved bridges is primarily distributed perpendicular to the traffic direction (Fig. 65(a)). This counterintuitive result is likely attributable to changes in the vertical loading path caused by deck skewness and curvature. Fig. 66(a) and (b) illustrate the change of fatigue damage between "Moderate" and "Busy" traffic conditions for the baseline and straight bridges, respectively. When traffic increases from "Free" to "Moderate", the fatigue changes in the straight bridge (Fig. 66 (b)) remain nearly symmetrical in the

longitudinal direction, while those for the curved and skewed bridges display more complex spatial distributions. Due to the randomness of traffic loads, some bridge deck elements for both straight and curved and skewed bridges experience more significant changes in fatigue damage. For the skewed and curved bridge (Fig. 66(a)), the increase in the fatigue index tends to be larger in certain areas in the middle portion (Fig. 65(a)) and between pier-columns and abutments (Fig. 65(a)).

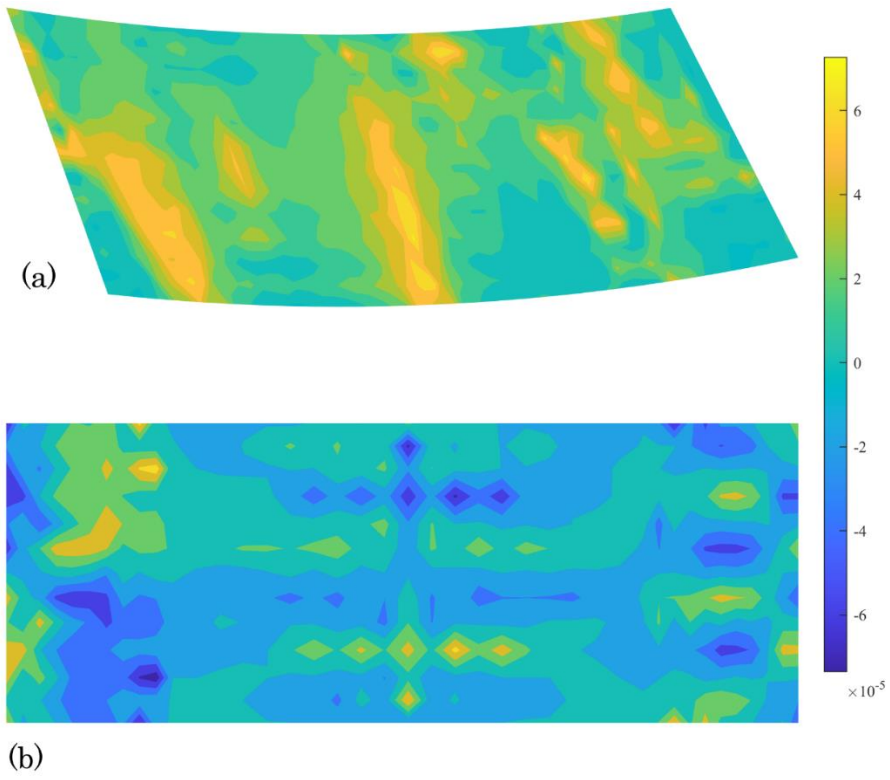

Fig. 66 Changes in fatigue damage from “Moderate” to “Busy” traffic conditions: (a) baseline, and (b) corresponding straight bridge

5.4 Conclusion

In this study, 3D FEM models based on existing skewed and curved bridge and its corresponding straight bridge are setup using SAP2000. Both bridge models are subjected to three different EMTL loads to simulate deck responses under varying traffic load conditions. The EMTLs are based on simulated stochastic traffic flow for traffic density, numbers of different vehicle types, and driver behaviors such as change of lane or braking. From the vertical dynamic responses, nodal stress time histories, and accumulated fatigue damages, the following conclusions are drawn:

1. Global dynamic bridge responses, such as maximum displacements, are not effective indicators for assessing the influence of different traffic loads on skewed and curved bridge decks. The analysis results indicate that deck areas near the corners, despite exhibiting low vertical displacements, accumulate significantly higher fatigue damage under traffic loads.
2. Stresses induced by "Moderate" and "Busy" traffic loads have almost twice the standard divination as those under "Free" traffic load. In this regard, analyzing the TBI on skewed and curved bridge decks can be more complex than the traditional DAF method when it comes to evaluating long-term structural performance.
3. Fatigue damage of skewed and curved bridge ($1.4\text{x}10^{-4}$ to $2.2\text{x}10^{-4}$) are generally higher than corresponding straight bridge ($1.2\text{x}10^{-4}$ to $1.8\text{x}10^{-4}$). Fatigue distribution of the counterpart straight bridge is symmetry in transverse and longitudinal directions. The longitudinal distribution clearly reflects the strong influence of traffic distribution (i.e., no vehicles travel in the middle of a two-

directional road section) and driver behavior, as features such as fast lanes, traffic islands, and slow lanes can be distinguished from the plots. The fatigue distribution of the skewed and curved bridge deck, on the other hand, exhibits only slight symmetry in the transverse direction and is more complex than that of the corresponding straight bridge. The deck was further divided into sections for analysis, revealing that fatigue damage near the deck corners is higher than that at the midspan.

4. As traffic flow increases on the straight bridge, fatigue accumulation intensifies at the mid-span while decreasing in other areas, corroborating the previously observed changes in the spatial distribution of standard deviation. Increasing traffic flow on skewed and curved bridges exacerbate fatigue concentration in transverse direction at abutment-to-column and mid-span locations.

5. This study examines the influence of a 50-second traffic flow on fatigue, but a gap remains between short-term fatigue response and the long-term fatigue progression during bridge service life. In this regard, events such as rebar corrosion and low-cycle fatigue at roadway-bridge span may need to be considered. This research gap will be addressed in the next chapter.

CHAPTER 6 INVESTIGATION OF IMPACT ON RC CONCRETE BRIDGE FATIGUE PERFORMANCE BY CONSIDERING REBAR CORROSION

6.1 Introduction

In the recent years, about 259,140 of bridges in the U.S. are over 50 years old (ASCE Committee on America's Infrastructure, 2021), which leads to an increased number of studies about bridge fatigue. Fatigue in reinforced concrete (RC) bridges may become a critical culprit for bridge deck replacement or renovation, negatively impacting the bridge's serviceability. While it may not pose a critical safety risk like fracture failure, fatigue of concrete bridges can be very costly for structure maintenance. For example, for RC bridges such as the Throgs Neck bridge (TN82) in NY (Mahmoud et al., 2006) and the prestressed concrete bridge in Ashammar, Sweden (Houtenbos, 2016), concrete fatigue have caused visual surface cracking, spalling of concrete, and chloride-induced rebar corrosion in the first 10 years after operating, resulting in repeatedly and costly renovation throughout their service life. The two bridges met their concrete fatigue design criteria, where the fatigue failure modes were controlled by rebar fracture or shear failure, but they suffered from fatigue-induced serviceability issues. Traditionally, structural fatigue analysis focuses on assessing structural failure risks by evaluating the components independently and then determining the dominant fatigue failure mode based on the structures' most serious fatigue damage or components with the lowest remaining cycles. However, the fatigue analysis that informs serviceability assessment and bridge

maintenance is rare. In a recent bridge fatigue case study by Chen et al. (2022), visible concrete cracks induced by deck fatigue in the transverse direction were observed on the deck and girder surfaces after six years of service. In contrast, the dominant fatigue failure identified from the traditional fatigue analysis is the longitudinal flexural rebar fracture of the girder. This past study indicated that the traditional fatigue analysis focusing on failure mode cannot provide rational predictions of fatigue that may impact the serviceability at an early stage of the structure's life. This gap in fatigue analysis has resulted in the overlooked impact of fatigue on serviceability during structural design, potentially leading to significant maintenance costs.

Concrete fatigue had not been considered in design codes until the 1960s. The earlier studies (Hewitt & Batchelor, 1975; Schläfli & Brühwiler, 1998) purely relied on material shear strength or bending strength assessment for fatigue analysis without considering the whole structure. This oversimplified approach has proven to be inaccurate. An experimental study conducted by Dyduch et al. (1994) indicated that evaluating fatigue loads based solely on material strength tends to overestimate fatigue life, likely due to the neglect of softening of localized concrete cross-sections under compressive loading. Over the past decades, the studies on concrete fatigue have shifted from using cyclic loads (Hewitt & Batchelor, 1975; Schläfli & Brühwiler, 1998) or code-specified truck loads (e.g., specified loads in AASHTO 2012, BS 5400 Part 2 and Eurocode model 4) to using simulated traffic loads or monitored traffic loads (Bayane et al., 2019; Chen et al., 2022). Indeed, applying detailed traffic loads for concrete fatigue analysis is a more realistic research

route. Experimental studies (Okada et al., 1978; Perdikaris & Beim, 1988; Sonoda & Horikawa, 1982) have verified that the concrete surface crack patterns induced by cyclic loading are very different from those caused by traffic loads. For example, scaled-down fatigue experiments revealed that when concrete specimens are subjected to cyclic loading, radial cracks often develop on the surface. On the other hand, applying moving truck loads will induce grid-like cracks, which has been verified in other field observation studies (Cavalline et al., 2017). Advanced methodologies that sample traffic loads from their spatial probabilistic distribution (Bayane et al., 2019) from the measurement data provided by the weigh-in-motion (WIM) system (Deng & Yi, 2023) have been used for predicting the flexural fatigue of concrete decks. The previous studies of traffic-induced fatigue assessment on reinforced concrete bridge decks generally oversimplify the traffic loads into time-independent concentrated or stational equivalent wheel loads in cycles on certain superstructure locations, while dynamic characteristics of traffic loads, such as driver behaviors and constitution of vehicle types, have not been taken into consideration. These methods also neglect the effect of traffic flows on irregular decks, such as skewed or horizontally curved decks.

Rebar corrosion in the concrete bridge deck is a critical factor coupled with reinforced concrete fatigue. In most regions in North America, chloride-based salt has been widely used on bridge decks during the snow season. The chemical solution could penetrate through concrete cracks induced by concrete fatigue, inducing rebar corrosion. It is reported that any visible surface cracks on the bridge deck may accelerate or immediately initiate rebar corrosion (Berrocal et al., 2015; Francois & Arliguie, 1999, 1999; Li et al., 2017;

Misra & Uomoto, 1991), eventually converting portions of the rebar surface into rust mass (Jaffer & Hansson, 2008; Michel et al., 2016; Schießl & Raupach, 1997). The rebar corrosion, in turn, may cause more severe concrete fatigue (Ahn & Reddy, 2001; Guo et al., 2019), potentially leading to more surface concrete fatigue cracks on the bridge deck. In this context, this study explicitly models the effects of rebar corrosion on bridge deck fatigue.

In general, when a bridge deck receives cyclic loadings, two different types of fatigue could happen. One is the common medium- to high-cycle fatigue (achieved with $10^3 \sim 10^7$ cycles of load). The other is low-cycle fatigue (LCF). If the stresses in the rebars approach a significant portion of the material's strength, it is recommended to consider low-cycle fatigue (LCF) effects for the concrete, rebar, or steel components (Karunananda et al., 2012; Matsumoto et al., 2008). Studies on bridge low-cycle fatigue (LCF) typically focus either on components susceptible to large plastic strains, such as bridge columns or piles (Dicleli & Erhan, 2013; Sheng & Gong, 1997; Su et al., 2023; Wu et al., 2022), or on components in direct contact with loads, such as bridge decks (Issa et al., 2007; Matsumoto et al., 2008). Several studies have highlighted that low-cycle fatigue (LCF) in specific rebars can lead to reduced ductility and fewer cycles to failure (Apostolopoulos, 2007), and along with a significant decrease in cyclic yield strength compared to monotonic yield strength (Bakkar et al., 2020, 2021). To develop a comprehensive understanding of fatigue, this study includes low-cycle fatigue (LCF) analysis in addition to the more commonly studied medium- and high-cycle fatigue, in order to assess its potential risks.

This study proposed a fatigue analysis framework for concrete bridge decks that considers the effects of realistic traffic loads and rebar corrosion. In this framework, the EMTL-traffic model (Chen et al., 2020) is adopted to model the realistic traffic loads. A finite element model with equivalent multi-layer shell elements is developed to permit the modeling of rebar corrosion and fatigue assessment. Comparative numerical analyses were performed on a skewed and curved bridge under different traffic loading conditions coupled with rebar corrosion. The analysis results demonstrated the versatility of the proposed framework in considering the coupled effects of traffic loads and rebar corrosion. Some interesting fatigue patterns have been revealed under various traffic loads as well as rebar corrosion. Results from the skewed and curved bridge are compared with those of a straight bridge to examine the impact of geometric configuration on concrete fatigue. This study also investigates the risks of low cycle fatigue on bridge decks under combined traffic overloads, seismic loads, and rebar corrosion. Overall, this framework facilitates the assessment of localized fatigue concentration and its progression under corrosion in long-service-life bridges.

6.2 Methodology

The study aims to investigate fatigue damage under realistic traffic loading and corrosion conditions for a skewed and curved bridge. To enable the modeling of corrosion, a finite element (FE) model using multi-layer shell elements is developed to explicitly model concrete cover, corrosion material, rebar, and underlying concrete. A deck-wise corrosion model is adopted to simulate the time-independent corrosion

states over the entire deck in terms of cross-section areas of rebar. Then, the simulated corrosion states are implemented in each element of the FE model to simulate rebar corrosion at a given year after the corrosion initiation. Equivalent moving traffic loads are applied to the FE model under different corrosion states to evaluate the resulting stresses and strains of the deck. Then Miner-Palmgren rule is applied to analyze the high cycle fatigue damages of the bridge deck using stresses. In addition, low-cycle fatigue analysis based on deck strains is also conducted. In the following, the FE model is first introduced. Then, the corrosion model is described, followed by the methodology of low-cycle fatigue. The methodology of high-cycle fatigue has been introduced in Chapter 5, which consists of time history analysis of traffic load, rain-flow counting method, and the Miner-Palmgren rule. Details are omitted here.

6.2.1 FE model

An existing three-span skewed and curved bridge located in Tacoma, Washington, shown in Fig. 67, was used as a prototype bridge for establishing a detailed FE model. The deck over the box girders, which has a radius of curvature of 436.1 m and skew angles of 41.7° and 31.7° at both ends, respectively, is supported by two sets of circular column bents and seat-type skewed abutments at the girder end.

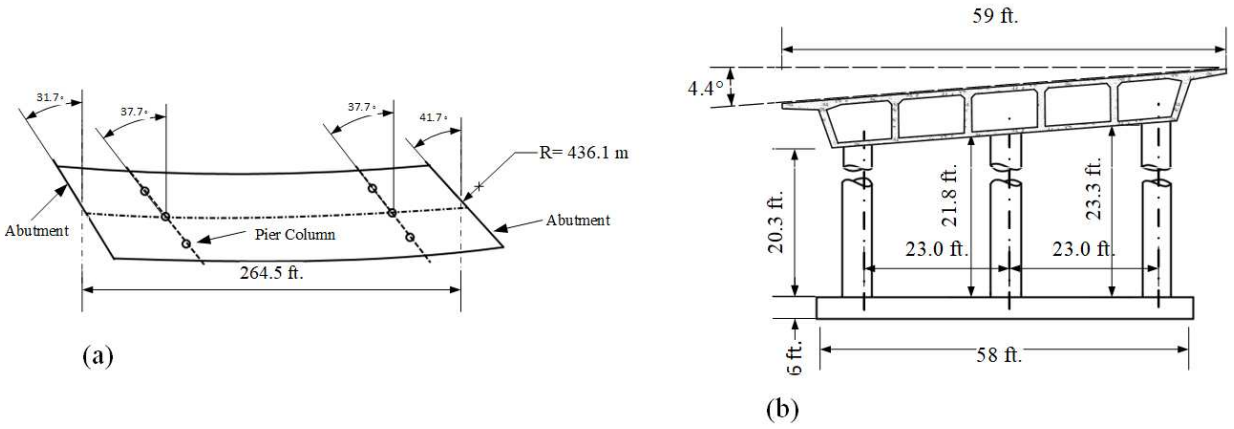

Fig. 67 Geometries of prototype bridge: (a) top view of girders and (b) elevation view

Based on the prototype bridge configuration, a 3D model was constructed using the software SAP2000. The modeling of the bridge is shown in Fig. 68. To represent the horizontal curvature of the deck, the box girders are discretized into five longitudinal segments, each assigned equivalent elastic properties to those of the prototype bridge and rigidly connected. The bridge deck elements are modeled as multi-layer shell elements with elastic membranes and are rigidly connected to the girder to ensure consistent DOFs. Above the column bents are the 12.7mm expansion joints modeled as gap elements.

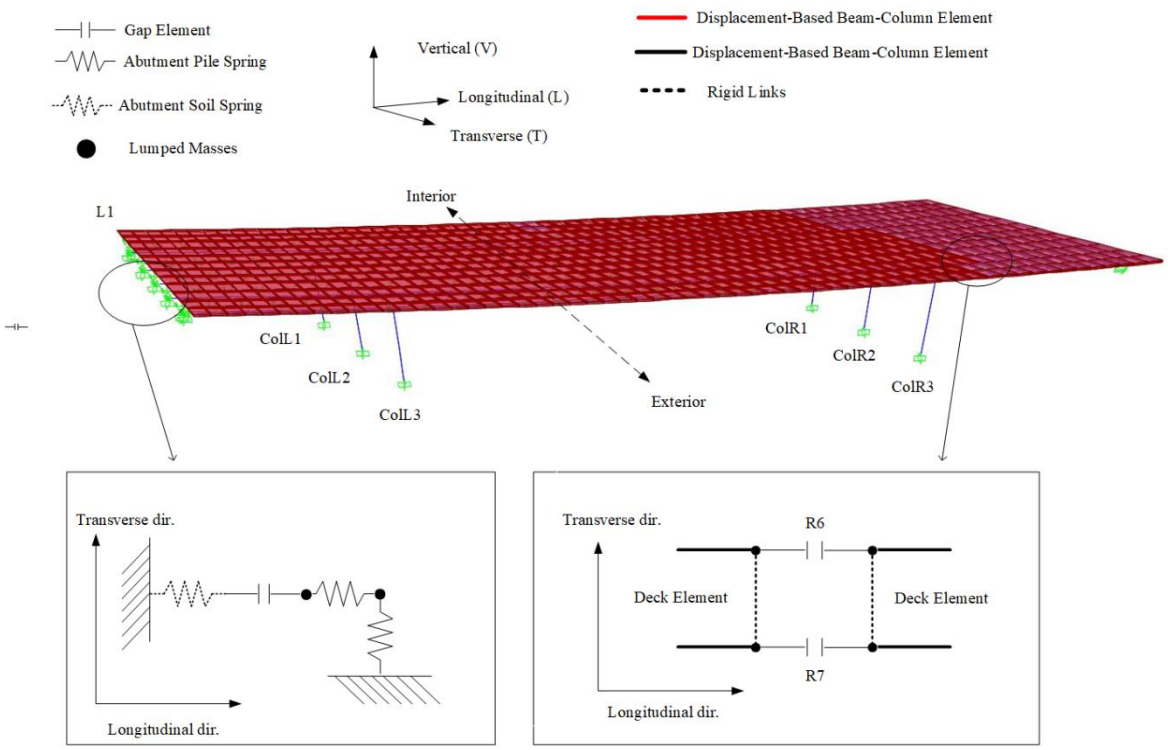

Fig. 68 3D bridge model of SAP2000

The vehicular live loads used in this study are based on the EMTLs in Chapter 3 (Chen et al., 2020). Three different EMTLs for “Free”, “Moderate”, and “Busy” traffic scenarios are generated. The EMTL modeling in this study is based on traffic density and vehicle types. For example, the “Busy” traffic flow has a traffic density of 32 vehicles/km/lane, and the proportions of different types of vehicles are assumed to be 25%, 25%, and 50% for heavy trucks, light trucks, and regular vehicles, respectively. Fig. 69 shows the nodal EMTLs for different traffic scenarios at the midspan deck as an example.

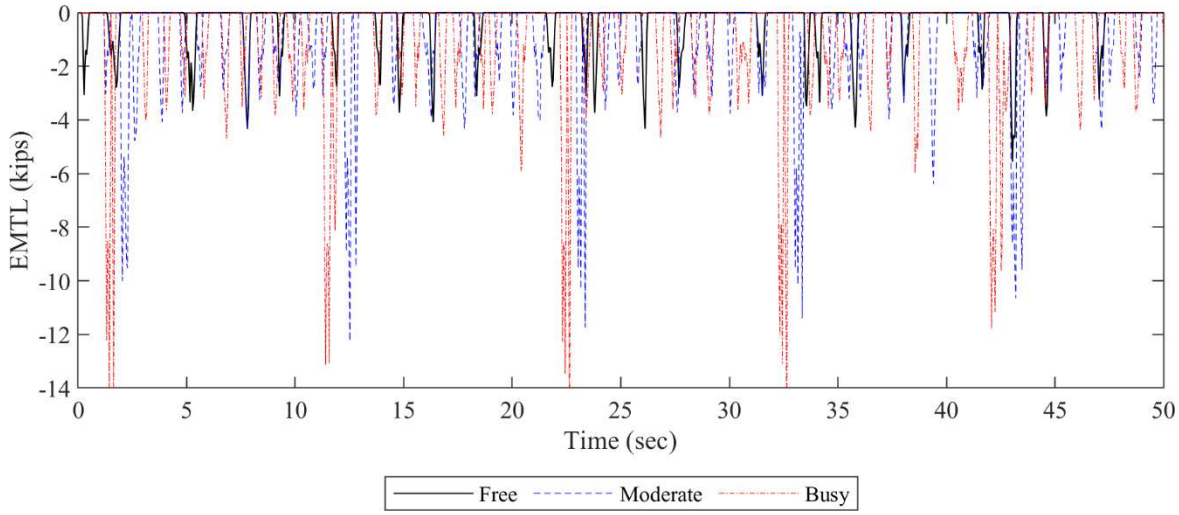

Fig. 69 Different traffic loads at midspan

After calculating the accumulated fatigue damage, the distribution of fatigue damage over the whole bridge deck can be illustrated as contour plots. The shell elements modeled for this study are meshed as 2x2 integration, resulting in a total of 793 nodal fatigue values.

6.2.2 A deck-wise corrosion model

Since this study aims to evaluate fatigue damage for the whole bridge deck, a rebar corrosion model with independent Gaussian distribution of corrosion for each deck element is applied for the sake of calculation efficiency. The corrosion model is developed based on the study by Oh et al. (2007), where deck rebar diameter at a certain point of the corrosion process is described as a time-variant function:

$$D_{(t)} = D_0 - \gamma i_{corr}(t - t_0) \quad \text{(6.1)}$$

where $D_{(t)}$ is a time-dependent function of corrosion rebar diameter, D_0 is the original rebar diameter, γ is the factor that correlates average corrosion density to penetration rate, t_0 is the corrosion initiation time, and i_{corr} is the corrosion rate.

The time-variant corrosion rate i_{corr} was further extended as below (Vu et al., 2005.):

$$i_{corr}(t) = i_{corr_{(1)}} \alpha (t - T_i(t))^{\beta} \ldots \text{for } t - T_i(t) \geq 1 \quad \text{(6.2)}$$

where $i_{corr_{(1)}}$ is the corrosion rate after one year of corrosion, α, β are 0.85 and -0.29, respectively, and T_i is known as the time when chloride concentration reaches the cover depth threshold, and is obtained from Flick's second law that correlate to time t and depth x:

$$T_i(t) = \frac{x^2}{4D_{cht}(t)\left[erf\left(1-\frac{c_r}{c_0}\right)\right]} \quad \text{(6.3)}$$

where c_r is the chloride threshold concentration constant known as 0.9; surface chloride concentration c_0 has a value of $2.95\ kg/m^3$ according to Val and Stewart (2003); the chloride diffusion coefficient D_{cht}, is described as a time-variant variable with a constant chloride diffusion coefficient D_{ch} (DuraCrete, 2000):

$$D_{cht}(t) = \sqrt{K_e K_t K_c D_{ch} \left(\frac{1}{t}\right)^{0.65}} \quad \text{(6.4)}$$

where environmental factor $K_e = 0.676$, test method factor $K_t = 1.0$, curing factor $K_c = 1.0$ and the coefficient D_{ch} is defined by the equation suggested by Papadakis (1992):

$$D_{ch} = 0.15 \frac{1+\rho_c \omega C}{1+\rho_c \omega C + \frac{\rho_c}{\rho_a} ac} \left[\frac{\rho_c \omega C - 0.85}{1+\rho_c \omega C}\right]^3 D_{cI,H_2o} \quad \text{(6.5)}$$

where ρ_c is the mass density of cement, ρ_a is the mass density of aggregate, D_{cI,H_2o} is the diffusion coefficient of chloride assumed as $1.6\text{x}10^{-9} m^2/s$ at 25℃, the aggregate -cement ratio ac is determined as the summation of sand-cement ratio sc and gravel-cement ratio gc (Xu et al., 2009):

$$ac = sc + gc = [6.703\omega c - 0.084] + [6.634\omega c - 0.258] \quad \text{(6.6)}$$

where the concrete water–cement ratio ωc can be determined based on its compressive strength f_c following Bolomey's formula (Bazant, 1983):

$$\omega c = \frac{27}{f_c + 13.5} \quad \text{(6.7)}$$

The corrosion rate after one year of corrosion $i_{corr(1)}$ is related to concrete cover depth, humidity, and temperature as:

$$i_{corr_{(1)}} = \frac{27(1-\omega c)^{-1.64}}{C} \quad \text{under 80\% humidity, 20℃} \quad \text{(6.8)}$$

Based on Eq. (6.1) through Eq. (6.8), Eq. (6.1) was reformulated as follows:

$$D_{(t)} = D_0 - 0.023 i_{corr}(t - t_0) \quad \text{(6.9)}$$

which can be further applied to the corrosion deck rebar area by the following equation:

$$A(t) = \begin{cases} nD_0^2 \frac{\pi}{4} & for \;\; t \le t_0 \\ n(D(t))^2 \frac{\pi}{4} & for \;\; t_0 < t < t_0 + \frac{D_0}{0.023 i_{coor}} \\ 0 & for \;\; \ge t_0 + \frac{D_0}{0.023 i_{coor}} \end{cases} \quad \text{(6.10)}$$

where D_0 is the initial diameter of the rebar.

Eventually, the time-variant corrosion rate $i_{corr}(t)$ for this study is illustrated in Fig. 70 and the corrosion rebar area ratio $A(t)/A_0$ (A_0 is the initial cross-section area) is shown in Fig. 71.

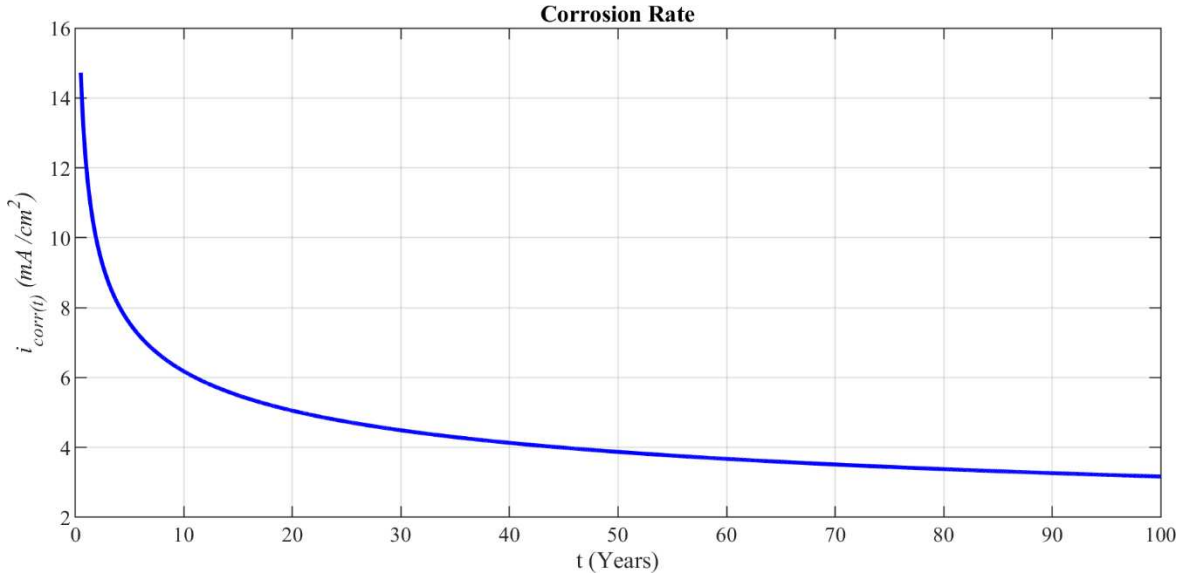

Fig. 70 Time invariant corrosion rate

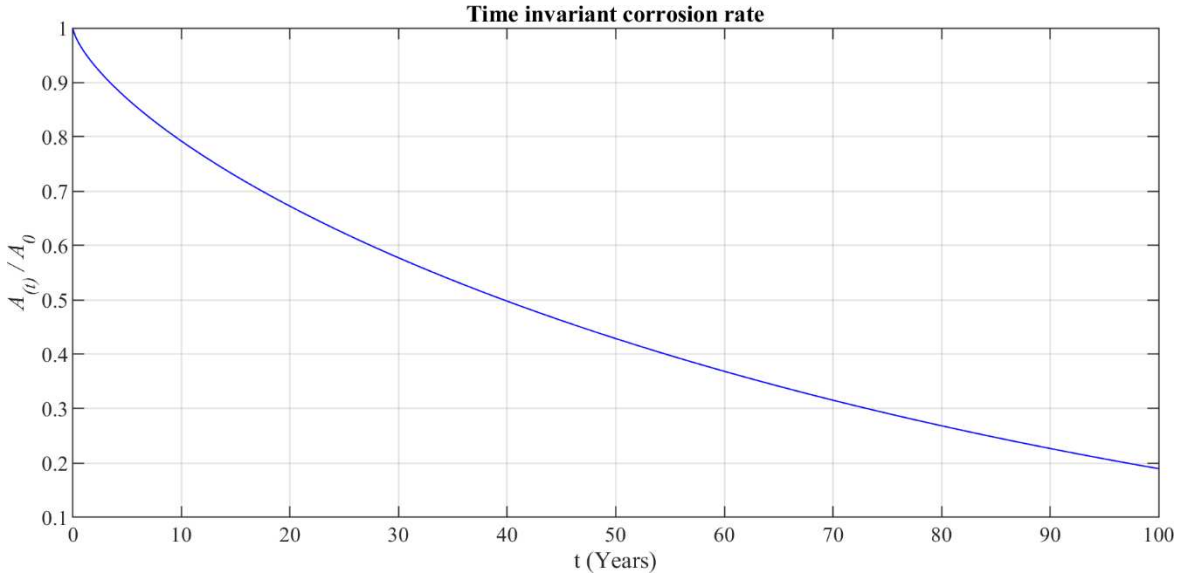

Fig. 71. Ratio of cross-section area due to corrosion and initial cross-section area

For each deck element in the FE model, the equivalent cross-section areas for the single RC deck will be reduced followed by the result in Fig. 71, while two layers of "corrosion soft material" with an assumed linear behavior replace the reduced cross-section areas as illustrated in Fig. 72.

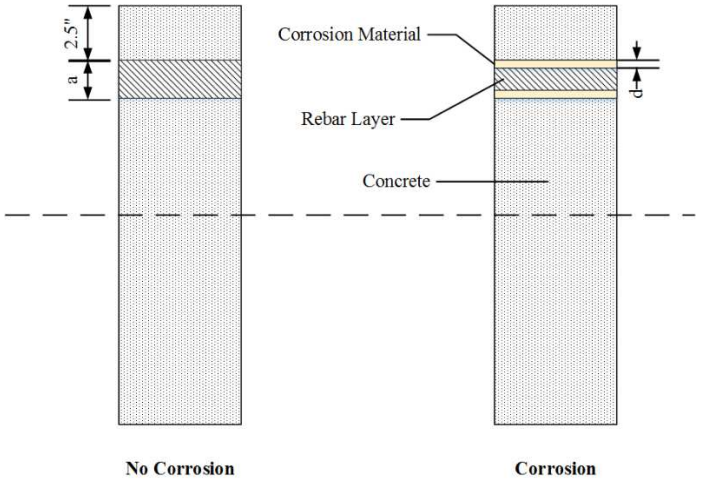

Fig. 72 Equivalent cross-section layers for RC deck elements

6.2.3 Corrosion distribution model

To simulate the deck rebar corrosion in a more realistic situation, this study used a Gaussian random field to simulate the distribution of rebar corrosion, which is based on Firouzi and Rahai's work of predicting deck crack propagation (2011). Due to the complexity of concrete crack initiation, the crack widths on the bridge deck in this study are assumed small enough so that they won't affect the pavement roughness, but still can initiate rebar corrosion immediately throughout the whole deck. The modeling for the deck rebar corrosion distribution applied in this study can be described as two steps. First, a broad literature review is carried out for the probability distribution of variables in Eq. (6.1-6.10) in Section 6.2.2, as shown in Table.

12. After performing a Monte Carlo simulation with 10^6 samples based on the variable distributions in Table. 12, the distribution of D_{ch} was obtained. It follows a normal distribution with a mean of 2.37x10$^8 m^2/s$ and a standard deviation of 232835 m^2/s.

Table. 12 Statistical description of variables

Variable	**Mean**	**Standard deviation**	**Distribution**	**Reference**
Concrete cover depth, *C* (in)	2.50	0.2	Normal	(Duprat, 2007; Stewart & Mullard, 2007)
Concrete compressive strength, f_c (ksi)	4.50	0.2	Lognormal	(Duprat, 2007)
Surface chloride concentration (kg/m3)	2.95	0.6	Lognormal	(Duprat, 2007)
Threshold chloride concentration (kg/m3)	0.6 – 1.2		Uniform	
Rebar diameter (in)	1	0.15	Uniform	
The mass density of cement, Pc (kg/m^3)	1506	93	Normal	(Novák, 2004)

Mass density of aggregate, Pa(kg/m^3)	1600	77	Normal	(Novák, 2004)

Then, the Gaussian random field of the coefficient D_{ch} is generated over 6x30 deck elements for the bridge model, as shown in Fig. 73. This random field was then be applied to Eq. (6.10) to calculate the remaining rebar cross-section area at a given year after the corrosion initiation.

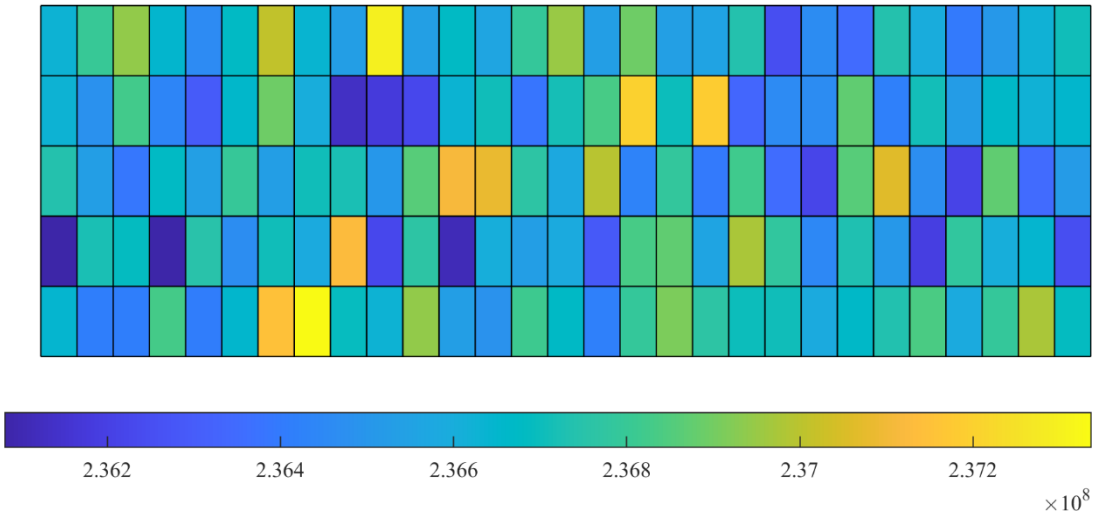

Fig. 73 Distribution of D_{ch} on deck element with correlation

With given specific time, such as 5 years, 10 years, 15 years, and 20 years after the corrosion initiation, respectively, the remaining rebar cross-section was estimated, as shown in Fig. 74. The results allows assigning the cross-section area for multilayer deck elements, as illustrated in Fig. 72. For example, the value 0.9 on the color bar in Fig. 74 means the rebar will remain 90% of its cross-section area as compared to rebar area with no corrosion.

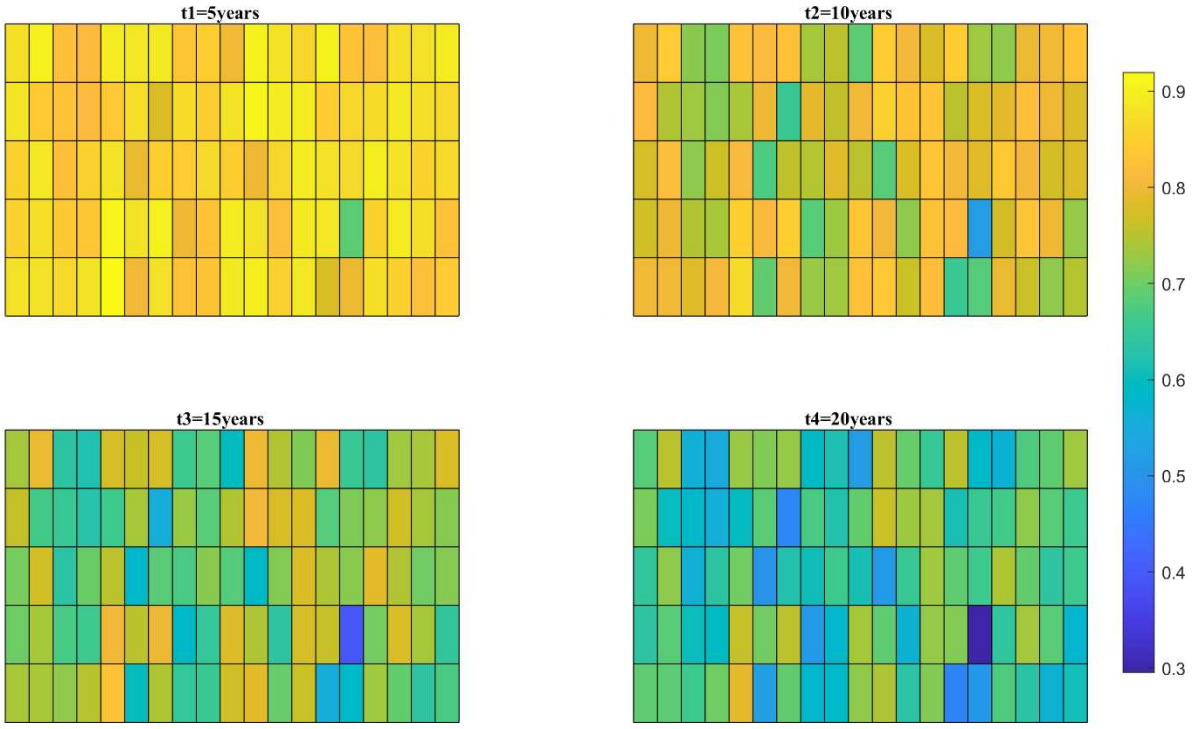

Fig. 74 Rebar remaining ratio after certain years of corrosion

6.2.4 Low cycle fatigue using strain life method

The elastic stress-based fatigue damage model based on the rain-flow counting algorithm and the Miner-pilgrim Rule are widely used nowadays. However, bridge components subject to significant loads such as earthquakes could result in fatigue failure within relatively low cycle counts due to their amplitudes being high enough to cause nonlinear plastic deformations, known as the low-cycle-fatigue (LCF) (Lee et al., 2020). The LCF is typically analyzed using the fatigue strain life method instead of the stress-based method that is typically used for the analysis of the HCF index (Chen et al., 2019). In this study, the Coffin-

Manson relation, known as the fatigue strain life method, is applied to analyze the strain of bridge deck rebar, i.e.,

$$\frac{\Delta\varepsilon_p}{2} = \varepsilon_f' \, (2N)^c \quad \text{..... (6.11)}$$

where $\Delta\varepsilon_p$ is the strain amplitude, which can be obtained from strain history analysis. In this study, the threshold is defined as 50% of yield strain (ASTM, 2004); ε_f' is the fatigue ductility coefficient, empirically assumed to be 0.2; *N* is the number of reversals to failure, representing the fatigue life in cycles; *c* is the fatigue ductility exponent, typically ranging from -0.5 to -0.7; a value of -0.6 is used in this study.

Traffic loads used for studying bridge deck LCF are defined based on the field experiment conducted by Issa et al. (2007). The study tested a full-scale reinforced concrete overlay in an outdoor exposed environment, where the equivalent AASHTO H20 loading, as well as ultimate traffic load with five times of the AASHTO H20 loading, was applied to the specimen. Applying a similar concept, the ultimate traffic load defined as five times of the "Busy" EMTLs is considered in the LCF analysis in this study. It was found in the study by Issa et al. (2007) that there was minor LCF effect on the specimen under the ultimate traffic load condition. This finding suggests that ultimate traffic load alone may not lead to significant LCF effects. In Chapter 3 (Chen et al., 2020), it was found that the combination of "Busy" EMTLs and seismic ground motion may induce plastic hinges. Therefore, this study further investigates if the combination of ultimate traffic load (i.e., five times of "Busy" EMTLs) and seismic ground motion could contribute to

significant LCF effects on the bridge deck. The 1994 Northridge earthquake is selected as the baseline seismic load, including both longitudinal and vertical direction excitation for the analysis, as shown in Fig. 75. Additional near-fault and far-field ground motions are also selected to determine the impact of seismic characteristics. Table. 13 lists the ground motions used for this study, along with their seismic intensities.

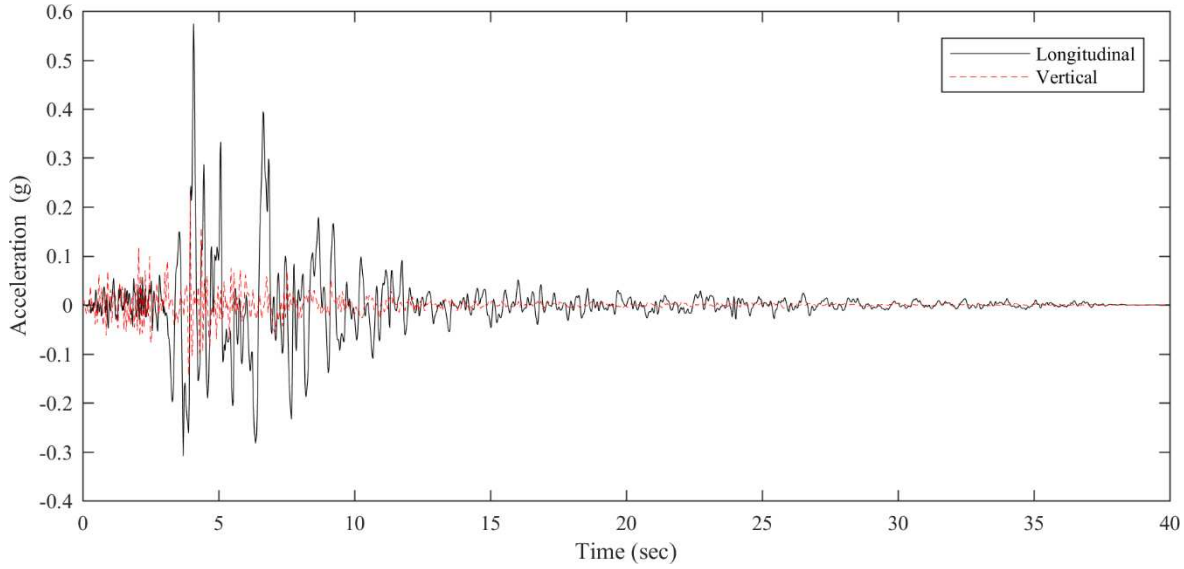

Fig. 75 Vertical-included ground motions from the 1995 Northridge earthquake to investigate LCF

Table. 13 Selected ground motions for LCF analysis

Case	**Earthquake**	**Mw**	**Station**	**R_{rup} (km)**	**L (sPGA)**	**V (sPGA)**
Near-fault	Superstition Hills	6.54	Parachute Test Site	0.95	0.53	0.21
Far-field	Imperial Valley	5.01	Brawley Airport	24.26	0.57	0.23

Note: **R_{rup}** is the distance between epicenter and site; L represents the longitudinal direction; V represents the vertical direction

6.3 Analysis of results

6.3.1 Influence of deck rebar corrosion on fatigue damage

In this section, a comparison study to investigate the impact of rebar corrosion was conducted under the three traffic loading conditions. Note that in the present study, there are three simulated traffic loads and four selected rebar corrosion states. It is important to select representative results from the total 12 cases beforehand for the sake of efficiency. As shown in Fig. 76, the changes in average deck fatigue damage over years of corrosion are illustrated to give a general view of the rebar corrosion impact. It is interesting to see that the fatigue increments from the point where rebar corrosion initiates to 5 years of corrosion are most significant for all three traffic loading conditions, while the fatigue damage stays almost constant from Year 5 to Year 20. The curves in Fig. 76 indicate that the first five years of corrosion initiation are critical for bridge maintenance to reduce the risk of fatigue damage. Accordingly, the following analysis of the fatigue distribution on deck will focus on conditions of rebar corrosion after 5 years, while the fatigue damage beyond five years will not be further discussed in this section.

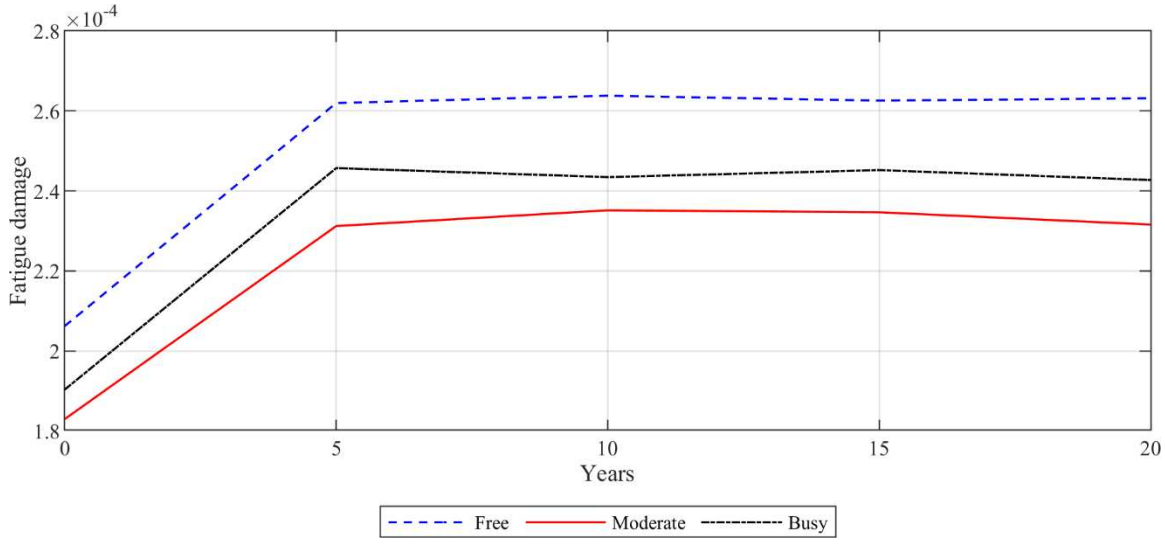

Fig. 76 Average deck fatigue over years after initiation of rebar corrosion

Fig. 77(a) shows the comparison between deck fatigue damages induced by traffic loads only and damages caused by traffic loads coupled with 5 years of rebar corrosion. To demonstrate the impact of rebar corrosion, the fatigue damage difference in percentage is plotted in Fig. 77(b). The section areas of obtuse corners, acute corners, and inner/outer radius are marked as Section A to Section F to facilitate the discussion on fatigue damage patterns. The results in Fig. 77(b) indicate that rebar corrosion cause about 20% increase of overall fatigue damage under the "Free" traffic load, which is uniformly distributed throughout the majority of the deck region. It is interesting to see that the region with low fatigue damage (less than $1.8\text{x}10^{-4}$) in the no corrosion case close to the obtuse corner on the right side (circle regions in Fig. 77(a) exhibits the greatest increase in fatigue damage (about 45%-50%) (Fig. 77(b)). As a result, these low fatigue damage regions in the no corrosion case show similar high fatigue damage ($2.6\text{x}10^{-4}$) as the majority of the deck in the corrosion case. The geometric features of the skewed and curved bridge have likely caused a high increase in local regions, leading to more local deck regions experiencing high fatigue damage.

It is also seen that high fatigue damage tends to occur near the four corners of the deck (Fig. 77(a)). There are considerably less fatigue areas next to the high fatigue diagonal obtuse corners on the deck (see Sections B and C in Fig. 77(a)), which is less obvious for the "Free" traffic loads case but becomes apparent for both the "Moderate" and "Busy" traffic load cases. The occurrence of the low fatigue next to high

fatigue at the diagonal obtuse corners on the deck may be a distinctive structural characteristic for the skewed and curved bridge. For the “Moderate” and “Busy” traffic cases in Fig. 77(b), rebar corrosion has caused considerable fatigue increment near the two diagonal obtuse corners. As the composition of heavy vehicles increases from “Moderate” to “Busy” traffic loads, corrosion seems to have a much greater effect on the middle of the deck (Sections E and F in Fig. 77(b)). Fig. 77(a) also indicates that even though the rebar corrosion of each element is modeled as independent and identically distributed random variables following a normal distribution (Fig. 74), the fatigue percentage change still roughly follows a grid-like distribution perpendicular to the traffic flow direction. This pattern can be used as a reference for planning deck repair.

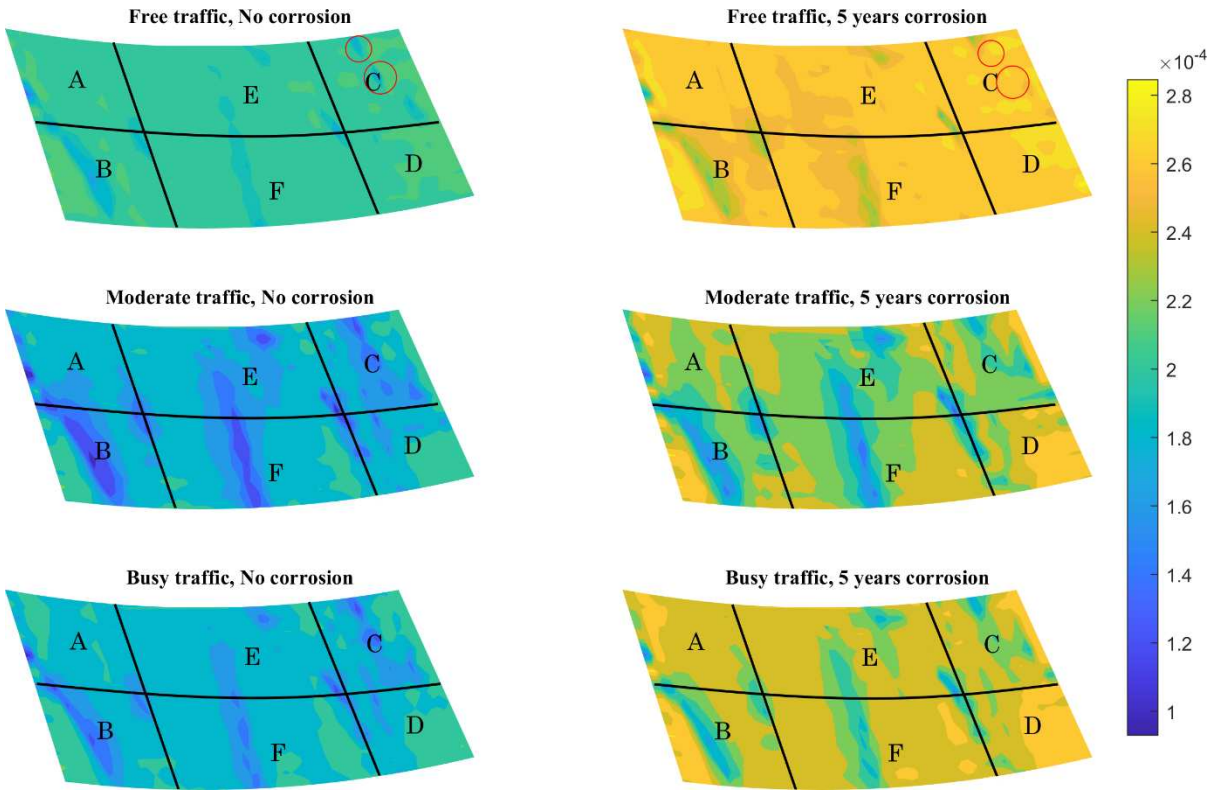
Free traffic, No corrosion
Free traffic, 5 years corrosion
Moderate traffic, No corrosion
Moderate traffic, 5 years corrosion
Busy traffic, No corrosion
Busy traffic, 5 years corrosion
A
B
C
D
E
F
×10-4
2.8
2.6
2.4
2.2
2
1.8
1.6
1.4
1.2
1

(a)

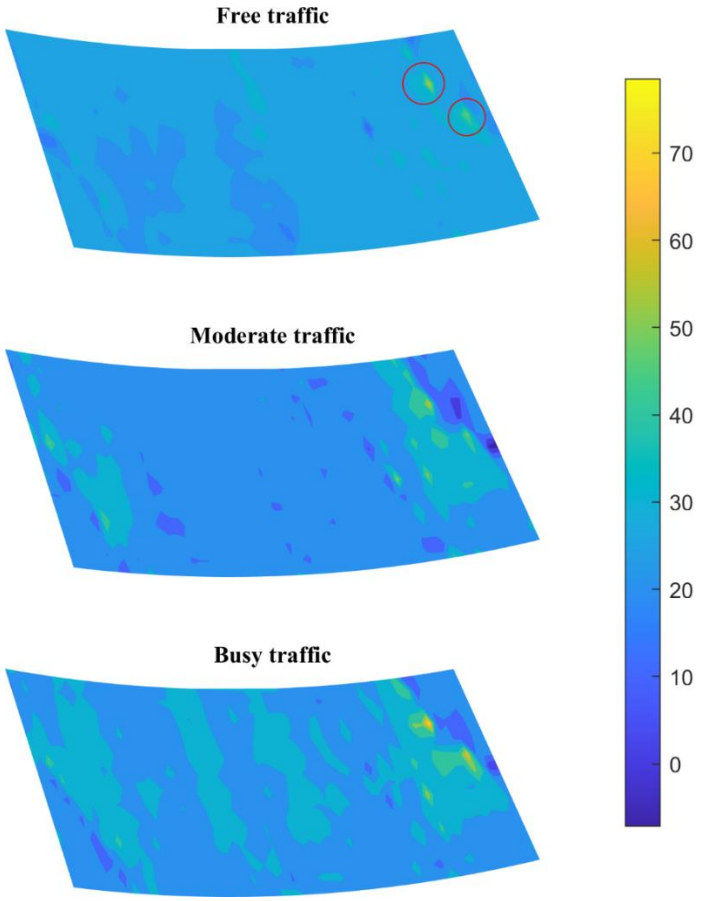

(b)

Fig. 77 Impact of rebar corrosion on fatigue damage: (a) comparisons of deck fatigue damage without and with rebar corrosion, and (b) fatigue damage increases after five years in percentage

6.3.2 Influence of traffic conditions on fatigue damage

Counterintuitively, the fatigue damage under "Free" traffic loads, as shown in Fig. 77 (a), is generally higher than that under "Moderate" and "Busy" traffic loads. To verify this result, several deck elements are selected for in-depth analysis, including one at the midspan and two others, i.e., Elements 1, 2, and 3 in Fig. 78.

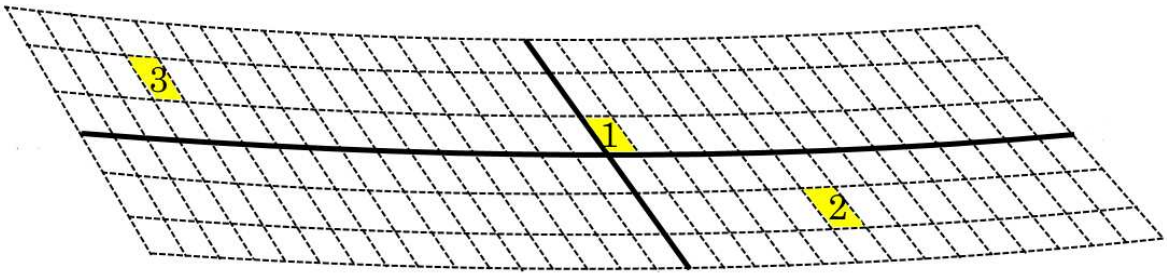

Fig. 78 Elements selected to verify traffic fatigue performance

The plane stress time histories at the Element 1 under different traffic loads are shown in Fig. 79. The comparison shows that the stress amplitudes under “Free” traffic load are significantly smaller than the stress amplitudes under “Moderate” and “Busy” traffic loads. This is due to the fact that the “Free” traffic load involves only regular vehicles, whereas the “Moderate” and “Busy” traffic loads include light trucks and heavy trucks. Fig. 79 also shows that as the number of heavy vehicles increases, the fluctuation of stress time histories becomes more random. Since the stress fluctuations are irregular—unlike those in standard cyclic fatigue tests—the maximum stress does not directly correlate with fatigue damage. Next, further analysis is conducted to determine the cause on the bridge deck with the highest fatigue damage under “Free” traffic loads.

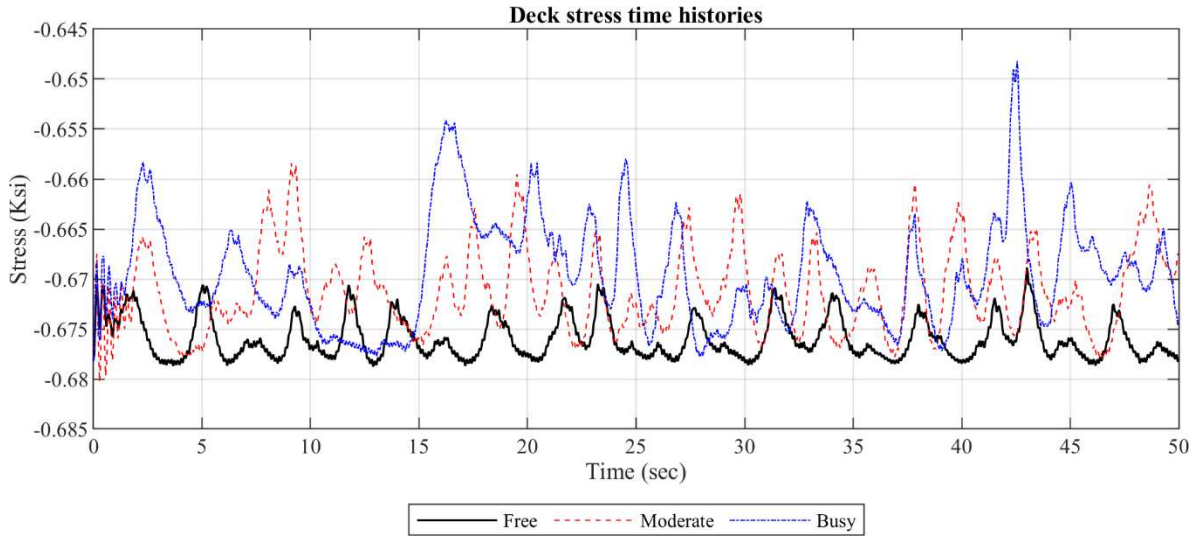

Fig. 79 Comparison of stress time histories for "Free", "Moderate", and "Busy" traffic loads at deck midspan

The widely-used linear accumulated damage (D) devised by Palmgren (Palmgren, 1924) and Miner (Miner, 1945) is defined as:

$$D = \sum_1^n D_i = \sum_1^n \frac{n_{i,S_{ai}}}{N(S_{ai})} \tag{6.12}$$

where D is the summation of a series of contributing stress cycles from 1 to n, $N(S_{ai})$ is determined from the S-N curve, and n_i is the number of stress cycles contributing to fatigue at stress amplitude at S_{ai}, which can be calculated through the rain-flow counting method.

To analyze the influence of heavy vehicles in "Moderate" and "Busy" traffic loads, fatigue damages D at Elements 1, 2, and 3 are discretized into $n_{i,S_{ai}}$ and D_i for analysis. Fig. 80 illustrates the number of contributing cycles $n_{i,S_{ai}}$ versus stress S_{ai}. It should be noted that for the Miner-Palmgren linear damage model, the contributing cycles are classified as full cycles and half cycles. The fatigue damage data points

clustered below $D_i = 3 \times 10^{-7}$ in Fig. 80 are the fatigue damage due to the contribution of half cycles. It is seen from Fig. 80 that the maximum stress contributed to fatigue damage for "Free" traffic loads is 0.068 ksi. Since the "Free" traffic load does not consist of any heavy vehicles, any contributing cycles beyond 0.068 ksi observed for "Moderate" and busy traffic loads can be regarded as the fatigue caused by heavy vehicles. Accordingly, the stress 0.068 ksi is used as a threshold to de-aggregate the contributing cycles due to regular and heavy vehicles, respectively (Fig. 81(a)). It is seen from Fig. 81(a) that for contributing cycles due to regular vehicles ($S_a \leq 0.068$), the "Free" traffic load condition has induced the largest cycle counts, followed by "Busy" and "Moderate" traffic loads. For contributing cycles due to heavy vehicles ($S_a > 0.068$), "Moderate" traffic condition has the largest cycle counts, followed by "Busy" traffic load condition. As defined by the simulated traffic load conditions before, the "Free" traffic condition does not have contributing cycles due to heavy vehicles. Next, the fatigue damage is de-aggregated into the fatigue damage due to regular ($S_a \leq 0.068$) and heavy vehicles ($S_a > 0.068$) in Fig. 81(b). Fig. 81(b) indicates that fatigue damage induced by heavy vehicles has only contributed a small proportion to the total fatigue damage of Element 1. Thus, the fatigue damage due to regular vehicles controls the magnitude of total fatigue damage. Among the three traffic loading conditions, "Free" traffic load has caused the highest contributing cycles due to regular vehicles (Fig. 81(a)) and thus the largest fatigue damage (Fig. 81(b)). The busy traffic load has induced more fatigue damage due to regular vehicles than "Moderate" traffic load

(Fig. 81(b) and Table. 14). Correspondingly, “Free” traffic load leads to the maximum total fatigue damage, followed by “Busy” and “Moderate” traffic loading conditions.

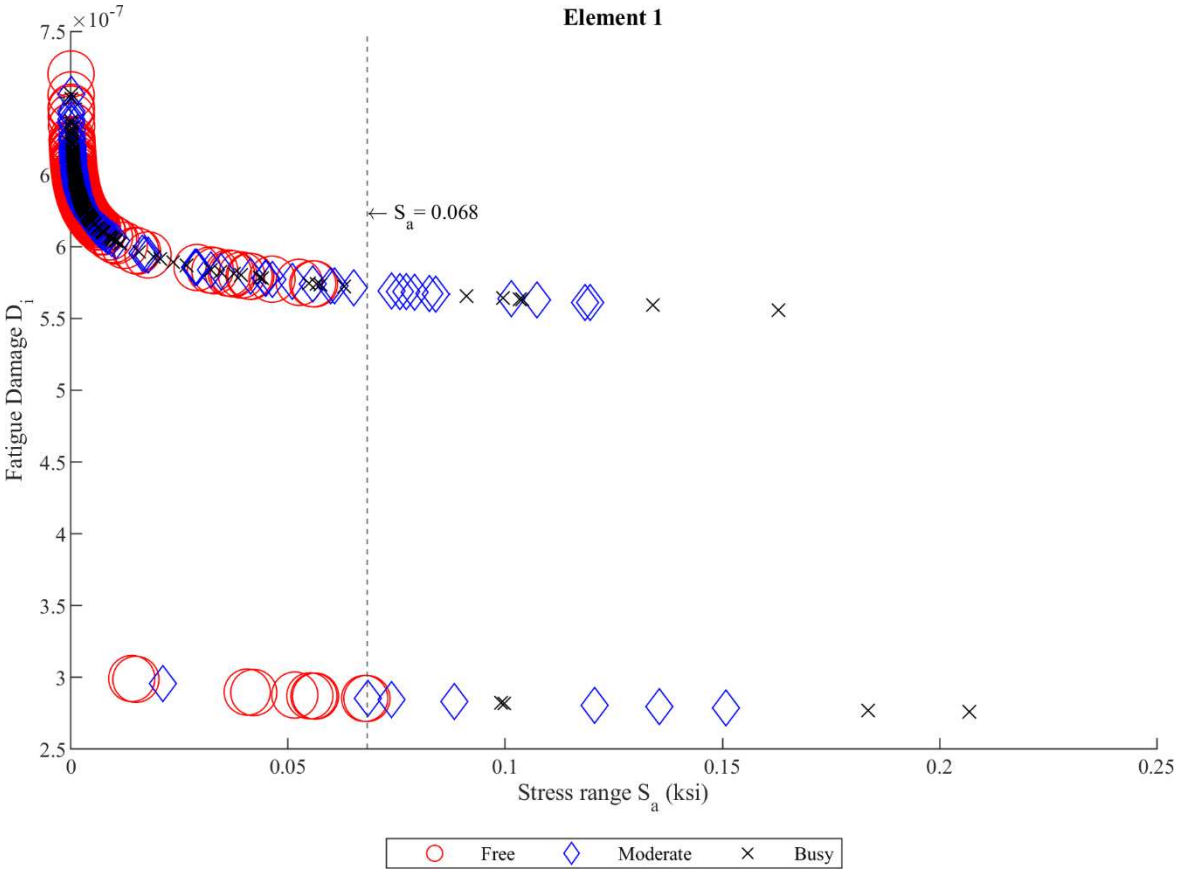

Fig. 80 Stress ranges contributed to fatigue damages

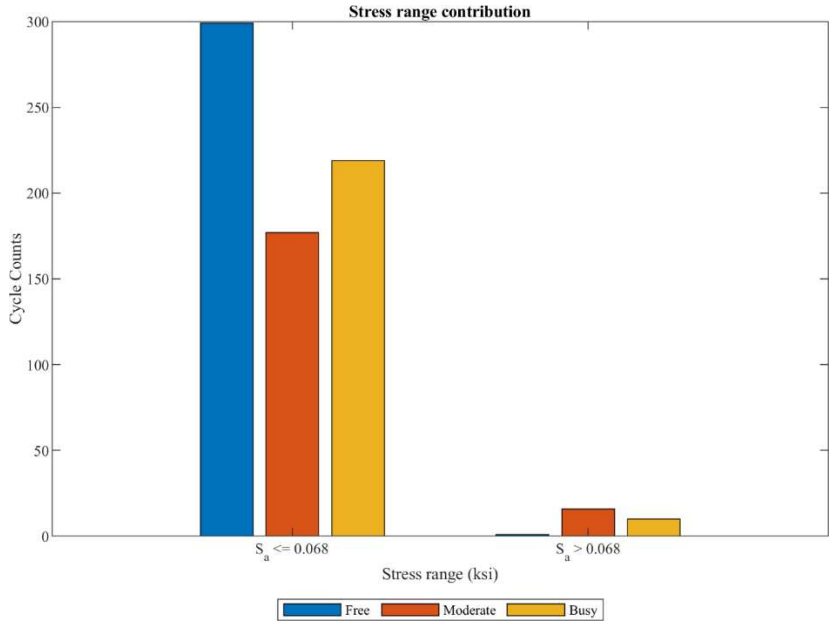

(a)

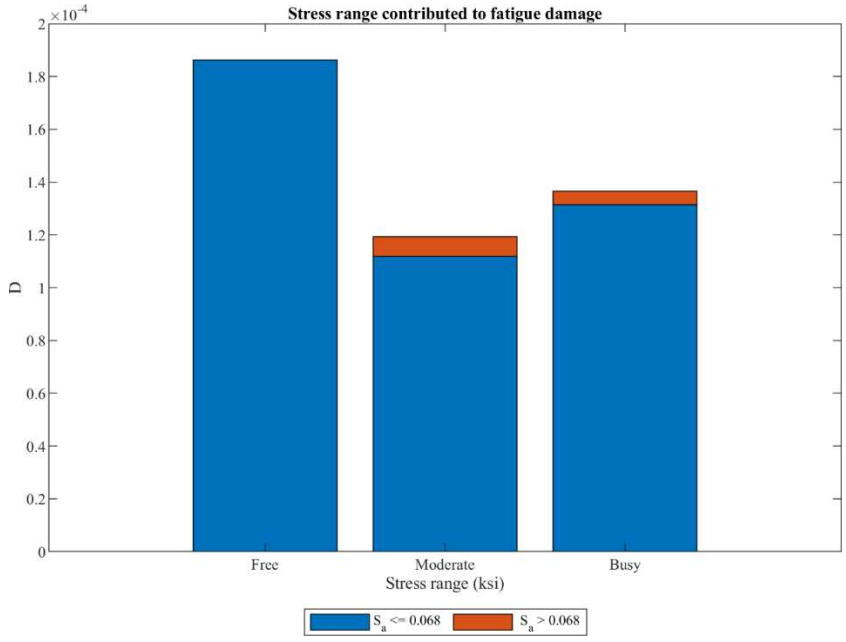

(b)

Fig. 81 Fatigue damage de-aggregation for Element 1: (a) de-aggregated contributing cycle counts due to regular ($S_a \leq 0.068$) and heavy vehicles (S_a>0.068), and (b) de-aggregated fatigue damage due to regular ($S_a \leq 0.068$) and heavy vehicles (S_a>0.068)

Table. 14 Fatigue damage contribution of regular ($S_a \leq 0.068$) and heavy vehicles ($S_a > 0.068$)

Stress range	"Free" traffic	"Moderate" traffic	"Busy" traffic
$S_a \leq 0.068$ (ksi)	100%	94%	96%
S_a>0.068 (ksi)	0%	6%	4%

The same de-aggregation analysis was also conducted for Elements 2 and 3 in Fig. 78. Similarly, it is found that "Free" traffic load causing the highest deck fatigue is a generalized outcome due to the dominant contribution to total fatigue by regular vehicles. This finding is consistent with the observation in a field monitoring project by Pircher et al. (2011), where girder fatigue damages become less when heavy vehicles are introduced to the traffic flow.

For the case of "Free" traffic loads, high fatigue damage deck distribution near the corners, particularly Sections C and D, are scattered and have less fatigue gradient compared to the results of the "Moderate" and "Busy" traffic loads, as shown in Fig. 77(a). On the other hand, the fatigue damage comparison between "Moderate" and "Busy" traffic loads reveals a highly similar spatial distribution across Sections B, C, and D, with only an increase in damage magnitude under "Busy" traffic. A slight difference is observed at Section A when comparing the two loading conditions. It should be noted that the fatigue damage in the bridge segment (Sections E and F) is generally lower than in the corners (Sections A to D). When traffic

loads change from “Moderate” to “Busy” traffic loads, most of the fatigue damage in Sections E and F increased by about 10%. Fatigue damage in several small areas near the outer radius (Section F) reached above $2.6\text{x}10^{-4}$, which is the same level at the corners.

After analyzing the impact of rebar corrosion and traffic loads separately, it is now reasonable to evaluate the coupled effect of traffic loads and rebar corrosion on bridge deck fatigue damage. Based on the fatigue contour plots of Fig. 77(a), the comparison focuses on the left and right sides of roadway segments (i.e., Sections A, B, C, and D in Fig. 77). The traffic conditions comparison are made between “Moderate” and “Busy” traffic conditions, considering the fatigue damage caused by “Free” traffic loads is completely different from the other two scenarios. The comparison results for Sections A and B are shown in Fig. 82 and Fig. 83. The results indicate that increasing traffic load from “Moderate” to “Busy” conditions—without considering corrosion—has a minimal impact, with only a 5–10% increase in most areas of the left segment (Sections A and B), as shown in the comparison between Fig. 82(a) and Fig. 82(b), as well as Fig. 83(a).

On the other hand, the change of fatigue damage in the left segment due to the change of rebar corrosion (from no corrosion to five-year corrosion) for the moderate traffic condition is significant with an increase of 20-30% for most of the area, as seen in the comparison of Fig. 82(a) and Fig. 82(c), as well as Fig. 83(b). For the high fatigue area of the left segment (Section A), the coupled effects due to changes from “Moderate” traffic load with no corrosion to “Busy” traffic load under 5 years of corrosion could induce a 40% to 50%

increase in fatigue damage in the majority of the area (see Fig. 82(a) and (d), as well as Fig. 83(c)). This result suggests that the coupled traffic and corrosion effects will be greater than the summation of effects of separate traffic change and corrosion state change, i.e., 40-50% > (5-10%) +(20-30%), indicating the necessity of conducting coupled traffic and corrosion analysis. Note that for this coupled effect, although the percentage increase in fatigue in Section B (Fig. 83(c)) is high, the fatigue damage level in this region is low, as shown in Fig. 82(d). So, the high percentage increase (up to 70%) in Fig. 83(c) is not important. Similar trends are observed for the right segment (Sections C and D) in Fig. 84 and Fig. 85.

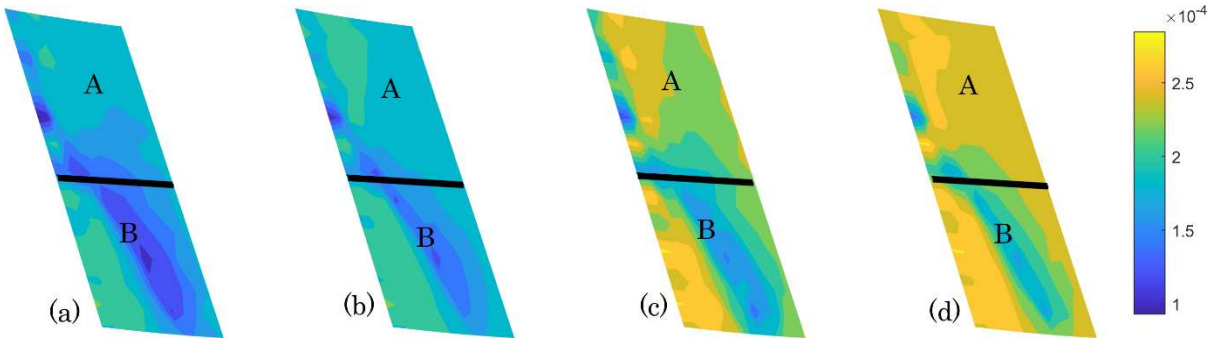

Fig. 82 Comparison of fatigue for Sections A and B under different traffic and corrosion conditions: (a) “Moderate” traffic load only without corrosion, (b) “Busy” traffic load only without corrosion, (c) “Moderate” traffic load after 5 years of corrosion, and (d) “Busy” traffic load after 5 years of corrosion.

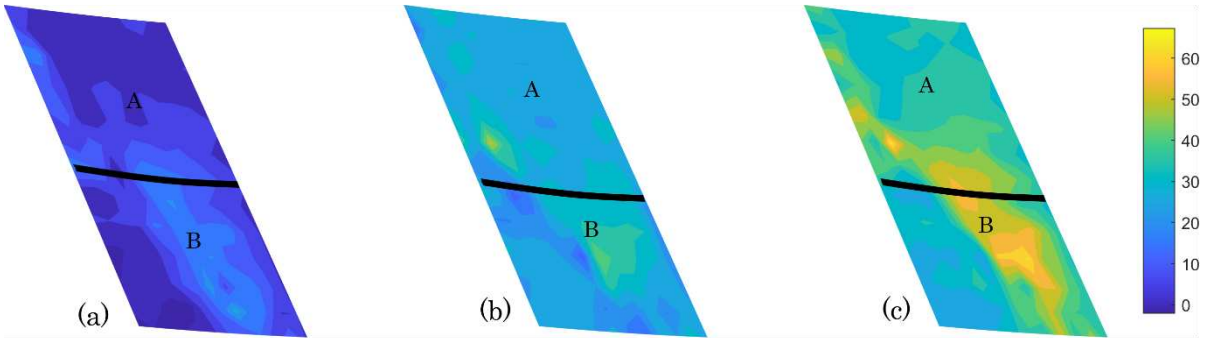

Fig. 83 Percentage change of fatigue damage for Sections A and B when: (a) changing traffic load from "Moderate" to "Busy" without corrosion, (b) changing from no-corrosion to 5-years corrosion for "Moderate" traffic load, and (c) changing from "Moderate" traffic load and no-corrosion to "Busy" traffic load with 5-years corrosion.

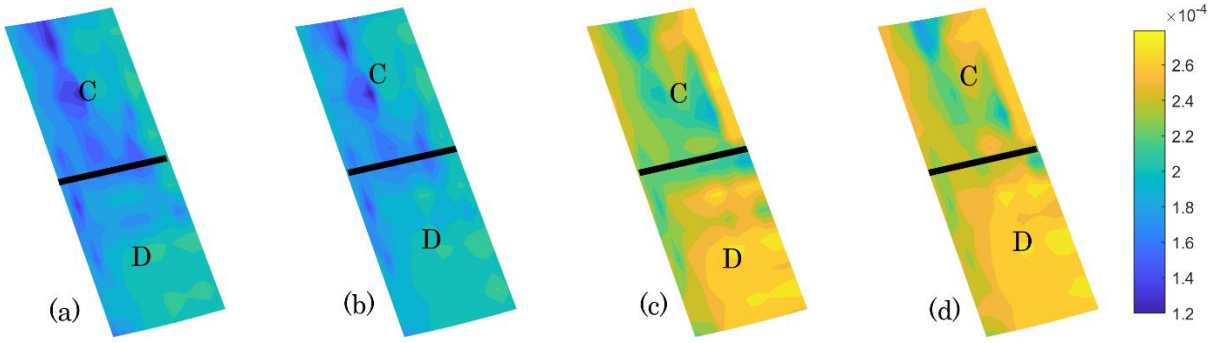

Fig. 84 Comparison of fatigue for Sections C and D under different traffic and corrosion conditions: (a) "Moderate" traffic load only without corrosion, (b) "Busy" traffic load only without corrosion, (c) "Moderate" traffic load after 5 years of corrosion, and (d) "Busy" traffic load after 5 years of corrosion.

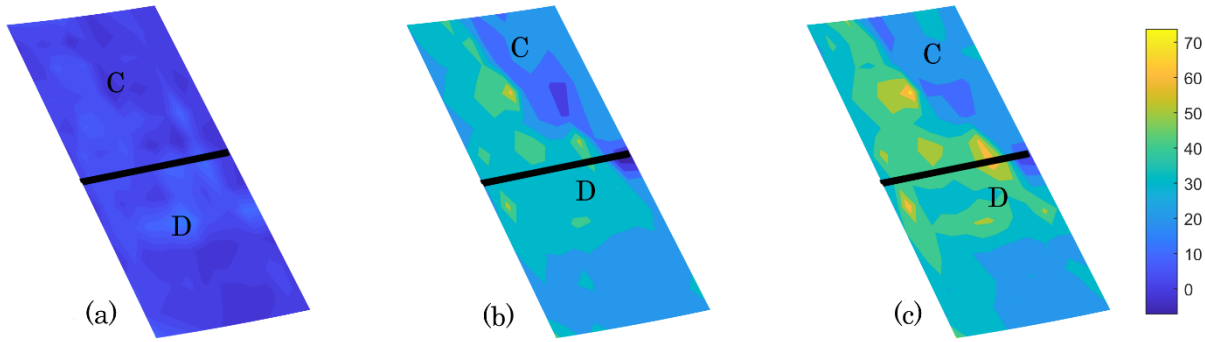

Fig. 85 Percentage change of fatigue damage for Sections C and D when: (a) changing traffic load from “Moderate” to “Busy” without corrosion, (b) changing from no-corrosion to 5-years corrosion for “Moderate” traffic load, and (c) changing from “Moderate” traffic load and no-corrosion to “Busy” traffic load with 5-years corrosion.

The framework proposed in this study allows for informed decision-making regarding deck repair. The fatigue analysis results can provide when-to and where-to guidance on the deck repair, which is illustrated in the following. Based on the contour plots of deck fatigue damage distribution, the range of fatigue damage can be further disaggregated into subranges to indicate different fatigue damage states. It is possible to quantify the percentage of the whole bridge deck area that falls within each fatigue damage subrange, as shown in Fig. 86. The results in Fig. 86 may be used in two ways in guiding repair decisions. First, one can make decisions about deck repair based on the overall severity of fatigue damage. For example, if the transportation department conducts the simulation and plans to replace deck areas with severe fatigue damage, they can highlight critical regions by selecting deck fatigue damage values exceeding a predefined threshold. In this study, a threshold of 2.6×10^{-4} is used as an example to demonstrate the concept. When the percentage of deck fatigue damage in this subrange is greater than a pre-determined threshold, the bridge owner/manager may decide to reconstruct the bridge deck. For example, using a 50% pre-determined threshold as an example, the bridge deck under “Free” traffic conditions with 5 years or 10 years of corrosion will need to be reconstructed. Second, one can identify the specific locations on the bridge deck

that experience severe fatigue damage (deck fatigue damage greater than $2.6x10^{-4}$), as shown in Fig. 87 for the "Busy" traffic load condition. In this case, local repairs can be performed in these identified critical regions.

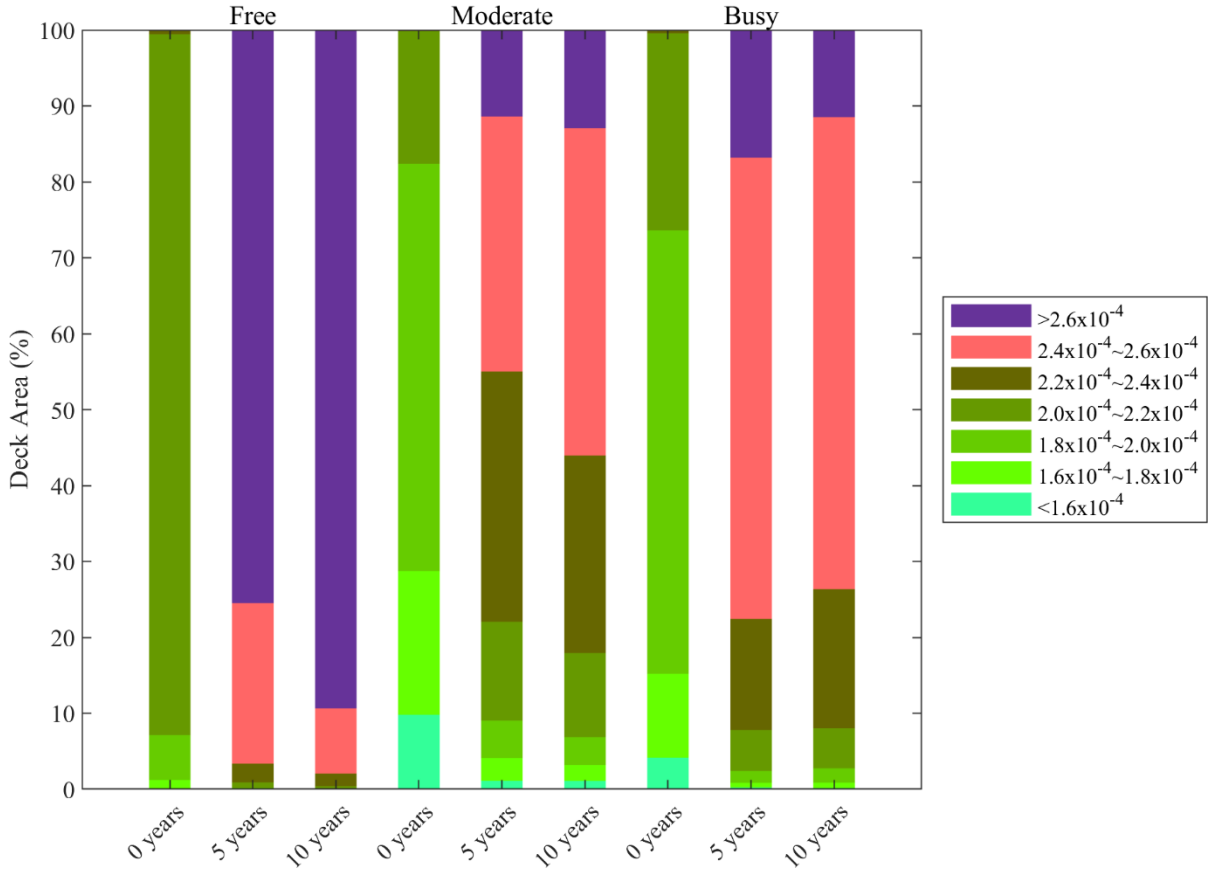

Fig. 86 de-aggregated fatigue damage percentage of each traffic load and rebar corrosion

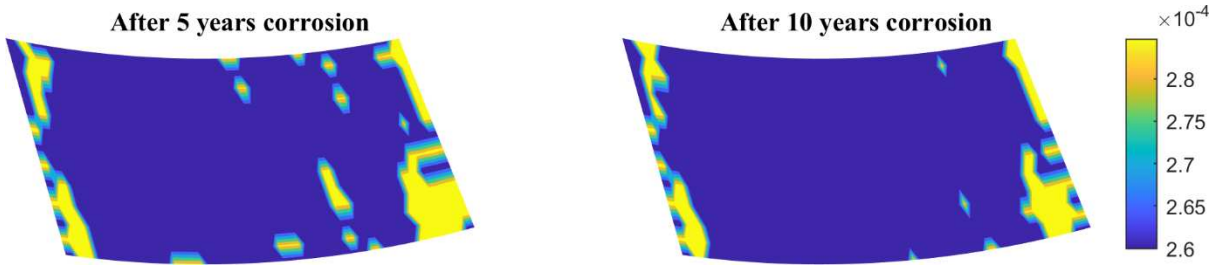

Fig. 87 Filtered fatigue damage distribution on bridge deck for fatigue damage larger than $2.6x10^{-4}$ under "Busy" traffic load

6.3.3 Counterpart straight bridge results

Compared to the deck fatigue damage for the baseline bridge (Fig. 77 (a)), rebar corrosion seems to have a minor influence on the counterpart straight bridge case as shown in Fig. 88. The changes in fatigue damage after 5 years of corrosion almost remain unchanged for the middle bridge segment, with very slight change of distribution for the left and right roadway segments.

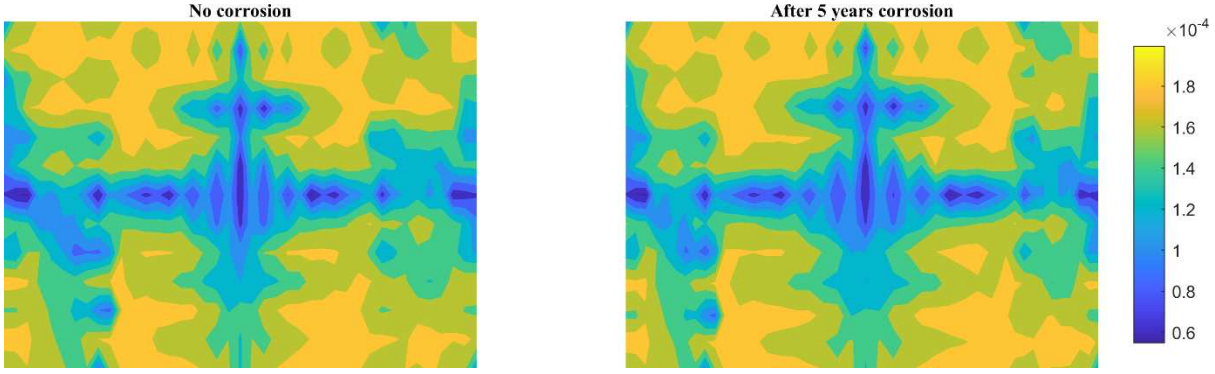

Fig. 88 Fatigue comparison of corrosion involvement for counterpart straight bridge (a)

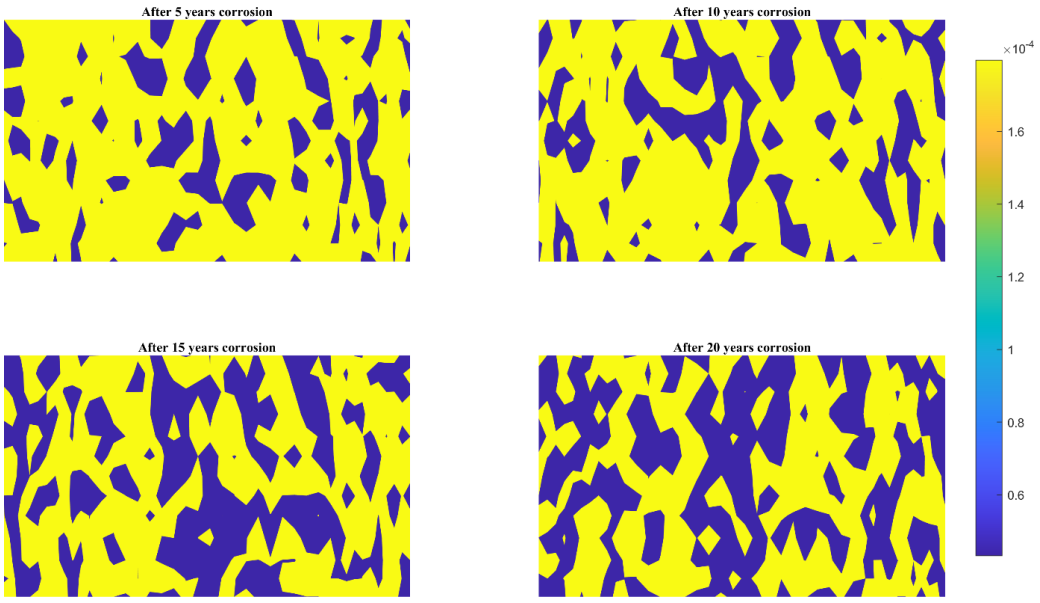

(b)

Fig. 90Fig. 89 Fatigue percentage difference for counterpart straight bridge under “Moderate” traffic loads

Further analysis of up to 20 years of corrosion shows that the order of change of the fatigue damage is $10^{-4}\%$ (Fig. 89) under both “Free” and “Moderate” traffic loads, indicating that there is a negligible change in fatigue under different corrosion states. The percentage change of fatigue damage for each time interval presented in Fig. 89 and Fig. 90 also shows a different distribution pattern as compared to the baseline bridge (Fig. 77(b)). For the baseline bridge results, the fatigue percentage change for each time interval distributes perpendicular to the direction of traffic flow, while the percentage changes of the counterpart straight bridge scatter randomly with no obvious patterns. The negligible effect of the rebar corrosion on

the straight bridge is most likely due to the symmetric geometry of the bridge deck, which can uniformly distribute the traffic loads to pier columns. On the other hand, for bridge decks with a horizontally curved design, traffic loads will generate eccentric loads and moments from the bridge center of mass.

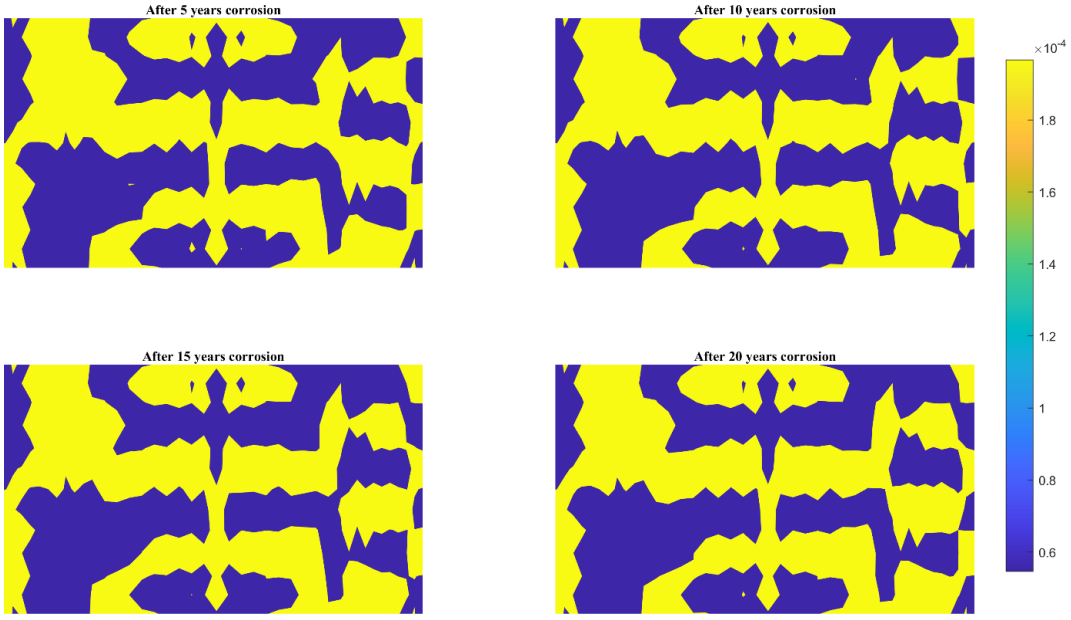

(a)

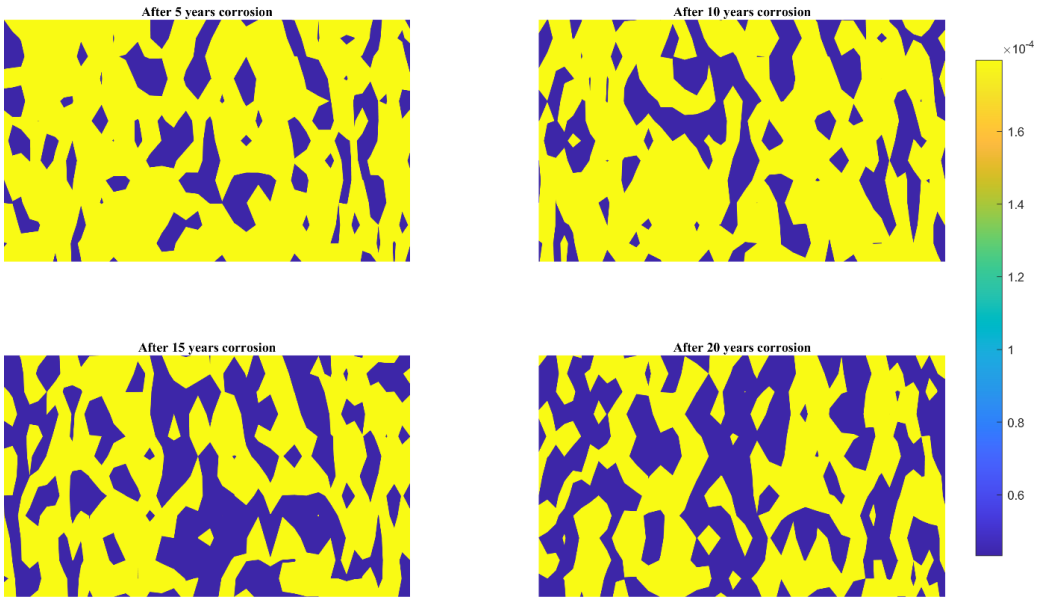

(b)

Fig. 90 Percentage change of fatigue damage for counterpart straight bridge under: (a) “Free” traffic loads, and (b) “Moderate” traffic loads

6.3.4 Plastic fatigue strain life estimation and potential risk of LCF

In this study, ultimate traffic loads, which are equivalent to 5 times of the “Busy” traffic loading as applied in fatigue loading tests in the literature (Issa et al., 2007), are used to study LCF in this research. Following the time history analysis of the FE model, rebar strains exceeding the predefined plastic strain threshold are used to compute the fatigue life of each deck element in cycles, based on Eq. (6.11). Fig. 91 illustrates the remaining fatigue life of the baseline bridge deck based on plastic strain, where lower cycle counts (indicated in yellow) correspond to shorter fatigue life and a higher risk of rebar fracture. All the elements’ fatigue life in the cycle is higher than 1000 cycles, meaning that there is very low risk for rebar fracture failure due to LCF. The result shows a concentration of higher fatigue life at the acute corners, indicating a relatively lower risk of LCF.

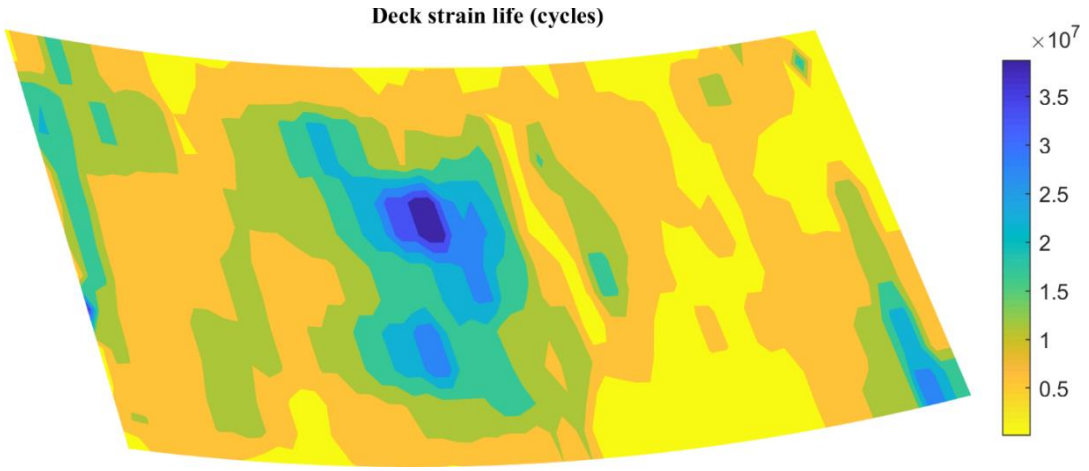

Fig. 91 Strain life of bridge deck under ultimate “Busy” traffic loads

To further look into the fatigue performance at the middle bridge segment, the ultimate traffic load case is then coupled with the ground motions described previously in Table. 13 to investigate the effect of seismic loads. The fatigue life for different ground motions is illustrated in Fig. 92. Compared with Fig. 91, the remaining cycles show little difference between the case with only ultimate traffic load and the case combining ultimate traffic load with ground motions, suggesting that seismic ground motions may have a minor impact on the fatigue performance of the concrete bridge deck.

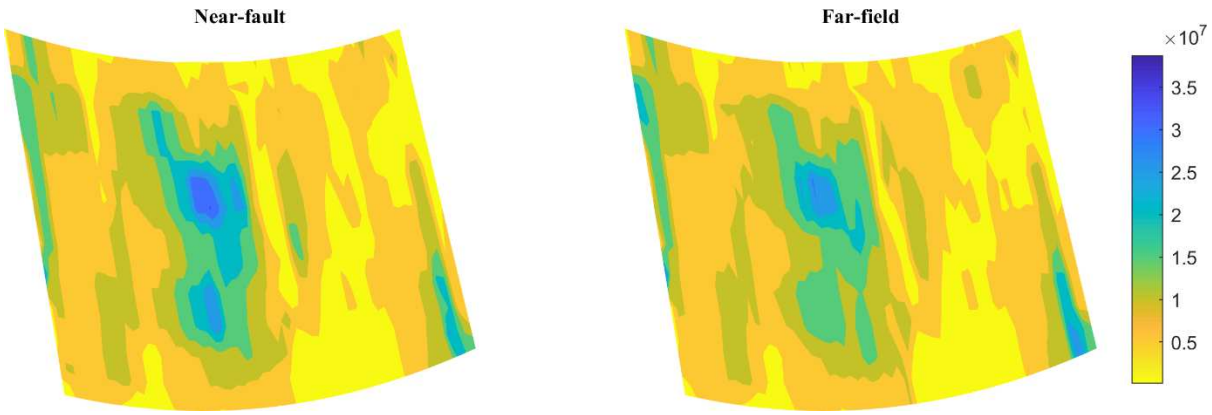

Fig. 92 Fatigue life distribution for different types of ground motions

A bridge deck rebar corrosion propagated with its service life; it is also necessary to evaluate such a corrosion effect on the LCF of the deck in coupled with an earthquake for the worst-case scenario. The result shows a significant reduction in the fatigue life (i.e., increased fatigue risk) compared to the ultimate traffic load-only case (Fig. 91) and the case with a couple of ultimate traffic load and ground motions (Fig. 92). Fig. 93 presents the spatial distribution of the bridge deck's fatigue life after 40 years of rebar corrosion, subjected simultaneously to ultimate traffic loads and near-fault ground motion. The lowest remaining fatigue life area at both the left and right sides, as well as the center of the bridge segment has significantly decreased, leading the whole bridge deck to have similar levels of LCF risk.

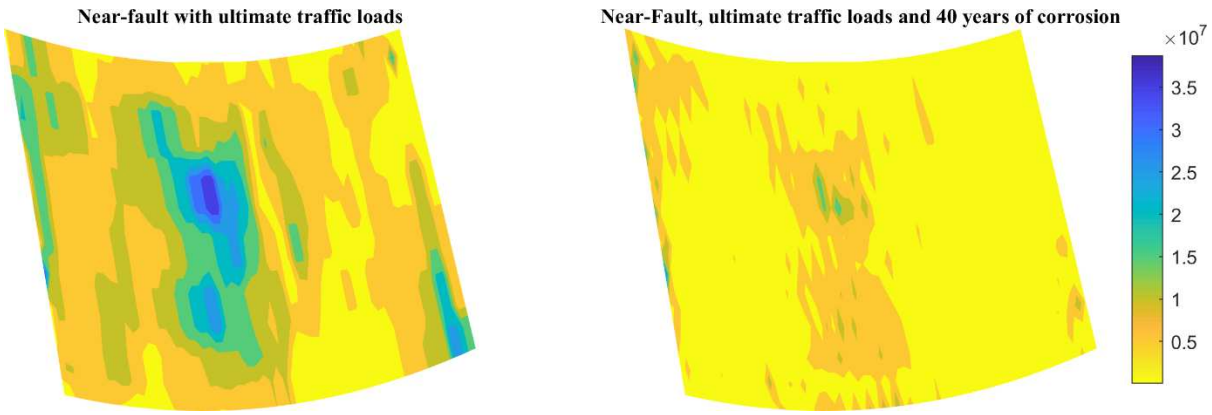

Fig. 93 Fatigue life distribution of bridge deck under coupled ultimate loads and baseline earthquake after 40 years of rebar corrosion

6.4 Conclusions

In this chapter, the framework of integrating the FE model with EMTLs developed for skewed and curved bridges has been extended to investigate the effect of chloride-induced rebar corrosion on high cycle fatigue. The study assumed the initiation of corrosion immediately after construction. The rebars for concrete decks are modeled as shell elements with equivalent cross-section properties. Corrosion factors applied in this study are assumed to be uniformly distributed, and then the Monte Carlo sampling method is adopted to distribute the corrosion state for each rebar element. Various corrosion states and three different traffic loads (i.e., “Free”, “Moderate”, and “Busy” traffic loads) are considered for evaluating the high cycle fatigue performance of the bridge deck. The results are also compared with the counterpart straight bridge results. This study also discusses the use of the proposed framework to evaluate the low cycle fatigue of bridge decks based on the strain life method. The framework allows for evaluating potential low cycle fatigue risks for the whole bridge deck under coupled effects of traffic overload conditions,

seismic ground motion inputs, and rebar corrosion. Based on the analysis results, the following conclusions are made:

1. For high cycle fatigue, skewness and curvature of the bridge deck result in the concentrated high fatigue area near the deck corners. The high-fatigue area near the two obtuse corners (Sections B and C) is adjacent to a significantly low-fatigue area. This pattern is observed under all conditions applied to the skewed and curved bridge, regardless of rebar corrosion and traffic loads.
2. The effect of rebar corrosion on deck fatigue for the skewed and curved bridge is the most significant after five years of corrosion initiation. The additional impact of rebar corrosion on fatigue becomes minimal beyond the first five years.
3. After five years of rebar corrosion, deck fatigue damages under the "Free" traffic loads have a more uniform distribution across the entire bridge deck than those for "Moderate" and "Busy" traffic loads. When heavy vehicles (light and heavy trucks) are introduced into the traffic flow composition, localized high fatigue concentration is more obvious, especially for "Moderate" traffic conditions. These results suggest that partial deck renovation might be adopted for "Moderate" and "Busy" traffic conditions under five years of corrosion.

4. “Free” traffic loads lead to the highest fatigue damage among the three traffic conditions. This is most likely because the dominant contribution to total fatigue is from the regular vehicles, and “Free” traffic condition has the highest percentage of regular vehicles.
5. Rebar corrosion has a very small, even negligible, effect on high cycle fatigue for the counterpart straight bridge, likely due to the symmetric bridge deck geometry.
6. Fatigue life calculated by the plastic strain life method indicates that the deck of the skewed and curved bridge has no significant risk of low cycle fatigue under simultaneous ultimate traffic loads, seismic excitation, and rebar corrosion. The right side of the middle bridge segment is the most vulnerable area of the whole bridge deck in terms of low cycle fatigue, likely due to the asymmetric geometry of the skewed and curved bridge.
7. The spatial distribution of fatigue damage enables the identification and quantification of areas with elevated fatigue risk. Such spatial distribution allows decision-makers to determine whether to replace only a partial or an entire concrete deck and the locations of repairs if partial renovation is desired. For example, many concrete bridges deck repair projects undertaken by the Colorado Department of Transportation rely on percentage-based estimates of deck defects. The proposed framework provides a quantitative evaluation of the deck area that needs repairs, thus facilitating repair decisions.

CHAPTER 7 SUMMARY AND FUTURE STUDIES

7.1 Summary and Conclusions

A comprehensive framework for analyzing the structural performance of skewed and curved concrete bridges under traffic and seismic loads simultaneously is proposed to address the limitations of existing analysis approaches. **First**, the research in Chapter 2 has employed finite element models with detailed geometry of superstructure for skewed and curved bridges to perform fragility analysis covering a wide range of seismic intensities. This new fragility analysis approach allows explicit quantification of structural component risks due to influence of skewness and curvature. **Second**, the study in Chapter 3 proposes to a hybrid bridge-traffic-earthquake interaction framework to simulate spatially and temporally varying realistic traffic loads with concurrent seismic ground motion to evaluate structural performance of skewed and curved bridges. A case study was conducted using a prototype skewed and curved bridge in Tacoma, Washington. **Third**, to further understand influence of various seismic load characteristics, skewness, curvature and traffic characteristics on bridge seismic performance, a comparative parametric study was conducted in Chapter 4 using the simulation framework developed in Chapter 3. **Forth**, although the influence of the various parameters on bridge performance is obtained from Chapter 3, these analysis results cannot be directly used for decision-making regarding bridge repair. In this context, Chapter 5 focuses on quantifying the deck fatigue for skewed and curved bridges to guide decision-making of bridge repair. **Fifth**,

besides traffic loads, corrosion of rebar in concrete deck is another major stressor that can negatively impact deck fatigue life of skewed and curved bridges. In this context, the study in Chapter 6 further analyzes combined traffic loads and rebar corrosion to quantify spatial distribution fatigue damage across bridge deck. Additionally, the low-cycle fatigue risks of concrete bridge deck due to seismic load are also evaluated.

The conclusion in this dissertation is summarized as the following:

1. Fragility analysis of structural components has been conducted for various bridge geometries with differing degrees of skewness and curvature. The fragilities of skewed and curved bridges are compared to those of the counterpart straight bridge. The results show that geometric feature of skewness and curvature have caused different columns exhibiting different seismic fragilities, unlike the case of straight bridge, where different columns have similar fragilities. The skewed, curved and skewed-and-curved bridges show distinguished patterns of fragility difference among columns. For example, fragility curves for different columns of the skewed bridge are similar to those of straight bridges, with fragilities for interior columns slightly higher than those of exterior columns in the high seismic intensity region. For the bridges with curvature, fragilities of the interior two columns are similar to each other, likewise, the two exterior columns show comparable fragilities; however, the interior columns exhibit significantly higher fragilities compared to the exterior ones. For skewed-and-curved bridges, the frailties among columns show even larger discrepancy in the high seismic intensity region due to the combined effects of skewness and curvature.
2. A hybrid framework for investigating the performance of bridges under concurrent traffic loads and ground motion is proposed in Chapter 3. A case study of a real skewed and curved bridge located in Tacoma, Washington, was used to demonstrate the proposed methodology. It is found that for bridge members that are vulnerable under seismic excitation, the stochastic traffic loads

can potentially raise the risk of failure of the members, which is a new finding compared to the previous research that under-estimated the negative impact of traffic loads during earthquakes. It is also found that traffic load has a much longer lasting effect on the vertical responses for both columns and deck than the column longitudinal responses after the earthquake main-shock dissipated.

3. A parametric study on bridge response under coupled seismic excitation and traffic load is presented in Chapter 4. The influence of various parameters, including seismic excitation directions, PGA ratio of vertical-longitudinal (V/L PGA ratio), as well as the traffic arrival time, on bridge response is studied. Overall, skewed and curved bridge responses are considerably higher than those of their counterpart straight bridge except for the case where the transverse earthquake is introduced. The study also revealed that even for the same traffic loads, different time offsets between traffic load and seismic excitation can significantly affect the bridge's vertical responses such as column axial forces and deck displacements, highlighting the importance of considering traffic loads as time histories.
4. In Chapter 5, fatigue assessment using the Palmgren-Miner's rule is applied to both a skewed and curved bridge and a straight bridge. The structural response is simulated using the proposed traffic-bridge-interaction simulation framework in Chapter 3. It is found that the skewed and curved bridge has overall higher deck stresses compared with the counterpart straight bridge. Deck stresses induced by traffic with heavy vehicles ("Moderate" and "Busy" traffic) have almost twice the amplitude than stresses induced only by regular vehicles ("Free" traffic). The skewed and curved bridge exhibits higher fatigue level than that of the straight bridge. The fatigue distribution patterns of the skewed and curved bridge and the straight bridge are very different. Further analysis revealed that the fatigue distribution in skewed and curved bridges—particularly the high fatigue damage near the deck corners—is primarily attributed to the geometric configuration of the deck rather than the traffic flow.
5. In Chapter 6, the proposed framework of traffic-bridge interaction model for skewed and curved

bridge has been extended to investigate the effect of chloride-induced rebar corrosion on high cycle fatigue. It is found that the spatial distribution patten of high cycle fatigue across the deck is unique for the skewed and curved bridge and determined by the geometry of bridge superstructure. “Free” traffic leads to the highest fatigue damage among three traffic conditions for the skewed and curved bridge. The effect of rebar corrosion on deck fatigue for the skewed and curved bridge is the most significant after five years of corrosion initiation, while the impact of further rebar corrosion on fatigue after five years is minimal. Rebar corrosion has a neglectable effect on high cycle fatigue for the counterpart straight bridge. The framework also allows evaluating potential low cycle fatigue risks for the whole bridge deck under coupled effects of traffic overload conditions, seismic ground motion inputs, and rebar corrosion.

7.2 Summary of contributions to the profession

The research in this dissertation offers the following contributions to the field:

Advanced modeling of skewed and curved bridge superstructures: The existing fragility analysis for skewed and curved bridges typically simplifies the bridge superstructure as line-like elements to reduce computational efforts. Such simplification has hindered the understanding of impact of skewed and curved bridges on structural performance/fragility. The fragility analysis conducted in this study includes a set of detailed finite element bridge models with different skewness and curvature for superstructures to give a comprehensive investigation of how irregular superstructure impacts seismic performance/fragility.

Sophisticated analysis of concurrent traffic and seismic impact on skewed and curved bridges: The past research on studying the combined effects of traffic and seismic loads is limited to either treating traffic load as a static load or applying an amplification factor to dynamic seismic load to consider the traffic load

effects (e.g., HL-93 AASHTO vehicular loading or EN 1991-2 traffic line loading). These rudimentary approaches for considering traffic load may cause underestimation of bridge failure risks during earthquakes. This study addresses this limitation by adopting detailed superstructure modeling of bridge superstructure to allow the traffic-bridge-interaction simulation that includes realistic spatial and time information of traffic. The equivalent moving traffic loads proposed in Chapter 3 incorporate both the spatial distribution of vehicles on the bridge deck and stochastic driver behaviors, such as lane changes, and have been shown to significantly influence structural response during earthquake events. The parametric study in Chapter 4 further indicated that the coupling of traffic effects with seismic excitation is more complex than just simple superposition of individual loading effects, highlighting the significance of the proposed framework that integrates time-varying traffic-bridge-interaction simulation and seismic analysis.

Improved fatigue analysis of the skewed and curved concrete bridge deck: The existing bridge fatigue analysis typically investigates the connections of steel bridges or piers of concrete bridges, while the analysis on bridge deck is lacking. Considering the potential high maintenance costs of deck due to fatigue damage, this study conducted traffic load-induced concrete bridge deck fatigue analysis by leveraging the capability of detailed superstructure modeling of the proposed bridge-traffic interaction framework. The framework proposed in this dissertation can provide accurate spatial information of deck fatigue for decision-making regarding bridge deck repairing (e.g., partial deck replacement v.s. whole deck

replacement). The importance of including spatial information is also critical for evaluating the rebar conditions of skewed and curved RC bridges. The ability to provide spatial information of fatigue in this study is superior than that of the existing studies, which often overlook spatial variation across the entire bridge deck. Additionally, this study modeled the coupling effects of the corrosion of rebar in concrete deck and traffic loading for a time-dependent fatigue analysis, which further provided temporal information of deck fatigue. This unique temporal-spatial information of fatigue for concrete decks is valuable for long-term planning of deck maintenance regarding when-to-repair and where-to-repair.

7.3 Directions for Future Studies

Fragility analysis of the entire structural system for skewed and curved bridges: Although the component fragility curves of skewed and curved bridges developed in this study are valuable for component level maintenance of the bridge, its usage in determining the failure probability of the bridge is limited. Future study can focus on developing fragility for the entire structural system of the skewed and curved bridges. To develop such a system level fragility, all possible failure modes of skewed and curved bridges with various geometry need to be investigated and identified in future studies.

Further study of coupling effects of traffic load and earthquake on skewed and curved bridges: In Chapter 4, it is found from limited number of simulations that the bridge's vertical response can vary significantly depending on the time offset between the traffic load and earthquake load time histories, even when the traffic and seismic loading conditions remain the same. In addition, the change of drivers'

behavior during earthquake was not considered in the current study, which may induce more uncertainties in traffic loading and thus the bridge vertical response. In future studies, stochastic simulation can be conducted to systematically quantify the uncertainties due to time offsets between time histories of traffic and earthquake loading, as well as variation in drivers' behavior.

Fatigue crack propagation: Severe concrete cracks may lead to more rebar corrosion. On the other hand, rebar corrosion may accelerate the propagation of concrete cracks. In addition, the mechanism of initiation of concrete fatigue crack is not well understood. The current study considered neither the complex relationship between the extent of deck cracking and rebar corrosion, nor the mechanism of concrete fatigue crack initiation. Future study can focus on investigating the aforementioned knowledge gaps, which will enable prediction of propagation of concrete fatigue crack over time. Such information is valuable for supporting maintenance decisions on bridge deck, as severe cracks may negatively impact comfort of driving.

Fatigue analysis for composite bridges: The bridge deck fatigue has not been analyzed for composite skewed and curved bridges with steel substructure and concrete bridge deck. Such bridges may experience the similar type of deck damage as concrete bridges and need repairs depending on the severity of concrete fatigue damage. In future studies, the proposed framework can be extended to enable the fatigue analysis of such composite bridges to predict the temporal and spatial distribution of deck fatigue damage and inform

repair decisions, such as when-to-repair and where-to-repair (partial repair of a portion of the bridge deck or full re-construction of bridge deck).

Generalization of the proposed farmwork: The proposed framework may be hard to be applied in practice by engineers due to its complexity. Future efforts should be devoted on the generalization of the framework, so that engineers can quickly implement the proposed framework with a few basic inputs. For example, the framework can be implemented as a program that automatically generates discretized shell elements for skewed and curved bridge decks based on key geometric inputs such as skew angle, curvature radius, and the coordinates of the four deck corners. Then, the remaining structural components, such as girders, abutments, and columns, can then be modeled based on their relative positions to the deck. The appropriate connection types can be determined by the users. The simulation of traffic loads and rebar corrosion states can also be automated using a few user-defined input parameters.

REFERENCES

AASHTO (2013). LRFD Bridge Design Specifications, Customary U.S. Units, 6th Edition, with 2013 Interim Revisions

AASHTO, G. (1989). Guide specifications for strength evaluation of existing steel and concrete bridges. Washington, DC.

AASHTO, L. (2012). "AASHTO LRFD bridge design specifications." American Association of State Highway and Transportation Officials, Washington, DC.

Ahmed, T. M. A., Burley, E., & Rigden, S. R. (1999). The effect of alkali—silica reaction on the fatigue behaviour of plain concrete tested in compression, indirect tension and flexure. Magazine of Concrete Research, 51(6), 375–390.

Ahn, W., & Reddy, D. V. (2001). Galvanostatic testing for the durability of marine concrete under fatigue loading. Cement and Concrete Research, 31(3), 343–349.

Aldea, S., Bazaez, R., Astroza, R., & Hernandez, F. (2021). Seismic fragility assessment of Chilean skewed highway bridges. Engineering Structures, 249, 113300.

Alsharqawi, M., Dawood, T., Abdelkhalek, S., Abouhamad, M., & Zayed, T. (2022). Condition assessment of concrete-made structures using ground penetrating radar. Automation in Construction, 144, 104627.

American Society of Civil Engineers. Seismic Analysis of Safety Nuclear Structures and Commentary on Standard for Seismic Analysis of Safety Related Nuclear Structures, New York, 1986; 91.

Apostolopoulos, C. A. (2007). Mechanical behavior of corroded reinforcing steel bars S500s temp core under low cycle fatigue. Construction and Building Materials, 21(7), 1447–1456.

ASCE, A. (2010). Minimum design loads for buildings and other structures. Reston, VA.

ASCE Committee on America's Infrastructure. (2021). 2021 Infrastructure report card. www.infrastructurereportcard.org

Ashebo, D. B., Chan, T. H., & Yu, L. (2007). Evaluation of dynamic loads on a skew box girder continuous bridge Part I: Field test and modal analysis. Engineering Structures, 29(6), 1052-1063.

Association, J. R. (2002). "Design specifications of highway bridges, Part V seismic design." Maruzen, Tokyo, Japan.

Ates, S., & Constantinou, M. C. (2011). Example of application of response spectrum analysis for seismically isolated curved bridges including soil-foundation effects. Soil Dynamics and Earthquake Engineering, 31(4), 648-661.

Azizinamini, A. (2009). A short-span bridges. In MODERN STEEL CONSTRUCTION.

Baker, J. W., and Cornell, C. A. (2005). A vector-valued ground motion intensity measure consisting of spectral acceleration and epsilon. Earthquake Engineering and Structural Dynamics, 34(10), 1193-1217.

Baker, J. W., and Cornell, C. A. (2006). Vector-valued ground motion intensity measures for probabilistic seismic demand analysis. Pacific Earthquake Engineering Research Center, College of Engineering, University of California, Berkeley.

Bakkar, M. A., Kanrar, B., Saha, R., & Das, D. (2020). High-strain low-cycle fatigue behavior of thermomechanically treated rebar. Journal of Failure Analysis and Prevention, 20, 1029–1037.

Bakkar, M. A., Saha, R., & Das, D. (2021). Low cycle fatigue performance and failure analysis of reinforcing bar. Metals and Materials International, 27, 4952–4966.

Barnoff, R. M., Nagle, G., Suarez, M. G., Geschwindner, L. F., Merz, H. W., & West, H. H. (n.d.). Design, Fabrication, and Erection of a Curved, Prestressed Concrete Bridge with Continuous Girders.

Basaga, H. B., Bayraktar, A., & Kaymaz, I. (2012). An improved response surface method for reliability analysis of structures. Structural Engineering and Mechanics, 42(2), 175–189.

Basöz, N. I., & Kiremidjian, A. S. (1998). Evaluation of bridge damage data from the Loma Prieta and Northridge, California earthquakes. In Evaluation of bridge damage data from the Loma Prieta and Northridge, California earthquakes (p. 167).

Basöz, N. I., Kiremidjian, A. S., King, S. A., & Law, K. H. (1999). Statistical analysis of bridge damage data from the 1994 Northridge, CA, earthquake. Earthquake Spectra, 15(1), 25–54.

Baumgartner, W. (1999). Bridge–vehicle interaction using extended FE analysis. International Journal of Heavy Vehicle Systems, 6(1–4), 1–12.

Bavirisetty, R., Vinayagamoorthy, M., and Duan, L. (2000). "Dynamic Analysis." Bridge Engineering Handbook, W.-F. Chen and L. Duan, eds., CRC Press.

Bayane, I., Mankar, A., Brühwiler, E., & Sørensen, J. D. (2019). Quantification of traffic and temperature effects on the fatigue safety of a reinforced-concrete bridge deck based on monitoring data. Engineering Structures, 196. https://doi.org/10.1016/j.engstruct.2019.109357

Benedettini, F., Dilena, M., & Morassi, A. (2015). Vibration analysis and structural identification of a curved multi-span viaduct. Mechanical Systems and Signal Processing, 54, 84–107. https://doi.org/10.1016/j.ymssp.2014.08.008

Berkeley, C. S. I. (2011). Computer program SAP2000 v14. 2.4. Computers and Structures Inc., Berkeley, California.

Berrocal, C. G., Löfgren, I., Lundgren, K., & Tang, L. (2015). Corrosion initiation in cracked fiber reinforced concrete: Influence of crack width, fiber type, and loading conditions. Corrosion Science, 98, 128–139.

Billah, A. H. M. M., Alam, M. S., & Bhuiyan, M. A. R. (2013). Fragility analysis of retrofitted multicolumn bridge bent subjected to near-fault and far-field ground motion. Journal of Bridge Engineering, 18(10), 992–1004.

Billah, A. M., Alam, M. S., and Bhuiyan, M. R. (2012). Fragility Analysis of Retrofitted Multicolumn Bridge Bent Subjected to Near-Fault and Far-Field Ground Motion. Journal of Bridge Engineering, 18(10), 992-1004.

Blejwas, T. E., Feng, C. C., & Ayre, R. S. (1979). Dynamic interaction of moving vehicles and structures. Journal of Sound and Vibration, 67(4), 513–521.

Borjigin, S., Kim, C.-W., Chang, K.-C., & Sugiura, K. (2018). Nonlinear dynamic response analysis of vehicle–bridge interactive system under strong earthquakes. Engineering Structures, 176, 500–521.

Borjigin, S., Kim, C. W., Chang, K. C., & Sugiura, K. (2015). Non-linear seismic response analysis of vehicle-bridge interactive systems. Steel Construction, 8(1), 2-8.

Bridges, T. Officials. S. on. (2011). AASHTO guide specifications for LRFD seismic bridge design. AASHTO.

California Department of Transportation. (2006). Caltrans Seismic Design Criteria, (1.6), 161.

Caprani, C. C. (2013). Lifetime Highway Bridge Traffic Load Effect from a Combination of Traffic States Allowing for Dynamic Amplification. Journal of Bridge Engineering, 18(9), 901–909. https://doi.org/10.1061/(ASCE)BE.1943-5592.0000427

Cavallini, T. L., Calamusa, J. T., Kitts, A. M., & Tempest, B. Q. (2017). Field-observed cracking of paired lightweight and normalweight concrete bridge decks. International Journal of Concrete Structures and Materials, 11(1), 85–97.

Chalhoub, C., François, R., & Carcasses, M. (2020). Effect of Cathode–Anode distance and electrical resistivity on macrocell corrosion currents and cathodic response in cases of chloride induced corrosion in reinforced concrete structures. Construction and Building Materials, 245. https://doi.org/10.1016/j.conbuildmat.2020.118337

Chan, T. H. T., Guo, L., & Li, Z. X. (2003). Finite element modelling for fatigue stress analysis of large suspension bridges. Journal of Sound and Vibration, 261(3), 443–464.

Charhi, O. Ben, & Baba, K. (2023). Modeling the Fatigue Behavior of Pavement Using the Finite Element Method. The Scientific Conference on Geosciences and Environmental Management (GeoME), 368–379.

Chen, H., Zhan, X., Zhu, X., & Zhang, W. (2022). Fatigue evaluation of steel-concrete composite deck in steel truss bridge—A case study. Frontiers of Structural and Civil Engineering, 16(10), 1336–1350.

Chen, L., & Chen, S. (2016). Seismic fragility performance of skewed and curved bridges in low-to-moderate seismic region. Earthquakes and Structures, 10(4), 789–810. https://doi.org/10.12989/eas.2016.10.4.789

Chen, L., and Chen, S. (2016). “Seismic fragility performance of skewed and curved bridges in low-to-moderate seismic region.” Earthquakes and Structures, 10(4), 789–810.

Chen, L., Zhou, Y., & Chen, S. (2020). Hybrid Nonlinear Seismic Analysis of Bridges with Moving Traffic. Journal of Aerospace Engineering, 33(1), 04019102. https://doi.org/10.1061/(ASCE)AS.1943-5525.0001098

Chen, L., Zhou, Y. and Chen, S. (2020). Hybrid nonlinear seismic analysis of bridges with moving traffic, J. Aerosp. Eng., 2020, 33(1): 04019102.

Chen, S. R., & Wu, J. (2011). Modeling stochastic live load for long-span bridge based on microscopic traffic flow simulation. Computers & Structures, 89(9), 813–824. https://doi.org/10.1016/j.compstruc.2010.12.017

Chen, S. R., & Wu, J. (2011). Modeling stochastic live load for long-span bridge based on microscopic traffic flow simulation. Computers & Structures, 89(9–10), 813–824.

Chen, S. R., and Cai, C. S. (2007). “Equivalent wheel load approach for slender cable-stayed bridge fatigue assessment under traffic and wind: Feasibility study.” Journal of Bridge Engineering, 12(6), 755–764.

Chen, S. R., and Wu, J. (2009). “Dynamic performance simulation of long-span bridge under combined loads of stochastic traffic and wind.” Journal of Bridge Engineering, 15(3), 219–230.

Chen, S. R., and Wu, J. (2011). “Modeling stochastic live load for long-span bridge based on microscopic traffic flow simulation.” Computers & Structures, 89(9–10), 813–824.

Choi, E. (2002). “Seismic analysis and retrofit of Mid-America bridges.” Ph.D. thesis, Georgia Institute of Technology, Atlanta.

Choi, E., DesRoches, R., and Nielson, B. (2004). “Seismic fragility of typical bridges in moderate seismic zones.” Engineering Structures, 26(2), 187–199.

Chouw, N., and Hao, H. (2008). “Significance of SSI and nonuniform near-fault ground motions in bridge response I: Effect on response with conventional expansion joint.” Engineering Structures, 30(1), 141–153.

Chun, J. (2010). Skewed Bridge Behaviors: Experimental, Analytical, And Numerical Analysis. http://digitalcommons.wayne.edu/oa_dissertations

Deepu, S. P., Prajapat, K., & Ray-Chaudhuri, S. (2014). Seismic vulnerability of skew bridges under bi-directional ground motions. Engineering Structures, 71, 150-160.

Deng, L., and Cai, C. S. (2010). “Development of dynamic impact factor for performance evaluation of existing multi-girder concrete bridges.” Engineering Structures, 32(1), 21–31.

Deng, L., Yu, Y., Zou, Q., and Cai, C. S. (2014). “State-of-the-art review of dynamic impact factors of highway bridges.” Journal of Bridge Engineering, 20(5), 04014080.

Deng, M., & Yi, J. (2023). Fatigue life prediction of orthotropic steel deck strengthened with UHPC under stochastic traffic load—frontiers in Materials, 10, 1208363.

DesRoches, R., and Muthukumar, S. (2002). “Effect of pounding and restrainers on seismic response of multiple-frame bridges.” Journal of Structural Engineering, 128(7), 860–869.

Dicleli, M., & Erhan, S. (2013). Low cycle fatigue effects in integral bridge steel H-piles under seismic displacement reversals. Bridge Structures, 9(4), 185–190. https://doi.org/10.3233/BRS-130064

Dimitrakopoulos, E. G. (2011). Seismic response analysis of skew bridges with pounding deck–abutment joints. Engineering Structures, 33(3), 813-826.

di Prisco, M., Colombo, M., & Dozio, D. (2013). Fibre-reinforced concrete in fib Model Code 2010: principles, models and test validation. Structural Concrete, 14(4), 342–361.

Duprat, F. (2007). Reliability of RC beams under chloride-ingress. Construction and Building Materials, 21(8), 1605–1616. https://doi.org/10.1016/j.conbuildmat.2006.08.002

DuraCrete, K. (2000). Probabilistic performance based durability design of concrete structures The European Union–Brite EuRam III, Final technical report of Duracrete project, Document BE95-1347/R17.

Dyduch, K., Szerszeń, M., & Destrebecq, J.-F. (1994). Experimental investigation of the fatigue strength of plain concrete under high compressive loading. Materials and Structures, 27, 505–509.

Eisenmann, D., Margetan, F., Chiou, C.-P. T., Roberts, R., & Wendt, S. (2013). Ground penetrating radar applied to rebar corrosion inspection. AIP Conference Proceedings, 1511(1), 1341–1348.

Ellingwood, B. and H. Hwang (1985). Probabilistic descriptions of resistance of safety related structures in nuclear plants." Nuc. Engrg and Des. 88(2):169-178.

Ellingwood, B. R., and Kinali, K. (2009). Quantifying and communicating uncertainty in seismic risk assessment. Structural Safety, 31(2), 179-187.

En, B. S. (2003). 2. Eurocode 1: Actions on Structures–Part 2: Traffic Loads on Bridges. British Standard Institution, UK: London.

EN 1992-1-1: Eurocode 2: Design of concrete structures - Part 1-1: General rules and rules for buildings. (2004).

Endo, T. (1974). Damage evaluation of metals for random or varying loading. 1, 371–380.

Fafard, M., Bennur, M., & Savard, M. (1997). A general multi-axle vehicle model to study the bridge-vehicle interaction. Engineering Computations, 14(5), 491–508.

Fahmy, M. F., Wu, Z., Wu, G., and Sun, Z. (2010). “Post-yield stiffnesses and residual deformations of RC bridge columns reinforced with ordinary rebars and steel fiber composite bars.” Engineering Structures, 32(9), 2969–2983.

Fang, J., Li, Q., Jeary, A., and Liu, D. (1999). Damping of Tall Buildings: Its Evaluation and Probabilistic Characteristics. Structural Design of Tall Buildings, 8(2), 145–153.

Faris, N., Zayed, T., Fares, A., Abdelkhalek, S., & Abdelkader, E. M. (2024). Automated rebar recognition and corrosion assessment of concrete bridge decks using ground penetrating radar. Automation in Construction, 166. https://doi.org/10.1016/j.autcon.2024.105631

FEMA (1997) HAZUS. Earthquake loss estimation methodology. Technical Manual, National Institute of Building for the Federal Emergency Management Agency, Washington (DC), 1997

FEMA (2003). HAZUS-MH MR1: Technical Manual, Vol. Earthquake Model. Federal Emergency Management Agency, Washington DC.

FHWA (1995). Seismic Retrofitting Manual for Highway Bridges, Vol. FHWA-RD-94- 052. Office of Engineering and Highway Operations R&D, Federal Highway Administration, McLean, VA.

Firouzi, A., & Rahai, A. R. (2011). Prediction of extent and likelihood of corrosion-induced cracking in reinforced concrete bridge decks.

Francois, R., & Arliguie, G. (1999). Effect of microcracking and cracking on the development of corrosion in reinforced concrete members. Magazine of Concrete Research, 51(2), 143–150.

Frangopol, D. M., Strauss, A., & Kim, S. (2008). Bridge reliability assessment based on monitoring. Journal of Bridge Engineering, 13(3), 258–270.

Frýba, L., & Yau, J.-D. (2009). Suspended bridges subjected to moving loads and support motions due to earthquake. Journal of Sound and Vibration, 319(1–2), 218–227.

Ghobarah, A. (2001). "Performance-based design in earthquake engineering: state of development." Engineering structures, 23(8), 878–884.

Ghosh, J., Caprani, C. C., & Padgett, J. E. (2014). Influence of traffic loading on the seismic reliability assessment of highway bridge structures. Journal of Bridge Engineering, 19(3), 04013009.

Ghosh, J., Caprani, C. C., and Padgett, J. E. (2013). "Influence of traffic loading on the seismic reliability assessment of highway bridge structures." Journal of Bridge Engineering, 19(3), 04013009.

Ghotbi, A. R. (2016, February). Response sensitivity analyses of skewed bridges with and without considering soil–structure interaction. In Structures (Vol. 5, pp. 219-232). Elsevier.

Goel, R. K., & Chopra, A. K. (1997). Evaluation of bridge abutment capacity and stiffness during earthquakes. Earthquake Spectra, 13(1), 1–23.

Goel RK, Chopra AK. Evaluation of bridge abutment capacity and stiffness during earthquakes. Earthq Spectra 1997;13(1):1–24.

González, A., & Znidaric, A. (2009). Recommendations on dynamic amplification allowance. European Commission.

González, A., Dowling, J., O'Brien, E. J., & Žnidarič, A. (2012). Testing of a bridge weigh-in-motion algorithm utilising multiple longitudinal sensor locations. Journal of Testing and Evaluation, 40(6), 961–974.

Graf, O., & Brenner, E. (1934). Experiments for investigating the resistance of concrete under often repeated compression loads. Bulletin, 1, 17–25.

Gu, C., Ye, G., & Sun, W. (2015). A review of the chloride transport properties of cracked concrete: experiments and simulations. Journal of Zhejiang University-SCIENCE A, 16(2), 81–92.

Guo, Z., Ma, Y., Wang, L., & Zhang, J. (2019). Modeling guidelines for corrosion-fatigue life prediction of concrete bridges: Considering corrosion pit as a notch or crack. Engineering Failure Analysis, 105, 883–895.

Haddadi, H., Shakal, A., Stephens, C., Savage, W., Huang, M., Leith, W., ... & Borcherdt, R. (2008, January). Center for engineering strong-motion data (CESMD). In Proceedings of the 14th World Conference on Earthquake Engineering, Beijing, October (pp. 12-17).

Han, Q., Du, X., Liu, J., Li, Z., Li, L., & Zhao, J. (2009). Seismic damage of highway bridges during the 2008 Wenchuan earthquake. Earthquake Engineering and Engineering Vibration, 8(2), 263-273.

Han, W., Yuan, Y., Huang, P., Wu, J., Wang, T., & Liu, H. (2017). Dynamic impact of heavy traffic load on typical T-beam bridges based on WIM data. Journal of Performance of Constructed Facilities, 31(3), 04017001.

Haseli, B., Nouri, G., Taromi, M. M., Bahari, M., Adili, E., & Keyghobadi, A. (2024). Effect of Skew Angle on Seismic Response of Irregular Concrete Bridges with Horizontal Curve. KSCE Journal of Civil Engineering, 28(6), 2329–2343. https://doi.org/10.1007/s12205-024-1464-y

Heidari, S., & Gerami, M. (2019). The Effect of Skewness on Rotational Response of the Curved Bridge Deck under Near-Fault Motions. KSCE Journal of Civil Engineering, 23(11), 4836-4845.

Hewitt, B. E., & Batchelor, B. deV. (1975). Punching shear strength of restrained slabs. Journal of the Structural Division, 101(9), 1837–1853.

Hou, G., & Chen, S. (2017). Bent Connection Options for Curved and Skewed SMC Bridges in Low-to-Moderate Seismic Regions. Practice Periodical on Structural Design and Construction, 22(4), 04017011.

Houtenbos, J. R. (2016). Fatigue Load Model Safety: Verifying Reliability for Reinforced Concrete Railway Structures.

Hwang, H., Jernigan, J. B., & Lin, Y. W. (2000). Evaluation of seismic damage to Memphis bridges and highway systems. Journal of Bridge Engineering, 5(4), 322-330.

International Conference of Building O cials (ICBO). Uniform Building Code, Vol. 2, Structural Engineering Design Provisions, Whittier, CA, 1997; 492.

Issa, M. A., Alhassan, M. A., & Shabila, H. I. (2007). Low-Cycle Fatigue Testing of High-Performance Concrete Bonded Overlay–Bridge Deck Slab Systems. Journal of Bridge Engineering, 12(4), 419–428. https://doi.org/10.1061/(ASCE)1084-0702(2007)12:4(419)

Jaffer, S. J., & Hansson, C. M. (2008). The influence of cracks on chloride-induced corrosion of steel in ordinary Portland cement and high-performance concretes subjected to different loading conditions. Corrosion Science, 50(12), 3343–3355.

Jang, S. Y., Kim, B. S., & Oh, B. H. (2011). Effect of crack width on chloride diffusion coefficients of concrete by steady-state migration tests. Cement and Concrete Research, 41(1), 9–19.

Jeon, J. S., DesRoches, R., Kim, T., & Choi, E. (2016). Geometric parameters affecting seismic fragilities of curved multi-frame concrete box-girder bridges with integral abutments. Engineering Structures, 122, 121–143. https://doi.org/10.1016/j.engstruct.2016.04.037

Kameda, H. (1992). Dynamic structure-vehicle interaction for seismic load evaluation of highway bridges. Proc. of 10th WCEE, 4861–4866.

Kameshwar, S., & Padgett, J. E. (2018). Effect of vehicle bridge interaction on seismic response and fragility of bridges. Earthquake Engineering & Structural Dynamics, 47(3), 697–713.

Karunananda, K., Ohga, M., Dissanayake, R., Siriwardane, S., & Chun, P.-J. (2012). New combined high and low-cycle fatigue models to estimate the life of steel bridges considering the interaction of high and low amplitude loadings. Advances in Structural Engineering, 15(2), 287–302.

Kataria, N. P., & Jangid, R. S. (2016). Seismic protection of the horizontally curved bridge with semi-active variable stiffness damper and isolation system. Advances in Structural Engineering, 19(7), 1103–1117. https://doi.org/10.1177/1369433216634477

Kawashima, K., Unjoh, S., Hoshikuma, J. I., & Kosa, K. (2011). Damage of bridges due to the 2010 Maule, Chile, earthquake. Journal of Earthquake Engineering, 15(7), 1036-1068.

Kesharee Patra, B., Pradeep, A., Bagchi, A., & Bagchi, A. (n.d.). Seismic analysis of skew deck slab bridges. https://www.researchgate.net/publication/383087410

Kim, C. W., Kawatani, M., Konaka, S., and Kitaura, R. (2011). “Seismic responses of a highway viaduct considering vehicles of design live load as dynamic system during moderate earthquakes.” Structure and Infrastructure Engineering, 7(7–8), 523–534.

Kim, J., & Song, J. (2021). Time-Dependent Reliability Assessment and Updating of Post-tensioned Concrete Box Girder Bridges Considering Traffic Environment and Corrosion. ASCE-

ASME Journal of Risk and Uncertainty in Engineering Systems, Part A: Civil Engineering, 7(4). https://doi.org/10.1061/ajrua6.0001188

Kim, W. S., Laman, J. A., & Linzell, D. G. (2007). Live load radial moment distribution for horizontally curved bridges. Journal of Bridge Engineering, 12(6), 727–736.

Konecny, P., & Lehner, P. (2017). Effect of cracking and randomness of inputs on corrosion initiation of reinforced concrete bridge decks exposed to chlorides. Frattura Ed Integrità Strutturale, 11(39), 29–37.

Kowalsky, M. J., and Priestley, M. N. (2000). Improved analytical model for shear strength of circular reinforced concrete columns in seismic regions. ACI Structural Journal, 97(3).

Kunnath Sashi K., Erduran Emrah, Chai Y. H., and Yashinsky Mark. (2008). "Effect of Near-Fault Vertical Ground Motions on Seismic Response of Highway Overcrossings." Journal of Bridge Engineering, 13(3), 282–290.

Kwon, K., & Frangopol, D. M. (2010). Bridge fatigue reliability assessment using probability density functions of equivalent stress range based on field monitoring data. International Journal of Fatigue, 32(8), 1221–1232.

Kwon, O. S., and Elnashai, A. S. (2007). Fragility Analysis of a Bridge with Consideration of Soil-Structure-Interaction Using Multi-Platform Analysis. In Structural Engineering Research Frontiers (pp. 1-14). ASCE.

Leahy, C., OBrien, E. J., Enright, B., & Hajializadeh, D. (2015). Review of HL-93 bridge traffic load model using an extensive WIM database. Journal of Bridge Engineering, 20(10), 04014115.

Lee, J.-H., Dong, P., & Kim, M.-H. (2020). Low-cycle fatigue evaluation for girth-welded pipes based on the structural strain method considering cyclic material behavior. International Journal of Naval Architecture and Ocean Engineering, 12, 868–880.

Lei, L., Xingang, S., Yunhua, C., Lefan, W., & Xiangcheng, Y. (2021). A new fatigue damage model for pavement concrete beams bearing multi-level bending loads. Plos One, 16(8), e0255048.

Li, N., Xu, W., Chen, Y., & Yan, W. (2019). Experimental research on adjacent pounding effect of midspan curved bridge with longitudinal slope. Engineering Structures, 196, 109320.

Li, W., Liu, W., & Wang, S. (2017). The effect of crack width on chloride-induced corrosion of steel in concrete. Advances in Materials Science and Engineering, 2017.

Li, W., Liu, W., & Wang, S. (2017). The Effect of Crack Width on Chloride-Induced Corrosion of Steel in Concrete. Advances in Materials Science and Engineering, 2017(1), 3968578.

Li, X., Zhang, D.-Y., Yan, W.-M., Chen, Y.-J., & Xie, W.-C. (2015). Shake-table test for a typical curved bridge: Wave passage and local site effects. Journal of Bridge Engineering, 20(2), 04014061.

Li, X., Zhang, D. Y., Yan, W. M., Chen, Y. J., & Xie, W. C. (2014). Shake-table test for a typical curved bridge: Wave passage and local site effects. Journal of Bridge Engineering, 20(2), 04014061.

Li. (2018). The dynamic response analysis of curved bridge under the moving load.

Lim, Y.-C., Kim, T.-S., & Hwang, C.-S. (2020). Modeling for apparent resistivity estimation along direction of electrode array above rebar in electrical resistivity measurement. Journal of Building Engineering, 31, 101417.

Lindorf, A., & Curbach, M. (2010). S–N curves for fatigue of bond in reinforced concrete structures under transverse tension. Engineering Structures, 32(10), 3068–3074.

Liu, H., Zhong, J., Ding, F., Meng, X., Liu, C., & Cui, J. (2022). Detection of early-stage rebar corrosion using a polarimetric ground penetrating radar system. Construction and Building Materials, 317, 125768.

Liu, M. F., Chang, T. P., & Zeng, D. Y. (2011). The interactive vibration behavior in a suspension bridge system under moving vehicle loads and vertical seismic excitations. Applied Mathematical Modelling, 35(1), 398-411.

Liu, R., & Yang, Y. (2021). Research on fatigue performance of steel-plate-concrete composite slab. Thin-Walled Structures, 160, 107339. https://doi.org/10.1016/j.tws.2020.107339

Lu, C., Jin, W., & Liu, R. (2011). Reinforcement corrosion-induced cover cracking and its time prediction for reinforced concrete structures. Corrosion Science, 53(4), 1337–1347.

Lu, T., Liu, J., Guo, T., Zhang, L., & Xia, Y. (2025). Traffic-induced fatigue damage evaluation of long-span suspension bridge integrating 27-year monitoring data and multi-scale finite element analysis. Journal of Civil Structural Health Monitoring, 1–21.

MacGregor, J. G., Wight, J. K., Teng, S., & Irawan, P. (1997). Reinforced concrete: mechanics and design (Vol. 3). Upper Saddle River, NJ: Prentice Hall.

Mackie, K. R., and Stojadinović, B. (2007). Performance-based seismic bridge design for damage and loss limit states. Earthquake Engineering and Structural Dynamics, 36(13), 1953-1971.

Mahmoud, H., Hodgson, I. C., & Bowman, C. A. (2006). Instrumentation, field testing, and fatigue evaluation of the selected approach spans the Throgs Neck Bridge (TN-82) over the East River, New York. ATLSS, Lehigh University.

Mallick, M., & Raychowdhury, P. (2015). Seismic analysis of highway skew bridges with nonlinear soil–pile interaction. Transportation Geotechnics, 3, 36-47.

Mander, J. B., Kim, D. K., Chen, S. S., & Premus, G. J. (1996). Response of steel bridge bearings to reversed cyclic loading.

Maragakis, E. (1984). A model for the rigid body motions of skew bridges.

Marsh, M. L., Buckle, I. G., & Kavazanjian Jr, E. (2014). LRFD seismic analysis and design of bridges: Reference manual. United States. Federal Highway Administration.

Martin, H., & Schiessl, P. (1969). The Influence of Cracks on the Corrosion of Steel in Concrete. International Symposium on the Durability of Concrete.

Martino, N., Maser, K., Birken, R., & Wang, M. (2016). Quantifying bridge deck corrosion using ground penetrating radar. Research in Nondestructive Evaluation, 27(2), 112–124.

Maruyama, Y., and Yamazaki, F. (2006). "RELATIONSHIP BETWEEN SEISMIC INTENSITY AND DRIVERS' REACTION IN THE 2003 MIYAGIKEN-OKI EARTHQUAKE." STRUCTURAL ENGINEERING / EARTHQUAKE ENGINEERING, 23(1), 69s–74s.

Matsumoto, K., Sato, Y., Ueda, T., & Wang, L. (2008). Mesoscopic analysis of mortar under high-stress creep and low-cycle fatigue loading. Journal of Advanced Concrete Technology, 6(2), 337–352.

Matthews, V. (2003). The challenges of evaluating earthquake hazard in Colorado. Engineering Geology in Colorado: Contributions, Trends, and Case Histories.

Mazzoni, S., Mckenna, F., Scott, M. H., and Fenves, G. L. (2006). The Open System for Earthquake Engineering Simulation (OpenSEES) User Command-Language Manual.

Meng, J. Y., Lui, E. M., & Liu, Y. (2001). Dynamic response of skew highway bridges. Journal of Earthquake Engineering, 5(02), 205–223.

Menun, C., and Der Kiureghian, A. (1998). “A Replacement for the 30%, 40%, and SRSS Rules for Multicomponent Seismic Analysis.” Earthquake Spectra, 14(1), 153–163.

Miarka, P., Seitl, S., Bílek, V., & Cifuentes, H. (2022). Assessment of fatigue resistance of concrete: SN curves to the Paris’ law curves. Construction and Building Materials, 341, 127811.

Michel, A., Otieno, M., Stang, H., & Geiker, M. R. (2016). Propagation of steel corrosion in concrete: Experimental and numerical investigations. Cement and Concrete Composites, 70, 171–182.

Michel, A., Otieno, M., Stang, H., & Geiker, M. R. (2016). Propagation of steel corrosion in concrete: Experimental and numerical investigations. Cement and Concrete Composites, 70, 171–182.

Miner, M. A. (1945). Cumulative damage in fatigue.

Misra, S., & Uomoto, T. (1991). Reinforcement corrosion under simultaneous diverse exposure conditions. Special Publication, 126, 423–442.

Mitchell, D., Huffman, S., Tremblay, R., Saatcioglu, M., Palermo, D., Tinawi, R., & Lau, D. (2012). Damage to bridges due to the 27 February 2010 Chile earthquake. Canadian Journal of Civil Engineering, 40(8), 675-692.

Monzon, E. V., Buckle, I. G., & Itani, A. M. (2016). Seismic performance and response of seismically isolated curved steel I-girder bridge. Journal of Structural Engineering, 142(12), 04016121

Morales-Nápoles, O., & Steenbergen, R. D. (2014). Large-scale hybrid Bayesian network for traffic load modeling from weigh-in-motion system data. Journal of Bridge Engineering, 20(1), 04014059.

Morris, W., Vico, A., & Vázquez, M. (2004). Chloride induced corrosion of reinforcing steel evaluated by concrete resistivity measurements. Electrochimica Acta, 49(25), 4447–4453. https://doi.org/10.1016/j.electacta.2004.05.001

Mukhopadhyay, S., & Gupta, V. K. (2013). Directivity pulses in near-fault ground motions—I: Identification, extraction and modeling. Soil Dynamics and Earthquake Engineering, 50, 1-15.

Mwafy, A. M., and Elnashai, A. S. (2007). Assessment of seismic integrity of multi-span curved bridges in mid-America.

Nettis, A., Nettis, A., Ruggieri, S., & Uva, G. (2024). Corrosion-induced fragility of existing prestressed concrete girder bridges under traffic loads. Engineering Structures, 314. https://doi.org/10.1016/j.engstruct.2024.118302

Neves, L. A., Frangopol, D. M., and Cruz, P. J. (2006). Probabilistic lifetime-oriented multi-objective optimization of bridge maintenance: Single maintenance type. Journal of Structural Engineering, 132(6), 991-1005.

Newmark, N. M., Blume, J. A., and Kapur, K. K. (1973). "Seismic design spectra for nuclear power plants." J. Power Div., Amer. Soc. Civil Eng., v. 99, no. PO2, pp. 287-303.

Newmark, N. M., University of Illinois at Urbana-Champaign, Department of Civil Engineering, and Trans-Alaska Pipleine System. (1975). Seismic design criteria for structures and facilities, Trans-Alaska Pipeline System. Dept. of Civil Engineering, University of Illinois at Urbana-Champaign, Urbana, Ill.

Nguyen, K., Velarde, C., & Goicolea, J. M. (2019). Analytical and simplified models for dynamic analysis of short skew bridges under moving loads. Advances in Structural Engineering, 22(9), 2076–2088. https://doi.org/10.1177/1369433219831481

Nielson, B. G. (2005). Analytical fragility curves for highway bridges in moderate seismic zones, Ph.D. dissertation, Georgia Institute of Technology.

Nielson, B. G., and DesRoches, R. (2007). Seismic fragility methodology for highway bridges using a component level approach. Earthquake Engineering and Structural Dynamics, 36(6), 823-839.

Nikoukalam, M. T., and Sideris, P. (2016). “Low-Damage Posttensioned Segmental Bridge Columns with Flexible End Joints for Seismic Accelerated Bridge Construction.” Transportation Research Record, 2592(1), 151–161.

Novák, Z. K., B. Teplý, D. (2004). Uncertainty in Service Life Prediction Based on Carbonation of Concrete. In Durability of Building Materials & Components 7 vol.1. Routledge.

OBrien, E. J., González, A., Dowling, J., & Žnidarič, A. (2013). Direct measurement of dynamics in road bridges using a bridge weigh-in-motion system. The Baltic Journal of Road and Bridge Engineering, 8(4), 263–270.

Oh, B. H. (1986). Fatigue analysis of plain concrete in flexure. Journal of Structural Engineering, 112(2), 273–288.

Oh, B. H., Asce, M., Lew, ; Young, & Choi, Y. C. (2007). Realistic Assessment for Safety and Service Life of Reinforced Concrete Decks in Girder Bridges. https://doi.org/10.1061/ASCE1084-0702200712:4410

Okada, K., Okamura, H., & Sonoda, K. (1978). Fatigue failure mechanism of reinforced concrete bridge deck slabs. Transportation Research Record, 664, 136–144.

Padgett, J. E., and DesRoches, R. (2007). Sensitivity of seismic response and fragility to parameter uncertainty. Journal of Structural Engineering, 133(12), 1710-1718.

Padgett, J. E., and DesRoches, R. (2008). Methodology for the development of analytical fragility curves for retrofitted bridges. Earthquake Engineering and Structural Dynamics, 37(8), 1157-1174.

Palmgren, A. (1924). Die Lev/bensdauer von kugellagern. VDI. Z., 68, 339–341.

Pan, Y., Agrawal, A. K., and Ghosn, M. (2007). Seismic fragility of continuous steel highway bridges in New York State. Journal of Bridge Engineering, 12(6), 689-699.

Pantelides, | C, Ibarra, L., Wang, Y., & Upadhyay, A. (n.d.). Seismic Rehabilitation of Skewed and Curved Bridges Using A New Generation of Buckling Restrained Braces.

PEER (Pacific Earthquake Engineering Research Center). (2011). "Pacific earthquake engineering research center PEER strong motion database." https://ngawest2.berkeley.edu (Mar. 28, 2018).

Perdikaris, P. C., & Beim, S. (1988). RC bridge decks under pulsating and moving load. Journal of Structural Engineering, 114(3), 591–607.

Pircher, M., Lechner, B., Mariani, O., & Kammersberger, A. (2011). Damage due to heavy traffic on three RC road bridges. Engineering Structures, 33(12), 3755–3761. https://doi.org/10.1016/j.engstruct.2011.08.012

PRC, A. C. I. (2021). 215-21. Concrete Structure Design for Fatigue Loading–Report. American Concrete Institute (ACI), Farmington Hills,(MI, USA).

Priestley, M. J. N., Seible, F. and Calvi, G. M. (1996), Seismic Design and Retrofit of Bridges, John Wiley &Sons, New York, USA

Protection, E. (1983). SEISMIC RETROFITTING GUIDELINES, FOR HIGHWAY BRIDGES.

Puckett, J. A., & Barker, R. M. (1997). Design of highway bridges: Based on AASHTO LRFD, bridge design specifications. Wiley-Interscience.

Rix, G. J., and Fernandez-Leon, J. A. (2004). Synthetic ground motions for Memphis, TN. http://www. ce. gatech. edu/research/mae_ground_ motionæ (Jul. 5, 2008).

Rosenblueth, E., and Contreras, H. (1977). "Approximate Design for Multicomponent Earthquakes." Journal of the Engineering Mechanics Division, 103(5), 881–893.

Saiidi, M., and Orie, D. (1992). Earthquake design forces in regular highway bridges. Computers and structures, 44(5), 1047-1054.

Samson, G., Deby, F., Garciaz, J.-L., & Perrin, J.-L. (2018). A new methodology for concrete resistivity assessment using the instantaneous polarization response of its metal reinforcement framework. Construction and Building Materials, 187, 531–544.

Sato, R., Shimomura, T., Maruyama, I., & Nakarai, K. (2008). Durability mechanics of concrete and concrete structures-re-definition and a new approach. JCI Committee Report), In: Tanabe, T. et al. Eds, Creep, Shrinkage and Durability Mechanics of Concrete and Concrete Structures, CRC Press, Leiden, 2, 1073–1098.

Schießl, P., & Martin, H. (1969). The Influence of Cracks on the Corrosion of Steel in Concrete. RILEM-Symposium" Durability of Concrete".

Schießl, P., & Raupach, M. (1997). Laboratory studies and calculations on the influence of crack width on chloride-induced corrosion of steel in concrete. Materials Journal, 94(1), 56–61.

Schläfli, M., & Brühwiler, E. (1998). Fatigue of existing reinforced concrete bridge deck slabs. Engineering Structures, 20(11), 991–998.

Seo, J., & Rogers, L. P. (2017). Comparison of curved prestressed concrete bridge population response between area and spine modeling approaches toward efficient seismic vulnerability analysis. Engineering Structures, 150, 176–189. https://doi.org/10.1016/j.engstruct.2017.07.033

Serdar, N., & Folić, R. (2018). Vulnerability and optimal probabilistic seismic demand model for curved and skewed RC bridges. Engineering Structures, 176, 411-425.

Shao, Y., Miao, C., Brownjohn, J. M. W., & Ding, Y. (2022). Vehicle-bridge interaction system for long-span suspension bridge under random traffic distribution. 44, 1070–1080.

Sheng, G.-M., & Gong, S.-H. (1997). INVESTIGATION OF LOW CYCLE FATIGUE BEHAVIOR OF BUILDING STRUCTURAL STEELS UNDER EARTHQUAKE LOADING. 金属学报英文版, 10(1), 51.

Shinozuka, M., Kim, S. H., Kushiyama, S., and Yi, J. H. (2002). Fragility curves of concrete bridges retrofitted by column jacketing. Earthquake Engineering and Engineering Vibration, 1(2), 195-205.

Sivaramakrishnan, B. (2010). “Non-linear modeling parameters for reinforced concrete columns subjected to seismic loads.” thesis.

Song, S.-T., Chai, Y. H., & Hida, S. E. (2003). Live-load distribution factors for concrete box-girder bridges. Journal of Bridge Engineering, 8(5), 273–280.

Sonoda, K., & Horikawa, T. (1982). Fatigue strength of reinforced concrete slabs under moving loads. Fatigue of Steel and Concrete Structures, 455–462.

Spathelf, C. A., & Vogel, T. (2018). Fatigue performance of orthogonally reinforced concrete slabs: Experimental investigation. Engineering Structures, 168, 69–81.

SSRC Task Group 14. (1991). In Report of Workshop on Horizontally Curved Girders.

Standard, B. (1993). Eurocode 3—Design of steel structures—. BS EN, 1(1), 2005.

Standard, T. O. (2004). Standard Specification for Deformed and Plain Carbon Steel Bars for Concrete.

Stanton, J. F., and Mcniven, H. D. (1979). “THE DEVELOPMENT OF A MATHEMATICAL MODEL TO PREDICT THE FLEXURAL RESPONSE OF REINFORCED CONCRETE BEAMS TO CYCLIC LOADS, USING SYSTEM IDENTIFICATION.”

Stewart, M. G., & Mullard, J. A. (2007). Spatial time-dependent reliability analysis of corrosion damage and the timing of first repair for RC structures. Engineering Structures, 29(7), 1457–1464. https://doi.org/10.1016/j.engstruct.2006.09.004

Su, J., Wu, D., & Wang, X. (2023). Influence of ground motion duration on seismic behavior of RC bridge piers: The role of low-cycle fatigue damage of reinforcing bars. Engineering Structures, 279, 115587.

Sucuoğlu, H., and Erberik, A. (2004). Energy-based hysteresis and damage models for deteriorating systems. Earthquake engineering and structural dynamics, 33(1), 69-88.

Sullivan, I., and Nielson, B. G. (2010, May). Sensitivity analysis of seismic fragility curves for skewed multi-span simply supported steel girder bridges. In Proceedings of 19th Analysis and Computation Specialty Conference, Structures Congress (pp. 226-237).

Sun, C., Hennessey, S. A., Project Manager, P. E., Ahlman, M. S., Tadros, M. K., & Vranek, C. J. (n.d.). Value Engineering Arbor Road Bridge with Curved Precast Concrete Girders.

Tan, Z.-X., Xu, Y.-L., Zhu, L.-D., & Zhu, Q. (2024). Effect of Distributed Loading and Refined Modeling on Wind-Induced Stress Analysis of Long-Span Bridges. International Journal of Structural Stability and Dynamics, 24(10), 2450109.

Timoshenko, S., Young, D. H., and Weaver, W. (1974). Vibration Problems in Engineering [By] S. Timoshenko, D.H. Young [And] W. Weaver, Jr. Wiley, New York.

Tondini, N., & Stojadinovic, B. (2012). Probabilistic seismic demand model for curved reinforced concrete bridges. Bulletin of earthquake engineering, 10(5), 1455-1479.

Tremper, B. (1947). The corrosion of reinforcing steel in cracked concrete. Journal Proceedings, 43(6), 1137–1144.

Unjoh, S., Nakatani, S., Tamura, K., Fukui, J., & Hoshikuma, J. (2002). 2002 Seismic Design Specifications for Highway Bridges. NIST SPECIAL PUBLICATION SP, 231–240.

Verma, M., & Mishra, S. S. (2019). Coupled fatigue-corrosion life estimation of reinforced concrete beam: Numerical versus experimental approach. Structural Concrete, 20(6), 2194–2205.

Vickery, P. J., Skerlj, P. F., Lin, J., Twisdale Jr, L. A., Young, M. A., and Lavelle, F. M. (2006). HAZUS-MH hurricane model methodology. II: Damage and loss estimation. Natural Hazards Review, 7(2), 94-103.

Vu, K. A. T., Stewart, M. G., & Asce, M. (2005.). Predicting the Likelihood and Extent of Reinforced Concrete Corrosion-Induced Cracking. https://doi.org/10.1061/ASCE0733-94452005131:111681

Wang, C., Zhang, P., Duan, L., Wang, Q., & Zhai, M. (2018). Fatigue Performance Evaluation of Existing Concrete Girder Bridges. Structural Engineering International, 28(3), 280–287.

Wang, T., Zhao, D. D., & Wu, S. Y. (2023). Fatigue reliability evaluation of reinforced concrete bridges under stochastic traffic loading based on truck weight limits. Advances in Structural Engineering, 26(11), 1973–1987. https://doi.org/10.1177/13694332231178983

Wang, Y. (2020). Eccentricity-Induced Seismic Behavior of Curved Bridges Based on Controllability. Symmetry, 12(10), 1633.

Wardhana, K., Hadipriono, F. C., & Asce, F. (2003). Analysis of Recent Bridge Failures in the United States. https://doi.org/10.1061/ASCE0887-3828200317:3144

Weaver Jr, W., Timoshenko, S. P., & Young, D. H. (1991). Vibration problems in engineering. John Wiley & Sons.

Wen, Y. K., and Wu, C. L. (2001). Uniform hazard ground motions for Mid-America cities. Earthquake spectra, 17(2), 359-384.

Werner, S. D., Beck, J. L., & Levine, M. B. (1987). Seismic response evaluation of Meloland Road Overpass using 1979 Imperial Valley earthquake records. Earthquake Engineering & Structural Dynamics, 15(2), 249–274.

Wibowo, H., Sanford, D. M., Buckle, I. G., & Sanders, D. H. (2012). Effects of live load on seismic response of bridges: a preliminary study. Civil Engineering Dimension, 14(3), 166–172.

Wibowo, H., Sanford, D. M., Buckle, I. G., & Sanders, D. H. (2013). Effect of live load on the seismic response of bridges.

Wibowo, H., Sanford, D. M., Buckle, I. G., and Sanders, D. H. (2012). “Effects of Live Load on Seismic Response of Bridges: A Preliminary Study.” Civil Engineering Dimension, 14(3), 166–172.

Wilson, T., Chen, S., and Mahmoud, H. (2015). “Analytical case study on the seismic performance of a curved and skewed reinforced concrete bridge under vertical ground motion.” Engineering Structures, 100, 128–136.

Wilson, T., Mahmoud, H., & Chen, S. (2014). Seismic performance of skewed and curved reinforced concrete bridges in mountainous states. Engineering Structures, 70, 158-167.

WSDOT (2002). Design Manual, Program Development Division, Washington State Department of Transportation, Olympia, WA. (http://www.wsdot.wa.gov/Publications/Manuals/M22-01.htm)

Wu, D., Ding, Y., Su, J., Li, Z.-X., & Zong, L. (2022). Investigation on low-cycle fatigue performance of high-strength steel bars including the effect of inelastic buckling. Engineering Structures, 272, 114974. https://doi.org/10.1016/j.engstruct.2022.114974

Wu, H., Wu, X., He, W., Wang, F., & Deng, L. (2023). A computer vision-assisted method for identifying wheel loads of moving vehicles from dynamic bridge responses. Mechanical Systems and Signal Processing, 197. https://doi.org/10.1016/j.ymssp.2023.110372

Wu, S., Buckle, I. G., Itani, A. M., & Istrati, D. (2019). Experimental studies on seismic response of skew bridges with seat-type abutments. I: Shake table experiments. Journal of Bridge Engineering, 24(10), 04019096.

Wysokowski, A. (2020). Impact of Traffic Load Randomness on Fatigue of Steel Bridges. The Baltic Journal of Road and Bridge Engineering, 15(5), 21–44. https://doi.org/10.7250/bjrbe.2020-15.505

Xia, C., Wang, B., Luo, T., Min, Q., Sekulic, D., & Li, Y. (2022). Dynamic amplification factor of multi-span simply supported beam bridge under traffic flow. Advances in Structural Engineering, 25(8), 1829–1847.

Xiao, Y., and Ma, R. (1997). Seismic retrofit of RC circular columns using prefabricated composite jacketing. Journal of Structural Engineering, 123(10), 1357-1364.

Xu, J., Jiang, L., & Wang, J. (2009). Influence of detection methods on chloride threshold value for the corrosion of steel reinforcement. Construction and Building Materials, 23(5), 1902–1908.

Yang, D.-H., Yi, T.-H., & Li, H.-N. (2017). Coupled Fatigue-Corrosion Failure Analysis and Performance Assessment of RC Bridge Deck Slabs. Journal of Bridge Engineering, 22(10). https://doi.org/10.1061/(asce)be.1943-5592.0001108

Yi, W., & Tang, F. (2010). Fatigue Behavior of Reinforced Concrete Beams with Corroded Steel Reinforcement. In ACI Structural Journal (Vol. 107, Issue 5). https://www.researchgate.net/publication/266384685

Yin, W., & Hsu, T. T. C. (1995). Fatigue behavior of steel fiber reinforced concrete in uniaxial and biaxial compression. Materials Journal, 92(1), 71–81.

Zakeri, B., Padgett, J. E., and Amiri, G. G. (2014). Fragility analysis of skewed single frame concrete box girder bridges. Journal of Performance of Constructed Facilities, 28(3), 571–582.

Zayed & Faris (2023). Synthesized evaluation of reinforced concrete bridge defects, their non-destructive inspection and analysis methods: a systematic review and bibliometric analysis of the past three decades. Buildings, 13(3), 800.

Zhang, J., and Huo, Y. (2009). Evaluating effectiveness and optimum design of isolation devices for highway bridges using the fragility function method. Engineering Structures, 31(8), 1648-1660.

Zhang, L., Sun, Z., Zhang, C., Dong, F., & Wei, P. (2018). Numerical Investigation of the Dynamic Responses of Long-Span Bridges With Consideration of the Random Traffic Flow Based on the Intelligent ACO-BPNN Model. IEEE Access, 6, 28520–28529. https://doi.org/10.1109/ACCESS.2018.2840333

Zhang, M., Wang, X., & Li, Y. (2024). Fatigue Reliability Assessment of Bridges Under Heavy Traffic Loading Scenario. Infrastructures, 9(12), 238.

Zhang, W., & Yuan, H. (2014). Corrosion fatigue effects on life estimation of deteriorated bridges under vehicle impacts. Engineering Structures, 71, 128–136. https://doi.org/10.1016/j.engstruct.2014.04.004

Zhang, W., Liu, X., & Gu, X. (2016). Fatigue behavior of corroded prestressed concrete beams. Construction and Building Materials, 106, 198–208.

Zhi, Z., Xiaojun, L., Riqing, L., & Chenning, S. (2019). Shaking table tests and numerical simulations of a small radius curved bridge considering SSI effect. Soil Dynamics and Earthquake Engineering, 118, 1-18.

Zhou, Y., & Chen, S. (2018). Full-response prediction of coupled long-span bridges and traffic systems under spatially varying seismic excitations. Journal of Bridge Engineering, 23(6), 04018031.

Zhou, Y., and Chen, S. (2014). Dynamic simulation of a long-span bridge-traffic system subjected to combined service and extreme loads. Journal of Structural Engineering, 141(9), 04014215.

Zhou, Y., and Chen, S. (2015). Numerical investigation of cable breakage events on long-span cable-stayed bridges under stochastic traffic and wind. Engineering Structures, 105, 299-315.

Zhou Yufen, and Chen Suren. (2015). “Dynamic Simulation of a Long-Span Bridge-Traffic System Subjected to Combined Service and Extreme Loads.” Journal of Structural Engineering, 141(9), 04014215.

Zhu, B., & Frangopol, D. M. (2012). Risk-based approach for optimum maintenance of bridges under traffic and earthquake loads. Journal of Structural Engineering, 139(3), 422-434.

Zhu, B., & Frangopol, D. M. (2013). Risk-based approach for optimum maintenance of bridges under traffic and earthquake loads. Journal of Structural Engineering, 139(3), 422–434.

[Original source: https://studycrumb.com/alphabetizer] you to play with in the 'Reference Lists' section.